A Mathematical Analysis of Digestive Processes in a Model Stomach

A thesis submitted to the School of Mathematics of the University of East Anglia
in partial fulfilment of the requirements for the degree of Doctor of Philosophy

By Lydia M. Rickett
School of Mathematics,
University of East Anglia,
Norwich Research Park,
Norwich,
NR4 7TJ

August 2013

Abstract

It is of great medical interest to gain a better understanding of digestion in the human stomach, not least because of the relevance to nutrient and drug delivery. The Institute of Food Research has developed the Dynamic Gastric Model, a physical, *in vitro* model stomach capable of re-creating the physiological conditions experienced *in vivo*.

The aim of this thesis is to examine mathematically digestion in the main body (top section) of the Dynamic Gastric Model, where gentle wall movements and gastric secretions result in the outside layer of the digesta "sloughing off", before passing into the bottom section for further processing. By considering a simplified, local description of the flow close to the wall, we may gain an insight into the mechanisms behind this behaviour. This description focuses on the mixing of two layers of creeping fluid through temporal instability of the perturbed fluid interface. Some attention is also paid to a more general study of the surrounding flow field.

Linear, two-fluid flow next to a prescribed, sinusoidally moving wall is found to be stable in all cases. Studies of thin film flow next to such a wall suggest that the same may be true of the nonlinear case, although in the case of an inclined wall wave steepening is found to occur for early times. A linear instability is found for small wavenumber disturbances when the wall is modelled as an elastic beam or when we include a scalar material field that acts to alter the surface tension at the interface. An examination of Navier–Stokes flow of a single fluid through a diverging channel (representing a small strip through the centre of the main body) reveals that the flow loses symmetry at a lower Reynolds number than flow through a channel of uniform width. Our results are interpreted in terms of the Dynamic Gastric Model.

Acknowledgements

First, I would like to thank my advisors from the University of East Anglia, Mark Blyth, Mark Cooker and Richard Purvis, and from the Institute of Food Research, Rob Penfold, for their tireless mentoring throughout my PhD. I am also appreciative to the Institute of Food Research for securing the funding that enabled me to undertake a postgraduate studentship.

I am grateful to all who have contributed to the many interesting discussions that I have had the opportunity to attend on the topic of the gastrointestinal tract, both from the Institute of Food Research and elsewhere. In particular I would like to thank Richard Faulks and Martin Wickham for their illuminating explanations of the workings of both the Dynamic Gastric Model and the human stomach.

I would like to thank my husband, Chris, for his limitless support while I worked on this thesis and my daughter, Georgia, for providing an endearing distraction in the stages of writing up. Finally, I would like to thank my father for encouraging an interest in mathematics from an early age.

Contents

List of Tables

List of Figures

Chapter 1

Introduction

1.1 Physical Motivation

It is of great medical interest to understand the processes governing the availability of nutrients from food (and drugs) for absorption by the human digestive system, or gastrointestinal (GI) tract. During digestion, food passes through the mouth and esophagus into the stomach, before moving on to the small and large intestines. Studies of the passage of food or drugs through the GI tract are generally limited to simple laboratory experiments, using for instance the paddle dissolution apparatus, or *in vivo* measurements, which raise difficulties both physically and ethically. In recent years this has led to the development of physical, *in vitro* models of some of the major digestive organs. Such devices are either static or dynamic; the latter aim to replicate both the physical and physiological conditions experienced in the respective organs. Amongst the physical devices produced have been dynamic models of the mouth (Salles *et al.*, 2007), stomach (Kong and Singh, 2008b), small intestine (Tharakan, 2008) and large intestine (Spratt *et al.*, 2005). The Netherlands Organisation for Applied Scientific Research Gastro-Intestinal Tract Model is a dynamic system that physically models both the stomach and small intestine (Krul *et al.*, 2000), although the focus is more on the small intestine and proximal colon. The focus of this thesis is the Dynamic Gastric Model (DGM), a physical, *in vitro* model stomach based at the Institute of Food Research (IFR).

1.1.1 The Human Stomach

The human stomach is a complex organ. Together with the mouth, its role is to break down food such that nutrients may be released and absorbed into cells via the bloodstream. A good summary of its physiology can be found in Kong and Singh (2008a). The stomach is generally divided into two sections (as shown in figure 1.1); the main body (or body), of which the very top section is called the fundus, and below this, the antrum, ending in the pylorus. The pylorus leads into the duodenum, which is the top section of the small intestine. Our work concentrates on a description of the main body,

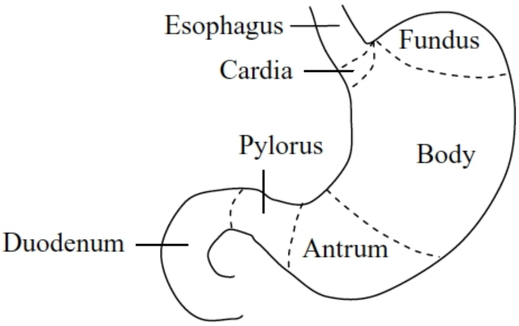

Figure 1.1: A figure showing the regions of the human stomach (Kong and Singh, 2008a).

which has received considerably less focus in the literature due to its primary function as a reservoir for undigested material.

The process of digestion begins even before food enters the stomach, as chewing, combined with the action of enzymes in saliva, begins to break down a meal. The meal therefore reaches the stomach as an inhomogeneous mixture, or food "bolus". The entry of food provokes the addition of gastric secretions, which enter through the walls of the main body and are made up of low pH, sterilising acids, salts, enzymes and water. The food bolus acts as a buffer in terms of pH so that the main body tends to contain higher pH and higher viscosity material in the bulk surrounded by low pH and low viscosity material around the outside. The pH may be particularly low close to the stomach wall. The secretions are combined with very gentle wall movements (as shown *in vivo* by Echo-Planar Nuclear Magnetic Resonance Imaging in Marciani *et al.* (2001)). The wall motion causes the more hydrated part of the food bolus to "slough off" in layers and pass into the antrum. This process is sometimes called the "onion peeling" effect. For this reason there are areas of the food bolus that are not in immediate contact with enzymes and this stage of digestion is a gradual process.

In the antrum, which has a higher density of smooth muscle, peristaltic waves grind and compress the digesta against the closed pylorus. The resulting backwash promotes a high shear environment, which causes mixing and significant break down of the food structure and produces a suspension of soft solid, partially digested food particles known as "chyme". The backwash also causes the sorting of particles by size, so that when the pylorus opens at the very end of a contraction, smaller particles are preferentially discharged.

Gastric contractions occur at a rate of approximately three per minute and gastric processing times can vary between around 15 minutes for water to between 45 minutes and an hour for a full meal (which is generally between 150 ml and 700 ml in volume, although the stomach capacity can be up to 4 litres). The contraction depth and frequency has been found to be independent of the meal composition, implying that in the case of a more substantial meal the stomach does more work. The general speed of digestion in the stomach is regulated by the rate of emptying and can vary greatly depending on, for instance, the meal temperature, energy content and viscosity, the amount of nutrients, sugars or fat present and the food structure and texture (see, for example, Marciani *et al.* (2001), Marciani *et al.* (2007)). On leaving the stomach, the meal enters the small intestine, where the majority of nutrient absorption takes place.

1.1.2 The Dynamic Gastric Model

Descriptions of the DGM and its use experimentally can be found in Mercuri *et al.* (2011) and Wickham *et al.* (2012). The DGM is an *in vitro*, computer controlled system, which is capable of processing real food in real time. The model accounts for the physical, mechanical and biochemical environment experienced during digestion and is the first model capable of processing a bolus of food and producing chyme. It can therefore be regarded as the first model to simulate human digestion from a genuinely physiological perspective.

Figure 1.2 gives an overview of the design. In this model the term "main body" describes the entire top half of the machine, whilst the "body" is the part of the machine that represents the stomach body itself. The body has dimensions of the $O(10^{-1})$ and is

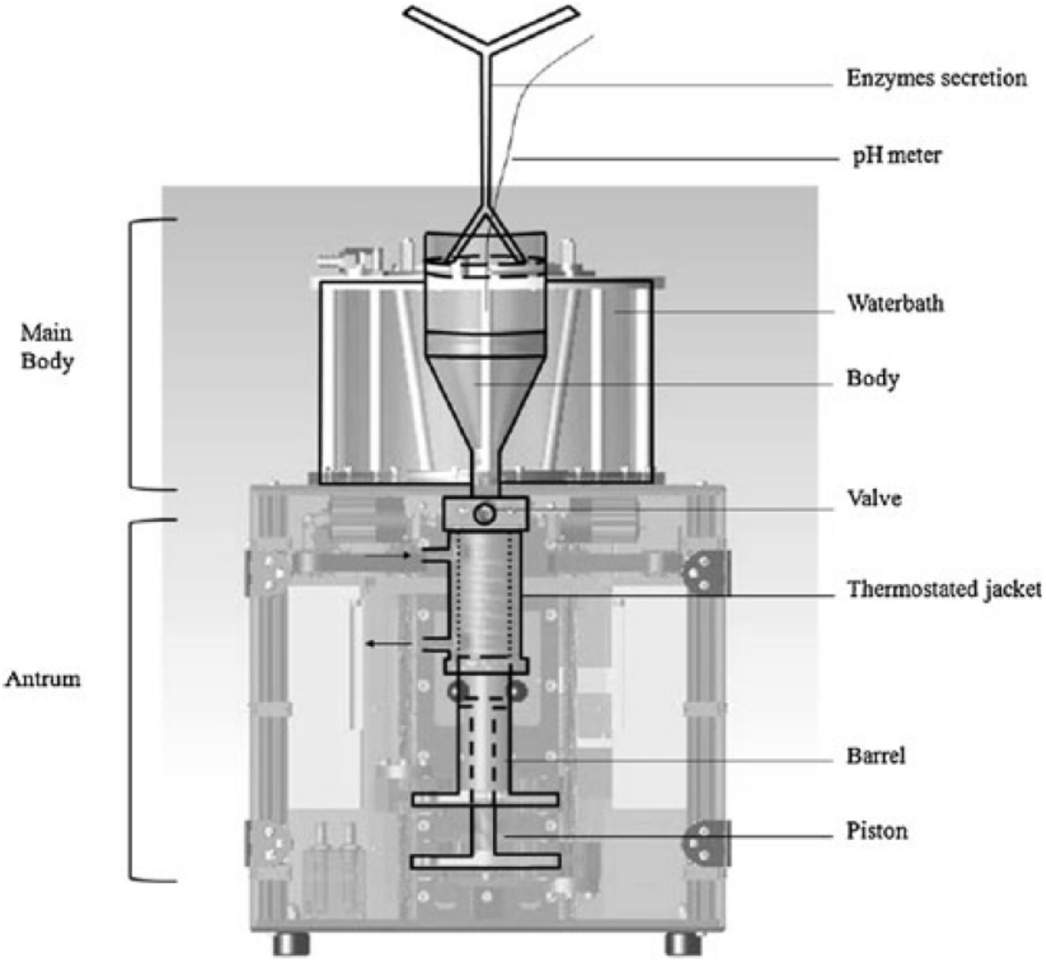

Figure 1.2: A schematic diagram of the Dynamic Gastric Model (Mercuri *et al.*, 2011).

modelled by a thermally-jacketed, elastic cone which is surrounded by a heated water bath. The cone is hydraulically squeezed by cyclic pumping of the surrounding water to promote the right mixing behaviour (as found in *in vivo* imaging in Marciani *et al.* (2001)). The temperature is set to 37 °C as in the *in vivo* stomach. Prior to an experiment, 20 ml of acid is added to simulate an empty stomach and the added pre-chewed digesta generally has a volume of around 400 to 450 ml, filling the cone and part of the plastic cylinder above. Sitting on top of the mixture inside the cone is a cap, or secretion distributor, from the rim of which a mixture of acids, bases, surfactants and proteolytic solutions, representing the gastric secretions, is added. The exact distribution and volume of added secretions is computer controlled. The addition of acid is determined by dynamically monitoring the pH inside the model and enzyme addition follows *in vivo* rates and is therefore governed by the quantity and type of meal being processed. The conical shape of the body has been chosen to allow for the best flow of secretions down the sides. A thin layer of low pH and low viscosity material can therefore be observed at the body wall. The cap itself is free to move as the contractions provide a volume displacement of around 40 ml. An intervening valve between the main body and antrum is only closed when the latter is emptying, and thus it is possible to obtain flux back into the main body (in a way similar to the *in vivo* stomach).

The antrum part of the machine comprises a vertically moving barrel and piston. The piston is responsible for both filling and emptying of material. Working in a complementary fashion with the conical geometry of the body, the piston draws the most hydrated, lower viscosity material from the walls of the main body into the antrum, simulating the "onion peeling" effect observed in the human stomach. Peristaltic waves are simulated by periodic movements of the barrel, which has a flexible annulus at its end, whilst small movements of the piston compensate for any volume changes that occur. The high shears created by this process result in mechanical breakdown of the food structure. During emptying the piston moves upwards and chyme exits through a tube, as shown figure 1.2. During this process smaller particles are more likely to be ejected, as seen *in vivo*, whilst larger particles remain for additional processing. The emptying of chyme from the antrum occurs in a series of pulses over time. Due to the realistic nature of food processing inside the DGM, the composition and distribution of the output varies depending on the meal contents. The process ends with a “housekeeper” wave, as seen in the human stomach, a strong contraction which is responsible for complete emptying of the stomach contents.

The IFR model provides a screening tool for evaluating novel and existing foodstuffs, diets and pharmaceutical preparations, and is also an opportunity to develop new mathematical descriptions of how the stomach works, in this case focussing on the main body. A mathematical model will give insight into the flow structure within the IFR model. It will also lead to a better understanding of the mixing of gastric secretions, a vital process within the digestive system.

1.2 Building a Mathematical Model

In this thesis we do not attempt to produce an all-encompassing mathematical description of digestive processes in the DGM main body, or to consider the global transport of material. Such an analysis would need to account for the non-Newtonian, inhomogeneous nature of the main body contents and would require computational modelling. By limiting our analysis to a subset of the set of flows relevant to the DGM main body, we hope to gain a more general understanding of the underlying mechanisms that guide, for example, the "onion peeling" effect that is observed in practice. After some initial work considering a very simple representation of the elastic cone, we choose to focus instead on a thin region close to the wall. In this analysis we take "digestion" to mean the mixing of two layers of fluid, in particular through temporal instability of the fluid interface between the two.

1.2.1 Assumptions

We consider incompressible, isothermal, Newtonian flow and all fluids are taken to be immiscible and of equal densities. In the majority of our work we do not include the effects of gravity and so choose not to focus on such phenomena as the Rayleigh–Taylor instability, which results when a heavier fluid sits above a lighter fluid, or Rayleigh–Bénard convection, where a layer of fluid is heated from below and can become unstable due to the effects of buoyancy.

Aside from a brief consideration of a plane polar geometry in the introduction of chapter 6, in the rest of this thesis we use a Cartesian co-ordinate system. The problem is simplified through the use of a two-dimensional planar geometry. Such a simplification does not allow for the Plateau–Rayleigh instability associated with a three-dimensional stream or jet of water. However, the squat geometry of the DGM main body suggests that the size of wavelength necessary for such an instability cannot be supported.

Most of our work focuses on inertia-free flow. The non-dimensional Reynolds number, Re, is defined as the ratio of inertial forces compared to viscous forces in a fluid and is given by

$$Re = \frac{UL}{\nu}, \tag{1.1}$$

where U and L are the characteristic speed and length scale in the fluid and ν is the constant kinematic viscosity, which is equal to the dynamic viscosity, μ, divided by the fluid density, ρ. Estimates for some of these values in the human stomach can be obtained from Pal *et al.* (2004). Together with local values for the DGM main body, this leads us to take a typical length scale to be of the $O(10^{-2})$ and a typical speed to be no more than 10^{-4} ms^{-1}. Kong and Singh (2008a) quote gastric juice as having a dynamic viscosity of between 10^{-2} and 2 kgm^{-1}s^{-1} with a density close to that of water (approximately 10^3 kgm^{-3}). The Reynolds number for gastric flow is then estimated to have an upper bound of the $O(10^{-1})$. Any increase in viscosity due to an intake of food will decrease this estimate further and so we can be confident in claiming that we are a dealing with a low Reynolds number flow in this analysis.

1.2.2 The Model

An idealised mathematical description of the flow field local to the wall of the DGM body is shown in figure 1.3. In this description, we envisage a fixed, solid food bolus suspended in the centre of the body and surrounded by a layer of homogeneous, liquid material. A second layer of homogeneous, liquid material is present at the body wall. These fluid layers are taken to represent two phases of partially digested food mixed with gastric secretions. The homogeneous nature of these fluids could also incorporate tablets in powder form, for instance, whose effect on the overall flow field is negligible. We next focus on a small region close to the body wall, such that any curvature of the food bolus can be taken to be negligible and the section of liquid between the bolus and the wall is relatively thin. The problem is therefore simplified to the case of two fluid flow in a channel, where the interface between the two fluids is taken to be well defined. In its most complex form this model may include a scalar material field, representing the propagation of gastric juices. We perturb the fluid interface and examine the temporal stability to determine whether perturbation growth and interfacial break down is likely to occur. Such growth is taken as an indication of mixing of the two fluid layers.

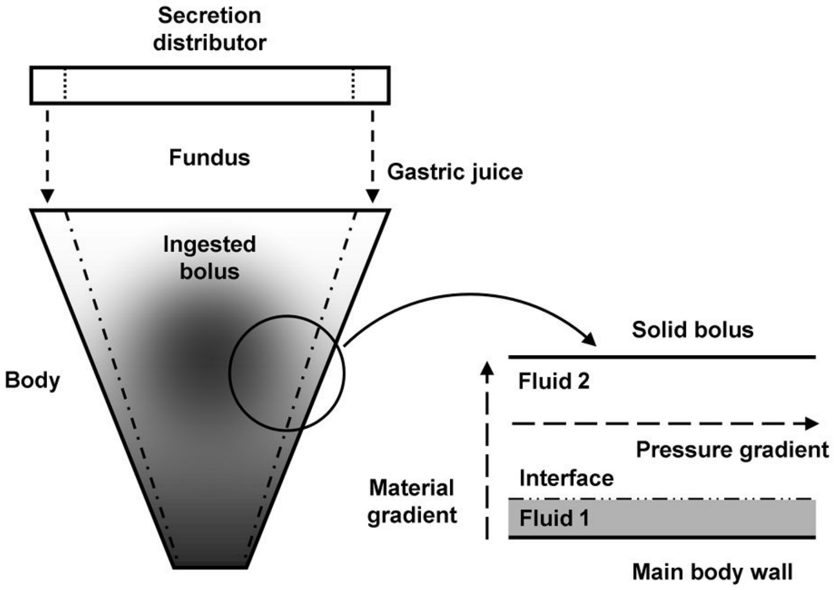

Figure 1.3: The model derived from a mathematical idealisation of the flow local to the wall of the DGM body.

We focus on a single possible mechanism for instability in each variation of this model considered so that to begin with, we do not include a material gradient. Also, we initially discount the second wall provided by the food bolus, so that the domain of the second fluid is taken to be infinite. In this case the liquids may be subject to a shear-driven, or possibly even a gravity-driven, flow. In chapters 2 and 3 we consider a prescribed, periodic wall motion. Chapter 3, which uses a thin film approximation, is the only chapter to deal with a fully nonlinear description of the flow field. Elsewhere we use a linear approximation. In an effort to promote an interaction between a free-moving wall and the interface, which it is thought may lead to an instability, chapter 4 focuses on an elastic wall with unprescribed position. In chapter 5 we strive to model the addition of gastric secretions to the DGM main body by including a scalar material field, which may act to alter the surface tension at the fluid interface. We also include the second wall representing the food bolus and consider flow through a fixed channel. In this case the fluids may be subject to a constant pressure gradient. In chapter 6 we consider a larger scale portion of the DGM flow field in order to gain an insight into the flow field surrounding, and therefore influencing, our idealised model. Here we depart from interfacial stability studies and, after some initial studies taking the Reynolds number to be small, we include the effect of inertia. As a model of the local flow field in a strip through the middle of the main body, we consider a single fluid between moving walls in a slowly diverging channel.

1.3 Literature Review

Due to the previously discussed difficulty in making accurate *in vivo* measurements of the GI tract, there have been a number of attempts to mathematically model the various organs. Trelea *et al.* (2008) considered aroma release during the process of swallowing food. Nicosia and Brasseur (2002) developed a model of food transport through the esophagus which allowed for both active and inactive muscle tensions. A general study of peristaltic flow as a means of transport at zero Reynolds numbers can be found in Pozrikidis (1987). More specifically, peristalsis has been studied as a mechanism for movement through the small intestine (Leger, 2005). Other studies considering the small intestine include Stoll *et al.* (2000), who studied molecular absorption in relation to drug uptake, and Tharakan (2008), who used computational fluid dynamics to model the physical, *in vitro* Small Intestinal Model. The effect of wall movements on intestinal absorption was examined in Macagno *et al.* (1982). More generally, Woollard *et al.* (2009) studied solute transport in a wavy channel and noted that their work is relevant to transport through the gut.

Previous studies of mathematical models of flow in the human stomach are few. Published work tends to be purely numerical. Two particularly notable papers, which use the lattice-Boltzmann method, are Pal *et al.* (2004) and Pal *et al.* (2007). In the first of these the effect of antral contraction waves on mixing was examined. Here mixing was defined by measuring the hypothetical spread of small particles released at a known location at a prescribed time. It was found that mixing occurs through a combination of circulatory motions and jets; the jets propagate in the opposite direction to the advancing waves. In Pal *et al.* (2007) the method was extended to consider gastric emptying and a "gastric emptying Magenstrasse" was found to exist; a narrow passage which experiences rapid emptying from deep within the fundus. Fluid mixing in a time-reversible, low Reynolds number environment is considered more generally in Cartwright *et al.* (2012), who suggested that non-reciprocal wall motions may be the cause of mixing in the stomach.

Published papers concerning the stability of interfacial flow are great in number. An important contribution came from Yih (1967), who considered the instability that is present for Couette–Poiseuille, channel flow of two fluids of different viscosities. It was shown that in the absence of inertia or a surfactant at the fluid interface, the solution is always stable. In this review we concentrate on the analyses of incompressible, interfacial flow where unstable solutions are found at zero Reynolds number.

Moving away from stability analysis, but still relevant to our work, is the problem of steady film flow down a fixed sinusoidal wall. In chapter 3 we consider thin film flow next to a moving sinusoidal wall. Wang (1981) considered the low Reynolds number, gravity-driven, steady flow of two fluids over a fixed sinusoidal surface, whose corrugations have a small amplitude compared to the thicknesses of the fluid domains. The amplitude and phase shift of the free surface were found to depend on the wavelength of the wall, as well as the surface tension of the free surface. This work was extended numerically by Pozrikidis (1988) to account for, amongst other factors, more general wall amplitudes. Shetty and Cerro (1993) used an asymptotic analysis, valid when inertial and surface tension effects are neglected, to look at the specific case where the amplitude of the wall is much larger than the film thickness. Wierschem and Aksel (2003) and Wierschem *et al.* (2005) focused on the stability of the free surface. They found that a critical Reynolds number exists, above which unstable solutions occur. A more detailed description of some of these papers can be found in chapter 3.

Kang and Chen (1995) performed an analogous perturbation analysis to Wang (1981) for two-layer flow. They found that the largest free surface and interface amplitudes were seen for a wall with long wavelength, and the largest phase shifts with respect to the wall were seen for waves whose wavelength is comparable to the thickness of the lower fluid layer. Luo and Pozrikidis (2006) completed a similar analysis, but for shear-driven Stokes flow in a channel with one fixed sinusoidal, and one fixed planar wall. When the interface is surfactant-free, the largest interface amplitudes (those comparable to the wall amplitude) were seen when the thickness of the film next to the wavy wall is small compared to the wavelength of the wall. The largest phase shifts were seen for moderate wall wavelengths compared to film thickness.

Yih (1963) and Benjamin (1957) considered the temporal stability of flow of a single fluid down an inclined plane. They found that above a critical Reynolds number (which depends on the angle of inclination), the flow is unstable to waves with long wavelengths. These waves travel at double the speed of the unperturbed flow at the free surface. The flow of two liquid films, of differing viscosities, moving down an inclined plane in the absence of surface tension has been shown to be unstable for all Reynolds numbers (including zero) when the less viscous fluid occupies the region next to the wall (Loewenherz and Lawrence, 1989; Chen, 1993). The instability is strongest when the two fluid layers have the same thickness, and the interface is always stable when the upper fluid thickness is infinite. Including surface tension at either the free surface or interface is stabilising, particularly for short-wavelength disturbances. These works imply that some kind of interaction or resonant effect between the interface and free surface is responsible for the instability. It is suggested that this instability relies on the fact that the free surface is able to deform and exhibit tangential motions. This inspires chapter 4.

In chapter 4 we consider the effect of a free-moving elastic wall on a perturbed fluid interface. There has been a large amount of work focusing on the stability of two-dimensional, incompressible flow over an elastic or compliant surface. Some of the earliest papers are those of Benjamin (1960), Landahl (1962) and Benjamin (1963), who considered the evolution of linear waves in the inviscid boundary layer above an elastic plate. Lingwood and Peake (1999) revisited this problem and investigated the absolute instability that occurs above a certain flow speed. This instability was first discovered by Crighton and Oswell (1991), where a uniform flow was taken above the plate and a localised forcing applied.

More directly relevant to our work are models where the fluid is viscous. Of particular relevance to the formulation of the tension in our problem is the work of Luo and Pedley (1995) and Pedley and Luo (1998), who studied uniform and shear channel flows, where one section of one of the channel walls is elastic. Here the authors adopt the practice of assuming that the tension varies by a negligible amount along the beam and so is taken to be constant. For the case of channel flow between compliant walls it has been shown that a critical Reynolds number for linear instability exists (Hains and Price, 1962). The effect of a flexible surface on the Tollmien–Schlichting instability has also been investigated in some detail (for example in Rotenberry and Saffman (1990) and Davies and Carpenter (1997)). To our knowledge there have been no studies of the interaction between an elastic wall and fluid interface, as considered in our chapter 4. It is worth mentioning that the problem of creeping Couette flow of two fluids separated by a membrane has been shown to be linearly stable if tangential movements of the membrane are neglected (Kumaran and Srivatsan, 1998), but unstable in the long-wavelength limit if such movements are included (Thaokar and Kumaran, 2002).

The phenomenon of surface tension driven flows was first noted by Thomson (1855). Many experiments examining these effects have been performed over the years. Most notable are those of Bénard (1900), in which a thin layer of liquid is heated from below. Above a critical temperature, convection cells (Bénard cells) form. Pearson (1958) showed that gradients in surface tension were responsible for the motion in these experiments. Small variations in surface temperature lead to surface tractions and hence fluid flow. The induced flow, in turn, causes further variations in temperature. The effect is termed Bénard–Marangoni convection (although Thomson was the first to comment on surface tension driven flows, they were most famously reported by Marangoni). Scriven and Sternling (1960) provide a thorough summary of early work on Marangoni (surface tension driven) effects. It is worth mentioning that in Scriven and Sternling (1964) it was found that when surface-tension gradients drive convection in a thin fluid layer, the "zero" wavenumber is always unstable. This instability is known to be present at long wavelengths or in very viscous fluid layers.

It has been shown that flow of a liquid film down a heated incline has a lower critical Marangoni number than for a flat wall (Sreenivasan and Lin, 1978). Here the Marangoni number expresses the sensitivity of the surface tension to thermal effects. In the case of film flow over a heated, wavy wall, the film is generally less stable than for a flat wall (Kabova *et al.*, 2006). At times, very thin stable areas of the fluid act to promote heat transfer, whereas at others vortices are seen within the grooves where fluid is found to accumulate. Deformation of the film can result and sometimes even rupture. It is also found that cooling from below leads to a film with uniform thickness.

Also relevant to our work are so-called "doubly-diffusive" problems where convective motions result from the consideration of two different components with different diffusivities, for instance heat and salt concentration. When allowing the surface tension coefficient to vary linearly with respect to both temperature and solute concentration, it is possible to have two instability modes with different wavenumbers and frequencies of oscillation (Chen and Su, 1992). Building on work such as that of Chen and Chen (1994) and taking the limit of zero gravity, Skarda *et al.* (1998) also mapped the regions of stability when an imposed temperature gradient induces a concentration gradient.

There has been much work extending the study of thermocapillary flows to two fluids, and considering the effect of heating on a perturbed fluid interface. Whilst heating from above is stabilizing for waves of most wavelengths, increased heating from below lowers the critical Marangoni number for instability (Zeren and Reynolds, 1972). When heating from below, however, surface tension has been shown to be stabilizing for short wavelength disturbances (Busse, 1982; Renardy and Joseph, 1985)). Busse (1982) found that, in addition to solutions in which there are layers of convection cells, other solutions exist for which one fluid is surrounded by streamlines of the other.

Apart from the heating of fluid, a gradient in surface tension may be provoked through the addition of an insoluble surfactant to the interface between two fluids. There have been many studies examining this effect. In particular, it has been shown that two-layer, zero-Reynolds number, Couette–Poiseuille flow yields unstable solutions when under the influence of such a surfactant (Frenkel and Halpern, 2002; Halpern and Frenkel, 2003). Here the surface tension is allowed to depend on the surfactant concentration, and the Marangoni instability that occurs relies upon the presence of a shear flow in the base-state. The regions of stability depend on the wavenumber, capillary number, layer thickness, and viscosity ratio (although a viscosity difference between the two fluids is not a necessary condition for instability). Using a lubrication model, Blyth and Pozrikidis (2004) extended this analysis to consider an inclined plane. Here a nonlinear analysis revealed evidence of the saturation of the unstable waves, as well as wave steepening. The problem of two-layer shear flow next to a wall, where surfactant is present at the interface, was considered by Pozrikidis and Hill (2011). Here the upper fluid is semi-infinite. Although the majority of this paper considers a flat, horizontal wall, the authors touch on flow past a fixed sinusoidal wall. An instability is found for disturbances with long wavelengths, but disappears when the wall is removed, such that both fluid domains are semi-infinite.

In chapter 5 we consider the problem of instability due to an imposed concentration gradient in two fluids. This problem is related, but not equivalent, to the case of instability due to an insoluble surfactant. It is essentially equivalent to the case of instability due to an imposed temperature gradient.

Chapter 6 of this thesis can be thought of as an extension of the work of Hall and Papageorgiou (1999). In this paper, the authors consider the case of channel flow where one of the plane walls moves transversally and periodically in time. They proceed by seeking a stagnation-point type solution (essentially an unsteady version of the classical Hiemenz solution) to the full Navier–Stokes equations, finding that for small enough Reynolds numbers, there exists a unique, periodic, symmetric solution, synchronised with the wall motion. As the Reynolds number is increased, a bifurcation is observed, giving rise to a periodic, asymmetric solution. The solution for larger Reynolds numbers depends on the amplitude of the wall oscillation. In all cases further bifurcations are seen, eventually leading to a chaotic flow, but the route to chaos may include a Feigenbaum cascade or quasi-periodic solutions. A more detailed description of their work can be found in chapter 6. This work is closely related to two papers. The first is that of Secomb (1978), who considered a similar problem, but only allowed for wall oscillations with high and low frequencies or with general frequencies and small amplitudes. Secondly, Stuart *et al.* (1990) used lubrication theory to study the growth of Tollmien–Schlichting waves in a squeeze bearing with time-dependent walls, finding that the growth of such waves depends on their wavenumber, the Reynolds number and whether the plates are being pulled apart or squeezed. Their method, however, did not extend to time-periodic flows.

There are a number of subsequent papers building on the work of Hall and Papageorgiou (1999). Li and Blyth (2009) extended the analysis to deal with an axisymmetric pipe, Blyth *et al.* (2003) considered a three dimensional pipe and multiple layers of fluid were examined in Blyth (2007). Heil and Waters (2006) studied an elastic tube subject to high frequency, small amplitude oscillations and drew a comparison between their work and that of Hall and Papageorgiou (1999) in order to make predictions about the stability of their symmetric solutions. Blyth and Hall (2003) asked whether analogous self-similar solutions are possible when considering stagnation point flow at a wall where the solution at infinity is modulated periodically in time. They found that two modes of solution are possible. For oscillations above a critical frequency regular and periodic solutions are found, whilst below this frequency, the solution ends in a finite-time singularity. Espin and Papageorgiou (2009) found that so long as the Reynolds number is not too large, self-similar branches resembling those found by Hall and Papageorgiou (1999) exist in a finite channel driven by accelerating walls and Watson *et al.* (2008) found similar behaviours when the accelerating walls of the channel are taken to be porous and a uniform, steady suction is applied.

Also relevant to chapter 6 is the body of research considering squeeze flows. Here the lubrication approximation is used to describe flow in a channel with squeezing or separating walls. Particularly relevant are those papers in which the height of the channel varies, for example Khaled and Vafai (2003), Bujurke *et al.* (2007). However, such a rich variety of solutions as mentioned above is not found in these cases. It is also significant to mention Jeffery–Hamel flow. Here two fixed, inclined plates meet at an angle. A line source or sink is placed at the intersection of the plates, which induces a flow that is either divergent or convergent in the radial direction. Several authors have examined the effect of spatial or temporal perturbations to the overall flow field (Banks *et al.*, 1988; Hamadiche *et al.*, 1994; McAlpine and Drazin, 1998). The angle between the plates and the Reynolds number are found to be instrumental in determining the stability of resulting solutions. A good review of some of these papers and other work in this area is given in Drazin (1999).

1.4 Mathematical Tools

We next introduce some mathematical tools which are used frequently in the course of our work.

1.4.1 The Governing Equations

In general, neglecting body forces, the governing equations are the Navier–Stokes equations and the incompressibility condition,

$$\frac{\partial \mathbf{u}}{\partial t} + \mathbf{u}\cdot\nabla\mathbf{u} = -\frac{\nabla p}{\rho} + \nu\nabla^2\mathbf{u}, \quad \nabla\cdot\mathbf{u} = 0, \tag{1.2}$$

where, using a Cartesian co-ordinate system, $\mathbf{u}(x,y,z,t) = (u,v,w)$ denotes the velocity field and $p(x,y,z,t)$ the pressure, ρ is the density of the fluid and ν the constant kinematic viscosity.

Given the gentle mixing that occurs in the DGM main body, as mentioned above, we may expect the Reynolds number to be very small ($Re \to 0$) and this is the assumption made in the majority of this thesis. In this case the Navier–Stokes equations reduce to the Stokes equations, so that we have

$$\frac{\nabla p}{\mu} = \nabla^2 \mathbf{u}, \quad \nabla \cdot \mathbf{u} = 0, \tag{1.3}$$

where μ is the dynamic viscosity of the fluid. Assuming two-dimensional flow, equations (1.3) can be satisfied by introducing the streamfunction, $\psi(x, y, t)$, such that

$$u = \frac{\partial \psi}{\partial y}, \quad v = -\frac{\partial \psi}{\partial x}, \tag{1.4}$$

in which case the flow is governed by the biharmonic equation,

$$\nabla^4 \psi = 0, \tag{1.5}$$

as outlined in Acheson (1990).

An example of the application of these equations (found in later chapters) is the case of Poiseuille or shear flow. Here we consider a velocity field of the form $\mathbf{u} = (u(y, t), 0)$. In this case the first of the Stokes equations, (1.3), yields

$$\frac{1}{\mu}\frac{\partial p}{\partial x} = \frac{\partial^2 u}{\partial y^2}, \quad \frac{\partial p}{\partial y} = 0. \tag{1.6}$$

The second equation implies that p is a function of x and t at most, whilst u is a function of y and t at most, and hence we must have

$$\frac{\partial^2 u}{\partial y^2} = \frac{1}{\mu}\frac{\partial p}{\partial x} = -G, \tag{1.7}$$

where μG is the pressure gradient, which may be dependent on t at most.

1.4.2 Boundary Conditions at an Impermeable Wall

At an impermeable wall, $y = h(x, t)$, it is necessary to satisfy the kinematic condition, which ensures that any fluid particle sitting on the wall must remain on the wall. This necessitates

$$\frac{D}{Dt}\left(y - h(x, t)\right) = 0 \tag{1.8}$$

on $y = h$. This gives us the impermeability condition,

$$v(x, h, t) - \frac{\partial h}{\partial t}(x, t) - u(x, h, t)\frac{\partial h}{\partial x}(x, t) = 0. \tag{1.9}$$

At a fixed, flat, horizontal wall, where h is constant, this condition reduces to

$$v(x,h,t) = 0. \tag{1.10}$$

Alongside this condition we must satisfy a no-slip condition, $\mathbf{u} \cdot \hat{\mathbf{t}} = \mathbf{u_b} \cdot \hat{\mathbf{t}}$, where $\mathbf{u_b}$ is the velocity of the boundary and

$$\hat{\mathbf{t}} = \left(1 + \left(\frac{\partial h}{\partial x}\right)^2\right)^{-\frac{1}{2}} \left(1, \frac{\partial h}{\partial x}\right) \tag{1.11}$$

is the unit tangent vector to the wall. We consider a wall that moves vertically at most so that every part moves parallel to the y-axis and $\mathbf{u_b} = (0, \partial h/\partial t)$. This gives us the boundary condition

$$\left(1 + \left(\frac{\partial h}{\partial x}\right)^2\right)^{-\frac{1}{2}} \left(u(x,h,t) + v(x,h,t)\frac{\partial h}{\partial x}\right) = \left(1 + \left(\frac{\partial h}{\partial x}\right)^2\right)^{-\frac{1}{2}} \frac{\partial h}{\partial t}\frac{\partial h}{\partial x}. \tag{1.12}$$

Making use of condition (1.9), equation (1.12) may be re-written as

$$\left(1 + \left(\frac{\partial h}{\partial x}\right)^2\right)^{\frac{1}{2}} u(x,h,t) = 0, \tag{1.13}$$

giving us the condition

$$u(x,h,t) = 0. \tag{1.14}$$

1.4.3 Boundary Conditions at an Interface

1.4.3.1 The Stress Condition

In Cartesian co-ordinates the stress tensor, σ, for a Newtonian fluid is given by

$$\sigma_{ij} = -p\delta_{ij} + 2\mu e_{ij}, \quad e_{ij} = \frac{1}{2}\left(\frac{\partial u_i}{\partial x_j} + \frac{\partial u_j}{\partial x_i}\right), \tag{1.15}$$

where σ_{ij} is the i-component of stress acting on a surface element with unit normal pointing in the j-direction. Here $i, j = x, y$ in two-dimensions, p is the pressure, μ is the constant dynamic viscosity and the Kronecker delta,

$$\delta_{ij} = \begin{cases} 1 & \text{if} \quad i = j \\ 0 & \text{if} \quad i \neq j \end{cases}. \tag{1.16}$$

When two or more fluids are included in our analysis, a stress condition must be satisfied at the fluid interface, $y = \eta(x,t)$, say. We assume that the fluids below and above the interface are known as fluid 1 and 2, respectively. The unit normal vector to the interface, $\hat{\mathbf{n}}$, points into fluid 1 and the unit tangent vector, $\hat{\mathbf{t}}$, points in the direction of increasing l, where l is the arc length along the interface. Therefore

$$\hat{\mathbf{n}} = \left(1+\left(\frac{\partial \eta}{\partial x}\right)^2\right)^{-\frac{1}{2}} \left(\frac{\partial \eta}{\partial x}, -1\right), \quad \hat{\mathbf{t}} = \left(1+\left(\frac{\partial \eta}{\partial x}\right)^2\right)^{-\frac{1}{2}} \left(1, \frac{\partial \eta}{\partial x}\right). \tag{1.17}$$

We consider the balance of forces on a small element of the interface, dl (see figure 1.4). The element is subject to forces due to surface tension, γ, in the tangential direction and forces exerted by fluids 1 and 2 in the normal direction. Taking the inertia of the element to be negligible, a force balance gives us

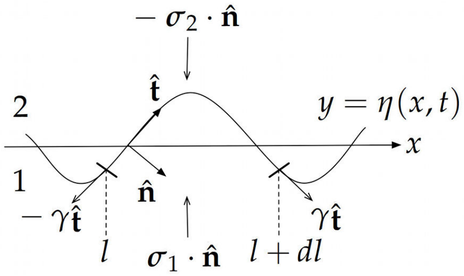

Figure 1.4: The force balance on a small interface element, dl, of an interface, $y = \eta(x,t)$.

$$\gamma(l+dl)\hat{\mathbf{t}}(l+dl) - \gamma(l)\hat{\mathbf{t}}(l) + dl\,(\sigma_1 \cdot \hat{\mathbf{n}} - \sigma_2 \cdot \hat{\mathbf{n}}) = \mathbf{0}, \tag{1.18}$$

where σ_1 (or σ_{1ij}) denotes the stress tensor in fluid 1 and σ_2 (or σ_{2ij}) denotes the stress tensor in fluid 2. Expanding the first term in Taylor series (neglecting terms of $O(dl^2)$), dividing the equation by dl, taking the limit as $dl \to 0$ and defining the curvature, κ, such that $-\kappa\hat{\mathbf{n}} = \partial\hat{\mathbf{t}}/\partial l$, this leads to the condition at the interface,

$$(\sigma_1(x,\eta,t) - \sigma_2(x,\eta,t)) \cdot \hat{\mathbf{n}} = \gamma(x,\eta,t)\kappa(\eta)\hat{\mathbf{n}} - \frac{\partial \gamma}{\partial l}(x,\eta,t)\hat{\mathbf{t}}. \tag{1.19}$$

Here,

$$\kappa = \left(1+\left(\frac{\partial \eta}{\partial x}\right)^2\right)^{-\frac{3}{2}} \frac{\partial^2 \eta}{\partial x^2}. \tag{1.20}$$

It is clear from the second term on the right hand side of (1.19) that a variation in surface tension along the interface promotes a tangential force (the Marangoni force). This term represents the phenomena that since a high surface tension is more attracting than a low surface tension, there tends to be a movement of liquid away from areas of low surface tension to areas of high surface tension. This is known as the Marangoni effect.

In the case that surface tension is constant, the stress condition reduces to

$$(\sigma_1(x,\eta,t) - \sigma_2(x,\eta,t)) \cdot \hat{\mathbf{n}} = \gamma\kappa(\eta)\hat{\mathbf{n}}. \tag{1.21}$$

1.4.3.2 Other Boundary Conditions

In addition to the stress condition, we must satisfy velocity continuity at a fluid interface, $y = \eta(x,t)$. This gives us

$$u_1(x,\eta,t) = u_2(x,\eta,t), \quad v_1(x,\eta,t) = v_2(x,\eta,t), \tag{1.22}$$

where the subscripts 1 and 2 denote the lower and upper fluid, respectively.

Finally, the kinematic condition must also be satisfied at the moving interface. This gives us

$$v_2(x,\eta,t) - \frac{\partial\eta}{\partial t}(x,t) - u_2(x,\eta,t)\frac{\partial\eta}{\partial x}(x,t) = 0, \tag{1.23}$$

where, due to condition (1.22), it makes no difference whether we choose to take the interface velocity components from fluid 1 or 2.

Chapter 2

Two-Fluid Flow Next to an Oscillating Wall

2.1 Introduction

This chapter comprises a first simple attempt at modelling the mechanics of the DGM main body by considering the response of a flow field and fluid interface between two creeping fluids next to a sinusoidally moving wall. The model can be thought of as a local description of the flow in the region close to the wall of the machine, where the two fluids represent two different phases of partially digested liquid material mixed with gastric secretions. The representation is taken in the very simplest case in that the only distinction drawn between the two fluids is that of differing, constant viscosities. The choice of a sinusoidally moving wall is inspired by the sinusoidally varying external pressure induced in the water bath surrounding the cone in the DGM main body (Wickham *et al.*, 2012).

2.2 Problem Description

We consider small Reynolds number, two-fluid flow next to a moving wall, $y^* = s^*(x^*, t^*)$, oscillating about $y^* = 0$, as shown in figure 2.1. The free interface between the fluids, $y^* = \eta^*(x^*, t^*)$, has the flat equilibrium position $y^* = h$. Here stars denote dimensional variables that have a dimensionless counterpart. We allow a small perturbation to the state where the wall and interface are both flat, letting the wall and interface both vary periodically with x^*, so that

$$s^* = \epsilon h a(\omega t^*) \sin(k^* x^*), \quad \eta^* = h + \epsilon h \left[b(\omega t^*) \sin(k^* x^*) + c(\omega t^*) \cos(k^* x^*) \right], \tag{2.1}$$

where $0 < \epsilon \ll 1$ is a small parameter and k^* and ω are prescribed and denote the positive, real wavenumber and frequency of the perturbation, respectively. Here the interface description has been chosen to allow for a phase difference in x between the

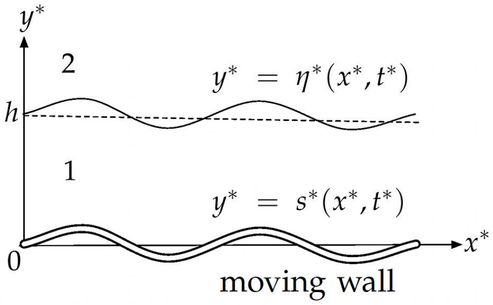

Figure 2.1: The two-fluid problem

wall and interface. The function a is prescribed and the functions b and c are to be determined. We denote the lower and upper fluid with subscript 1 and 2, respectively, and let the viscosity in fluid j be μ_j. The interface has constant surface tension, γ.

We non-dimensionalise using the characteristic length scale h, time scale $1/\omega$ and viscosity scale μ_1, resulting in the non-dimensional parameters

$$\Lambda = \frac{\mu_2}{\mu_1}, \quad Ca = \frac{h\mu_1\omega}{\gamma}, \tag{2.2}$$

where Λ is the viscosity ratio and Ca is the capillary number. Taking non-starred variables as non-dimensional, we introduce the stream function, $\psi_j(x, y, t)$, in addition to the velocity field, $\mathbf{u}_j(x, y, t) = (u_j, v_j)$, and pressure, $p_j(x, y, t)$ in fluid j. In non-dimensional variables we write

$$\begin{aligned} s =&\epsilon a(t)\sin(kx), \quad \eta = 1 + \epsilon\left[b(t)\sin(kx) + c(t)\cos(kx)\right], \\ \psi_j =&\epsilon\left[f_j(y,t)\cos(kx) + g_j(y,t)\sin(kx)\right], \\ p_j =&\epsilon\left[p_0(t) + m_j(y,t)\sin(kx) + n_j(y,t)\cos(kx)\right], \end{aligned} \tag{2.3}$$

where the forms of the streamfunction and pressure are chosen to satisfy the governing equations, (1.3) and (1.5), and boundary conditions (1.9), (1.21), (1.22) and (1.23).

Non-dimensionalising and linearising all boundary conditions, the no-slip and kinematic conditions at the moving wall, (1.14) and (1.9), give us

$$\frac{\partial f_1}{\partial y}(0,t) = 0, \quad f_1(0,t) = \frac{1}{k}\frac{da}{dt}(t), \quad \frac{\partial g_1}{\partial y}(0,t) = g_1(0,t) = 0, \tag{2.4}$$

the velocity continuity and kinematic conditions at the interface, (1.22) and (1.23), yield

$$\frac{\partial f_1}{\partial y}(1,t) = \frac{\partial f_2}{\partial y}(1,t), \quad f_1(1,t) = f_2(1,t), \quad \frac{\partial g_1}{\partial y}(1,t) = \frac{\partial g_2}{\partial y}(1,t), \quad g_1(1,t) = g_2(1,t), \tag{2.5}$$

$$\frac{db}{dt}(t) = kf_2(1,t), \quad \frac{dc}{dt}(t) = -kg_2(1,t), \tag{2.6}$$

and the stress condition (1.21), evaluated in the normal and tangential directions to the interface, implies that

$$\begin{aligned}-m_1(1,t)+m_2(1,t)+2k\left(\frac{\partial f_1}{\partial y}(1,t)-\Lambda\frac{\partial f_2}{\partial y}(1,t)\right)&=-\frac{k^2b(t)}{Ca},\\ -n_1(1,t)+n_2(1,t)-2k\left(\frac{\partial g_1}{\partial y}(1,t)-\Lambda\frac{\partial g_2}{\partial y}(1,t)\right)&=-\frac{k^2c(t)}{Ca},\end{aligned}\tag{2.7}$$

and

$$\begin{aligned}k^2f_1(1,t)+\frac{\partial^2 f_1}{\partial y^2}(1,t)&=\Lambda\left(k^2f_2(1,t)+\frac{\partial^2 f_2}{\partial y^2}(1,t)\right),\\ k^2g_1(1,t)+\frac{\partial^2 g_1}{\partial y^2}(1,t)&=\Lambda\left(k^2g_2(1,t)+\frac{\partial^2 g_2}{\partial y^2}(1,t)\right).\end{aligned}\tag{2.8}$$

We perturb about a state of rest so that as $y\to\infty$ the velocity is zero. Hence, the far field conditions are

$$\frac{\partial f_2}{\partial y}\,,\ f_2\,,\ \frac{\partial g_2}{\partial y}\,,\ g_2\to 0\quad\text{as}\quad y\to\infty.\tag{2.9}$$

2.3 Problem Solution

We solve the non-dimensionalised biharmonic equation, (1.5), subject to conditions (2.4) and (2.9). Here we non-dimensionalise the Stokes equations, (1.3), from which we may obtain the pressure. Defining, for brevity,

$$s_y=\sinh(ky),\quad c_y=\cosh(ky),\quad s_1=\sinh(k),\quad c_1=\cosh(k),\tag{2.10}$$

and

$$l_1=c_1+\Lambda s_1,\quad l_2=s_1+\Lambda c_1,\quad l_3=\left(\frac{{l_2}^2}{{l_1}^2}-1\right)k^2-1,\quad l_4=\frac{{l_2}^2}{{l_1}^2}+\frac{1}{k}\frac{l_2}{l_1}-1,\tag{2.11}$$

the streamfunction and pressure perturbations are defined by

$$\begin{aligned}f_1=&\frac{1}{k}\frac{da}{dt}c_y+A_1(t)\left(s_y-kyc_y\right)+B_1(t)ys_y,\quad f_2=\left(A_2(t)+B_2(t)y\right)e^{-ky},\\ g_1=&C_1(t)\left(s_y-kyc_y\right)+D_1(t)ys_y,\quad g_2=\left(C_2(t)+D_2(t)y\right)e^{-ky},\end{aligned}\tag{2.12}$$

and

$$\begin{aligned}m_1=&2k\left(B_1(t)s_y-kA_1(t)c_y\right),\quad m_2=2k\Lambda B_2(t)e^{-ky},\\ n_1=&2k\left(D_1(t)s_y-kC_1(t)c_y\right),\quad n_2=2k\Lambda D_2(t)e^{-ky}.\end{aligned}\tag{2.13}$$

From equations (2.5), (2.7) and (2.8), we find that

$$\begin{aligned} A_1(t) &= \frac{l_4}{l_3}\frac{da}{dt} + \frac{1}{2Cal_1l_3}\left(1 + k\frac{l_2}{l_1}\right) b(t), \quad B_1(t) = \frac{1}{l_3}\frac{da}{dt} + \frac{1}{2Cal_1l_3} b(t), \\ C_1(t) &= -\frac{1}{2Cal_1l_3}\left(1 + k\frac{l_2}{l_1}\right) c(t), \quad D_1(t) = -\frac{1}{2Cal_1l_3} c(t), \end{aligned} \tag{2.14}$$

and

$$\begin{aligned} A_2(t) &= e^k\left(\alpha_1\frac{da}{dt} + \frac{\beta_1}{2Cal_1l_3} b(t)\right), \quad B_2(t) = e^k\left(\alpha_2\frac{da}{dt} + \frac{\beta_2}{2Cal_1l_3} b(t)\right), \\ C_2(t) &= -\frac{e^k\beta_1}{2Cal_1l_3} c(t), \quad D_2(t) = -\frac{e^k\beta_2}{2Cal_1l_3} c(t). \end{aligned} \tag{2.15}$$

Here

$$\begin{aligned} \alpha_1 =& \frac{1}{k}c_1 - e^k + \frac{1}{l_3}\left(l_4\left(s_1 + k(ke^k - s_1 - c_1)\right) - ke^k\right), \\ \beta_1 =& \left(1 + k\frac{l_2}{l_1}\right)\left(s_1 + k(ke^k - s_1 - c_1)\right) - k^3e^k, \\ \alpha_2 =& (e^k + \frac{1}{l_3}\left(-l_4k(ke^k - s_1) + ke^k + s_1\right), \\ \beta_2 =& -\left(1 + k\frac{l_2}{l_1}\right) k(ke^k - s_1) + k^2(ke^k + s_1). \end{aligned} \tag{2.16}$$

Considering the DGM main body, it is relevant to choose $a(t) = \cos(t)$ for a standing wave wall motion. Then (2.6) becomes

$$\frac{db}{dt} - h_1b(t) = -h_2\sin(t), \quad \frac{dc}{dt} - h_1c(t) = 0, \tag{2.17}$$

where

$$h_1 = \frac{k}{2Cal_1l_3}(\beta_1 + \beta_2), \quad h_2 = k(\alpha_1 + \alpha_2). \tag{2.18}$$

We then find that

$$b(t) = Ae^{h_1t} + \frac{h_2}{(1 + h_1{}^2)^{\frac{1}{2}}}\cos(t + \delta), \quad \delta = \tan^{-1}(-h_1), \quad c(t) = Be^{h_1t}, \tag{2.19}$$

where A and B are constants determined by our choice of the initial conditions $b(0)$ and $c(0)$. It can be shown, after some algebra, that

$$h_1 = -\frac{k\left(\Lambda(s_1{}^2 - k^2) + s_1c_1 - k\right)}{2Ca\left(k^2(1 - \Lambda^2) + (c_1 + \Lambda s_1)^2\right)}, \tag{2.20}$$

and, since it is true that $\sinh(k) > k$ and $\cosh(k) > 1$ for $k > 0$, the numerator is positive

and

$$k^2(1-\Lambda^2)+(c_1+\Lambda s_1)^2 > k^2-\Lambda^2{s_1}^2+{c_1}^2+2\Lambda c_1 s_1+\Lambda^2{s_1}^2 > 0, \tag{2.21}$$

and we can conclude that h_1 is less than zero for all positive k. Hence the function $c(t)$ and the exponential term in $b(t)$ always decay, and we approach a stable, periodic solution for η that is in phase with the wall in x. Plots of h_1 show a function that decreases monotonically with k and letting $k \to \infty$ in (2.20), we find that $h_1 \to -k$.

We choose to consider the case where $b(0) = c(0) = 0$, so that the interface is flat at $t = 0$. This gives us

$$A = -\frac{h_2}{(1+{h_1}^2)}, \quad B = 0. \tag{2.22}$$

Choosing a different initial condition does not change the solution qualitatively, although for a specific choice, namely $b(0) = h_2/(1+{h_1}^2)$, $c(0) = 0$, the exponential term disappears from our solution, which is periodic for all time.

We note that the presence of the exponential terms in (2.19) means that the flow is not subject to the usual Stokes flow time-reversibility. If we take the limit $Ca \to \infty$ (zero surface tension) we find that $h_1 \to 0$ and the exponential terms disappear. It is therefore clear that the non time-reversibility is a result of surface tension acting to flatten the interface. This means that for a fixed, sinusoidal wall, $b(t)$ and $c(t) \to 0$ and the displaced interface relaxes back to the flat rest state, as we would expect.

Since we have shown that h_1 is always negative, δ is always positive and the interface will lag behind the wall in time. As $-\infty \le h_1 \le 0$, this implies $0 \le \delta \le \pi/2$. A consequence of this phase shift is that, for the settled solution, the thickness of fluid 1, $\eta - s$, changes with time (except at $x = n\pi$, $n \in \mathbb{Z}$, where the thickness is always 1) as well as x.

Once the solution has settled, the amplitude of $b(t)$, and hence the interface, is ϵ when $k = 0$. The sign of the amplitude depends only on h_2 and since

$$h_2 = \frac{(k+\Lambda)\,s_1 + (1+\Lambda k)\,c_1}{k^2(1-\Lambda^2)+(c_1+\Lambda s_1)^2}, \tag{2.23}$$

the denominator of which we have already shown to be positive for all $k > 0$, the amplitude is greater than zero for all positive k. Plots of h_2 show an exponentially decreasing function and letting $k \to \infty$ in (2.23), we find that $h_2 \to ke^{-\frac{k}{2}}$. Therefore the amplitude decreases as k increases and is never larger than the amplitude of the wall.

2.4 Streamline Plots

Figure 2.2 shows typical plots of the streamlines for this problem. We observe two rows of cells divided by one horizontal and many vertical lines of zero ψ. The bottom set

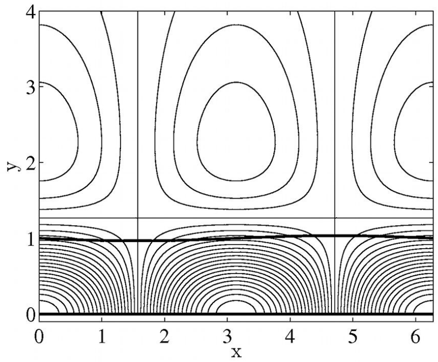

Figure 2.2: Typical streamline plots for the two-fluid standing wave problem. Here $k = \Lambda = 1$, $Ca = 0.05$ and $t = \frac{\pi}{2}$. The wall and interface are shown with thick lines. Streamlines are shown with thin lines.

of cells appear as open arcs, whilst the top set are closed. Consecutive cells spin in opposite directions. By altering the various parameters we may slow the flow of one fluid relative to the second and increasing the wavenumber, k, more cells are found in the same area.

Since $\psi = 0$ on the horizontal streamline, it must occur in fluid 2 when $f_2 = 0$. Therefore, from equation (2.12), its position, y_0, in the y-direction in fluid 2 is given by

$$y_0 = -\frac{A_2(t)}{B_2(t)}. \tag{2.24}$$

Figure 2.3 shows typical plots of y_0 against Ca and k for $y > 1$. We find that in both

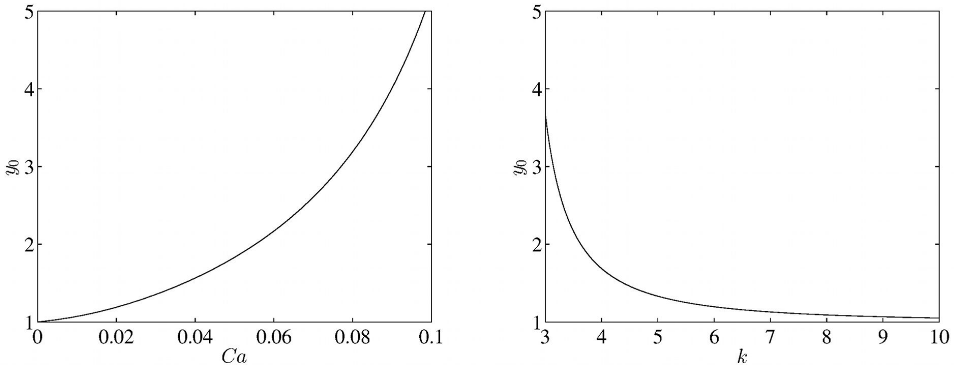

(a)

(b)

Figure 2.3: The position of the horizontal streamline, y_0 plotted against (a) Ca when $k = \Lambda = 1$ and (b) k when $\Lambda = Ca = 1$. Here $t = \frac{\pi}{3}$.

the cases $Ca \to \infty$ and $k \to 0$, for a given time (except at $t = m\pi$, $m \in \mathbb{N}$, where the horizontal streamline always sits at $y = 0$), $y_0 \to \infty$ so that we only have one set of cells.

Since increasing Ca and decreasing k appear to have a similar effect on the flow field, this suggests that we require tangential movements of the interface to be comparable in size to normal movements for the appearance of a second set of cells. In both cases normal movements are less constrained, in the former due to a weaker surface tension and in the latter due to surface tension being felt less strongly due to a larger horizontal length scale.

2.5 A Single Fluid Next to a Normally and Tangentially Moving Wall

We briefly consider the simpler case of a single fluid extending up to infinity next to a moving wall where, as well as allowing normal movements of the wall, $y = s$, we allow tangential movements. We suppose that $u = \epsilon\zeta \cos(kx) \sin(t)$ on $y = s$ for some constant ζ together with the previous normal oscillations. We assume that the only mode present in our solution is that for which f_j (here f) appears in the streamfunction, m_j (here m) in the pressure and $b(t)$ in the interface description. In this case the only boundary conditions are the far-field conditions (2.9) and the conditions at the wall, (2.4), the first of which (the no-slip condition) is instead given by

$$\frac{\partial f}{\partial y}(0, t) = \zeta \sin(t). \tag{2.25}$$

Solving the non-dimensionalised version of the biharmonic equation, (1.5), subject to the above conditions, we find that

$$\psi = \epsilon \left(-\frac{1}{k} + (\zeta - 1)\, y \right) e^{-ky} \sin(t) \cos(kx). \tag{2.26}$$

In this case, for a horizontal streamline of zero ψ with equation

$$y = y_0 = \frac{1}{k(\zeta - 1)}, \tag{2.27}$$

and a second set of cells to appear, we require $\zeta > 1$ and the horizontal movements of the wall must be larger than the vertical movements.

Likening this model wall to the interface in our two-fluid problem, this result is in favour of our hypothesis that tangential movements of the interface must be comparable to normal movements for the appearance of a second set of cells.

2.6 Extension to Other Types of Wall Motion

Since we are working with a linear problem, our work can easily be extended to look at other wall motions by summing over known solutions (so that the wall motion could be given by, for instance, a Fourier sum). An interesting alternative case to consider is that of a travelling wave wall motion, which may also be relevant in terms of the DGM main body. Here, in non-dimensional variables, we consider the sum of our standing wave solution, ψ_j, $j = 1, 2$, (taking the only mode to be that for which f_j appears in the streamfunction, m_j in the pressure and $b(t)$ in the interface description) plus an alternative standing wave solution, $\bar{\psi}_j$, such that the wall is described by

$$y = S = \epsilon \sin(kx - t) = \epsilon h \left(\sin(kx)\cos(t) - \cos(kx)\sin(t)\right). \tag{2.28}$$

Then, the (again stable) solution for the streamfunction, Ψ_j in fluid j is given by

$$\Psi_j = \psi_j - \bar{\psi}_j. \tag{2.29}$$

Figure 2.4 shows typical plots of the streamlines for this problem. The interface moves with a travelling wave wall motion. Once the solution has settled, it is found to be out of phase with the wall, with a smaller amplitude. The streamline pattern also has travelling wave form. The streamlines at any moment in time are qualitatively similar to the pattern seen in the case of a standing wave wall motion, but are tilted towards the direction of motion. In this case there is no horizontal streamline of zero ψ and instead, as we increase Ca, the streamlines pattern is tilted to the right and compressed to such an extent that a second row of closed streamlines is formed, as shown in figure 2.4.

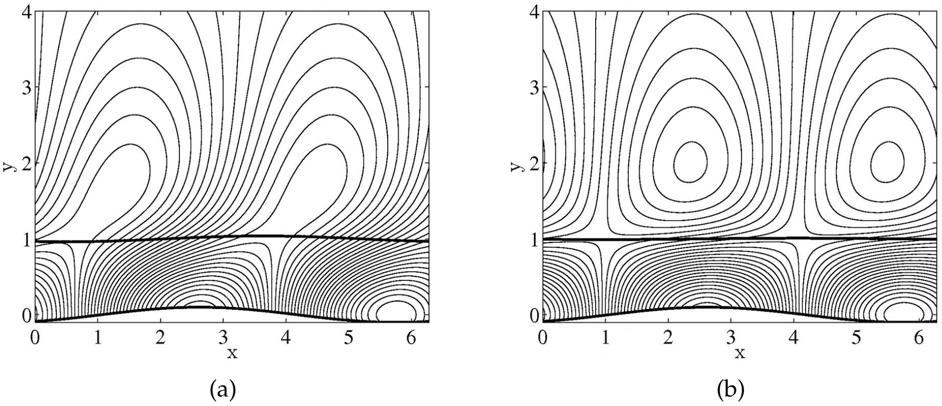

(a) (b)

Figure 2.4: Typical streamline plots for the two-fluid travelling wave problem. Here $k = \Lambda = 1$, $t = \frac{19\pi}{3}$ and $Ca =$ (a) 0.05 and (b) 0.01. The wall and interface are shown with thick lines. Streamlines are shown with thin lines.

2.7 Discussion

We have performed a linear stability analysis for the flow of two fluids next to a sinusoidally moving wall. The introduction of surface tension at the interface removes the time-reversibility of the flow and exponentially decaying terms are found to be present in the solution. Once initial transients have decayed, the solution is stable and periodic, suggesting that an alternative mechanism is needed to induce fluid mixing.

The interface is found to lag behind the wall with a phase difference of between zero and $\pi/2$. The amplitude of the interface equals the amplitude of the wall when the wavenumber of the disturbance is zero and decreases as the wavenumber increases.

Streamline plots show a row of closed cells sitting above a row of open cells. The rows are divided by horizontal and vertical lines on which the streamfunction is equal to zero. It is suggested that tangential movements of the interface must be comparable in size to normal movements for the appearance of a second set of cells. More evidence is found for this suggestion when we consider the case of a single fluid next to a wall that moves tangentially as well as normally.

We may construct the solution for a travelling wave wall motion from the sum of two standing wave solutions and find that following the decay of initial transients, the solution itself has travelling wave form. The pattern of streamline cells is similar to the standing wave case, but the cells are tilted towards the direction of motion.

We note that our work may be compared to that of Pozrikidis (1987), who considered Stokes flow moving through a channel with walls that move peristaltically. In particular, the cells observed in our streamline plots are similar to those found in this paper when the walls have equal amplitude and move symmetrically about the centre of the channel.

In the next chapter we consider a nonlinear analysis where, instead of two fluids, we study the flow of a single thin film next to a sinusoidally moving wall with general amplitude.

Chapter 3

Thin-Film Flow Next to an Oscillating Wall

3.1 Introduction

Having considered the linear analysis of a problem in which a sinusoidal wall undergoes small amplitude oscillations and shown that the fluid interface is stable, it is of interest to determine whether this is also the case for the nonlinear problem. Here we may allow for a wall motion with general amplitude. We make progress with such a model by considering a single thin film rather than two fluids. In the chapter discussion we then speculate as to how the addition of a second, semi-infinite, fluid layer would affect the results. We note that modelling the fluid next to the wall as a thin film is a relevant assumption in terms of the DGM body. In the DGM, as mentioned in chapter 1, the fluid layer at the wall (comprising for the most part of gastric juices) is likely to be thin. In this chapter we make no assumptions about the x and t dependencies of the interface, thus allowing for a description that may not necessarily have the same dependencies as the wall.

3.2 Problem Description

We consider a thin film of fluid of density ρ and viscosity μ flowing next to a moving wall, $y^* = s^*(x^*, t^*)$, where starred variables are dimensional variables with a non-dimensional counterpart. The mean position of the wall is located at $y^* = 0$. The free surface (above which is static air) is at $y^* = \eta^*(x^*, t^*)$, and has the flat position $y^* = h$ when at rest. We consider two cases (illustrated in figure 3.1). In case (i) the x^* axis is horizontal and the characteristic velocity scale, U, is taken to be the typical flow velocity in the x^*-direction, $L\omega$, where L denotes the typical wavelength of the wall and ω is the frequency of the wall oscillations. In case (ii) the x^* axis is inclined at an angle α to the horizontal and gravity, of magnitude g, is allowed to act vertically downwards. In this case U is taken to be equal to U_N, the Nusselt surface speed for a flat film flowing down

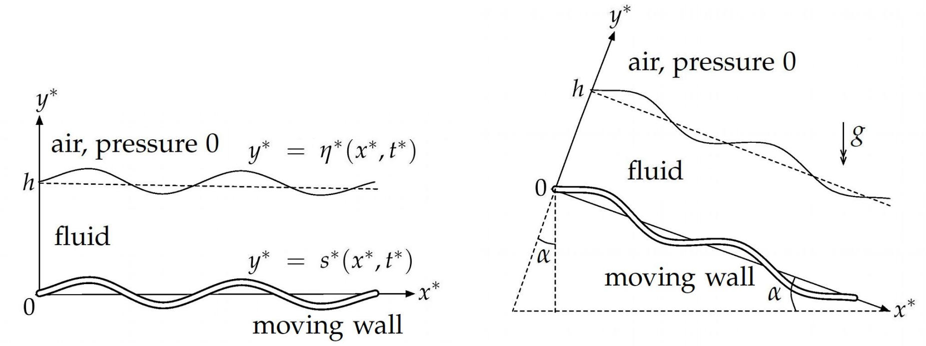

(a) (b)

Figure 3.1: Schematic diagram of thin film flow of one fluid next to a moving wall. In case (i) the x^* axis is horizontal, whilst in case (ii) the x^* axis is inclined at an angle α to the horizontal and gravity acts such that the free surface flows with speed U_N. The positions of the perturbed wall, $y^* = s^*(x^*, t^*)$ and free surface, $y^* = \eta^*(x^*, t^*)$, are shown.

an inclined plane, as derived in Nusselt (1916). Ignoring condensation, U_N is given by

$$U_N = \frac{\rho g h^2 \sin(\alpha)}{2\mu}. \tag{3.1}$$

Here gravity is accounted for by defining and solving for the shifted pressure,

$$\tilde{p}^* = p^* - \rho g \left(x^* \sin(\alpha) - y^* \cos(\alpha) \right). \tag{3.2}$$

In case (i), on the other hand, we simply take $\tilde{p}^* = p^*$.

We return momentarily to the full Navier–Stokes equations and incompressibility condition, (1.2), for the velocity field, $\mathbf{u}^*(x^*, y^*, t^*) = (u^*, v^*)$ and pressure $\tilde{p}^*(x^*, y^*, t^*)$, and make use of lubrication theory as described in Acheson (1990). We first non-dimensionalise using the characteristic horizontal length scale L, vertical length scale h, horizontal velocity U, time scale L/U and pressure scale $\mu L U/h^2$. This results in the non-dimensional parameters

$$Re = \frac{UL}{\nu}, \quad \delta = \frac{h}{L}, \quad Ca = \frac{\mu U}{\gamma}, \quad Bo = \frac{\rho g L^2 \delta^2}{\gamma}, \tag{3.3}$$

where ν is the kinematic viscosity, Re is the Reynolds number, Ca is the capillary number and Bo is the Bond number for the flow. Using the Stokes approximation and assuming that the fluid is a thin film, we may take $Re \ll 1$ and $\delta \ll 1$ (in fact, given $\delta \ll 1$, only the weaker condition $\delta^2 Re \ll 1$ is necessary in the following analysis). In order to retain the effects of surface tension in the stress condition, (1.21), we must assume that γ is large (of the $O(1/\delta^3)$). We therefore define the $O(1)$ parameter

$$Ca' = \frac{Ca}{\delta^3}. \tag{3.4}$$

From this point, non starred variables are non-dimensional. Given the above assumptions, the Navier–Stokes equations and incompressibility condition, (1.2), reduce to, at leading order,

$$0 = -\frac{\partial \tilde{p}}{\partial x} + \frac{\partial^2 u}{\partial y^2}, \qquad 0 = -\frac{\partial \tilde{p}}{\partial y}, \qquad \frac{\partial u}{\partial x} + \frac{\partial v}{\partial y} = 0. \tag{3.5}$$

Non-dimensionalising the no-slip and kinematic boundary conditions, (1.14) and (1.9), at the wall, $y = s$, gives us

$$u(x, s, t) = 0, \quad v(x, s, t) = \frac{\partial s}{\partial t}, \tag{3.6}$$

and the kinematic condition on the free surface, $y = \eta$, yields

$$v(x, \eta, t) - \frac{\partial \eta}{\partial t} - u(x, \eta, t)\frac{\partial \eta}{\partial x} = 0. \tag{3.7}$$

Taking the stress condition, (1.21), for the case of one fluid with air above it and non-dimensionalising, we find that in the directions normal and tangential to the free surface, we have

$$p(x, \eta, t) = -\frac{1}{Ca'}\frac{\partial^2 \eta}{\partial x^2}, \qquad \frac{\partial u}{\partial y}(x, \eta, t) = 0. \tag{3.8}$$

The second of equations (3.5) implies that $\tilde{p}$ is a function of x and t at most (and so the first of (3.8) gives us an expression for p for all y). We may then solve the first equation using the conditions on u from (3.6) and (3.8) to give us

$$u = \frac{\partial \tilde{p}}{\partial x}\left(\frac{(y-s)^2}{2} - (y-s)(\eta - s)\right). \tag{3.9}$$

Solving the third of (3.5) for v using the condition on v from (3.6), we find that

$$\begin{aligned} v = &\frac{\partial s}{\partial t} - \frac{\partial^2 \tilde{p}}{\partial x^2}\frac{(y-s)^3}{6} + \frac{\partial}{\partial x}\left(\frac{\partial \tilde{p}}{\partial x}(\eta - s)\right)\frac{(y-s)^2}{2} \\ &+ \frac{\partial \tilde{p}}{\partial x}\frac{\partial s}{\partial x}\left(\frac{(y-s)^2}{2} - (\eta - s)(y - s)\right). \end{aligned} \tag{3.10}$$

Substituting our expressions for u and v into equation (3.7) and defining the film thickness, $H = \eta - s$, gives us the thin film equation,

$$\frac{\partial H}{\partial t} - \frac{1}{3}\frac{\partial}{\partial x}\left(H^3 \frac{\partial \tilde{p}}{\partial x}\right) = 0. \tag{3.11}$$

In case (i) $\tilde{p} = p$ and, using the first of equations (3.8), we obtain

$$\frac{\partial H}{\partial t} + \frac{1}{3}\frac{\partial}{\partial x}\left(\frac{H^3}{Ca'}\frac{\partial^3}{\partial x^3}(H+s)\right) = 0. \tag{3.12}$$

We note that taking $s = \epsilon \sin(kx)\cos(t)$ and $\eta = 1 + \epsilon \sin(kx) b(t)$, for $0 < \epsilon \ll 1$ a small parameter, in equation (3.12) and retaining only terms of $O(\epsilon)$, we find that

$$\frac{db}{dt} + \frac{k^4 b}{3Ca'} = -\sin(t). \tag{3.13}$$

We can compare this equation with the equation for $b(t)$, (2.17), in chapter 2. Taking $\Lambda = 0$ in this equation (since $y = \eta$ is now a free surface) and letting $k \to \delta k$ (and expanding functions of k using a Taylor series approximation) and $t \to (1/\delta)t$, this leaves us with (3.13) to first order in δ, therefore validating our work.

In case (ii), using (3.1) and given the first of equations (3.8) at $y = \eta$ and the second of equations (3.5), we find that equation (3.2) gives us

$$\tilde{p} = -\frac{1}{Ca'}\frac{\partial^2 \eta}{\partial x^2} - 2x + 2\delta\eta\cot(\alpha). \tag{3.14}$$

Assuming that either $\delta\cot(\alpha) \ll 1$ or $\delta\cot(\alpha) \ll 1/Ca'$, we may neglect the last term of this expression and our thin film equation is found to be

$$\frac{\partial H}{\partial t} + \frac{1}{3}\frac{\partial}{\partial x}\left(2H^3 + \frac{H^3}{Ca'}\frac{\partial^3}{\partial x^3}(H+s)\right) = 0. \tag{3.15}$$

3.3 A Linear Solution

We first seek a linear solution by writing $H = 1 + \epsilon f(x,t)$ where $0 < \epsilon \ll 1$ is a small parameter and $f = O(1)$. We assume that $s = \epsilon \sin(k_w x)\cos(t)$, where $k = k_w$ is the wavenumber of the wall.

3.3.1 Case (i); Horizontal Thin Film Flow

In case (i), to first order in ϵ, equation (3.12) yields

$$\frac{\partial f}{\partial t} + \frac{1}{3Ca'}\frac{\partial^4 f}{\partial x^4} + \frac{{k_w}^4}{3Ca'}\sin(k_w x)\cos(t) = 0. \tag{3.16}$$

3.3.1.1 An Analytical Solution

We assume for a moment that f takes the form of the inverse Fourier transform, such that

$$f(x,t) = \int_{-\infty}^{\infty} c(k,t) e^{ikx} dk \quad \text{where} \quad c(k,t) = \frac{1}{2\pi}\int_{-\infty}^{\infty} f(x,t) e^{-ikx} dx. \tag{3.17}$$

Then since

$$\begin{aligned}\frac{1}{2\pi}\int_{-\infty}^{\infty}\sin(k_w x)e^{-ikx}dx =& \frac{1}{4\pi i}\int_{-\infty}^{\infty}e^{-i(k-k_w)x}-e^{-i(k+k_w)x}dx\\ =&\frac{i}{4\pi}(\delta(k+k_w)-\delta(k-k_w)),\end{aligned} \tag{3.18}$$

where δ denotes the delta function, we have that

$$\sin(k_w x)=\frac{i}{2}\int_{-\infty}^{\infty}(\delta(k+k_w)-\delta(k-k_w))e^{ikx}dk, \tag{3.19}$$

and equation (3.16) implies that

$$\frac{dc}{dt}+\frac{k^4}{3Ca'}c+\frac{ik_w{}^4}{6C'}\cos(t)(\delta(k+k_w)-\delta(k-k_w))=0. \tag{3.20}$$

If $k\neq\pm k_w$, then $\delta(k\pm k_w)=0$ and $c=C_0\exp(-k^4t/(3Ca'))$ for some constant C_0, and these modes decay with time. If $k=\pm k_w$ we integrate (3.20) with respect to k from $\pm k_w-\epsilon$ to $\pm k_w+\epsilon$ and take the limit $\epsilon\to 0$, finding that

$$\frac{dc}{dt}(k_w,t)+\frac{k_w{}^4}{3Ca'}c(k_w,t)\mp\frac{ik_w{}^4}{6Ca'}\cos(t)=0. \tag{3.21}$$

If we assume that $f=A(t)\cos(k_w x)+B(t)\sin(k_w x)$ and substitute into (3.16) this gives us

$$A=A_0\exp\left(-\frac{k_w{}^4t}{3Ca'}\right),\quad \frac{dB}{dt}+\frac{k_w{}^4}{3Ca'}\left(B+\cos(t)\right)=0, \tag{3.22}$$

for some constant A_0, and so the modes depending on $\cos(k_w x)$ also die out (at the same rate as modes with $k\neq\pm k_w$) and any general initial free surface deflection settles down to be in phase with the wall in x. We are therefore justified in assuming that the x-dependence of the free surface is the same as the wall in the linear case.

This therefore suggests an analytical solution of the form

$$f=\Re\left[ig(t)\exp(ik_w x)\right], \tag{3.23}$$

whereby (3.16) becomes

$$\frac{dg}{dt}+\frac{k_w{}^4}{3Ca'}\left(g-\cos(t)\right)=0, \tag{3.24}$$

where it is understood that our solution is obtained by taking the real part. Assuming that the free surface is at rest when $t=0$, so that $\eta(x,0)=1$ and hence

$$f(x,0)=-\frac{s(x,0)}{\epsilon}=-\sin(k_w x), \tag{3.25}$$

we find that the solution is given by

$$f = \frac{1}{1 + 9Ca'^2/{k_w}^8} \left(-\frac{9Ca'^2}{{k_w}^8} \exp\left(-\frac{{k_w}^4}{3Ca'} t \right) - \cos(t) - \frac{3Ca'}{{k_w}^4} \sin(t) \right) \sin(k_w x). \quad (3.26)$$

Therefore, after the transient has decayed, the solution is periodic in both x and t for all time. Taking a different initial condition does not affect the behaviour of the settled solution, but simply alters the length of time before this solution is reached. Recalling that $\eta = s + 1 + \epsilon f$, we find that the larger we take Ca' or smaller we take k_w, the closer the phase and amplitude of the free surface to the wall. As we decrease Ca' or increase k_w, the amplitude of the free surface tends to zero.

3.3.1.2 A Numerical Solution

We may also solve (3.16) numerically. The numerical solution has no advantage over the analytical solution aside from being a useful check on our analytical results and requiring the use of an interesting numerical scheme. This scheme could be used for more complicated equations for which an analytical solution is not possible. Letting wide hats denote the Fourier transform as described in (3.17) and using integration by parts we find that

$$\widehat{\frac{\partial f}{\partial x}} = \frac{1}{2\pi} \int_{-\infty}^{\infty} \frac{\partial f}{\partial x} e^{-ikx} dx = \frac{ik}{2\pi} \int_{-\infty}^{\infty} f e^{-ikx} dx, \quad (3.27)$$

where we assume that $f \to 0$ as $x \to \pm\infty$. Therefore, taking the transform of (3.16) gives us

$$\frac{\partial \widehat{f}}{\partial t} + \frac{k^4}{3Ca'} \widehat{f} + \frac{{k_w}^4}{3Ca'} \cos(t) \widehat{\sin(k_w x)} = 0, \quad (3.28)$$

and each choice of k yields a first order ordinary differential equation for $\widehat{f}(k, t)$. The "stiff" second term in this equation leads to instabilities when solving numerically using the Runge–Kutta method (see Trefethen (2000)). We overcome this problem by multiplying (3.28) by an integrating factor and partially solving the equation analytically, such that

$$\frac{\partial}{\partial t} \left(\widehat{f} \exp\left(-\mathcal{L} t\right) \right) = \mathcal{N} \exp\left(-\mathcal{L} t\right), \quad \mathcal{L} = -\frac{k^4}{3Ca'}, \quad \mathcal{N} = -\frac{{k_w}^4}{3Ca'} \cos(t) \widehat{\sin(k_w x)}. \quad (3.29)$$

Equation (3.29) is then solved using an exponential time differencing (ETD) method, as outlined in Beylkin *et al.* (1998). This works by integrating equation (3.29) with respect to t from t_n to $t_{n+1} = t_n + \Delta t$, whereby we obtain an equation for stepping forward in time,

$$\widehat{f}(t_{n+1}) = \exp\left(\mathcal{L} \Delta t\right) \widehat{f}(t_n) + \exp\left(\mathcal{L} \Delta t\right) \int_0^{\Delta t} \exp\left(-\mathcal{L} \tau\right) \mathcal{N}(k, t_n + \tau) d\tau, \quad (3.30)$$

where $\tau = t - t_n$. Various ETD schemes arise depending on how the integral in (3.30) is approximated (see Cox and Matthews (2002)). Letting $\widehat{f}_n = \widehat{f}(t_n)$, the simplest ($ETD1$) scheme assumes that $\mathcal{N}$ is constant and therefore

$$\widehat{f}_{n+1} = \exp\left(\mathcal{L}\Delta t\right)\widehat{f}_n + \frac{1}{\mathcal{L}}\left(\exp\left(\mathcal{L}\Delta t\right) - 1\right)\mathcal{N}(k, t_n). \tag{3.31}$$

For small magnitudes of $\mathcal{L}$ this equation is equivalent to taking an Euler step forward. We use the more accurate second-order Runge–Kutta exponential time differencing method (ETD2RK), in which one step of the form (3.31) is taken before using the approximation

$$\mathcal{N} = \mathcal{N}(k, t_n) + \tau\frac{\mathcal{N}(k, t_n + \Delta t) - \mathcal{N}(k, t_n)}{\Delta t} + O(\Delta t^2) \tag{3.32}$$

in (3.30), giving us the scheme

$$\begin{aligned} a_n =& \exp\left(\mathcal{L}\Delta t\right)\widehat{f}_n + \frac{1}{\mathcal{L}}\left(\exp\left(\mathcal{L}\Delta t\right) - 1\right)\mathcal{N}(k, t_n), \\ \widehat{f}_{n+1} =& a_n + \frac{1}{\mathcal{L}^2\Delta t}\left(\exp\left(\mathcal{L}\Delta t\right) - 1 - \mathcal{L}\Delta t\right)\left(\mathcal{N}(k, t_n + \Delta t) - \mathcal{N}(k, t_n)\right). \end{aligned} \tag{3.33}$$

Here we take $\Delta t = 10^{-2}$.

Figure 3.2 shows typical plots of the settled solution, where we again take $\eta(x, 0) = 1$ as our initial condition. The analytical and numerical solutions for the free surface are plotted alongside each other and are found to be visually indistinguishable. In a similar way to in chapter 2, we obtain rows of cells divided by vertical lines of zero ψ. These cells take the form of open arcs. In some cases we find simply a single row of cells, whereas in others there are two rows divided by a horizontal line of zero ψ. In all cases consecutive cells spin in opposite directions. Altering Ca' and k_w, we find that the flow

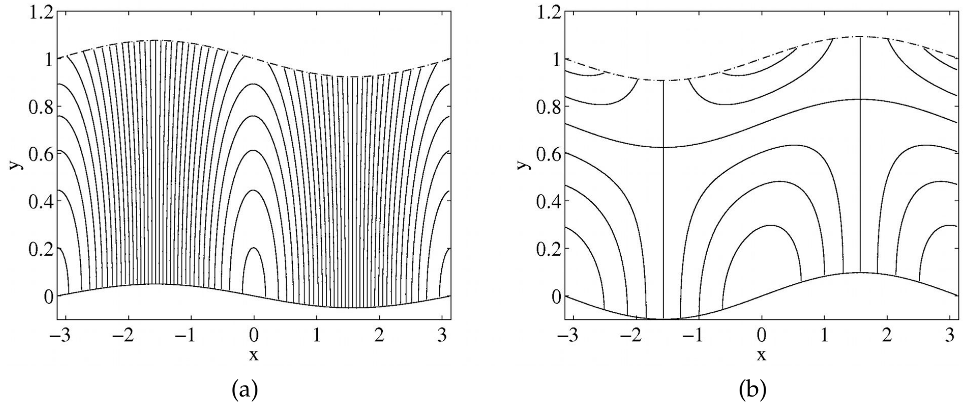

(a)

(b)

Figure 3.2: In case (i), typical plots of the analytical (dotted line) and numerical (dashed line) linear solutions for the free surface, η, plotted alongside typical streamlines and the wall, $s = \epsilon\sin(k_w x)\cos(t)$, (solid line). Here we take $\eta(x, 0) = 1$, $\epsilon = 0.1$, $Ca' = k_w = 1$ and $t =$ (a) $\frac{8\pi}{3}$ and (b) $\frac{256\pi}{65}$.

differs quantitatively from these plots but not qualitatively. Decreasing Ca' (increasing the surface tension coefficient), for example, we find that the flow more often takes the form of two rows of cells (as shown in 3.2b), and can be likened to flow in a channel with sinusoidally moving walls, as we might expect.

3.3.2 Case (ii); Inclined Thin Film Flow

In case (ii) our linearised equation for f obtained from (3.15) is

$$\frac{\partial f}{\partial t} + 2\frac{\partial f}{\partial x} + \frac{1}{3Ca'}\frac{\partial^4 f}{\partial x^4} + \frac{{k_w}^4}{3Ca'}\sin(k_w x)\cos(t) = 0, \tag{3.34}$$

which is the same as (3.16), but with an additional term (the second) describing the influence of gravity.

3.3.2.1 An Analytical Solution

Assuming that f takes the form of the inverse Fourier transform described in (3.17) and making use of (3.19), equation (3.34) yields

$$\frac{dc}{dt} + \left(\frac{k^4}{3Ca'} + 2ik\right)c + \frac{i{k_w}^4}{6Ca'}\cos(t)(\delta(k+k_w) - \delta(k-k_w)) = 0. \tag{3.35}$$

Then if $k \neq \pm k_w$, we find that $c = \exp(-(k^4/(3Ca') + 2ik)t)$, and all such modes decay with time. If $k = \pm k_w$, we again integrate from $\pm k_w - \epsilon$ to $\pm k_w + \epsilon$ and take the limit $\epsilon \to 0$. This gives us

$$\frac{dc}{dt} + \left(\frac{{k_w}^4}{3Ca'} \pm 2ik_w\right)c \mp \frac{i{k_w}^4}{6Ca'}\cos(t) = 0. \tag{3.36}$$

If we assume that $f = A(t)\cos(k_w x) + B(t)\sin(k_w x)$ and substitute into (3.34), this gives us

$$\frac{dA}{dt} + \frac{{k_w}^4}{3Ca'}A + 2k_w B = 0, \quad \frac{dB}{dt} + \frac{{k_w}^4}{3Ca'}(B + \cos(t)) - 2k_w A = 0, \tag{3.37}$$

and so in this case the modes depending on $\cos(k_w x)$ do not decay and although any initial free surface deflection settles down to have the same wavenumber as the wall, it may not be in phase in x.

We again take an analytical solution of the form (3.23), giving us, on substitution into (3.34),

$$\frac{dg}{dt} + \left(2k_w i + \frac{{k_w}^4}{3Ca'}\right)g - \frac{{k_w}^4}{3Ca'}\cos(t) = 0, \tag{3.38}$$

where it is understood that we need to take the real part. Supposing that the free surface is at rest when $t = 0$ and so $\eta(x, 0) = 1$, we may solve this equation. Defining, for brevity,

$$k_p = 1 + \frac{{k_w}^8}{9Ca'^2} + 4{k_w}^2, \quad k_{pm} = 1 + \frac{{k_w}^8}{9Ca'^2} - 4{k_w}^2, \quad k_m = 1 - \frac{{k_w}^8}{9Ca'^2} - 4{k_w}^2, \tag{3.39}$$

we obtain

$$\begin{aligned} f = & - \frac{3{k_w}^4 Ca'}{9{k_{pm}}^2 Ca'^2 + 16{k_w}^{10}} \left(- \exp\left(- \frac{{k_w}^4}{3Ca'} t \right) \left(2k_w k_m \cos(k_w(x - 2t)) \right. \right. \\ & \left. - \frac{1}{3Ca'} \left(\frac{1}{{k_w}^4} \left(9{k_{pm}}^2 Ca'^2 + 16{k_w}^{10} \right) - {k_w}^4 k_p \right) \sin(k_w(x - 2t)) \right) \\ & + \sin(k_w x) \left(\frac{{k_w}^4 k_p}{3Ca'} \cos(t) + k_{pm} \sin(t) \right) \\ & \left. + \cos(k_w x) \left(2k_w k_m \cos(t) - \frac{4{k_w}^5}{3Ca'} \sin(t) \right) \right), \end{aligned} \tag{3.40}$$

and following the decay of some travelling waves (with phase speed 2), the solution is again periodic in x and t for all time. A different initial condition simply results in the solution taking a different length of time to reach the settled solution. Since $\eta = s + 1 + \epsilon f$, we find that if Ca' is taken to be large or k_w small, $f \to 0$ and the phase and amplitude of the free surface tends to that of the wall. For general Ca' and k_w there is a phase difference in both x and t. As we decrease Ca' or increase k_w, we find that $f \to -s$ and the amplitude of the free surface tends to zero.

3.3.2.2 A Numerical Solution

Taking the Fourier transform of (3.34) gives us

$$\frac{\partial \widehat{f}}{\partial t} + \left(\frac{k^4}{3C'} + 2ik \right) \widehat{f} + \frac{{k_w}^4}{3C'} \cos(t) \widehat{\sin(k_w x)} = 0. \tag{3.41}$$

This equation can also be written in the form (3.29), where in this case,

$$\mathcal{L} = - \left(\frac{k^4}{3C'} + 2ik \right). \tag{3.42}$$

We may therefore solve using equation (3.30) and the scheme (3.33).

Figure 3.3 shows typical plots of the settled solution taking $\eta(x, 0) = 1$. Again plotting the analytical and numerical solutions for the free surface alongside each other, we find them to be visually indistinguishable. We find that due to the inclusion of gravity in the problem, the prevailing flow runs roughly parallel to the wall. In addition to this base-state flow, there is an $O(\epsilon)$ correction due to the wall motion. Therefore, at certain times, open arcs appear at $x = 0$ and $\pm\pi$ at the wall and free surface. The arcs

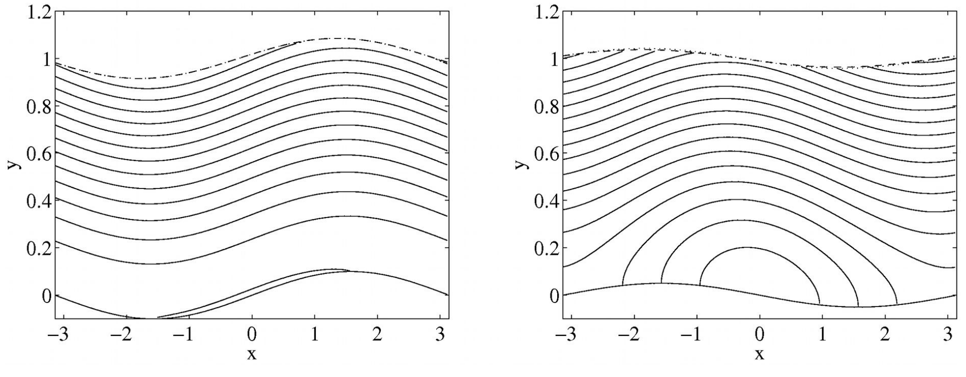

(a) (b)

Figure 3.3: In case (ii), typical plots of the analytical (dotted line) and numerical (dashed line) linear solutions for the free surface, η, plotted alongside typical streamlines and the wall, $s = \epsilon \sin(k_w x)\cos(t)$, (solid line). Here we take $\eta(x,0) = 1$, $\epsilon = 0.1$, $Ca' = k_w = 1$ and $t =$ (a) 2π and (b) $\frac{8\pi}{3}$.

turn in the same direction as the surrounding flow. Since, at the wall, the arcs appear at the stagnation points, this implies that fluid particles are restricted from flowing along and simply stay collected in these areas. Altering Ca' and k_w does not significantly change these observations.

3.4 A Nonlinear Solution

We now return to our thin film equations, (3.12) and (3.15), with the intention of solving numerically. Inspired by the periodicity of the linear solution, we use the implicit finite difference scheme outlined in Tseluiko and Papageorgiou (2006) for the general equation,

$$\frac{\partial H}{\partial t} + \frac{\partial}{\partial x}\left(a_1 \frac{\partial^3}{\partial x^3}(H+s)\right) + \frac{\partial}{\partial x}(a_2) = 0, \tag{3.43}$$

with periodic boundary conditions on the finite interval $[-\pi/k_w, \pi/k_w]$, where a_1 and a_2 are polynomials in H. We again let $s = \epsilon \sin(k_w x)\cos(t)$, but in this case the parameter ϵ is not necessarily small.

We first discretise in the x direction by writing $x_i = (i - N)\Delta x$ for $i = 1, \cdots, 2N$, and use the notation $H_k = H(x_k, t)$, $s_k = s(x_k, t)$, where s_k is known from the prescribed wall motion. Here the distance between grid points is $\Delta x = \pi/(k_w N)$. This gives us $2N$ equally spaced grid points in the interval. Since we have imposed H to be periodic, we may define the points outside the interval by letting $H_0 = H_{2N}$, $H_{-k} = H_{2N-k}$ and $H_{2N+k} = H_k$ for $k > 0$. Using central difference approximations of length Δx, (3.43) gives us

$$\frac{\partial \mathbf{H}}{\partial t} = \mathbf{F}(\mathbf{H}), \quad \mathbf{H} = (H_1, \cdots, H_{2N})^T, \quad \mathbf{F} = (F_1, \cdots, F_{2N})^T, \tag{3.44}$$

for

$$\begin{aligned} F_k = &- \frac{a_1\left(H_{k+1/2}\right)\delta_3(H+s)_{k+1/2} - a_1\left(H_{k-1/2}\right)\delta_3(H+s)_{k-1/2}}{\Delta x} \\ &- \frac{a_2\left(H_{k+1/2}\right) - a_2\left(H_{k-1/2}\right)}{\Delta x}, \end{aligned} \tag{3.45}$$

where

$$x_{1/2} = \frac{1}{2}\left(-L + x_1\right), \quad x_{i+1/2} = \frac{1}{2}\left(x_i + x_{i+1}\right), \quad i = 1, 2, \cdots, 2N-1, \tag{3.46}$$

and

$$\begin{aligned} \delta_3(H+s)_{k+1/2} &= \frac{\delta_2(H+s)_{k+1} - \delta_2(H+s)_k}{\Delta x}, \\ \delta_2(H+s)_k &= \frac{\delta_1(H+s)_{k+1/2} - \delta_1(H+s)_{k-1/2}}{\Delta x}, \\ \delta_1(H+s)_{k+1/2} &= \frac{(H_{k+1} + s_{k+1}) - (H_k + s_k)}{\Delta x}. \end{aligned} \tag{3.47}$$

We next discretise (3.44) with respect to time, writing

$$\frac{\mathbf{H}^{m+1} - \mathbf{H}^m}{\Delta t} = \mathbf{F}\left(\theta \mathbf{H}^{m+1} + (1-\theta)\mathbf{H}^m\right), \tag{3.48}$$

where $\mathbf{H}^m = \mathbf{H}(t = t_m)$, the timestep $\Delta t = t_{m+1} - t_m$ and θ is some real number in $[0, 1]$, which we take to be 1. The solution at $t = t^{m+1}$, $\mathbf{H}^{m+1}$, is then given by solving (3.48) iteratively using Newton's method.

In the calculation Δx and Δt change with time and their sizes alter so that a number of constraints are satisfied, as detailed in Tseluiko and Papageorgiou (2006). In general, they are chosen to increase accuracy without rendering the solution unnecessarily computationally expensive. We let $N = 100$ and $\Delta t = 10^{-2}$ for the first timestep. If we choose Δx and Δt to be progressively smaller for this initial step and compare the resulting solutions over time, we find that they converge, suggesting that our results are consistent.

In Tseluiko and Papageorgiou (2006) it is shown that H is always positive and the surface of the thin film never touches the wall. Although our problem differs from theirs since we have included a moving wall, this suggests that the same may be true in our case.

3.4.1 Case (i); Horizontal Thin Film Flow

In case (i) (3.12) can be written in the form (3.43) by taking $a_1 = H^3/(3Ca')$ and $a_2 = 0$. We validate our solution by decreasing the wall amplitude, ϵ, and checking that the linear and nonlinear solutions converge.

Figure 3.4 shows a typical evolution of the wall and free surface when ϵ is taken to be 0.9 and taking the initial condition $\eta(x, 0) = 1$. The solution for the free surface is qualitatively similar to when $\epsilon = 0.1$ but with a larger free-surface amplitude (especially initially). The settled solution remains in phase with the wall in x, but is slightly more noticeably out of phase in time. In addition, unlike in the case of smaller ϵ, the film is no longer of constant thickness at $x = n\pi$, $n \in \mathbb{Z}$. We also compare the nonlinear solution to the linear prediction. Although at times the linear solution appears to give a good approximation for large ϵ, this is not the case for all k_w and Ca'.

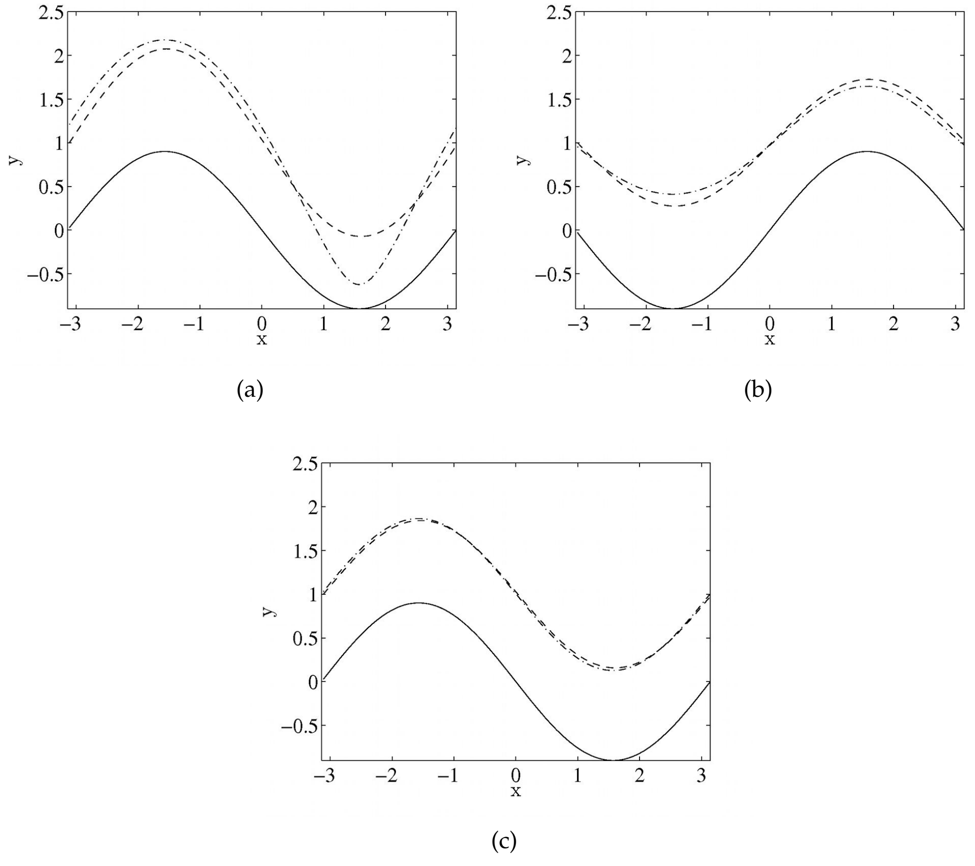

(a)

(b)

(c)

Figure 3.4: In case (i), typical plots of the nonlinear (dash-dotted line) and linear (dashed line) solutions for the free surface, η, plotted alongside the wall, $s = \epsilon \sin(k_w x)\cos(t)$, (solid line) when $\epsilon = 0.9$. Here we take $\eta(x, 0) = 1$ and $Ca' = k_w = 1$. In (a) $t = \pi$, (b) $t = 2\pi$ and (c) $t = 3\pi$.

As a check on the accuracy of our results and the validity of the periodic solution for large times, we consider the integrals

$$I_1(t) = \int_{-\pi/k_w}^{\pi/k_w} H dx, \quad I_2(t) = \int_{-\pi/k_w}^{\pi/k_w} H^2 dx, \tag{3.49}$$

using the trapezium rule, which is found to give a good approximation, especially when integrating a periodic function over its period. Once the solution has settled, I_1 is found to be constant (to within the accuracy of the program), as we would expect. Plots of I_2 give us an indication as to when the solution has settled and afterwards show a periodic solution.

We focus on a single choice of parameters, namely $Ca' = 0.1$ and $k_w = 1$, which we feel relevant to the DGM. Preliminary work for general values of Ca' and k_w suggested that the solution is qualitatively similar in all cases. However, a more rigorous study of the solution for general values would be time consuming, especially for larger values of Ca' and smaller values of k_w, for which the solution takes a lot longer to settle. We therefore leave a more thorough examination in (Ca', k_w)-space as a possible topic of future research. The choice of Ca' comes from consideration of the values stated in chapter 1, taking μ to be of the $O(10^{-2})$ to represent the lower viscosity gastric juice and U to be of the $O(10^{-4})$. From Kong and Singh (2008a), we may also take γ to be of the $O(10^{-2})$. Then, letting $\delta = 10^{-1}$, a realistic order of magnitude for Ca' as defined in (3.3) is 10^{-1}.

Letting $I_{2\,i} = I_2(t_i)$, in figure 3.5 we plot the set of points $(I_{2\,i}, I_{2\,i+1})$ for $i = 1, ..., 9$, where $t_{i+1} = t_i + 2\pi$ and t_1 is chosen such that the solution has settled. We obtain a single dot, indicating that the period is either 2π or divides 2π. Given our plots of I_2, we conclude that the period is 2π, the same as the wall. We also plot a phase portrait of $\partial H/\partial t$ against H for a fixed x, which we choose to be $-\pi/2$. Here the time derivative is given by equation (3.12), in which x derivatives can be obtained by a transformation into Fourier space. Once the solution has settled, we obtain a closed curve, again indicating

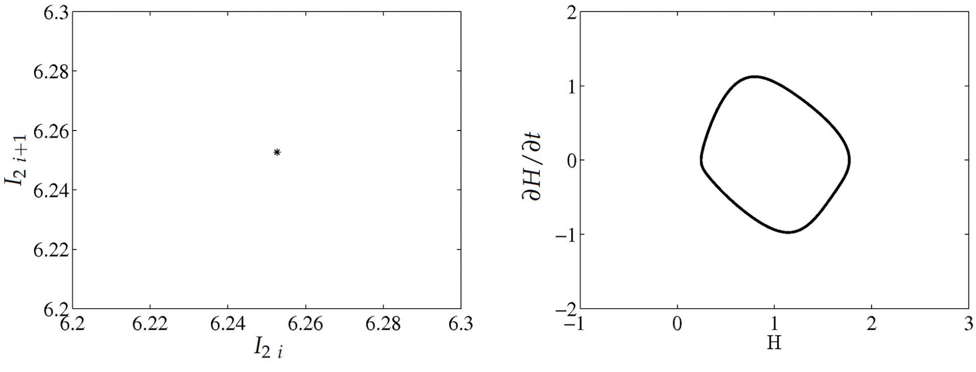

(a) (b)

Figure 3.5: In case (i), when $\epsilon = 0.9$, $C' = 0.1$ and $k_w = 1$, plots of (a) $I_{2\,i+1}$ against $I_{2\,i}$ and (b) $\partial H/\partial t$ against H.

a periodic solution, at least in the (relatively long) time period that we consider.

3.4.2 Case (ii); Inclined Thin Film Flow

In case (i) (3.15) can be written in the form (3.43) by taking $a_1 = H^3/(3Ca')$ and $a_2 = 2H^3/3$. The convergence of our solution is checked by decreasing the wall amplitude, ϵ, and checking that the linear and nonlinear solutions correspond.

Figure 3.6 shows typical plots of the wall and free surface when $\epsilon = 0.9$ and $\eta(x,0) = 1$. Similar to case (i), the settled solution is like that when $\epsilon = 0.1$, but is slightly more out of phase in time, leading to more variation in H over a period in x. For early times we now clearly see the appearance of modes with a different shape and wavenumber to that of the wall. These modes appear to take the form of a right-travelling wave, which can sometimes be relatively steep, before settling down. As we increase Ca', we find that the wave steepening becomes more severe (see figure 3.7a). It is interesting to note

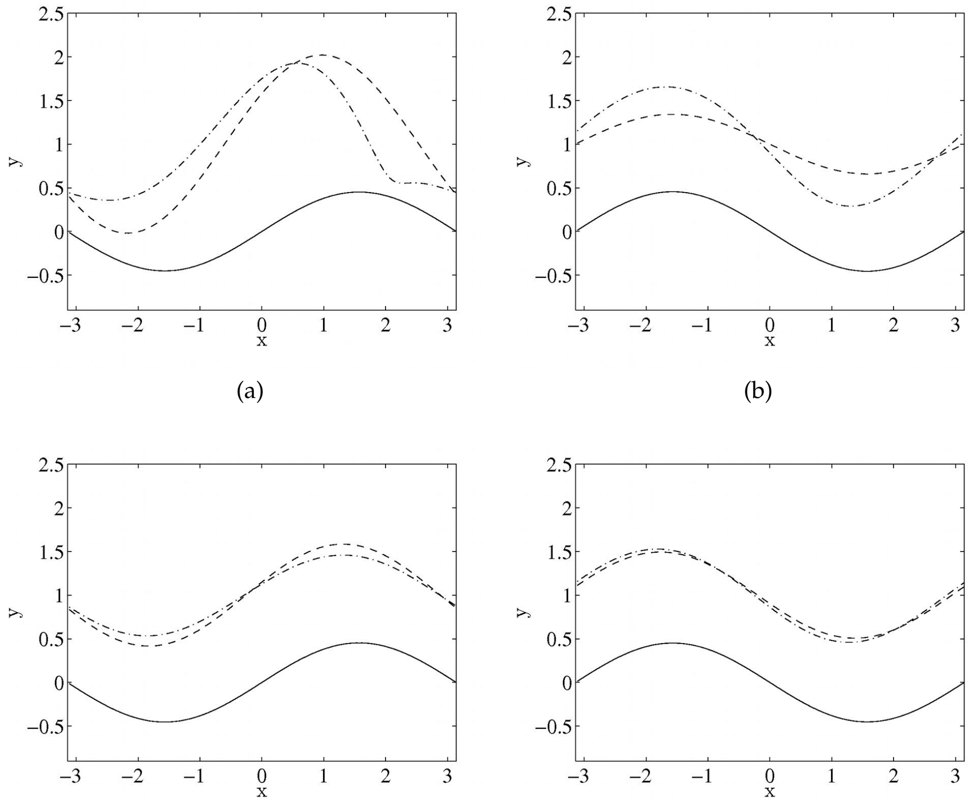

(a) (b)

(c) (d)

Figure 3.6: In case (ii), typical plots of the nonlinear (dash-dotted line) and linear (dashed line) solutions for the free surface, η, plotted alongside the wall, $s = \epsilon \sin(k_w x)\cos(t)$, (solid line) when $\epsilon = 0.9$. Here we take $\eta(x,0) = 1$ and $Ca' = k_w = 1$. In (a) $t = \frac{\pi}{3}$, (b) $t = \frac{4\pi}{3}$, (c) $t = \frac{7\pi}{3}$ and (d) $t = \frac{10\pi}{3}$.

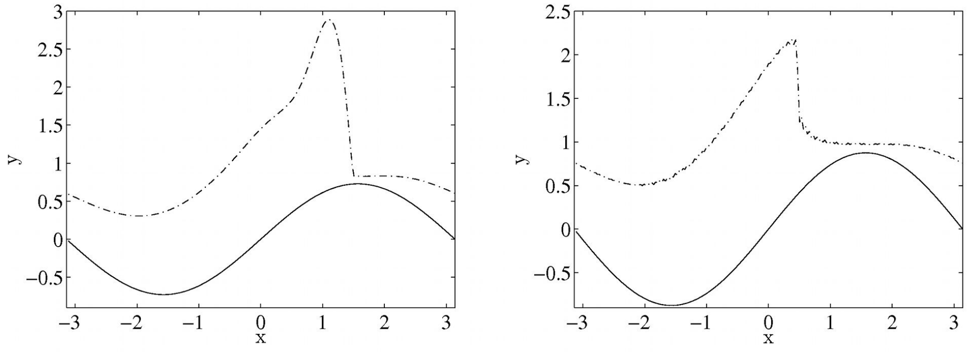

(a) (b)

Figure 3.7: In case (ii), a plot of the nonlinear (dash-dotted line) and linear (dashed line) solutions for the free surface, η, plotted alongside the wall, $s = \epsilon \sin(k_w x)\cos(t)$, (solid line) when $\epsilon = 0.9$ and when (a) $Ca' = 100$ and $t = \frac{3\pi}{15}$ and (b) the right-hand side of (3.50) is taken to be zero and $t = \frac{9\pi}{120}$. Here we take $\eta(x, 0) = 1$ and $k_w = 1$.

that we can re-write equation (3.15) as

$$\frac{\partial H}{\partial t} + 2H^2\frac{\partial H}{\partial x} = -\frac{\partial}{\partial x}\left(\frac{1}{3Ca'}H^3\frac{\partial^3}{\partial x^3}(H+s)\right), \tag{3.50}$$

which, with the right hand side equal to zero, can be compared to the equation $\partial H/\partial t + H\partial H/\partial x = 0$, which is known to lead to wave steepening and breaking. Since we do not see wave breaking in our solution (although the wave front appears to be almost vertical at times, $\partial H/\partial x$, which seems to be proportional to Ca', is simply found to be very large at this point), this suggests that the term on the right hand side of (3.50) is stabilising and that breaking can only occur in the infinite Ca' limit.

We use the method of characteristics to analyse equation (3.50) with right hand side equal to zero. Letting $H = H(x(\theta), t(\theta))$ for some parameter θ, we can re-write this equation as

$$\frac{dH}{d\theta} = \frac{\partial H}{\partial x}\frac{dx}{d\theta} + \frac{\partial H}{\partial t}\frac{dt}{d\theta}, \tag{3.51}$$

where

$$\frac{dH}{d\theta} = 0, \quad \frac{dx}{d\theta} = 2H^2, \quad \frac{dt}{d\theta} = 1. \tag{3.52}$$

The third of equations (3.52) implies, without loss of generality, that $\theta = t$. The first implies that H is constant along a characteristic and then the second gives us the equation of the characteristics, $x = \xi + 2H(\xi, 0)^2 t$, for some constant ξ. Supposing that a neighbouring curve has the characteristic equation $x = \xi + d\xi + 2H(\xi + d\xi, 0)^2 t$, this curve meets the first curve when x and t are the same for both. Equating the two equations, we find that wave breaking occurs if t is positive and

$$t = t_b = -\frac{1}{4H(\xi,0)dH/d\xi(\xi,0)} = \frac{1}{4\epsilon k_w \cos(k_w\xi)(1-\epsilon\sin(k_w\xi))}\,, \tag{3.53}$$

where we let $d\xi \to 0$. Here we recall that $H = \eta - s$ and $s = \epsilon\sin(k_w x)\cos(t)$ and let $\eta(x,0) = 1$. The breaking time, t_b, marks the moment when H (and therefore η) becomes multivalued. We note that if we had instead taken $\eta(x,0) = 1+\epsilon\sin(k_w x)$, so that the free surface has the same initial shape as the wall, then we could delay breaking until infinity. The minimum time to break is given when $d/d\xi\,(1/t_b) = 0$, suggesting that

$$\sin(k_w\xi) = \frac{1 \pm (1+8\epsilon^2)^{1/2}}{4\epsilon}. \tag{3.54}$$

If we take $\epsilon = 0.9$ and $k_w = 1$, then only the second root in (3.54) is relevant and we find that $t_b \approx 0.22$. Plots of the solution to (3.50) when the right hand side is taken to be zero are found to agree with this prediction (see figure 3.7b).

We emphasise that these results are subject to an initially flat free surface and sinusoidal wall, which, especially when ϵ is large, means that we are perturbing the system quite dramatically. If we were to take a gentler initial condition, such as a wall and free surface that are just out of phase with each other, then any wave steepening would be much less pronounced. Equally, we could push the solution even further with a harsher initial condition, leading to worse steepening.

We again focus on a single choice of parameters to check the validity of our solution for large times. Preliminary work using other parameter choices, however, suggested that the periodic solution persists. Taking, in addition to the values quoted in case (i), ρ to be of the $O(10^3)$, g to be of the $O(10)$ and $\alpha = \pi/4$, we find that a realistic order of magnitude for Ca', as defined in (3.3) using (3.1), is 10^2. We also take $k_w = 1$. Since Ca' has been chosen to be large and the film thickness varies by a small amount, plots of both I_1 and I_2 (as defined in (3.49)) show constant functions and plots of $I_{2\ i+1}$ against $I_{2\ i}$ and $\partial H/\partial t$ against H show a single dot (to within the accuracy of our program). We find no evidence of further wave steepening in our results and the settled solution persists for as long as we calculate.

3.5 Inclined Thin Film Flow When the Wall is Held Fixed

It is relatively easy for us to adapt our work for case (ii) to examine the case of a fixed sinusoidal wall inclined at an angle α to the horizontal, by simply taking $s = \epsilon\sin(k_w x)$ for all time. Some typical plots of the settled solution for small ϵ are shown in figure 3.8. We compare our results to those of Pozrikidis (1988), who considered the same problem. When $\epsilon = 0.1$, their results suggest that for small surface tension (or in our case large Ca') and moderate k_w, the free-surface amplitude becomes close to that of

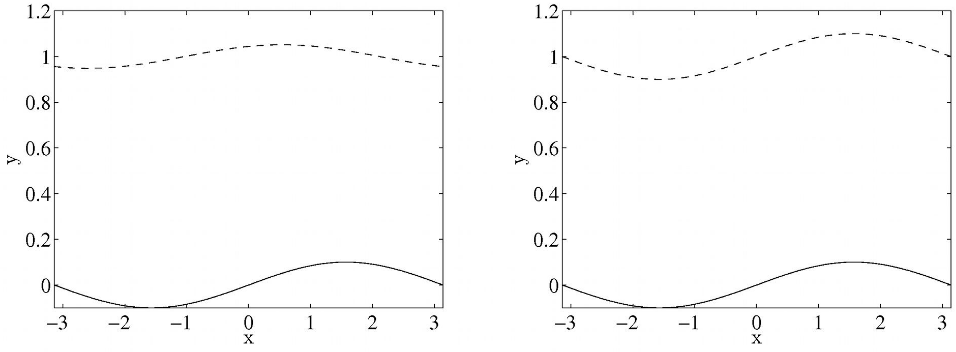

(a) (b)

Figure 3.8: In the case of thin film flow next to a fixed, inclined sinusoidal wall, a plot of the settled solution for the free surface, η, (dashed line) and the wall, $s = \epsilon \sin(k_w x)$, (solid line) when $\epsilon = 0.1$, $k_w = 1$ and (a) $Ca' = 0.1$ and (b) 100.

the wall (between 0.8ϵ and 0.9ϵ) and the free surface is around -10 ° out of phase. As Ca' is decreased, the amplitude of the free surface decreases relative to the wall and the free surface lags further behind the wall. When Ca' is small, the amplitude of the free surface is somewhere between 0.6ϵ and 0.75ϵ and is out of phase by ≈ -30 °. The results of Pozrikidis (1988) are in agreement with our work.

Figure 3.9 shows our results for the settled solution when $\epsilon = 0.9$. Here the work

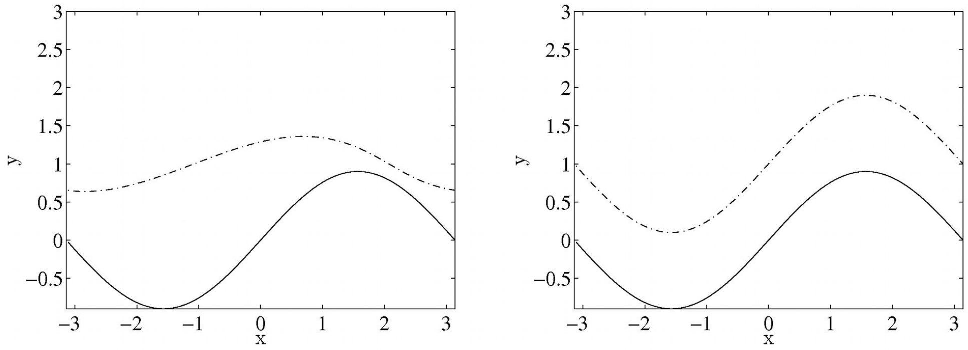

(a) (b)

Figure 3.9: In the case of thin film flow next to a fixed, inclined sinusoidal wall, a plot of the settled solution for the free surface, η, (dashed line) and the wall, $s = \epsilon \sin(k_w x)$, (solid line) when $\epsilon = 0.9$, $k_w = 1$ and (a) $Ca' = 0.1$ and (b) 100.

of Pozrikidis (1988) suggests that for large Ca' and moderate k_w, the amplitude of the free surface reduces to between around 0.75ϵ and 0.85ϵ, and lags behind the wall with a phase shift of around $-11°$. For small Ca', the amplitude should be around half that of the wall and the free surface around -50 ° out of phase. Again, this agrees with our results.

Interestingly, we see wave steepening in the nonlinear solution before the settled solution is reached. Wierschem and Aksel (2003) and Wierschem *et al.* (2005) considered the stability of thin film flow down a fixed sinusoidal wall for general Reynolds numbers, finding that there exists a critical Reynolds number, Re_{cr}, above which the steady solution for the free surface is unstable to perturbations of certain wavelengths. The value of Re_{cr} was found to be proportional to the surface tension coefficient, suggesting that the only way to obtain unstable solutions (or wave breaking) in the case of Stokes flow would be to let the surface tension tend to zero (similar to the case of a moving wall). It was found that Re_{cr} is larger than the critical Reynolds number for flow down a flat wall, showing that the fixed wavy wall is stabilising (a property which may extend to the moving wavy wall).

3.6 Inclined Thin Film Flow With Stress at the Free Surface

To give us an idea as to whether adding a second fluid above an inclined thin film would worsen or lessen wave steepening, we briefly consider the idealised addition of a constant, non-dimensional shear stress, S, to the tangential components of stress, σ_{ij}, $i \neq j$, at the free surface. In this case we solve the non-dimensionalised Navier–Stokes equations, (3.5), subject to boundary conditions (3.6) and (3.7) and with equations (3.8) replaced by

$$p(x,\eta,t) = -\frac{1}{Ca'}\frac{\partial^2 \eta}{\partial x^2}, \qquad \frac{\partial u}{\partial y}(x,\eta,t) = -\frac{S}{\delta} = -\tilde{S}, \tag{3.55}$$

and the thin film equation becomes

$$\frac{\partial H}{\partial t} + \frac{\partial}{\partial x}\left(\frac{2}{3}H^3 + \frac{1}{3Ca'}H^3\frac{\partial^3}{\partial x^3}(H+s) - \frac{\tilde{S}}{2}H^2\right) = 0. \tag{3.56}$$

It is interesting that if we take the wall description to be $s = 0$ (so that we have a flat wall), then (3.56) becomes

$$\frac{\partial H}{\partial t} + 2H^2\frac{\partial H}{\partial x} + \frac{1}{Ca'}H^2\frac{\partial^3 H}{\partial x^3} + \frac{1}{3Ca'}H^3\frac{\partial^4 H}{\partial x^4} - \tilde{S}H\frac{\partial H}{\partial x} = 0. \tag{3.57}$$

This problem has been studied by Wei (2008), who found that all disturbances decay regardless of the sign or size of the imposed shear. Taking the first, third and fifth terms or the first, fourth and fifth terms, (3.57) can be likened to a KDV or KS type equation, respectively, both of which have solitary wave solutions. This suggests that a soliton solution to (3.57) is possible. Plots of the free surface show that, taking the initial perturbation to be sinusoidal, a negative stress of -10 results in a right travelling wave initially whilst a positive stress of 10 results in a more slowly advancing left travelling wave (see figure 3.10). In this case, to leading order, $u = y\left(2 - \tilde{S} - y\right)$, and so takes the value $1 - \tilde{S}$ when $y = 1$, suggesting that waves at the free surface travel to the left if

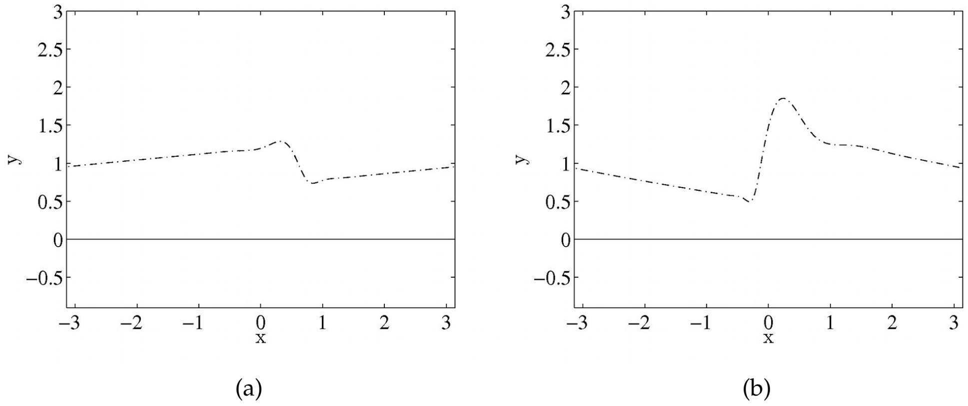

(a) (b)

Figure 3.10: In the case of an inclined thin film with stress at the free surface, a plot of the free surface, η, (dash-dotted line) and the wall, s, (solid line) when $s = 0$, $\eta(x,0) = 0.9\sin(k_w x)$, $k_w = 1$, $Ca' = 100$, $t = \frac{4\pi}{15}$ and $\tilde{S} =$ (a) -10 and (b) 10.

$\tilde{S} > 1$ and to the right if $\tilde{S} < 1$. From equation (3.55), there is a positive velocity gradient at the free surface if $\tilde{S}$ is negative, and a negative gradient if $\tilde{S}$ is positive. Evidently if $\tilde{S}$ is positive with magnitude greater than 1, it is possible for the flow to be uphill at the free surface.

Returning to equation (3.56) and taking $s = \epsilon\sin(k_w x)\cos(t)$, we observe wave steepening at the free surface initially in a similar way to when $\tilde{S} = 0$. Some typical plots are shown in figure 3.11, where $\epsilon = 0.9$. Once again, we do not see wave breaking, suggesting that the term inversely proportional to Ca' is stabilising. Like for the case of a flat wall, taking $\tilde{S} = -10$ results in a right-travelling wave, whilst $\tilde{S} = 10$ results in a left travelling wave. The settled solution for the free surface is qualitatively similar to when $\tilde{S} = 0$ (discussed previously).

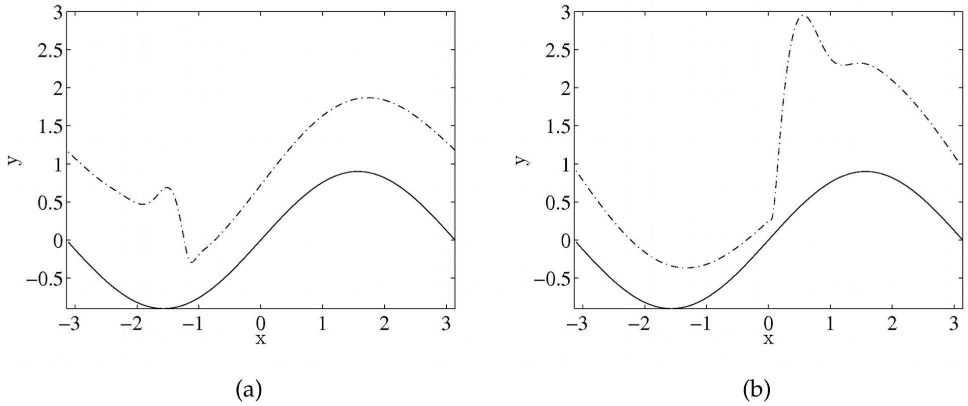

(a) (b)

Figure 3.11: In the case of an inclined thin film with stress at the free surface, a plot of the free surface, η, (dash-dotted line) and the wall, $s = \epsilon\sin(k_w x)\cos(t)$, (solid line) when $\epsilon = 0.9$, $\eta(x,0) = 0$, $k_w = 1$, $Ca' = 100$, $t = \frac{2\pi}{15}$ and $\tilde{S} =$ (a) -10 and (b) 10.

If we instead take a fixed, sinusoidal wall, $s = \epsilon\sin(k_w x)$, the wave steepening at the interface for early times is qualitatively similar to that seen for the case of a moving, sinusoidal wall. The settled solution is qualitatively similar to when $\tilde{S} = 0$.

3.7 Discussion

We have considered two cases of thin film flow next to a sinusoidally moving wall. In case (i) the wall was held horizontal, whilst in case (ii) it was inclined an an angle to the horizontal and gravity was allowed to act. In each case we derived a thin film equation.

For small amplitudes of the wall we obtained an exact solution. In case (i) the x-dependence of the free surface is the same as that of the wall, whilst in case (ii) there is a phase difference between the two. In both cases, after an initial transient has decayed, the solution for the free surface is periodic in x and t, with a phase and amplitude that tend to the phase and amplitude of the wall as either the capillary number is increased or the wavenumber of the wall is reduced. The amplitude of the free surface tends to zero as the capillary number is decreased or the wavenumber increased. Streamline plots show rows of cells similar to those found in chapter 2, although in case (ii) they are superposed with a prevailing flow running roughly parallel to the wall.

It is found that for larger wall amplitudes, the settled solution is qualitatively similar to the linear solution in both cases, although more variation is seen in the film thickness. In case (ii) wave steepening may be seen at early times, although breaking can only occur for an infinite capillary number.

Although we have not found any similar work considering thin film flow next to a moving sinusoidal wall, there has been a large amount of work considering flow next to a fixed sinusoidal wall. In the case of an inclined, fixed sinusoidal wall our results are found to agree with those of Pozrikidis (1988), who considered a similar problem.

When we add a constant shear stress at the free surface in case (ii), this does not promote wave-breaking. This suggests that if we were to include a second fluid above the thin film, the solution would be no more likely to include interfacial breakdown than the solution for the case of a single thin film.

In the next chapter we focus our efforts elsewhere by considering the flow of two fluids next to an elastic wall. We hope that such a flow will yield unstable solutions.

Chapter 4

Shear-Driven Flow Next to an Elastic Wall

4.1 Introduction

The results of the previous chapter do not give us a reason to expect an unstable solution when considering a semi-infinite fluid sitting above a thin film of different, constant viscosity, both of which flow past a moving, sinusoidal wall. Rather than focussing on such a problem, we instead draw inspiration from the work of Chen (1993). Here unstable solutions are found when considering the flow of a two-layer liquid film down an inclined plane if the fluid next to the wall is taken to be the least viscous. In this work it is hypothesised that some kind of interaction between the interface and free surface is responsible for the instability. Transverse movements of the interface are highlighted as crucial to this effect.

Returning to the analysis in chapter 2, we might expect to make some progress by imposing a tangential velocity at the wall, as discussed in the discussion, section 2.5. Here we would need to allow for two fluids and could take the vertical velocity at the wall to be zero, so that the wall is flat. However, in this case the solution is found to remain stable. The main difference between this case and the vertically moving wall case is that the streamlines are now closed curves. Typical plots of these streamlines are shown in figure 4.1.

Therefore, in this chapter we choose to consider two-fluid, creeping flow next to a wall which is modelled as an elastic beam. Since both the beam and interface are free to move, with positions which are unprescribed, it is hoped that an interaction between the two may yield unstable solutions. The use of an elastic wall is a fair assumption in terms of the DGM, since the walls of the body are made of an elastic material.

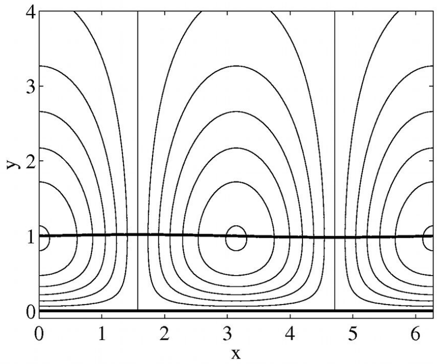

Figure 4.1: Typical streamlines for two-fluid flow next to a tangentially moving wall, with non-dimensional tangential velocity $\epsilon \cos(kx) \cos(t)$ and zero normal velocity.

4.2 Problem Description

We consider the linear stability of two fluids next to an elastic wall modelled as a beam, as described in appendix A. The problem is summarised in figure 4.2. The amplitude of the wall, $y^* = s^*(x^*, t^*)$, is assumed to be of $O(\epsilon)$, where $0 < \epsilon \ll 1$ is a small parameter and the interface is described by $y^* = \eta^*(x^*, t^*)$. Here stars denote dimensional variables that have a non-dimensional counterpart. We take the subscripts $j = 1$ and 2 to denote the lower and upper fluid, respectively, and μ_j is the viscosity in fluid j. The pressure in the static air below the wall is held at p_0. Above the wall, in fluid 1, the stress tensor σ_1, is as defined in (1.15). The traction on the beam due to the surrounding fluid is

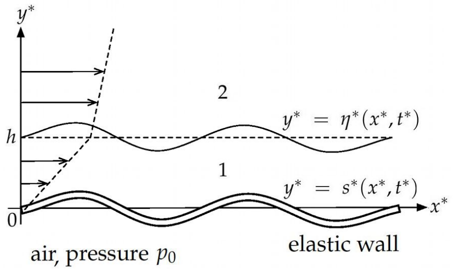

Figure 4.2: The problem of two fluids subject to a shear flow, flowing past an elastic wall.

$$\mathbf{f} = \sigma_1 \cdot \hat{\mathbf{n}} + p_0 \hat{\mathbf{n}}, \tag{4.1}$$

where the unit vector, $\hat{\mathbf{n}}$, points into fluid 1. The governing equations for the wall, the beam equations (A.10), then become

$$-E_B s_{xxxx} + \tau s_{xx} = \left(-\sigma_{1yy} + s_x(\sigma_{1xy} + \sigma_{1yx})\right)_{y=s} - p_0 + O\left(\epsilon^2\right), \tag{4.2}$$

and

$$\frac{d\tau}{dx} = -\left(\sigma_{1xy} + s_x(-\sigma_{1xx} + \sigma_{1yy})\right)_{y=s} + O\left(\epsilon^2\right), \tag{4.3}$$

where E_B is the bending modulus and τ is the tension along the wall, which we take to be the constant τ_0 when $x = 0$. In addition to modelling the wall using the beam equations, we also imagine it to be held in place with springs which are held vertical; this is the "spring model" adopted by Jensen *et al.* (2002) amongst others. By using this condition we may continue to consider a wall that is displaced in the y-direction only and so we may still use the no-slip condition, (1.14). In the base-state we assume a shear flow. The constant strength of the shear at infinity is taken to be S. The unperturbed, flat wall and interface descriptions are $y^* = 0$ and $y^* = h$, respectively, and the unperturbed pressure is p_0 everywhere.

Non-dimensionalising using the characteristic length scale h, time-scale $1/S$ and viscosity scale μ_1 results in the non-dimensional parameters,

$$\Lambda = \frac{\mu_2}{\mu_1}, \quad Ca = \frac{h\mu_1 S}{\gamma}, \quad E = \frac{E_B}{h^3\mu_1 S}, \quad T = \frac{\tau_0}{h\mu_1 S}, \quad \hat{p_0} = \frac{p_0}{\mu_1 S}, \tag{4.4}$$

where Λ is the viscosity ratio, Ca is the capillary number and E, T and $\hat{p_0}$ are the non-dimensional bending moment, underlying beam tension and underlying pressure, respectively. Non-starred variables are taken to be non-dimensional and we introduce the streamfunction, $\psi_j(x, y, t)$, velocity field, $\mathbf{u}_j(x, y, t) = (u_j, v_j)$, and pressure, $p_j(x, y, t)$ in fluid j.

The base-state is denoted with superscript (0). In the case of steady shear flow the base-state velocity in fluid j is assumed to take the form, $\mathbf{u}_j{}^{(0)} = (u_j(y)^{(0)}, 0)$. The Stokes equations then reduce to the steady version of (1.7). We non-dimensionalise and apply these equations in fluids $j = 1$ and 2. We solve for $u_j{}^{(0)}$, taking a zero pressure gradient and applying non-dimensionalised versions of the no-slip condition, (1.14), at the wall, $y = 0$, and the stress condition, (1.21) and the first of the velocity conditions, (1.22), at the interface, $y = 1$, (where the curvature is zero). We also ensure that $du_j{}^{(0)}/dy \to 1$ as $y \to \infty$. We then find that in the base-state, the streamfunction in fluid j is

$$\psi_j{}^{(0)} = \left(\frac{\mu_2 y^2}{2\mu_j} + y(\Lambda - 1)(j - 1)\right), \tag{4.5}$$

Although formally the base-state streamfunction and velocity are unbounded as $y \to \infty$, we consider only a local description of the flow field in this analysis. A global analysis would require a different description and the two descriptions would then need to be resolved for intermediate values of y.

4.2.1 Modelling the Tension in the Wall

Non-dimensionalising the beam equations, equation (4.3) gives us

$$\tau = T - \Lambda x + O(\epsilon). \tag{4.6}$$

Although the tension in the beam formally becomes infinite as $x \to \pm\infty$, we may argue that we only consider a local analysis in this problem. However, we run into problems when substituting (4.6) into (4.2), the resulting equation being very difficult to solve analytically. We might expect an improvement in the situation if we instead consider a stagnation point-type flow next to a stretching wall, as seen in Mahapatra and Gupta (2003). In this case the wall is allowed to move tangentially and the velocity, (u, v), is taken to be $(\alpha x, -\alpha y)$ away from the wall and $(\beta x, 0)$ on the wall, for α, β positive constants, so that a boundary layer is needed at the wall. This problem has the advantage that to leading order τ is independent of x. However, solving for the unknown, perturbed velocity and particle positions on the stretching wall is far from trivial.

We instead take the approach of Luo and Pedley (1995), and define

$$\tilde{\tau} = \frac{T}{\Lambda}, \tag{4.7}$$

whereby equation (4.6) can be rewritten

$$\tau = T\left(1 - \frac{x}{\tilde{\tau}}\right) + O(\epsilon). \tag{4.8}$$

We now take the large tension limit, $\tilde{\tau} \gg 1$, so that τ is approximated by the constant T. Here we assume that the wavelength in x is $O(1)$. Then (4.2) gives us

$$-Es_{xxxx} + Ts_{xx} = \left(p_1 - p_0 - 2\left(\frac{\partial v_1}{\partial y} - s_x \frac{\partial u_1}{\partial y}\right)\right)_{y=s} + O\left(\epsilon^2\right). \tag{4.9}$$

We note that this approximation breaks down as $x \to \pm\infty$, and so our solution must still be thought of as local.

4.2.2 The Perturbed Solution

The base-state solution is perturbed by a time-dependent excitation, denoted with superscript (1), such that

$$\begin{aligned} s =& \epsilon A \exp(ik(x - ct)), \quad \eta = 1 + \epsilon \exp(ik(x - ct)), \\ \psi_j =& \psi_j{}^{(0)}(y) + \epsilon \psi_j{}^{(1)}(y) \exp(ik(x - ct)), \\ p_j =& \hat{p}_0 + \epsilon p_j{}^{(1)}(y) \exp(ik(x - ct)), \end{aligned} \tag{4.10}$$

where k is the prescribed, real wavenumber of the disturbance and $c = c_R + ic_I$ and $A = A_R + iA_I$ are the complex wave speed and amplitude of the wall, respectively, which must both be determined as part of the solution. We introduce A since the wall position is governed by the beam equation rather than being fully prescribed. The assumed forms of η, ψ_j and p_j are chosen given the elected wall description and since we are solving a linear problem with constant coefficients, so that we expect that the solution will be a linear superposition of modes with the same x and t dependence. We note that in our solution, we may multiply the interface perturbation by some constant (so that the perturbation has a small, but arbitrary amplitude), and the above solution in that sense is non-unique. However, in this analysis, we can treat this constant as being absorbed into ϵ.

We non-dimensionalise and linearise all boundary conditions. The no-slip and kinematic conditions at the moving wall, (1.14) and (1.9), yield

$$\frac{d{\psi_1}^{(1)}}{dy}(0) = -\Lambda A, \quad {\psi_1}^{(1)}(0) = Ac, \tag{4.11}$$

whilst the beam equation, (4.9), gives us

$${p_1}^{(1)}(0) = -Ak^2\left(k^2E + T\right), \tag{4.12}$$

where we have used equations (4.11). The velocity continuity and kinematic conditions at the interface, (1.22) and (1.23), meanwhile, give us

$${\psi_1}^{(1)}(1) = {\psi_2}^{(1)}(1), \quad \frac{d{\psi_1}^{(1)}}{dy}(1) - \frac{d{\psi_2}^{(1)}}{dy}(1) = 1 - \Lambda, \tag{4.13}$$

and

$${\psi_2}^{(1)}(1) = c - \Lambda. \tag{4.14}$$

Evaluating the stress condition, (1.21), in the directions normal and tangential to the interface gives us

$${p_1}^{(1)}(1) - {p_2}^{(1)}(1) + 2ik\left(\frac{d{\psi_1}^{(1)}}{dy}(1) - \Lambda\frac{d{\psi_2}^{(1)}}{dy}(1)\right) = \frac{k^2}{Ca}, \tag{4.15}$$

and

$$\frac{d^2{\psi_1}^{(1)}}{dy^2}(1) + k^2{\psi_1}^{(1)}(1) - \Lambda\left(\frac{d^2{\psi_2}^{(1)}}{dy^2}(1) + k^2{\psi_2}^{(1)}(1)\right) = 0. \tag{4.16}$$

We must also satisfy the far-field conditions

$${\psi_2}^{(1)}(\infty) = \frac{d{\psi_2}^{(1)}}{dy}(\infty) = 0. \tag{4.17}$$

4.3 Problem Solution

For brevity we define the functions

$$s_y = \sinh(ky), \quad c_y = \cosh(ky), \quad s_1 = \sinh(k), \quad c_1 = \cosh(k), \tag{4.18}$$

and we let

$$k_b = \frac{Ek^2 + T}{2}. \tag{4.19}$$

Non-dimensionalising the biharmonic equation, (1.5), taken in fluids 1 and 2, we solve subject to boundary conditions (4.11), (4.12), (4.14) and (4.17). To determine the pressure in each fluid we use the Stokes equations, given by the first of (1.3). The streamfunction and pressure perturbations in fluids 1 and 2 are then given by the following:

$$\begin{aligned} {\psi_1}^{(1)} =& cAc_y + B_1 y s_y + A\left(\left(ik_b - \frac{\Lambda}{k}\right)s_y - ikk_b y c_y\right), \\ {\psi_2}^{(1)} =& \left(B_2\left(y-1\right) + \left(c - \Lambda\right)e^k\right)e^{-ky}. \\ {p_1}^{(1)} =& -2ik\left(B_1 s_y - Aikk_b c_y\right), \quad {p_2}^{(1)} = -2ik\Lambda B_2 e^{-ky}, \end{aligned} \tag{4.20}$$

From (4.13), we find that

$$\begin{aligned} B_1 =& \frac{1}{s_1}\left(-cAc_1 + c - \Lambda - A\left(\left(ik_b - \frac{\Lambda}{k}\right)s_1 - ikk_b c_1\right)\right), \\ B_2 =& e^k\left(-cA\left(\frac{k}{s_1} + c_1\right) + k\left(\frac{c_1}{s_1} + 1\right)(c - \Lambda) + c - 1 - A\left(\left(ik_b - \frac{\Lambda}{k}\right)s_1 - \frac{ik^2}{s_1}\right)\right). \end{aligned} \tag{4.21}$$

The amplitude, A, and wave speed, c, are then obtained from equations (4.15) and (4.16). The amplitude, A, obeys the quadratic equation,

$$\begin{aligned} A^2\left(ikk_b\alpha_2 + \alpha_4\right) - A\left(ikk_b\alpha_3 + \alpha_1\alpha_2 + \left(\Lambda s_1 + c_1\right)\alpha_4 - \Lambda\alpha_5\right) \\ + \left(\alpha_1\alpha_3 - \left(\Lambda s_1 + c_1\right)\Lambda\alpha_5\right) = 0, \end{aligned} \tag{4.22}$$

where

$$\begin{aligned} &\alpha_1 = \Lambda\left(\Lambda s_1 + c_1\right) - \frac{i}{2Ca}s_1, \quad \alpha_2 = \frac{{c_1}^2}{s_1} + \Lambda\left(\frac{k}{s_1} + c_1\right), \quad \alpha_3 = \frac{c_1}{s_1} + k + \Lambda\left(k\frac{c_1}{s_1} + 1\right), \\ &\alpha_4 = \left(ik_b - \frac{\Lambda}{k}\right)\left(c_1 + \Lambda s_1\right) - \frac{ikk_b}{s_1}\left(1 + \Lambda k\right), \quad \alpha_5 = \frac{c_1}{s_1}\left(1 + \Lambda k\right) + k + 1. \end{aligned} \tag{4.23}$$

This equation may be solved, giving two solutions for A, and for each of these, the wave speed, c, is given by

$$c = \frac{-Aikk_b + \Lambda\left(\Lambda s_1 + c_1\right) - is_1/\left(2Ca\right)}{-A + \left(\Lambda s_1 + c_1\right)}. \tag{4.24}$$

4.4 Results

Figure 4.3 shows typical plots of the imaginary parts of the two solutions for the wave speed. For the first solution, which we label $c^+ = {c_R}^+ + i{c_I}^+$ (and which is shown in figure 4.3a), ${c_I}^+$ increases from zero to a maximum as we increase k, before becoming negative for large enough k. For the second solution, which we label $c^- = {c_R}^- + i{c_I}^-$ (shown in figure 4.3b), ${c_I}^-$ is always negative. Therefore, in the former case, for small wavenumbers (large wavelengths) the solution is unstable and for larger wavenumbers the solution is stable. In the latter case the solution is stable for all wavenumbers. Also in figure 4.3 we plot the small k and large k approximations to the wave speeds. For small k we use Taylor series expansions and the solution is given by

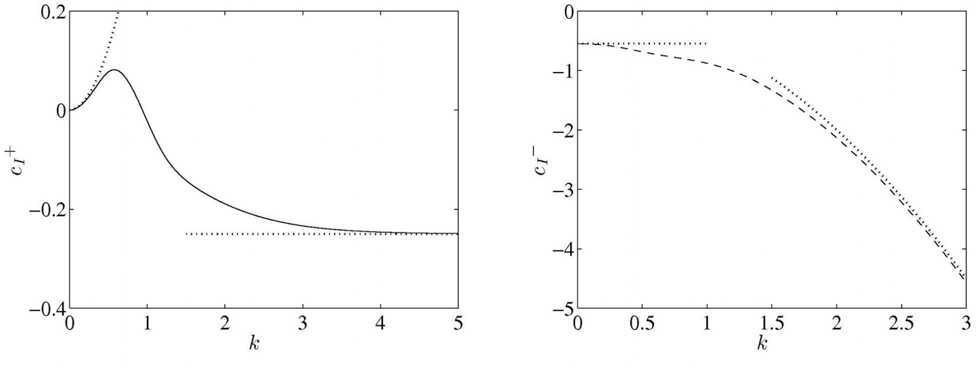

(a) (b)

Figure 4.3: Typical plots against k of the two wave speed solutions, (a) ${c_I}^+$ (solid line) and (b) ${c_I}^-$ (dashed line). Here $\Lambda = Ca = E = 1$ and $T = 0.1$. The dotted lines represent the small and large k solutions in each case.

$$\begin{aligned} {c_R}^+ &= \Lambda + O(k), \quad {c_I}^+ = \frac{1}{2Ca}k^2 + O\left(k^3\right), \\ {c_R}^- &= \frac{1}{k} + O\left(1\right), \quad {c_I}^- = -\frac{(TCa+1)}{2\Lambda Ca} + O\left(k^2\right). \end{aligned} \tag{4.25}$$

In the small k limit ${c_I}^+$ is always positive, showing that this mode can always be found to be unstable if we take k small enough, whilst ${c_I}^-$ is always negative. For large k we use the approximation s_1, $c_1 \sim \exp(k)/2$.

We focus on the more interesting first solution, c^+, and plot the maximum value of ${c_I}^+$, $max({c_I}^+)$, and value of k at which this occurs, which we label k_{max}. In general, in the cases where k_{max} increases with the variation of a parameter, the period of wavenumbers for which ${c_I}^+$ is positive also increases. Figure 4.4 shows the results of altering Λ whilst letting $Ca = E = T = 1$. We find that both $max(c_I{}^+)$ and k_{max}, at which it occurs, have a

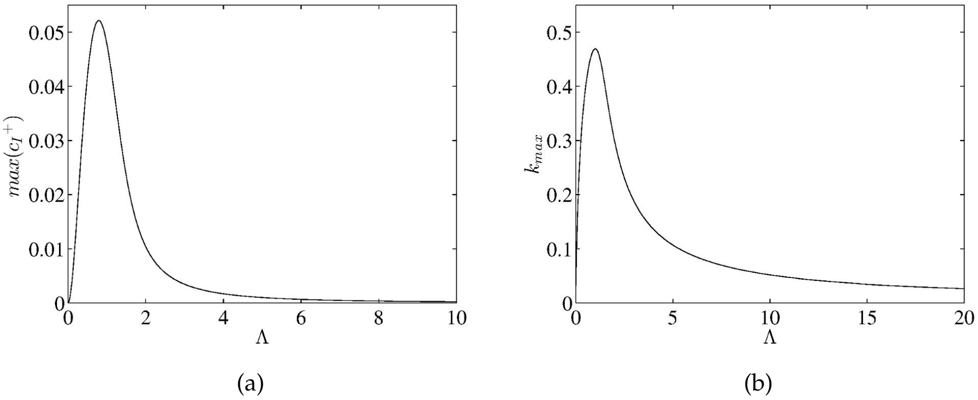

(a) (b)

Figure 4.4: When $Ca = E = T = 1$, plots against Λ of (a) $max(c_I{}^+)$ and (b) the critical value of k at which this occurs, k_{max}.

maximum with respect to Λ, above and below which both decrease. This suggests that a viscosity difference is stabilising. In figures 4.5 and 4.6 we increase T and E in turn, finding that in both cases $max(c_I{}^+)$ and k_{max} decrease exponentially. This is as we might expect since the limit $T, E \to \infty$ corresponds to the case of a rigid wall, in which case the wall no longer interacts with the interface. We note that unstable solutions may also

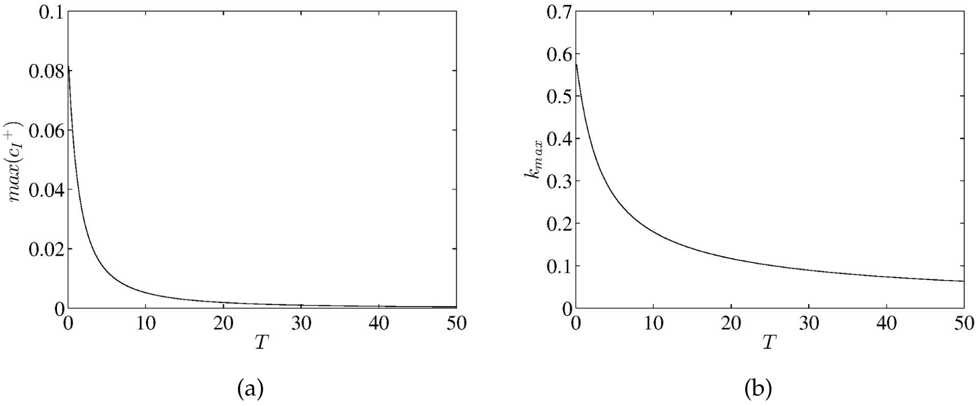

(a) (b)

Figure 4.5: When $\Lambda = Ca = E = 1$, plots against T of (a) $max(c_I{}^+)$ and (b) the critical value of k at which this occurs, k_{max}.

be found for small wavenumbers when we let T be negative (so that the beam is under compression), but that in reality T would be a function of t and would become positive once the beam has returned to its natural shape. We therefore do not investigate this case in any detail. When we set $\Lambda = E = T = 1$ and vary Ca, $max(c_I{}^+)$ behaves in qualitatively the same way as in figure 4.4a, but k_{max} increases logarithmically with Ca, before tending to a fixed value for large Ca. Since Ca is inversely proportional to the surface tension, when Ca is small the interface is rigid whilst when Ca is large the two

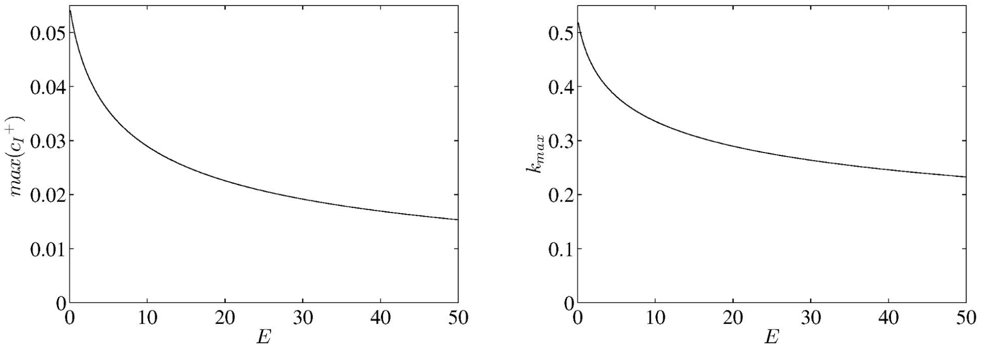

(a) (b)

Figure 4.6: When $\Lambda = Ca = T = 1$, plots against E of (a) $max(c_I{}^+)$ and (b) the critical value of k at which this occurs, k_{max}.

fluids behave as one. In both cases we no longer have two free boundaries to interact with each other and a stable solution makes physical sense.

We may re-write the wall description given in (4.10) as

$$s = \epsilon A_m \exp(i(kx + A_a - kct)), \tag{4.26}$$

where A_a is the argument of A, and A_m is the modulus. From this description we see that the argument of A gives us the phase difference between the wall and the interface. Considering a number of typical parameter values, in the case of c^+ we find that for smaller wavenumbers, where the solution is unstable, the wall and interface are out of phase (A_a is close to $\pi/2$ or π or somewhere between the two), whereas in the case of the always stable c^- the wall and interface are close to being in phase. A typical plot of the two arguments is given in figure 4.7. In the small k limit, assuming that A^+ is

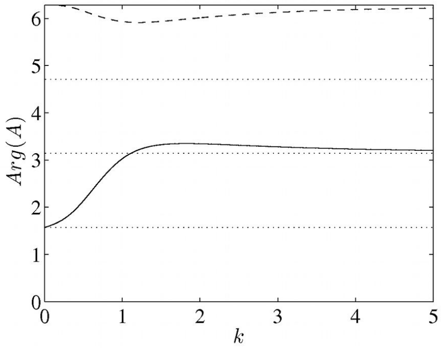

Figure 4.7: A typical plot of $Arg(A)$ against k in the case where the solution for the wave speed $c = c^+$ (solid line) and c^- (dashed line). Here $\Lambda = Ca = E = T = 1$. The dotted lines represent the positions where the argument is $\frac{\pi}{2}$, π and $\frac{3\pi}{2}$.

the solution for A that corresponds to the solution $c = c^+$ and A^- is the solution for A

corresponding to $c = c^-$, we find that

$$A^+ = \left((1-\Lambda) + \frac{i}{2\Lambda Ca}\right) k + O\left(k^2\right), \quad A^- = 1 + O\left(k^2\right). \tag{4.27}$$

To leading order, for the fully stable mode, $Arg(A^-)$ is zero and the wall is in phase with the free surface. If $\Lambda = 1$, then $Arg(A^+) = \pi/2$. For $\Lambda < 1$, then $Arg(A^+) = \tan^{-1}\left(1/(2\Lambda Ca(1-\Lambda))\right)$ and provided that Ca is not large the argument will be close to $\pi/2$. For $\Lambda > 1$, we now have $Arg(A^+) = \pi - \tan^{-1}\left(1/(2\Lambda Ca(\Lambda - 1))\right)$, and the larger Λ is, provided Ca is not very small, the closer this argument is to π. This analysis is interesting and suggests that in this problem, a phase difference between the wall and interface promotes instability at small wavenumbers.

Figure 4.8 shows typical plots of the real part of the two solutions for the wave speed, ${c_R}^+$ and ${c_R}^-$. In both cases the real part is always found to be positive and hence waves always travel to the right.

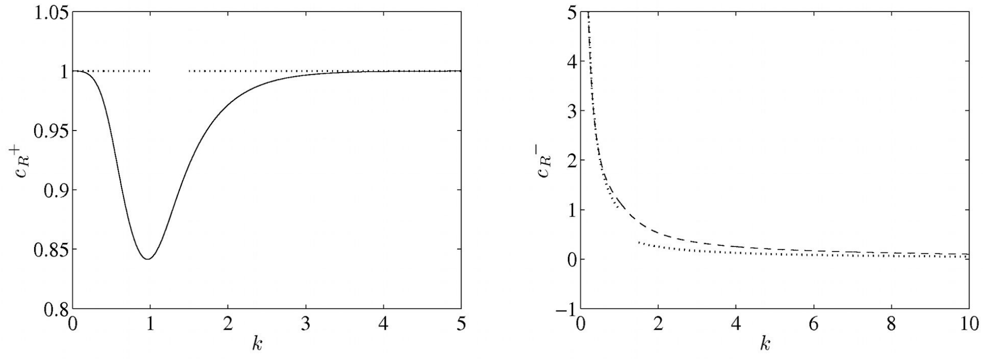

(a) (b)

Figure 4.8: Typical plots against k of the two wave speed solutions, (a) ${c_R}^+$ (solid line) and (b) ${c_R}^-$ (dashed line). Here $\Lambda = Ca = E = 1$ and $T = 0.1$. The dotted lines represent the small and large k solutions in each case.

4.5 A Single Fluid Next to an Elastic Wall

We briefly consider the simpler problem of a single fluid extending up to infinity next to the elastic wall, $y = s = \epsilon A \exp(ik(x - ct))$. Since this problem is equivalent to the $Ca \to \infty$, $\Lambda = 1$ limit of our earlier work, we would expect the solution to be stable in this case. We may solve the non-dimensional versions of the biharmonic equation, (1.5), and Stokes equations, (1.3) for the streamfunction and pressure perturbations, subject to boundary conditions (4.11), (4.12) and (4.17). This give us the overall streamfunction and pressure solutions,

$$\psi = \frac{1}{2}y^2 + \epsilon A\left(\frac{1}{k} - i\left(\frac{Ek^2+T}{2}\right)(1+ky)\right)\exp(-ky+ik(x-ct)), \tag{4.28}$$

$$p = \hat{p}_0 - \epsilon k A\left(Ek^3+Tk\right)\exp(-ky+ik(x-ct)), \tag{4.29}$$

where the wave speed is given by

$$c = \frac{1}{k} - i\left(\frac{Ek^2+T}{2}\right). \tag{4.30}$$

Since E and k are always positive, and assuming that T is positive, c_I is negative as expected and the solution is stable. If T is negative (so that the beam is under compression) and large enough, it is possible for c_I to be positive. However, in reality, as the perturbations grow and the beam returns back to its natural shape, the tension becomes positive and we do not have unlimited growth of solutions. In our solution we have assumed that the tension in the beam is constant, and so cannot capture this behaviour. This supports the idea that in order to obtain unstable solutions we need not only an elastic wall, but also an interface for this wall to interact with.

Taking the limit $Ca \to \infty$, $\Lambda = 1$ in equation (4.24) also gives us (4.30). This is a useful check on the accuracy of our results.

4.6 The Rigid Wall Limit

We may also check the accuracy of our results by comparing the solution for infinite E and T to the case of two fluids next to a rigid wall. We should find that the two solutions are identical.

In the limit $E, T \to \infty$ equation (4.22) yields the two solutions, $A \to 0$ and

$$A \to \frac{k^2\left(1-\Lambda^2\right) + \left(\Lambda s_1 + c_1\right)\left(c_1 + \Lambda s_1\right)}{k\left(s_1 + \Lambda c_1\right) + \left(c_1 + \Lambda s_1\right)}. \tag{4.31}$$

Equation (4.31) implies that we have a bent beam with an infinite bending modulus, and therefore bending moment, m. The beam equation, (4.12), gives us

$$A = -\frac{{p_1}^{(1)}(0)/E}{k^2\left(k^2 + T/E\right)}, \tag{4.32}$$

which suggests that ${p_1}^{(1)}(0) \to \infty$ as $E \to \infty$ to support the deflection. From (4.24) we also find that

$$\frac{c}{\left(Ek^2+T\right)} \to \frac{ik}{2\left(1 - \left(\Lambda s_1 + c_1\right)/A\right)}, \tag{4.33}$$

where we divide by $(Ek^2 + T)$ due to the appearance of this factor on the right hand side of (4.24). The right hand side of (4.33) can be shown to be always negative and hence $c_I < 0$ (because $s_1 > k$ and $c_1 > 1$) and so this mode instantly dies out. We therefore discount this solution and assume that $A \to 0$. Then, from equation (4.24),

$$\begin{aligned} c \to & \frac{1}{k^2(1-\Lambda^2)+(\Lambda s_1+c_1)^2}\Bigg(\Lambda\left(k^2(1-\Lambda^2)+(\Lambda s_1+c_1)^2+k(1-\Lambda)\right) \\ & \qquad\qquad\qquad\qquad - \frac{i}{2Ca}\left(s_1\left(\Lambda s_1+c_1\right)-k\left(1+k\Lambda\right)\right)\Bigg), \end{aligned} \tag{4.34}$$

the imaginary part of which can also be shown to be always negative. Thus we can conclude that in the stiff plane limit, the solution is always stable. This provides further evidence that for instability we need both the wall and the interface to be free to move and interact with each other.

We next consider replacing the elastic wall, $y = s$, in our problem with a fixed, rigid wall, $y = 0$. In this case, we solve the non-dimensional versions of the biharmonic equation, (1.5), and Stokes equations, (1.3) for the streamfunction and pressure perturbations, subject to boundary conditions (4.13) to (4.17). In addition, satisfying the no slip and impermeability conditions, (1.14) and (1.10), we find that equations (4.11) and (4.12) must be replaced by

$$\frac{d{\psi_1}^{(1)}}{dy}(0) = {\psi_1}^{(1)}(0) = 0. \tag{4.35}$$

The solution is given by

$$\begin{aligned} {\psi_1}^{(1)} =& A_1\left(s_y - kyc_y\right) + B_1 y s_y, \quad {\psi_2}^{(1)} = \left(A_2\left(y-1\right)+\left(c-\Lambda\right)e^k\right)e^{-ky}, \\ {p_1}^{(1)} =& -2ik\left(-A_1kc_y + B_1s_y\right), \quad {p_2}^{(1)} = -2ik\Lambda B_2 e^{-ky}, \end{aligned} \tag{4.36}$$

where

$$\begin{aligned} B_1 =& \frac{1}{s_1}\left(-A_1\left(s_1-kc_1\right)+c-\Lambda\right), \\ A_2 =& e^k\left(\frac{A_1}{s_1}\left(k^2-{s_1}^2\right)+c\left(1+k\left(1+\frac{c_1}{s_1}\right)\right)-\left(1+\Lambda k\left(1+\frac{c_1}{s_1}\right)\right)\right), \\ A_1 =& \frac{1}{k-c_1s_1+\Lambda\left(k^2-{s_1}^2\right)}\left(-c\left(c_1+ks_1+\Lambda\left(s_1+kc_1\right)\right)\right. \\ & \qquad\qquad\qquad\qquad \left.+\Lambda\left(c_1+ks_1+s_1+\Lambda kc_1\right)\right), \end{aligned} \tag{4.37}$$

and the wave speed is found to be equal to that given by equation (4.34), as we expect.

4.7 Pressure Driven Flow Next to an Elastic Wall

It is fairly easy to alter our work so that instead of shear driven flow, we consider pressure driven flow. This may be a relevant problem to consider since in the DGM the walls of the cone that represents the body are driven by a cyclic pressure forcing in the surrounding water bath. In this case in the base-state the flow is quiescent. Since the external pressure in the DGM varies sinusoidally with time (Wickham *et al.*, 2012), we allow the dimensional pressure below the wall, p_0, to undergo a small fluctuation such that $p_0 = \epsilon A^*(\omega t^*)\sin(k^* x^*)$. We then simply replace the characteristic timescale $1/S$ with $1/\omega$ when non-dimensionalising, so that the non-dimensional parameters are now

$$\Lambda = \frac{\mu_2}{\mu_1}, \quad Ca = \frac{h\mu_1\omega}{\gamma}, \quad E = \frac{E_B}{h^3\mu_1\omega}, \quad T = \frac{\tau_0}{h\mu_1\omega}. \tag{4.38}$$

The non-dimensional, perturbed solution is then described by

$$\begin{aligned} s =& \epsilon B(t)\sin(kx), \quad \eta = 1 + \epsilon C(t)\sin(kx), \\ \psi_j =& \epsilon {\psi_j}^{(1)}(y,t)\cos(kx), \quad p_j = \epsilon {p_j}^{(1)}(y,t)\sin(kx). \end{aligned} \tag{4.39}$$

This problem has the advantage that since we no longer have an $O(1)$ base flow, non-dimensionalising the beam equation (4.3), gives us

$$\tau = T + O(\epsilon), \tag{4.40}$$

and we can legitimately neglect the x dependence of τ, which is of an order smaller than T, without making any extra assumptions.

In this case boundary conditions (4.11) to (4.17) are replaced by the conditions

$$\frac{d{\psi_1}^{(1)}}{dy}(0,t) = 0, \quad \frac{dB(t)}{dt} - k{\psi_1}^{(1)}(0,t) = 0, \tag{4.41}$$

$${p_1}^{(1)}(0,t) - A(t) = -B(t)k^2\left(k^2E + T\right), \tag{4.42}$$

$${\psi_1}^{(1)}(1,t) = {\psi_2}^{(1)}(1,t), \quad \frac{d{\psi_1}^{(1)}}{dy}(1,t) = \frac{d{\psi_2}^{(1)}}{dy}(1,t), \tag{4.43}$$

$${\psi_2}^{(1)}(1,t) = \frac{1}{k}\frac{dC(t)}{dt} \tag{4.44}$$

$${p_1}^{(1)}(1,t) - {p_2}^{(1)}(1,t) - 2k\left(\frac{d{\psi_1}^{(1)}}{dy}(1,t) - \Lambda\frac{d{\psi_2}^{(1)}}{dy}(1,t)\right) = \frac{k^2}{Ca}C(t), \tag{4.45}$$

$$\frac{d^2{\psi_1}^{(1)}}{dy^2}(1,t) + k^2{\psi_1}^{(1)}(1,t) - \Lambda\left(\frac{d^2{\psi_2}^{(1)}}{dy^2}(1,t) + k^2{\psi_2}^{(1)}(1)\right) = 0. \tag{4.46}$$

$${\psi_2}^{(1)}(\infty,t) = \frac{d{\psi_2}^{(1)}}{dy}(\infty,t) = 0. \tag{4.47}$$

The non-dimensional versions of the biharmonic equation, (1.5), and Stokes equations, (1.3) are solved for the streamfunction and pressure perturbations, subject to boundary conditions (4.41) to (4.47), yielding the solutions

$$\begin{aligned}\psi_1{}^{(1)} = &\left(\frac{1}{2k^2}A(t) - k_bB(t)\right)\left(kyc_y - \left(1 - \left(1 - k\frac{c_1}{s_1}\right)y\right)s_y\right)\\ &\qquad + \frac{1}{k}\left(\frac{dB}{dt}c_y - \frac{1}{s_1}\left(c_1\frac{dB}{dt} - \frac{dC}{dt}\right)ys_y\right),\end{aligned} \tag{4.48}$$

$$\begin{aligned}\psi_2{}^{(1)} = &\frac{1}{s_1}\Bigg(\left(\frac{1}{2k^2}A(t) - k_bB(t)\right)\left(s_1{}^2 - k^2\right)(y-1) - \frac{dB}{dt}\left(1 + \frac{1}{k}c_1s_1\right)(y-1)\\ &\qquad + \frac{1}{k}\frac{dC}{dt}\left(\left((1+k)s_1 + kc_1\right)(y-1) + s_1\right)\Bigg)e^{k(1-y)},\end{aligned} \tag{4.49}$$

and

$$p_1{}^{(1)} = \left(\frac{1}{k}A(t) - 2kk_bB(t)\right)\left(kc_y + \left(1 - k\frac{c_1}{s_1}\right)s_y\right) - \frac{2}{s_1}\left(c_1\frac{dB}{dt} - \frac{dC}{dt}\right)s_y, \tag{4.50}$$

$$\begin{aligned}p_2{}^{(1)} = &\frac{\Lambda}{s_1}\Bigg(\left(\frac{1}{k}A(t) - 2kk_bB(t)\right)\left(s_1{}^2 - k^2\right) - 2\frac{dB}{dt}\left(1 + \frac{1}{k}c_1s_1\right)\\ &\qquad + \frac{2}{k}\frac{dC}{dt}\left((1+k)s_1 + kc_1\right)\Bigg)e^{k(1-y)},\end{aligned} \tag{4.51}$$

where we again use the notation (4.18) and (4.19), and the system of ordinary differential equations,

$$\frac{d\mathbf{y}}{dt} - \mathbf{Q}\mathbf{y} = \mathbf{R}, \quad \mathbf{y} = \begin{pmatrix} B \\ C \end{pmatrix}, \tag{4.52}$$

where

$$\mathbf{Q} = \frac{1}{\alpha}\begin{pmatrix} -k_bB_1 & kC_1/(2Ca) \\ -k_bB_2/s_1 & kC_2/(2Ca) \end{pmatrix}, \quad \mathbf{R} = \frac{A}{2k^2\alpha}\begin{pmatrix} B_1 \\ B_2/s_1 \end{pmatrix}, \tag{4.53}$$

and

$$\begin{aligned}\alpha &= -\left(c_1 + \Lambda s_1\right)\left(s_1 + \Lambda c_1\right) + k\left(1 - \Lambda^2\right),\\ B_1 &= -k\left(c_1 + \Lambda s_1\right)^2 + k^3\left(\Lambda^2 - 1\right), \quad B_2 = -k\left(c_1 + \Lambda s_1\right)\left(s_1 + kc_1\right) + k^2,\\ C_1 &= c_1 + \Lambda s_1 + k\left(s_1 + \Lambda c_1\right), \quad C_2 = c_1\left(c_1 + \Lambda s_1\right) + \Lambda k.\end{aligned} \tag{4.54}$$

Letting $A = \cos(t)$ for a standing wave pressure fluctuation, we may solve the system (4.52), giving us

$$\begin{aligned}B &= \frac{kC_1}{Ca}\left(ae^{\beta_1 t} + be^{\beta_2 t}\right) + \alpha_1\cos(t) + \alpha_2\sin(t),\\ C &= \left(k_bB_1 + 2\alpha\beta_1\right)ae^{\beta_1 t} + \left(k_bB_1 + 2\alpha\beta_2\right)be^{\beta_2 t} + \alpha_3\cos(t) + \alpha_4\sin(t),\end{aligned} \tag{4.55}$$

where

$$\begin{aligned}
\alpha_2 =& \frac{1}{\alpha}\left(\frac{B_1}{2k^2} - k_b B_1 \alpha_1 + \frac{kC_1}{2Ca}\alpha_3\right), \quad \alpha_4 = \frac{1}{2\alpha}\left(\frac{B_2}{s_1 k^2} - \frac{k_b B_2}{s_1}\alpha_1 + \frac{kC_2}{Ca}\alpha_3\right), \\
\alpha_3 =& \frac{4kCa^2}{C_1\left(2k_b B_1 Ca - kC_2\right)}\left(\left(\frac{kB_2C_1}{2s_1Ca} - k_b {B_1}^2\right)\left(\frac{1}{2k^2} - k_b\alpha_1\right) + \alpha^2\alpha_1\right), \\
\alpha_1 =& \frac{\left(k^2 k_b/2\right)\left(B_2C_1/s_1 - B_1C_2\right)^2 + 2k_b {B_1}^2 Ca^2 - kB_2C_1Ca/s_1}{k^2\left(\left(2\alpha^2 Ca - kk_b(B_2C_1/s_1 - B_1C_2)\right)^2 + \alpha^2\left(2B_1k_bCa - kC_2\right)^2\right)},
\end{aligned} \tag{4.56}$$

β_1 and β_2 are the two roots of the equation

$$\beta^2 + \beta\frac{1}{\alpha}\left(k_b B_1 - \frac{kC_2}{2Ca}\right) + \frac{k}{4\alpha^2 Ca}k_b\left(\frac{B_2C_1}{s_1} - B_1C_2\right) = 0, \tag{4.57}$$

and the constants a and b are determined by the initial conditions on B and C.

Since E and Ca are positive and assuming that T is positive, we may use the property that $s_1 > k$ and $c_1 > 1$ for positive k to show that the coefficients of the second and third terms of (4.57) are positive. Using this information it is possible to reason that the real parts of β_1 and β_2 are always negative (if T is taken to be negative, it is possible for the real parts to be positive, although, as mentioned previously, in this situation unlimited growth of the solution is not physical). Therefore the solution is always stable and once the transients have decayed, we are left with a periodic solution for both B and C. We therefore find that a periodic pressure forcing leads to a periodic wall motion. This indicates that a prescribed periodic wall motion is a justifiable assumption when modelling the hydraulically driven DGM main body.

4.8 Discussion

A linear stability analysis was performed for the case of two-fluid flow next to an elastic wall, which was modelled using the beam equations. We assumed that variation in tension is negligible over the region of interest.

There are two solutions for the complex wave speed. For the first the solution is unstable to small wavenumber disturbances and stable for larger wavenumbers. For the second the solution is always stable. Our work suggests that a phase difference between the wall and interface is responsible for the small wavenumber instability.

Letting the viscosity ratio tend to zero or infinity is found to stabilise the first solution. The same is true as the bending moment and beam tension tend to infinity (corresponding to the case of a rigid wall), or the capillary number tends to zero or infinity (corresponding to a rigid interface or zero surface tension). In these limits we propose that the solution becomes stable since we no longer have two free boundaries that may interact with each other.

It is a little concerning that in the small k approximation, (4.25), neither T nor E appear in the approximation for $c = {c_I}^+$. This would suggest that the tension and bending moment are negligible in the beam equation, (4.9), in this limit. The concern is then that the unstable solution may simply be a result of taking the large tension limit, without which these terms might be larger. However, if we include the next order (k^3) term in our approximation for ${c_I}^+$, we find that T does appear and that there are parameter choices that result in ${c_I}^+$ positive, suggesting that the solution is unstable where T is included in the analysis. In addition, considering figures 4.5 and 4.6, we find that $max({c_I}^+)$ and k_{max} both depend on T and E. These figures show that the solution is unstable for not so small values of k, where the tension and bending moment are not neglected from our solution.

We also note that the assumption $T/\Lambda \equiv \tilde{\tau} \gg 1$ made following equation (4.8) results in a lower bound on the range of valid wavenumbers, $k = 2\pi/\lambda$. As $k \to 0$ the wavelength $\lambda \to \infty$, and at the point $x = \lambda$ we find that $x \to \infty$ and the assumption breaks down. Specifically we require $\tilde{\tau} \gg \lambda$ and so $k \gg 2\pi/\tilde{\tau}$. However, it is still possible for k to be small enough so that ${c_I}^+$ is positive but not so small that the solution is not valid. One such case occurs when $\Lambda = 0.1$, $Ca = 100$, $E = 1$ and $T = 10$. Here ${c_I}^+$ remains positive for wavenumbers up to $k = 0.67$ (to 2 decimal places). For waves with wavenumber $k = 0.67$ the ratio $\lambda/\tilde{\tau} \approx 0.094 \ll 1$ and the large tension approximation is valid. In fact there is a band of valid wavenumbers for which ${c_I}^+$ is positive and $\tilde{\tau}$ is sufficiently bigger than λ. This is illustrated in figure 4.9. For each choice of parameters the limits of this band varies.

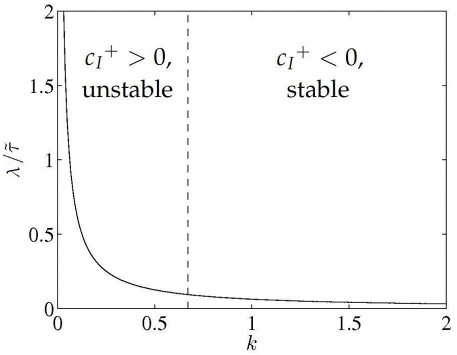

Figure 4.9: An illustration of the band of wavenumbers for which the unstable solution for ${c_I}^+$ is valid. The solid line shows the term $\lambda/\tilde{\tau}$ plotted against k when $\Lambda = 0.1$ and $T = 10$. The dashed line is $k = 0.67$, the largest value of k for which ${c_I}^+$ is positive when we also take $Ca = 100$ and $E = 1$.

It is relevant that our work can be compared to Thaokar and Kumaran (2002), who considered the linear stability of two fluids separated by a membrane which is allowed to move in both the horizontal and vertical directions. In this paper, in a similar way to mentioned above, the solution was found to be unstable in the small wavenumber limit, but a lower bound on the wavenumber was necessary. We have found no studies of two fluid flow next to an elastic wall which consider both a free moving fluid interface and wall and concentrate on the resulting flow stability, as in our work.

When we replace the base-state steady shear flow in our problem with a small periodic pressure forcing below the wall, we find that the solution is always stable and the wall motion is periodic. This suggests that we are justified in taking a prescribed periodic wall motion when modelling the DGM main body.

In the next chapter we focus on a different mechanism for instability. We consider two-fluid flow in a fixed channel under the influence of a scalar material field which acts to alter the surface tension at the interface.

Chapter 5

The Interaction of a Scalar Material Field with Fluid Flow in a Channel

5.1 Introduction

We consider the influence of a scalar material field on creeping flow of two fluids in a fixed channel as a simple model of the addition of gastric secretions to the DGM. This material gradient encapsulates the gastric juices, which comprise a mixture of substances such as acids, salts, enzymes and surfactants. The material acts to alter the surface tension at the fluid interface, which may induce a flow field due to the the Marangoni effect. The flow field, in turn, may cause further advection of the material. It is proposed that this process will promote interfacial break up and instability. In addition to a (stationary) lower wall, which represents the wall of the DGM body, and two fluids, which represent two stages of digesting liquid material, our local description now includes an upper wall, which can be thought of as representing the solid, undigested bolus of food.

5.2 Formulation of the Stability Problem

We consider the linear stability of two fluids separated by a free interface and confined between two fixed parallel walls at $y^* = 0, h_2$ (see figure 5.1), where starred variables are dimensional variables with a non dimensional counterpart. In the base-state the fluid is subject to a Poiseuille flow with uniform pressure gradient, G, and the unperturbed, flat interface is located at $y^* = h_1$, where h_1 is constant. The perturbed interface description is given by $y^* = \eta^*(x^*, t^*)$. The subscripts $j = 1$ and 2 denote the lower and upper fluid, respectively, and fluid j has viscosity μ_j.

The interface is subject to chemical activity, encapsulated by a material, whose concentration field is $C_j{}^*(x^*, y^*, t^*)$, present in the two fluids. Here $C_j{}^* = 0$ corresponds to a ground state. The material acts at the interface to alter the surface tension coefficient,

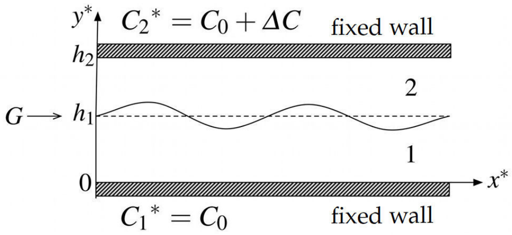

Figure 5.1: Schematic diagram of two-fluid flow in a channel subject to a Poiseuille gradient, G. The position of the perturbed interface, $y^* = \eta^*(x^*, t^*)$, is shown. The concentrations at the bottom and top walls are held at C_0 and $C_0 + \Delta C$, respectively.

γ^*, such that

$$\gamma^* = \gamma_0 + \beta C_j{}^*(x^*, \eta^*, t^*), \tag{5.1}$$

where γ_0 and β are prescribed constants and $\gamma^* = \gamma_0$ represents a clean interface. The material is transported (see below) and the concentration takes prescribed values C_0 at $y^* = 0$ and $C_0 + \Delta C$ at $y^* = h_2$. Furthermore, $C_j{}^*$ is continuous at the interface, $y^* = \eta^*$. The material diffusivity in fluid j is denoted D_j.

We note that in reality, we would expect the surface tension to exhibit a more complicated dependence on any material present in the fluid. However, equation (5.1) can be thought of as a linearised approximation of this more complicated behaviour. Physically, we expect that where $C_j{}^*$ models the concentration of, for instance, a surfactant, a clean interface will have the highest surface tension and an increase in surfactant at the interface will act to lower the surface tension, since any increase of material will lower the surface energy and therefore the resistance to external forces. This would suggest taking $\beta < 0$. However, the occurrence of certain chemical processes or protein interactions may in fact increase the surface tension. In these cases $C_j{}^*$ could model a concentration of salts, enzymes or pH and we would be justified in taking $\beta > 0$.

We non-dimensionalise using the characteristic length scale h_2, concentration scale C_0 and surface tension scale γ_0. In order to allow us to consider flow in the limit of zero pressure gradient we take our velocity scale to be γ_0/μ_1. This results in the non-dimensional parameters

$$\alpha = \frac{h_1}{h_2}, \quad \Lambda = \frac{\mu_2}{\mu_1}, \quad \hat{C} = \frac{\Delta C}{C_0}, \quad \Gamma = \frac{\beta C_0}{\gamma_0}, \quad \hat{G} = \frac{G h_2{}^2}{\gamma_0}, \quad Pe_j = \frac{\gamma_0 h_2}{D_j \mu_1}, \tag{5.2}$$

where α is the depth ratio, Λ is the viscosity ratio, $\hat{C}$, Γ and $\hat{G}$ are the non-dimensional concentration ratio, surface tension gradient and pressure gradient, respectively, and Pe_j is the Péclet number in fluid j. Henceforth, non-starred variables are non-dimensional.

We again assume that the Reynolds number is small and introduce the streamfunction, $\psi_j(x, y, t)$, alongside the velocity field, $\mathbf{u}_j(x, y, t) = (u_j, v_j)$, and the pressure, $p_j(x, y, t)$, in fluid j. In addition to the usual governing equations for small Reynolds number flow, the concentration field, $C_j(x,y,t)$, evolves according to the advection-diffusion equation,

$$\frac{\partial C_j}{\partial t} + \mathbf{u}_j \cdot \nabla C_j = \frac{1}{Pe_j}\nabla^2 C_j. \tag{5.3}$$

The concentration is fixed at the walls such that

$$C_1(x,0,t) = 1, \quad C_2(x,1,t) = 1 + \hat{C}, \tag{5.4}$$

and since the interface is neither a sink nor a source of material concentration, we must satisfy concentration continuity and flux continuity at $y = \eta$:

$$C_1(x,\eta,t) = C_2(x,\eta,t), \quad \frac{\partial C_1}{\partial y}(x,\eta,t) = Pe_{12}\frac{\partial C_2}{\partial y}(x,\eta,t), \quad Pe_{12} = \frac{Pe_1}{Pe_2}. \tag{5.5}$$

5.2.1 The Base-State Solution

For steady Poiseuille flow in the base-state (denoted with superscript (0)) we assume that the velocity in fluid j is given by $\mathbf{u}_j{}^{(0)} = (u_j{}^{(0)}(y), 0)$. In this case the Stokes equations in each fluid reduce to the steady version of (1.7). Taking these equations in fluids 1 and 2 and writing them in terms of non-dimensional variables, the base-state pressure in fluid j is then given by

$$p_j{}^{(0)} = p_0 - \hat{G}x, \tag{5.6}$$

where p_0 is a prescribed constant pressure.

Next, we may solve for $u_j{}^{(0)}$, applying the non-dimensionalised versions of the no-slip condition, (1.14), at the walls, $y = 0$ and 1 and the stress condition, (1.19), and the first of the velocity continuity conditions, (1.22), at the flat interface, $y = \alpha$ (where the curvature is zero and the surface tension is independent of arc length along the interface). This results in the base-state streamfunction in fluid j,

$$\psi_j{}^{(0)} = -\frac{\hat{G}\mu_1}{2\mu_j}\left(\frac{y^3}{3} - \frac{y^2\left(\alpha^2(\Lambda-1)+1\right) - 2y\alpha(\alpha-1)(\Lambda-1)(j-1)}{2\left(\alpha(\Lambda-1)+1\right)}\right). \tag{5.7}$$

We note that had we non-dimensionalised taking the characteristic velocity to be the characteristic speed of the interface in the basic state rather than γ_0/μ_1, then this would fix $\hat{G}$ and result in a capillary number replacing this parameter as a measure of the strength of the flow. However, as mentioned above, in order to consider flow in the limit $\hat{G} \to 0$, we do not use such a scaling. Instead we may choose to consider a pressure gradient

$$\hat{G} = \hat{G}_{u1} = \frac{2\left(\alpha\left(\Lambda-1\right)+1\right)}{\alpha\left(1-\alpha\right)}, \tag{5.8}$$

which is equivalent to taking the base-state, horizontal velocity at the interface, ${u_j}^{(0)}(\alpha)$, to be unity.

In view of the base-state flow field and (5.3) the base-state concentration must depend linearly on y in each fluid. Then, satisfying conditions (5.4) and (5.5), we find that in fluid j,

$$
{C_j}^{(0)} = 1 + \hat{C}\frac{Pe_j}{Pe_2}\left(\frac{y + (Pe_{12} - 1)\,\alpha(j-1)}{(Pe_{12} - 1)\,\alpha + 1}\right). \tag{5.9}
$$

5.2.2 The Perturbed Solution

The perturbed solution can be described by the base-state (superscript (0)) plus a time-dependent excitation (superscript (1)), as follows:

$$
\begin{aligned}
(\eta, \psi_j, p_j, C_j) = \Big(\alpha,\ {\psi_j}^{(0)}(y),\ {p_j}^{(0)}(x),\ {C_j}^{(0)}(y)\Big)& \\
+ \Big(\alpha,\ {\psi_j}^{(1)}(y),\ {p_j}^{(1)}(y), {C_j}^{(1)}(y)\Big)\, E(x,t),& \quad (5.10)
\end{aligned}
$$

where $0 < \epsilon \ll 1$ is a small parameter and we look for a solution of the form

$$
E = \epsilon \exp(ik[x - ct]), \tag{5.11}
$$

where k is the known, real wavenumber and $c = c_R + ic_I$ is the complex wave speed of the disturbance, to be determined as part of the solution. It is understood that the physical solution is given by the real part of (5.10). As in chapter 4, the interface perturbation is non-unique and may be multiplied by an arbitrary constant, but this constant can be treated as being absorbed into ϵ.

The surface tension on the interface at $y = \eta$ is given by

$$
\gamma = 1 + \Gamma C_j(x, \eta, t). \tag{5.12}
$$

For physical reasons we expect a non-negative surface tension and concentration. The base-state concentration is only less than 1 when $\hat{C}$ is negative and in this case, is clearly lowest at $y = 1$. Therefore, considering the base-state, this results in the constraints

$$
\hat{C} \geq -1, \quad \Gamma \geq -\frac{(Pe_{12} - 1)\,\alpha + 1}{\left(Pe_{12}\left(1 + \hat{C}\right) - 1\right)\alpha + 1}. \tag{5.13}
$$

As discussed above, we might also expect $\Gamma < 0$ in the case where the concentration field represents, for instance, a surfactant, but it is also justifiable to consider $\Gamma > 0$ since there are certain chemicals whose addition may act to increase the surface tension. If the concentration perturbations, ${C_j}^{(1)}$, grow, clearly concentration is still conserved since, due to the sinusoidal nature of the excitations, an increase in concentration at one point in x is balanced by a proportional decrease in another. As the perturbations become large (no longer $O(\epsilon)$), our analysis breaks down so that the overall concentration at any point is never assumed to be negative.

Non-dimensionalising and linearising the no-slip and impermeability conditions, (1.14) and (1.10), at the walls, $y = 0$ and 1, yields the conditions

$$\frac{d{\psi_1}^{(1)}}{dy}(0) = \frac{d{\psi_2}^{(1)}}{dy}(1) = {\psi_1}^{(1)}(0) = {\psi_2}^{(1)}(1) = 0, \tag{5.14}$$

whilst the velocity continuity and kinematic conditions at the interface, (1.22) and (1.23), give us

$${\psi_1}^{(1)}(\alpha) = {\psi_2}^{(1)}(\alpha), \quad \hat{G}_1 = \frac{\hat{G}\alpha(\alpha-1)}{2\left(\alpha(\Lambda-1)+1\right)}, \tag{5.15}$$

$$\frac{d{\psi_1}^{(1)}}{dy}(\alpha) - \frac{d{\psi_2}^{(1)}}{dy}(\alpha) = \hat{G}_2, \quad \hat{G}_2 = \frac{\hat{G}(\Lambda-1)\alpha\left(\alpha^2\Lambda-(\alpha-1)^2\right)}{2\Lambda\left(\alpha(\Lambda-1)+1\right)}, \tag{5.16}$$

$${\psi_2}^{(1)}(\alpha) = \alpha\left(c + \hat{G}_1\right). \tag{5.17}$$

Noting that differentiating along the interface, $\partial/\partial l = \hat{\mathbf{t}} \cdot \nabla$ can be approximated by $\partial/\partial x$ when we neglect terms of $O(\epsilon)$ and smaller, the stress condition, (1.19), non-dimensionalised and evaluated in the directions normal and tangential to the interface, results in the conditions

$${p_1}^{(1)}(\alpha) - {p_2}^{(1)}(\alpha) + 2ik\left(\frac{d{\psi_1}^{(1)}}{dy}(\alpha) - \Lambda\frac{d{\psi_2}^{(1)}}{dy}(\alpha)\right) = \alpha k^2\Gamma_1, \tag{5.18}$$

and

$$\frac{d^2{\psi_1}^{(1)}}{dy^2}(\alpha) + k^2{\psi_1}^{(1)}(\alpha) - \Lambda\left(\frac{d^2{\psi_2}^{(1)}}{dy^2}(\alpha) + k^2{\psi_2}^{(1)}(\alpha)\right) = ik\Gamma_2, \tag{5.19}$$

where

$$\Gamma_1 = 1 + \Gamma\left(1 + \frac{Pe_{12}\hat{C}\alpha}{\left(Pe_{12}-1\right)\alpha+1}\right), \quad \Gamma_2 = \Gamma\left(\frac{Pe_{12}\hat{C}\alpha}{\left(Pe_{12}-1\right)\alpha+1} + {C_1}^{(1)}(\alpha)\right). \tag{5.20}$$

Lastly, the conditions on the concentration at the walls, (5.4) and interface, (5.5), imply that

$${C_1}^{(1)}(0) = {C_2}^{(1)}(1) = 0, \tag{5.21}$$

$$\frac{\left(Pe_{12}-1\right)\hat{C}\alpha}{\left(Pe_{12}-1\right)\alpha+1} + {C_1}^{(1)}(\alpha) = {C_2}^{(1)}(\alpha), \quad \frac{d{C_1}^{(1)}}{dy}(\alpha) = Pe_{12}\frac{d{C_2}^{(1)}}{dy}(\alpha). \tag{5.22}$$

Next, we solve the non-dimensionalised version of the biharmonic equation, (1.5), subject to conditions (5.14), where we may make use of the non-dimensional form of the first of equations (1.3) in order to determine the pressure. First, we define for brevity the following functions:

$$\begin{aligned} s_y &= \sinh(ky), \quad c_y = \cosh(ky), \quad t_y = \tanh(ky), \\ s_\alpha &= \sinh(k\alpha), \quad c_\alpha = \cosh(k\alpha), \quad t_\alpha = \tanh(k\alpha), \\ s_1 &= \sinh(k), \quad c_1 = \cosh(k), \quad t_1 = \tanh(k), \end{aligned} \tag{5.23}$$

and we also let

$$\alpha_1 = t_1 + \frac{k(\alpha-1)}{c_1{}^2}, \quad \alpha_2 = t_1 + \frac{k(\alpha-1)}{c_1{}^2\alpha}, \quad \alpha_3 = \frac{1-\Lambda}{k\alpha}, \quad \alpha_4 = k^2\alpha^2 + 1, \tag{5.24}$$

and

$$\begin{aligned} \beta_1 =& \frac{1}{\alpha}\left(\Lambda\left(t_1 - \frac{k}{c_1{}^2}\right) - \alpha_3\alpha_4\right)s_\alpha + \frac{1}{\alpha}\left(\alpha_1\left(\alpha_3k^2\alpha^2 + \frac{\Lambda}{k\alpha}\right) - \Lambda\right)c_\alpha - \frac{\alpha_3}{\alpha}\left(s_\alpha{}^3 - \alpha_1c_\alpha{}^3\right), \\ \beta_2 =& \frac{1}{\alpha}\left(-t_1 + \frac{k}{c_1{}^2} - \alpha_3\alpha_4\right)c_\alpha + \frac{1}{\alpha}\left(\alpha_1\left(\alpha_3k^2\alpha^2 - \frac{1}{k\alpha}\right) + 1\right)s_\alpha + \frac{\alpha_3}{\alpha}\left(c_\alpha{}^3 - \alpha_1s_\alpha{}^3\right), \\ \beta_3 =& \alpha_2\left(\alpha_3k^2\alpha^2 + \frac{\Lambda}{k\alpha}\right)c_\alpha - \left(\alpha_3\alpha_4 + \frac{\Lambda k}{\alpha c_1{}^2}\right)s_\alpha - \alpha_3\left(s_\alpha{}^3 - \alpha_2c_\alpha{}^3\right), \\ \beta_4 =& \alpha_2\left(-\alpha_3k^2\alpha^2 + \frac{1}{k\alpha}\right)s_\alpha + \left(\alpha_3\alpha_4 - \frac{k}{\alpha c_1{}^2}\right)c_\alpha - \alpha_3\left(c_\alpha{}^3 - \alpha_2s_\alpha{}^3\right). \end{aligned} \tag{5.25}$$

Then the solutions for the disturbance streamfunction and pressure in fluids 1 and 2 are given by

$$\begin{aligned} \psi_1{}^{(1)} &= (A_1y + B_1)\,s_y - B_1kyc_y, \\ \psi_2{}^{(1)} &= (A_2y + B_2)\left(s_y - t_1c_y\right) - (A_2 + B_2)\,\frac{k(y-1)c_y}{c_1{}^2}, \end{aligned} \tag{5.26}$$

and

$$p_1{}^{(1)} = -2ik\left(A_1s_y - B_1kc_y\right), \quad p_2{}^{(1)} = -2ik\Lambda\left(A_2\left(s_y - t_1c_y\right) - (A_2 + B_2)\,\frac{kc_y}{c_1{}^2}\right). \tag{5.27}$$

From conditions (5.15), (5.16), (5.18) and (5.19) we find that

$$\begin{aligned} A_1 &= -\frac{B_1}{\alpha}\left(1 - \alpha kt_\alpha\right) + \frac{B_2\Lambda}{\alpha}\left(1 - \alpha_1t_\alpha\right) + A_2\Lambda\left(1 - \alpha_2t_\alpha\right) - \frac{i\Gamma_1}{2c_\alpha}, \\ B_1 &= -B_2\left(\alpha_3s_\alpha c_\alpha - \frac{\alpha_1}{k\alpha}\left(c_\alpha{}^2 - \Lambda s_\alpha{}^2\right)\right) - \frac{A_2}{k}\left((1-\Lambda)s_\alpha c_\alpha - \alpha_2\left(c_\alpha{}^2 - \Lambda s_\alpha{}^2\right)\right) - \frac{i\Gamma_1s_\alpha}{2k}, \\ A_2 &= -\frac{1}{2\left(\beta_2\beta_3 + \beta_1\beta_4\right)}\left(\beta_1\left(2\hat{G}_2 + \frac{i\Gamma_1}{k\alpha}\left(k^2\alpha^2 - s_\alpha{}^2\right)\right) + \beta_2i\left(\Gamma_2 + \frac{\Gamma_1}{k\alpha}\left(k\alpha - c_\alpha s_\alpha\right)\right)\right), \\ B_2 &= \frac{1}{2\left(\beta_2\beta_3 + \beta_1\beta_4\right)}\left(\beta_3\left(2\hat{G}_2 + \frac{i\Gamma_1}{k\alpha}\left(k^2\alpha^2 - s_\alpha{}^2\right)\right) - \beta_4i\left(\Gamma_2 + \frac{\Gamma_1}{k\alpha}\left(k\alpha - c_\alpha s_\alpha\right)\right)\right), \end{aligned} \tag{5.28}$$

and from (5.17) the wavespeed is given by

$$\begin{aligned} c = & -\hat{G}_1 - \frac{i}{2\alpha\beta_1}\left(s_\alpha - \alpha_1 c_\alpha\right)\left(\Gamma_2 + \frac{\Gamma_1}{k\alpha}\left(k\alpha - c_\alpha s_\alpha\right)\right) \\ & - \frac{\beta_1\alpha\left(s_\alpha - \alpha_2 c_\alpha\right) - \beta_3\left(s_\alpha - \alpha_1 c_\alpha\right)}{2\alpha\left(\beta_2\beta_3 + \beta_1\beta_4\right)}\Bigg(2\hat{G}_2 + \frac{i\Gamma_1}{k\alpha}\left(k^2\alpha^2 - {s_\alpha}^2\right) \\ & \qquad + \frac{\beta_2 i}{\beta_1}\left(\Gamma_2 + \frac{\Gamma_1}{k\alpha}\left(k\alpha - c_\alpha s_\alpha\right)\right)\Bigg). \qquad (5.29) \end{aligned}$$

Our solution depends (through c and Γ_2) on the unknown ${C_1}^{(1)}(\alpha)$. In order to acquire ${C_1}^{(1)}(\alpha)$ we must solve the advection-diffusion equations, (5.3), which, using (5.10), gives us

$$\frac{d^2{C_j}^{(1)}}{dy^2} + a_j(y){C_j}^{(1)} = b_j(y), \qquad (5.30)$$

where

$$a_j = ikPe_j\left(c - \frac{d{\psi_j}^{(0)}}{dy}\right) - k^2, \quad b_j = -\frac{ik{Pe_j}^2\hat{C}}{\left(Pe_1 - Pe_2\right)\alpha + Pe_2}{\psi_j}^{(1)}, \qquad (5.31)$$

subject to boundary conditions (5.21) and (5.22). Since equations (5.30) comprise of two second order ordinary differential equations depending on ${C_1}^{(1)}(\alpha)$, solving these equations will give us five unknowns. We may fully determine the solution using conditions (5.21) and (5.22) alongside the condition that results when we evaluate the equation for ${C_1}^{(1)}(y)$ at $y = \alpha$. We note that if the real part of ${C_1}^{(1)}(\alpha)$ is independent of the pressure gradient, $\hat{G}$, then the base flow does not affect the stability of the solution. Therefore, in case (i) below, we first concentrate on the simplest case when the pressure gradient is zero. In the later case (ii) we will take a non-zero pressure gradient.

5.3 Results

In general, only one significant solution is found for ${C_1}^{(1)}(\alpha)$ and therefore c (see below). For this solution a small k approximation to c may be shown, using Taylor series expansions in (5.29), to be given by

$$\begin{aligned} c = & \frac{\hat{G}c_m\left(\alpha^2(\Lambda - 1) + 1\right)\left(\alpha^2(\Lambda - 1) - 2\alpha(\Lambda - 1) - 1\right)}{\alpha(\Lambda - 1) + 1} \\ & - ik\Gamma c_m(\alpha - 1)\left(\alpha^2(\Lambda - 1) + 2\alpha - 1\right)\left(\frac{Pe_{12}\alpha\hat{C}}{\left(Pe_{12} - 1\right)\alpha + 1} + {C_1}^{(1)}(\alpha)\right) + O\left(k^2\right), \end{aligned} \qquad (5.32)$$

where

$$c_m = \frac{\alpha(\alpha-1)}{2\left(\Lambda\left(\alpha^4(\Lambda-1)+1\right)-(\alpha-1)^4(\Lambda-1)\right)}. \tag{5.33}$$

A small k approximation to ${C_1}^{(1)}(\alpha)$ can be found by performing a small wavelength analysis, redefining the characteristic length scale in the horizontal direction to be l, where $0 < \delta = h_2/l \ll 1$. Here, in order to retain the effects of surface tension in the problem, the surface tension is scaled such that $\delta\gamma_0 = O(1)$ and the velocity scales in the horizontal and vertical directions are taken to be $\delta\gamma_0/\mu_1$ and $\delta^2\gamma_0/\mu_1$, respectively. The advection-diffusion equation, (5.3), then becomes $\partial^2 C_j/\partial y^2 = 0$ and substituting in a perturbation of the form given in (5.10) yields the equation $\partial^2 {C_j}^{(1)}/\partial y^2 = 0$. Solving this equation subject to boundary conditions (5.21) and (5.22) and evaluating at $y = \alpha$, we find that

$${C_1}^{(1)}(\alpha) = -\frac{\hat{C}\alpha^2 Pe_{12}\left(Pe_{12}-1\right)}{\left(\left(Pe_{12}-1\right)\alpha+1\right)^2} + O\left(k\right), \tag{5.34}$$

and so, substituting ${C_1}^{(1)}(\alpha)$ into equation (5.32), we find that for small k the wave speed is given by

$$\begin{aligned} c = {} & \frac{\hat{G}c_m\left(\alpha^2(\Lambda-1)+1\right)\left(\alpha^2(\Lambda-1)-2\alpha(\Lambda-1)-1\right)}{\alpha(\Lambda-1)+1} \\ & - \frac{ik\hat{C}\Gamma Pe_{12}c_m\alpha(\alpha-1)\left(\alpha^2(\Lambda-1)+2\alpha-1\right)}{\left(\left(Pe_{12}-1\right)\alpha+1\right)^2} + O\left(k^2\right). \end{aligned} \tag{5.35}$$

Here we note that if we take $\Gamma = 0$, $\alpha = 0.5$ and choose $\hat{G} = \hat{G}_{u1}$ (as given in equation (5.8)), then to leading order this can be shown to reduce to

$$c = 1 + \frac{2\left(\Lambda-1\right)^2}{\Lambda^2+14\Lambda+1}. \tag{5.36}$$

This is equivalent to the expression for the wave speed derived in the work of Yih (1967), who considered the plane Poiseuille flow of two fluids of equal depth and density and different viscosities in an infinite channel.

5.3.1 Case (i); A Zero Pressure Gradient

In this case we may analytically solve the system (5.21), (5.22) and (5.30). For brevity we define the functions,

$$k_j = (ikPe_j c - k^2)^{1/2}, \quad j = 1, 2. \tag{5.37}$$

The solution for the disturbance concentration in fluid j is then given by [1]

$$\begin{aligned} {C_j}^{(1)} =& \frac{\hat{C}}{(Pe_{12}-1)\,\alpha+1}\left(\frac{2}{iPe_2c^2}\left(\hat{A}_j\cos\left(k_jy\right)+\hat{B}_j\sin\left(k_jy\right)\right)\right. \\ &\left.-\frac{Pe_j}{Pe_2c}\left({\psi_j}^{(1)}-\frac{2}{iPe_jc}\left(A_jc_y-\frac{B_jk+A_j\left(s_1c_1+k\right)\left(j-1\right)}{{c_1}^2+({c_1}^2-1)(j-2)}s_y\right)\right)\right), \end{aligned} \tag{5.38}$$

where we have divided by c since we are only interested in solutions for which $c \neq 0$ for all k, and

$$\begin{aligned} \hat{A}_1 =& -A_1, \\ \hat{B}_1 =& \frac{1}{\sin\left(k_1\alpha\right)}\left(\hat{A}_2\left(\cos\left(k_2\alpha\right)-\frac{\sin\left(k_2\alpha\right)}{\tan\left(k_2\right)}\right)+A_1\left(\cos\left(k_1\alpha\right)-c_\alpha\right)+B_1ks_\alpha\right. \\ &\left.+\left(A_2(kt_1-1)+B_2kt_1\right)\frac{\sin\left(k_2\alpha\right)}{c_1\sin\left(k_2\right)}-\left(\frac{A_2\left(s_1c_1+k\right)+B_2k}{{c_1}^2}s_\alpha-A_2c_\alpha\right)\right), \end{aligned} \tag{5.39}$$

and

$$\hat{A}_2=\hat{A}_{21}\hat{A}_{22}, \quad \hat{B}_2=-\frac{\hat{A}_2}{\tan\left(k_2\right)}+\frac{A_2\left(kt_1-1\right)+B_2kt_1}{c_1\sin\left(k_2\right)}, \tag{5.40}$$

where

$$\begin{aligned} \hat{A}_{21} =& -\frac{A_1}{\sin\left(k_1\alpha\right)}+\frac{A_1c_\alpha-B_1ks_\alpha}{\tan\left(k_1\alpha\right)}-\frac{A_1ks_\alpha-B_1k^2c_\alpha}{k_1} \\ &+\left(A_2(kt_1-1)+B_2kt_1\right)\frac{\cos\left(k_2\alpha\right)}{c_1\sin\left(k_2\right)}\left(\frac{Pe_{12}k_2}{k_1}-\frac{\tan\left(k_2\alpha\right)}{\tan\left(k_1\alpha\right)}\right) \\ &-\frac{A_2\left(s_1c_1+k\right)+B_2k}{{c_1}^2}\left(\frac{Pe_{12}kc_\alpha}{k_1}-\frac{s_\alpha}{\tan\left(k_1\alpha\right)}\right)+A_2\left(\frac{Pe_{12}ks_\alpha}{k_1}-\frac{c_\alpha}{\tan\left(k_1\alpha\right)}\right), \\ \hat{A}_{22} =& \frac{1}{\cos\left(k_2\alpha\right)}\left(\frac{1}{\tan\left(k_1\alpha\right)}\left(1-\frac{\tan\left(k_2\alpha\right)}{\tan\left(k_2\right)}\right)+\frac{Pe_{12}k_2}{k_1}\left(\tan\left(k_2\alpha\right)+\frac{1}{\tan\left(k_2\right)}\right)\right)^{-1}. \end{aligned} \tag{5.41}$$

Letting $y=\alpha$ in equation (5.38) when we take $j=1$ yields an implicit equation for ${C_1}^{(1)}(\alpha)$, which, subtracting ${C_1}^{(1)}(\alpha)$ from both sides, can be written in the form $f({C_1}^{(1)}(\alpha))=0$. This equation can be solved for ${C_1}^{(1)}(\alpha)$ using the secant method (although Newton's method is faster to converge, its use would require the derivative of $f({C_1}^{(1)}(\alpha))$). Here we let the ith guess for ${C_1}^{(1)}(\alpha)$ and $f({C_1}^{(1)}(\alpha))$ be given by z_i and f_i, respectively, where $i=1,2,\cdots$. We iterate such that

$$z_i=z_{i-1}-f_{i-1}\left(\frac{z_{i-1}-z_{i-2}}{f_{i-1}-f_{i-2}}\right), \quad i=3,4,\cdots, \tag{5.42}$$

---

[1] This solution does not take into account the additional solutions that may be obtained by adding extra terms proportional to $\sin(k_jy)$ and $\cos(k_jy)$ to the complementary function of ${C_j}^{(1)}$. These solutions are discussed in section 5.3.2, but are found not to be relevant to our model.

where the initial guesses, z_1 and z_2, are obtained by considering plots of f against ${C_1}^{(1)}(\alpha)$ to find the approximate location of any zeros (and are chosen such that $|z_1 - z_2| \ll 1$). At stage i of the iterative procedure, we define the error,

$$e_i = |C_i - C_{i-1}|, \tag{5.43}$$

and we continue iterating until e_i is sufficiently small.

Since $\hat{G} = 0$, it is clear that c, A_j and B_j, and therefore $\hat{A}_j$ and $\hat{B}_j$, are purely imaginary functions of ${C_1}^{(1)}(\alpha)$. Also, from boundary condition (5.17), ${\psi_1}^{(1)}(\alpha) = \alpha c$. It is therefore clear that f is a purely real function of ${C_1}^{(1)}(\alpha)$. We find a single solution of interest for ${C_1}^{(1)}(\alpha)$, which is found to be real.

5.3.1.1 The Infinite Péclet-Number Limit

The above-mentioned solution can be seen analytically if we consider the solution when the Péclet numbers, $Pe_1 = Pe_2 \to \infty$ (so that diffusion becomes negligible compared to advection), for which the advection-diffusion equation, (5.30), gives us ${C_j}^{(1)}(y) = -\hat{C}{\psi_j}^{(1)}(y)/c$, again assuming that $c \neq 0$ for all k. Evaluating this equation at $y = \alpha$ when $j = 1$ and using boundary conditions (5.15) and (5.17), we find the single solution for ${C_1}^{(1)}(\alpha)$,

$${C_1}^{(1)}(\alpha) = -\hat{C}\alpha. \tag{5.44}$$

In the infinite Péclet-number limit our work can be compared to that of Frenkel and Halpern (2002) and Halpern and Frenkel (2003), who considered a linear-stability analysis of Couette–Poiseuille driven Stokes flow of two fluids of equal density in a channel with an insoluble surfactant at the interface, and who assumed diffusion to be negligible. Here two solutions were found for the wave speed, rather than just one as in our case. In their case, since concentration absorption is allowed at the fluid interface, velocity is not conserved along the interface ($\nabla_l \cdot \mathbf{u}_j \neq 0$, where ∇_l denotes the vector differential operator along the interface) and at $y = \eta$, our advection-diffusion equation, (5.3), is replaced by an independent transport equation,

$$\frac{\partial C_j}{\partial t} + \mathbf{u}_j \cdot \nabla_l C_j + C_j \nabla_l \cdot \mathbf{u}_j = 0. \tag{5.45}$$

Since perturbations to the interface are small, ∇_l points in the x direction to leading order and differentiation with respect to l may be thought of as differentiation with respect to x, and y derivatives neglected. Substituting the concentration and velocities into (5.45) using (5.10) (letting $Pe_1 = Pe_2 \to \infty$) and considering first order terms in ϵ

gives us[2]

$$C_j{}^{(1)}(\alpha) = \frac{1}{c}\left(1 + \hat{C}\alpha\right)\frac{d\psi_j{}^{(1)}}{dy}(\alpha), \tag{5.46}$$

assuming that $c \neq 0$ for all k. It is clear that in this case we have a quadratic in $C_j{}^{(1)}(\alpha)$ and therefore two solutions for $C_j{}^{(1)}(\alpha)$ and hence c. In our case our choice of conditions at the interface must result in the free surface remaining passive with regards to the extra mode. Perhaps the reason for this is because we do not have the extra degree of freedom associated with a concentration that is allowed to move along the interface (which would mean that rather than the solution depending solely on $C_1{}^{(1)}(\alpha)$, the change in concentration along the interface would become important).

5.3.2 Additional Solutions for c

Returning to the solution for general Péclet numbers, we note that in addition to the single solution mentioned above, there are in fact an infinite number of extra solutions that may be obtained by adding a solution of the form $\hat{C}_j \sin(k_j y) + \hat{D}_j \cos(k_j y)$ to the complementary function for $C_j{}^{(1)}$ in (5.38). For these solutions, boundary conditions (5.21) give us $\hat{D}_1 = 0$, $\hat{C}_1 = \hat{C}_2$ and $\hat{D}_1 = \hat{D}_2$ along with the condition that either $\hat{C}_1 = 0$ or $k_j = n\pi$, for $n \in \mathbb{Z}$. If $\hat{C}_1 = 0$ then we simply return to the solution (5.38). If $k_j = n\pi$, on the other hand, from (5.37) this implies that

$$c = -\frac{i}{Pe_j k}\left(k^2 + n^2\pi^2\right). \tag{5.47}$$

In this case (5.29) may be used to obtain $C_j{}^{(1)}(\alpha)$ (through Γ_2) and we may then use the solution for $C_1{}^{(1)}$ evaluated at $y = \alpha$ to give us $\hat{C}_1$. However, since these extra solutions are associated with a wave speed with negative imaginary part, as shown in (5.47), we do not investigate them in any more detail. Furthermore, in Rickett *et al.* (2013) the system (5.21), (5.22) and (5.30) is solved numerically using a Chebychev collocation method and the only solution found is the single solution described above. We therefore reason that the extra solutions do not appear in practice.

The numerical method also verifies that there are no further solutions for $C_1{}^{(1)}(\alpha)$. Evidence for this can also be found in both the small wavenumber and infinite Péclet number limits of our work, where it is possible to solve analytically and in both cases only the above mentioned solutions can be found. Since we find that we are able to trace our general solutions towards the solutions in these limits (either by considering plots of f against $C_1{}^{(1)}(\alpha)$ or by observing the correspondence between the solutions for $C_1{}^{(1)}(\alpha)$ and the wave speed, c, as we move towards these limits), we have good evidence of their

---

[2] Here we note that whilst in Frenkel and Halpern (2002) and Halpern and Frenkel (2003), the $u_j\partial/\partial x$ term may be neglected since a Galilean transformation is used to consider the problem from the frame of reference of the interface (so that so $\partial/\partial t$ becomes $\partial/\partial t - u_j\partial/\partial x$), in our case this term disappears since it is of order ϵ^2.

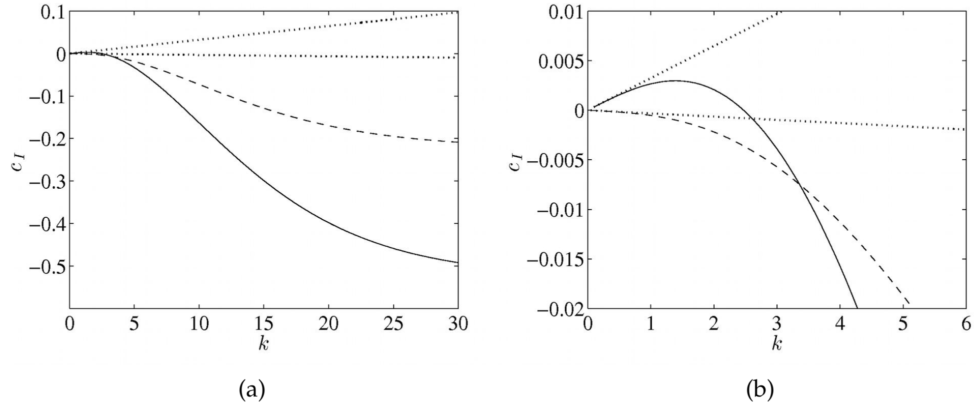

(a) (b)

Figure 5.2: Typical plots of c_I against k in the case $\hat{G} = 0$, illustrating the two possible forms of solution. Plot (b) shows a close-up of plot (a). Here $\Lambda = \hat{C} = Pe_1 = Pe_2 = 1$, $\alpha = 0.1$ and $\Gamma = 1$ (solid line) and -0.1 (dashed line). The dotted lines represent the small k solutions in each case.

exclusivity. Furthermore, if a bifurcation from these solutions occurred for some value of k or Pe_1 and Pe_2, we would expect to see a physical change in the nature of the flow at this point due to the extra degree of freedom that would be required, and we have no reason to expect such a change.

5.3.2.1 The Wave Speed, c, for the Single Solution of Interest

Since, for the single solution of interest, ${C_1}^{(1)}(\alpha)$ is found to be purely real, equations (5.20) and (5.29) imply that the solution for c is purely imaginary ($c = ic_I$) and there is no transverse movement of waves, which is as we might expect when the base-state is zero. In general, plots of c_I against the wavenumber, k, can take one of two forms, as shown in figure 5.2. In the first of these (shown by the solid curve) c_I increases from zero to a maximum as k increases from zero to some particular wavenumber, whilst in the second (the dashed curve) c_I simply decreases as k increases. In both cases c_I tends to some negative value for large k. In the former case the solution is unstable for small wavenumbers (large wavelengths) and stable for larger wavenumbers. In the latter case the solution is always stable, irrespective of k. We note that in the case where c_I changes from being positive to negative for increasing wavenumber, a wavenumber must exist for which $c_I = 0$ and the corresponding wave neither grows nor decays but is held in position by a balance of all of the forces involved.

Having seen the global view above, we can deduce which form the solution will take by considering the small k solution, (5.35), with $\hat{G} = 0$. Of the utmost importance are the parameters α and Λ. In figure 5.3 we have used the small k solution to plot the line $\partial c_I/\partial k|_{k=0} = 0$ in the (α, Λ) plane, revealing two distinct stability regions. If Γ and $\hat{C}$ both have the same sign, then in the unshaded region 1, the solution is unstable for smaller wavenumbers, whilst in the shaded region 2, the solution is stable for all k. If Γ

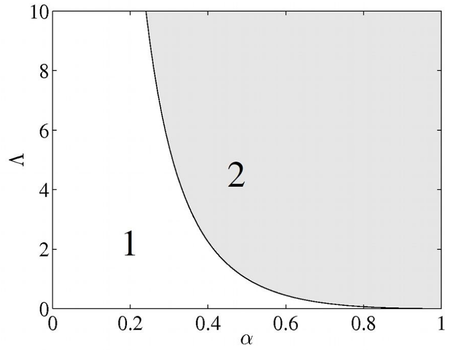

Figure 5.3: The two stability regions plotted in the (α, Λ)-plane. In region 1 the solution is unstable (stable) for smaller wavenumbers when Γ and $\hat{C}$ have the same (opposite) sign, whilst in region 2 the solution is stable (unstable).

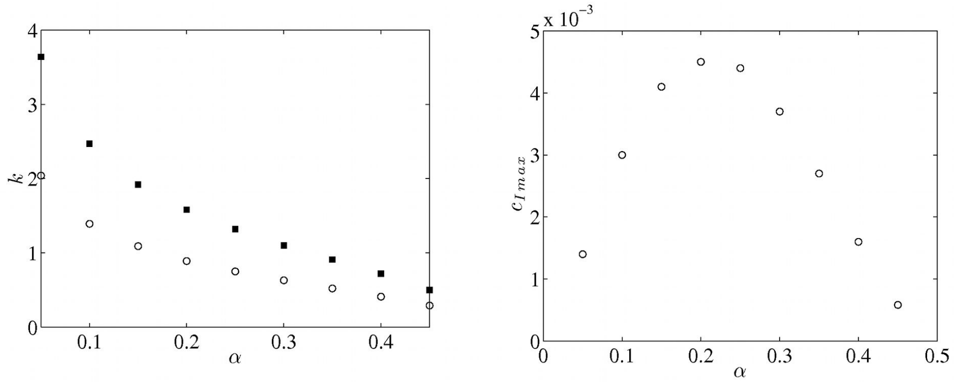

(a) (b)

Figure 5.4: When $\Lambda = \hat{C} = \Gamma = Pe_1 = Pe_2 = 1$ in the case $\hat{G} = 0$, plots against α of (a) the critical wavenumbers, k_{max}, (open circles) and k_c (shaded squares) and (b) the maximum value of the wave speed, c_{Imax}.

and $\hat{C}$ have opposite signs then in region 1 the solution is always stable, whilst in region 2, unstable solutions are found for small enough k.

Where the solution exhibits unstable behaviour, we label the upper limit on c_I, c_{Imax} and the wavenumber at which this occurs, k_{max}. The critical wavenumber for which the solution changes from positive to negative is labelled k_c, so that c_I is positive for $k \in (0, k_c)$. To illustrate how k_{max}, c_{max} and k_c change as as we move away from the boundary between the two regions, figure 5.4, shows how they depend on α in region 1 when we take $\Lambda = 1$ and $\hat{C} = \Gamma = Pe_1 = Pe_2 = 1$. We find that as we move away from the boundary (at $\alpha = 0.5$) and into region 1, both the wavenumbers k_{max} and k_c increase, so that there is a larger interval of k for which c_I is positive and in which the maximum value of c_I is found at a higher wavenumber. The maximum value of c_I also initially increases as we move away from the boundary, but reaches a peak at a certain depth ratio, after which decreasing α further results in c_{Imax} decreasing.

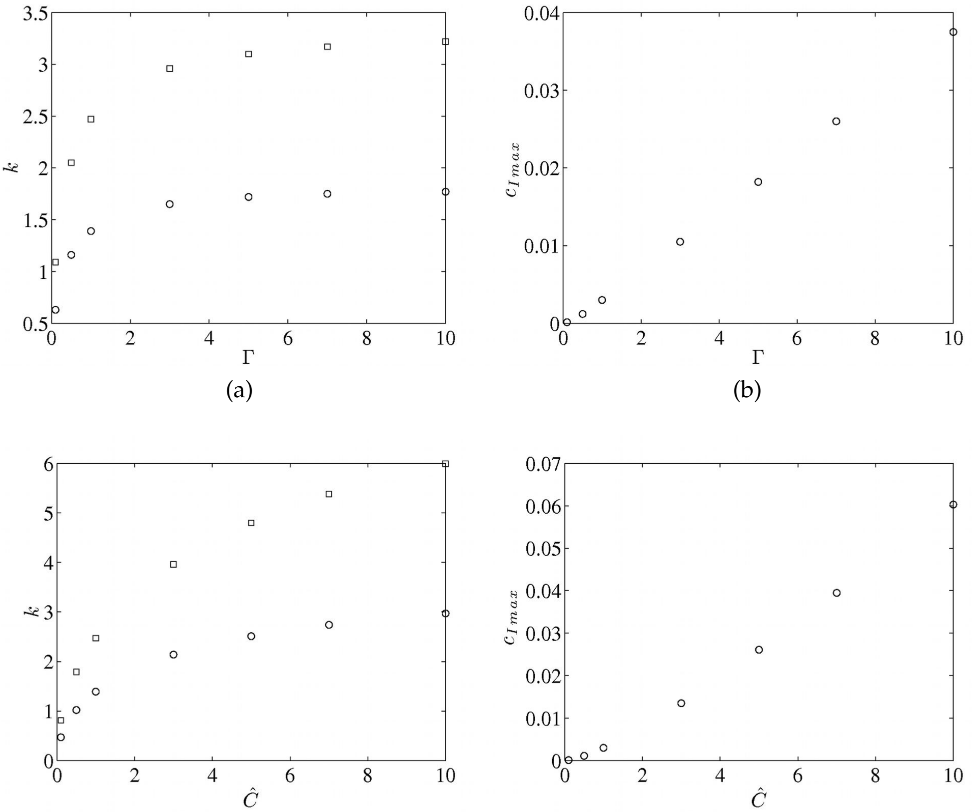

(a) (b)

(c) (d)

Figure 5.5: When $\Lambda = Pe_1 = Pe_2 = 1$ and $\alpha = 0.1$ in the case $\hat{G} = 0$, plots of (a) and (c) the critical wavenumbers, k_{max} (circles) and k_c (squares), and (b) and (d) the maximum value of the wave speed, c_{Imax}, against Γ and $\hat{C}$.

Although changing the sign of either Γ or $\hat{C}$ changes the qualitative nature of the solution, altering the magnitudes does not. As we might expect, varying either parameter has a very similar effect and when k is small, the magnitude of c_I increases when we increase either of the two parameters and decreases when they are decreased. Where c_I is positive, this results in a larger maximum wave speed (and wavenumber at which this occurs) and a larger region of positive k when one increases either parameter (see figure 5.5). We find that for larger values of these parameters c_{Imax} increases linearly with increasing Γ or $\hat{C}$, whereas k_{max} and k_c asymptote to a constant value. As either $\Gamma \to 0$ or $\hat{C} \to 0$ we find that the solution is always stable, as we would expect.

Considering equation (5.32), it is clear that since Pe_1 and Pe_2 are positive by definition, altering these parameters will not have an effect on which of the two forms of the solution for c_I we obtain. Instead, we focus on the effect on the magnitude of c_I. We plot a fraction that is instrumental in determining how altering Pe_{12} affects the wave

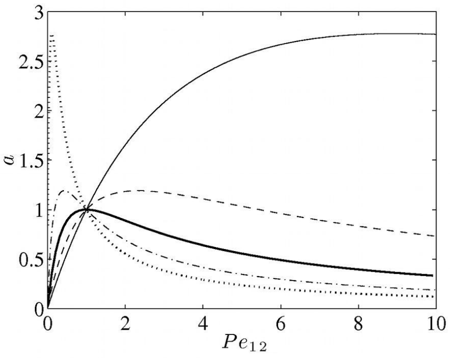

Figure 5.6: Plots of the fraction, a, which determines how Pe_{12} affects c_I in the small k solution, against Pe_{12} when $\alpha = 0.1$ (solid line), 0.3 (dashed line), 0.5 (thick solid line), 0.7 (dash-dotted line) and 0.9 (dotted line).

speed for small k. This is the fraction given by

$$a = \frac{Pe_{12}}{\left(\left(Pe_{12} - 1\right)\alpha + 1\right)^2}, \tag{5.48}$$

and plots are shown in figure 5.6. We find that, assuming that the first term of the small k solution is not zero (which occurs when $\Lambda = 1$ and $\alpha = 0.5$, for instance), increasing Pe_{12} from 1 results in an increase in the magnitude of c_I when $\alpha < 0.5$ and a decrease when $\alpha > 0.5$, whilst decreasing has the opposite effect. When $\alpha = 0.5$, both increasing and decreasing Pe_{12} from 1 results in a decrease in the magnitude of c_I. Where the magnitude is increased, however, there is an upper limit, beyond which the solution tends to zero, so that as either $Pe_{12} \to 0$ or $Pe_{12} \to \infty$, the magnitude of c_I always tends to zero. We consider in more detail the case $\Lambda = \hat{C} = \Gamma = 1$ and $\alpha = 0.1$ (see figure 5.7), finding that, in agreement with the above observations, in both the small and large limits of Pe_{12}, the critical wavenumbers, k_{max} and k_c, and the maximum wave speed, c_{Imax}, all tend to zero, suggesting that the solution is always stable here. Interestingly, we see peaks in the critical wavenumbers and c_{Imax} at an earlier value of Pe_{12} than the peak observed in c_I for the small k solution. In the case $Pe_1 = Pe_2 \to \infty$ the evidence suggests that c_I is always less than or equal to zero and the solution always stable. This can also be seen by considering the small k solution for the wave speed, (5.32), where ${C_1}^{(1)}(\alpha)$ is given by equation (5.44), for which we can see that to $O(k)$, the wave speed is now zero. This suggests that diffusion is necessary for an unstable solution.

We briefly mention a possible mechanism for instability. Streamline plots reveal closed cells separated by lines of zero ψ, with consecutive cells spinning in opposite directions (see figure 5.8). If Γ and $\hat{C}$ have the same sign, from equations (5.9) and (5.12), the combined effect of the surface tension gradient and base-state concentration ratio is to increase the surface tension as η increases. Since a high surface tension is more attracting than a low surface tension (due to the Marangoni effect), we conjecture that the Marangoni force will act to accentuate the peaks and smooth the troughs of the

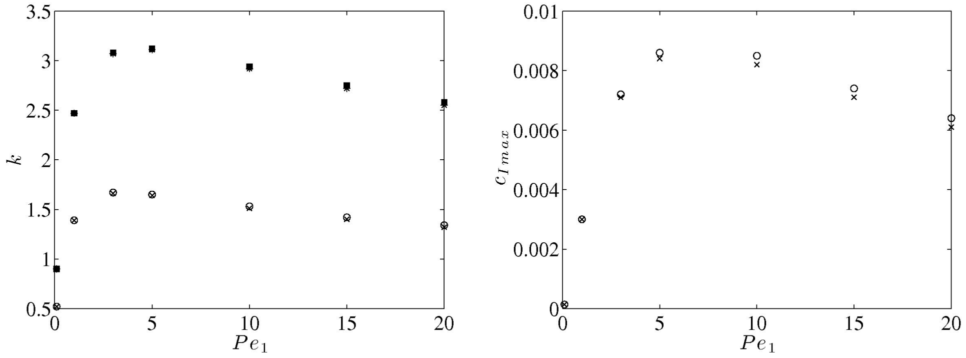

(a)

(b)

Figure 5.7: When $\Lambda = \hat{C} = \Gamma = Pe_2 = 1$ and $\alpha = 0.1$, plots against Pe_1 of (a) the critical wavenumbers, k_{max}, in the cases $\hat{G} = 0$ (open circles) and $\hat{G}_{u1}$ (crosses), and k_c in the cases $\hat{G} = 0$ (shaded squares) and $\hat{G}_{u1}$ (asterisks) and (b) the maximum value of the wave speed, c_{Imax}, in the cases $\hat{G} = 0$ (open circles) and $\hat{G}_{u1}$ (crosses).

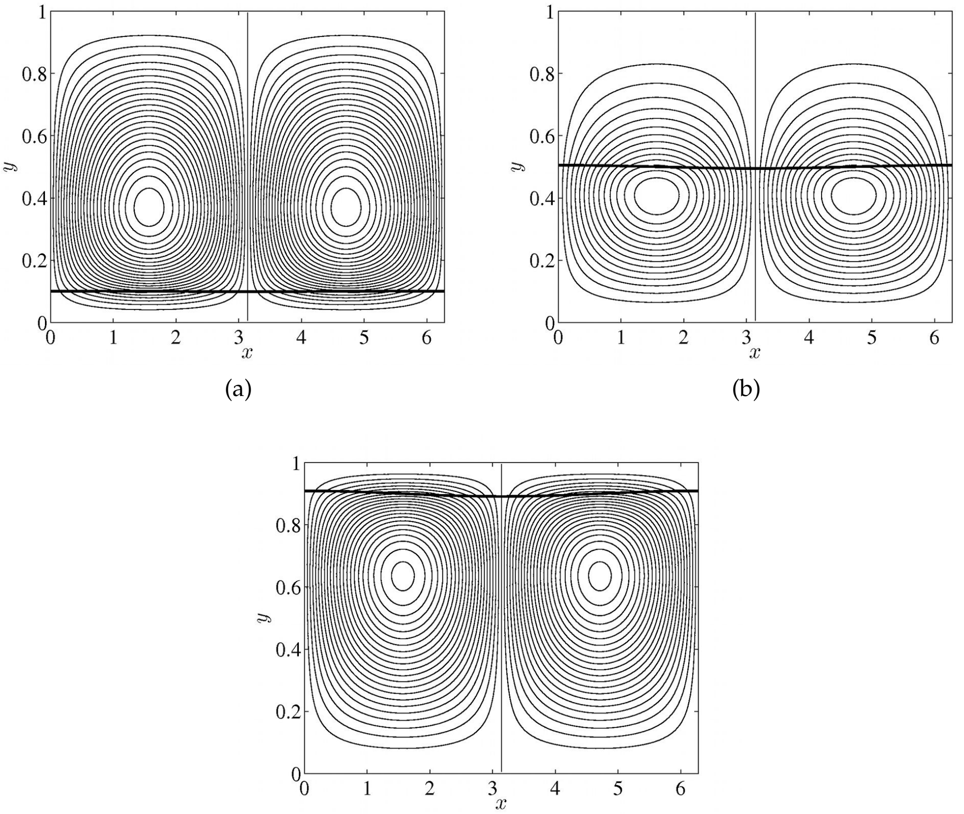

(a)

(b)

(c)

Figure 5.8: Streamline plots in the case $\hat{G} = 0$ using regular intervals of ψ (with a different range of ψ used each time) when $\epsilon = 0.01$, $t = \pi$, $\Lambda = \hat{C} = \Gamma = Pe_1 = Pe_2 = 1$ and $\alpha =$ (a) 0.1, (b) 0.5 and (c) 0.9.

interface (as illustrated in figure 5.9a). Then, in the cases where the solution is unstable,

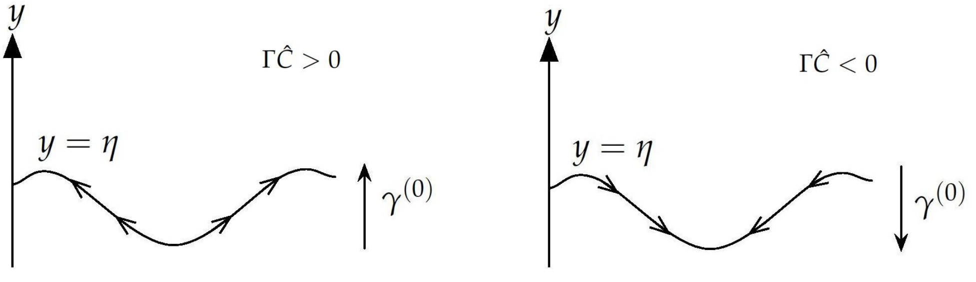

(a) (b)

Figure 5.9: An illustration of the effect of the Marangoni force on the fluid interface, with arrows showing the direction of this force when Γ and $\hat{C}$ are (a) the same sign and (b) opposite signs. Here we write $\gamma^{(0)} = 1 + \Gamma C_j^{(0)}$ $\Gamma\hat{C} > 0$ $\Gamma\hat{C} < 0$.

our plots suggest that the interface sits at the bottom half of the closed streamlines (as in figure 5.8a) and that the cells spin in a favourable direction (the left cell spinning clockwise in figure 5.8a, for example) so that peaks in the interface may grow and the effects of the Marangoni force are accentuated. In the stable cases, on the other hand, the interface sits at the top half of the cells (as in figures 5.8b and 5.8c), or in the case of larger wave numbers, the cells may spin in an unfavourable direction, so that the streamlines restrict the effect of the Marangoni force and the peaks are not allowed to grow. In some cases this arrangement of streamlines is achieved by an extra row of cells appearing either below or above the original set. This is the case when $\alpha = 0.5$ (figure 5.8b), although we note that here, since our problem is not symmetric about the centre of the channel (due to walls that are not symmetric about the x-axis and the presence of a surface tension gradient in the base-state), the bottom set of cells is larger with a stronger flow. If Γ and $\hat{C}$ are instead of opposite signs, then their effect is to decrease the surface tension as η increases. Then we conjecture that the Marangoni force accentuates the troughs and smooths the peaks (see figure 5.9b). Now when the interface sits at the bottom half of the cells (or the cells spin in an unfavourable direction), the effects of this force are restricted, whilst when it sits at the top half (and the cells spin in a favourable direction), the troughs are allowed to grow. We hypothesise that it is the Marangoni force that induces the closed flow seen in these plots and that this flow together with the presence of the walls dictates the position of the fluid interface. We also find that changing the magnitude of the various parameters can act to change the horizontal velocity above the interface compared to below, which appears to result in waves growing or decaying at a different speeds, although the overall stability is not affected.

5.3.3 Case (ii); A Non-Zero Pressure Gradient

5.3.3.1 An Analytical Solution

We may solve equations (5.21), (5.22) and (5.30) analytically by making use of parabolic cylinder functions, a class of special functions also known as Weber functions. First, we solve the homogeneous versions of (5.30),

$$\frac{d^2 C_j{}^{(1)}}{dy^2} + \left(\tilde{a}_j y^2 + \tilde{b}_j y + \tilde{c}_j\right) C_j{}^{(1)} = 0, \tag{5.49}$$

where

$$\tilde{a}_j = \frac{ikPe_j \hat{G} \mu_1}{2\mu_j}, \quad \tilde{b}_j = -\frac{ikPe_j \hat{G}\mu_1 \left(\alpha^2(\Lambda - 1) + 1\right)}{2\mu_j \left(\alpha(\Lambda - 1) + 1\right)},$$
$$\tilde{c}_j = ikPe_j \left(c + \frac{\hat{G}_1(\Lambda - 1)(j-1)}{\Lambda}\right) - k^2, \tag{5.50}$$

and where $\hat{G}_1$ is given in (5.15). Parabolic cylinder functions are defined as solutions to a differential equation of the form (5.49) (Abramowitz and Stegun, 1964). The differential equation is most often rewritten as one of the two distinct standard forms of Weber's equation,

$$\frac{d^2 C_j{}^{(1)}}{dy_j{}^2} + \left(\frac{1}{4} y_j{}^2 - \tilde{d}_j\right) C_j{}^{(1)} = 0, \quad \frac{d^2 C_j{}^{(1)}}{dy_j{}^2} - \left(\frac{1}{4} y_j{}^2 + \tilde{d}_j\right) C_j{}^{(1)} = 0, \tag{5.51}$$

where y_j and $\tilde{d}_j$ may be complex. The second of equations (5.51) can be obtained from the first by letting $\tilde{d}_j \to \tilde{d}_j i$ and $y_j \to y_j \exp(-i\pi/4)$. Equation (5.49) may be obtained from the second of (5.51) by taking

$$y_j = 2^{\frac{1}{2}} \tilde{a}_j^{\frac{1}{4}} e^{i\pi/4} \left(y + \frac{\tilde{b}_j}{2\tilde{a}_j}\right), \quad \tilde{d}_j = -\frac{i}{2\tilde{a}_j^{\frac{1}{2}}} \left(\frac{\tilde{b}_j^2}{4\tilde{a}_j} - \tilde{c}_j\right). \tag{5.52}$$

Independent even and odd solutions of the second of equations (5.51) are given by

$$C_j{}^{(1)}{}_1 = e^{-\frac{y_j{}^2}{4}} {}_1F_1\left(\frac{1}{2}\tilde{d}_j + \frac{1}{4}; \frac{1}{2}; \frac{1}{2} y_j{}^2\right), \quad C_j{}^{(1)}{}_2 = y_j e^{-\frac{y_j{}^2}{4}} {}_1F_1\left(\frac{1}{2}\tilde{d}_j + \frac{3}{4}; \frac{3}{2}; \frac{1}{2} y_j{}^2\right), \tag{5.53}$$

where

$${}_1F_1(a;b;z) = \sum_{n=0}^{\infty} \frac{(a)_n z^n}{(b)_n n!}, \quad (s)_n = s(s+1)(s+2)...(s+n-1), \quad s = a, b. \tag{5.54}$$

Here ${}_1F_1(a;b;z)$ is the confluent hypergeometric function of the first kind (or Kummer's function of the first kind). This function is regular at $z = 0$, single-valued and convergent, except at its poles.

The general solution of the second of equations (5.51) can be constructed by taking a linear combination of solutions (5.53) (since they are linearly independent). We therefore construct the complementary functions to (5.49), ${C_j^{(1)}}_{CF}$, by writing

$$ {C_j^{(1)}}_{CF} = \tilde{A}_j {C_j^{(1)}}_1 + \tilde{B}_j {C_j^{(1)}}_2, \tag{5.55} $$

where $\tilde{A}_j$, $\tilde{B}_j$ are constants. From Abramowitz and Stegun (1964), these complementary functions are convergent for all y_j. We note that the pair of solutions $\{{C_j^{(1)}}_1, {C_j^{(1)}}_2\}$ would not normally be used to directly construct a solution to a physical problem since they have very similar asymptotic behaviours as $y_j \to \infty$. Instead linearly independent pairs of solutions would be constructed such that certain behaviours are satisfied in the large y_j limit. In our problem, however, y is bounded between 0 and 1 and hence y_j is bounded. Furthermore it is known that C_{j1} and C_{j2} are well behaved for small y_j.

To find the particular integrals to (5.30), we use the method of variation of parameters. Since $\{{C_j^{(1)}}_1, {C_j^{(1)}}_2\}$ is a set of fundamental solutions to the homogeneous version of (5.30) and therefore the general solution of the homogeneous equation is given by (5.55), for the particular integral, ${C_j^{(1)}}_{PI}$, we let

$$ {C_j^{(1)}}_{PI} = q_{j1}(y) {C_j^{(1)}}_1 + q_{j2}(y) {C_j^{(1)}}_2, \tag{5.56} $$

where q_{j1} and q_{j2} are functions to be determined. We next assume that

$$ \frac{dq_{j1}}{dy} {C_j^{(1)}}_1 + \frac{dq_{j2}}{dy} {C_j^{(1)}}_2 = 0, \tag{5.57} $$

and substituting ${C_j^{(1)}}_{PI}$ into equation (5.30), remembering that ${C_j^{(1)}}_1$ and ${C_j^{(1)}}_2$ are solutions to the homogeneous equation, gives us

$$ \frac{dq_{j1}}{dy} \frac{d{C_j^{(1)}}_1}{dy} + \frac{dq_{j2}}{dy} \frac{d{C_j^{(1)}}_2}{dy} = b_j(y). \tag{5.58} $$

Rearranging equations (5.57) and (5.58), we find that

$$ \frac{dq_{j2}}{dy} = \frac{b_j {C_j^{(1)}}_1}{W({C_j^{(1)}}_1, {C_j^{(1)}}_2)}, \quad \frac{dq_{j1}}{dy} = -\frac{b_j {C_j^{(1)}}_2}{W({C_j^{(1)}}_1, {C_j^{(1)}}_2)}, \tag{5.59} $$

where the Wronskian of ${C_j^{(1)}}_1$ and ${C_j^{(1)}}_2$,

$$ W({C_j^{(1)}}_1, {C_j^{(1)}}_2) = {C_j^{(1)}}_1 \frac{d{C_j^{(1)}}_2}{dy} - \frac{d{C_j^{(1)}}_1}{dy} {C_j^{(1)}}_2, \tag{5.60} $$

is non-zero since ${C_j^{(1)}}_1$ and ${C_j^{(1)}}_2$ are linearly independent. In fact, from the theory of parabolic cylinder functions, $W({C_j^{(1)}}_1, {C_j^{(1)}}_2) = 1$.

Integrating equations (5.59) with respect to y (using a numerical method such as the trapezoidal rule or Simpson's rule) gives us q_{j1} and q_{j2} and the solution to (5.30) is given by

$$C_j{}^{(1)} = C_j{}^{(1)}{}_{CF} + C_j{}^{(1)}{}_{PI}. \tag{5.61}$$

Here the constants $\tilde{A}_j$ and $\tilde{B}_j$ can be found by solving the four equations resulting from the four boundary conditions given in (5.21) and (5.22). Letting $y = \alpha$ in equation (5.61) when $j = 1$ again gives us an implicit equation for $C_1{}^{(1)}(\alpha)$ which can be solved using the secant method.

5.3.3.2 A Numerical Solution

Although it is possible to write down an analytical solution to (5.21), (5.22) and (5.30) when $\hat{G} \neq 0$, we instead choose to seek a numerical solution using the shooting method, which is much simpler to implement. Writing

$$W_j(y) = C_j{}^{(1)}(y), \quad W_{Dj}(y) = \frac{dW_j}{dy}, \quad \mathbf{W}_j(y) = \begin{pmatrix} W_j(y) \\ W_{Dj}(y) \end{pmatrix}, \tag{5.62}$$

in fluid j, we can rewrite equation (5.30) as the first order system,

$$\frac{d\mathbf{W}_j}{dy} = \begin{pmatrix} W_{Dj}(y) \\ b_j(y) - a_j(y)W_j(y) \end{pmatrix}, \tag{5.63}$$

with boundary conditions, from (5.21) and (5.22),

$$\mathbf{W}_1(0) = \begin{pmatrix} 0 \\ \gamma_1 \end{pmatrix}, \quad \mathbf{W}_2(1) = \begin{pmatrix} 0 \\ \gamma_2 \end{pmatrix},$$

$$\xi_1 = \frac{(Pe_{12} - 1)\,\hat{C}\alpha}{(Pe_{12} - 1)\,\alpha + 1} + W_1(\alpha) - W_2(\alpha) = 0, \quad \xi_2 = W_{D1}(\alpha) - Pe_{12}W_{D2}(\alpha) = 0, \tag{5.64}$$

for γ_1 and γ_2 unknown. From equations (5.31), using (5.20), (5.26) and (5.28), a_j and b_j depend in a known way on $W_1(\alpha)$ and c, which itself depends on $W_1(\alpha)$ and is computed using (5.29) and (5.20). Given an initial guess for γ_1, γ_2 and $W_1(\alpha)$, we integrate $d\mathbf{W}_1/dy$ and $d\mathbf{W}_2/dy$ from $y = 0$ and 1, respectively, to α using the fourth-order Runge–Kutta method. We then compute ξ_1 and ξ_2 and update our guesses for γ_1 and γ_2 such that $\xi_1, \xi_2 \to 0$ using Newton's method (as described in appendix B). We update $W_1(\alpha)$ using the value computed in the integration. The process is repeated until the magnitudes of ξ_1 and ξ_2 are sufficiently small, giving us our numerical solution. By this method we have reduced the boundary value problem to an initial value problem, with the aim to satisfy a condition at an endpoint ($y = \alpha$).

Using this method, we may validate our results from previous case. Letting $\hat{G} = 0$ and plotting the wave speed, we find that the solution is visually indistinguishable from our earlier results where we used the secant method to solve the implicit equation resulting from taking $y = \alpha$ in the solution to the system (5.21), (5.22) and (5.30).

Returning to the case $\hat{G} \neq 0$, we again find only a single solution of interest for ${C_1}^{(1)}(\alpha)$. This can be seen if we consider the infinite Péclet-number limit. Here we find that evaluating the advection-diffusion equation, (5.30), at $y = \alpha$ when $j = 1$ gives us ${C_1}^{(1)}(\alpha) = -\hat{C}{\psi_1}^{(1)}(\alpha)/(c + \hat{G}_1)$, where we have divided by $c + \hat{G}_1$ since we are not interested in wave speed solutions with zero imaginary part for all k. Then, using boundary conditions (5.15) and (5.17), we are left with the single solution (5.44). The extra solutions described in the case $\hat{G} = 0$ (in section 5.3.2) can again be found in this case. However, since the imaginary part of the wave speed for these solutions is the same as in (5.47), they are found to always decay and we do not spend any more time investigating them.

5.3.3.3 The Wave Speed, c, for the Single Solution of Interest

In general, for the single solution of interest, ${C_1}^{(1)}(\alpha)$ now consists of an imaginary part in addition to a real part, so that the wave speed, c, has both a real and an imaginary part, as we would expect in the case of a horizontal pressure gradient in the base-state. Plots of the imaginary part, c_I, are found to take one of the two forms discussed in the results for the case $\hat{G} = 0$. In the small k analysis, (5.35), c_I does not depend on $\hat{G}$, so that the regions of stability are the same as those shown in figure 5.3 and the general solution for c_I is not affected qualitatively by varying $\hat{G}$. We find that the quantitative effect of the addition of a pressure gradient on c_I is not straightforward, being a complex problem in $(\hat{G}, k, \alpha, \hat{C}, \Gamma, \Lambda, Pe_1, Pe_2)$ parameter space. Furthermore, the results for c_I are not changed substantially from the case $\hat{G} = 0$. The addition of a pressure gradient simply slightly increases or decreases the magnitude of c_I. In our results we choose to consider the addition of the pressure gradient given in (5.8), which is equivalent to taking the base-state, horizontal velocity at the interface, given by $\partial{\psi_j}^{(0)}/\partial y(\alpha)$, to be unity. The limited effect on c_I can then be seen in figure 5.7, which shows one of the more notable cases. Of course, a larger pressure gradient will affect the results more noticeably, but since the qualitative nature of the solution is not affected by letting $\hat{G} \neq 0$, we choose to focus instead on the real part of the wave speed, c_R, in our analysis and a full study of the effect on c_I is a suggested topic for future research. We simply note that (assuming Γ and $\hat{C}$ both positive) in those cases where the addition results in an increase in the magnitude of $\Re({C_1}^{(1)}(\alpha))$, the effect appears to be stabilising, whilst a decrease in $\Re({C_1}^{(1)}(\alpha))$ is destabilising, although the exact mechanism behind this effect is not clear.

Plots of the real part of c, c_R, against k are found to take one of six forms, as shown in figure 5.10. In all cases, for large wavenumbers, c_R tends to the speed of the base-state horizontal velocity at the interface. In the first case (shown by the solid curve in figure 5.10a) c_R is independent of k so that waves travel at the speed of the base-state velocity for all wavenumbers. In the second and third cases (the dashed curve and the

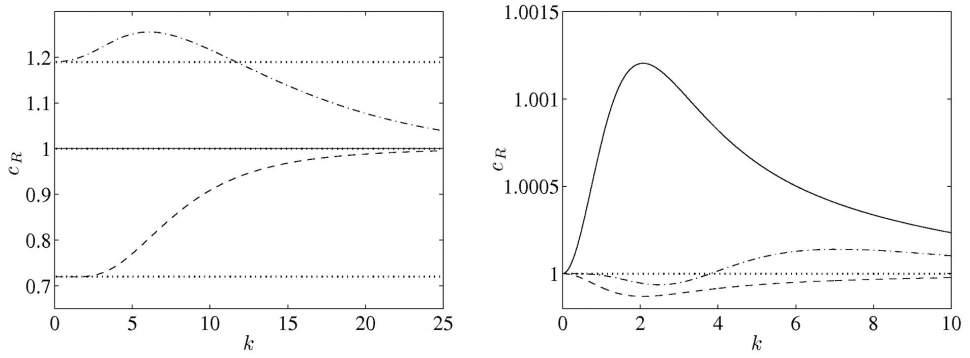

(a) (b)

Figure 5.10: Typical plots of c_R against k in the case $\hat{G} = \hat{G}_{u1}$, illustrating the six possible forms of solution. Here plot (a) shows the case $\hat{C} = \Gamma = Pe_1 = Pe_2 = 1$, $\alpha = 0.1$ and $\Lambda = 1$ (solid line), 10 (dashed line) and 0.1 (dash-dotted line), whilst plot (b) shows the case $\Lambda = \hat{C} = Pe_2 = 1$ and $\alpha = 0.1$, $Pe_1 = 10$ and $\Gamma = 1$ (solid line), $\alpha = 0.9$, $Pe_1 = 0.1$ and $\Gamma = 1$ (dashed line) and $\alpha = 0.1$, $Pe_1 = 1$ and $\Gamma = 10$ (dash-dotted line). The dotted lines represent the small k solutions in each case.

dash-dotted curve in figure 5.10a) waves with small wavenumbers (large wavelengths) travel slower and faster, respectively, than the base-state velocity, whilst in the fourth to sixth cases (seen in figure 5.10b) the small wavenumber speed is that of the basic state velocity, but it is for moderate k that we see a deviation from this speed. In the fourth and fifth cases (the solid and dashed curves) the moderate wavenumber speed is greater than and less than that of the basic-state velocity, respectively, whilst in the sixth case (the dash-dotted curve) the speed alternates from being less than to greater than the basic state-velocity as we increase k.

The small k solution, (5.35), is again useful in distinguishing which form of result we will obtain, and can be used to determine whether the solution takes the second form, the third form or one of the first and fourth to sixth forms (for which c_R is given by the base-state velocity for small k). We note that in the small wavenumber solution, c_R depends only on α and Λ (and $\hat{G}$, although altering this parameter only alters the magnitude of the solution), so that once again, these two parameters are critical in determining the qualitative nature of the solution. Figure 5.11 shows the curves obtained in the (α, Λ) plane by setting $c_R|_{k=0} = \partial\psi_j{}^{(0)}/\partial y(\alpha) = 1$ in the small k solution. On these curves, we obtain one of the first and fourth to sixth forms of solution. We note that one of the curves coincides with the same curve that divides the stability regions in figure 5.3, suggesting some correspondence between the stability of the solution and the wave speed of waves at the interface. These curves divide two wave speed regions. In the unshaded region 1 the wave speed of small wavenumber waves is less than that of the base-state velocity at the interface, and in the shaded region 2 the wave speed is greater.

Also from the small k solution, in figure 5.12 we plot $c_R|_{k=0}$ against Λ for various

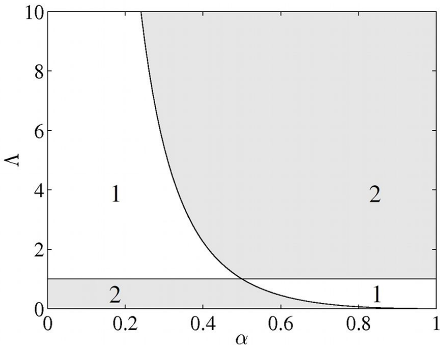

Figure 5.11: The two wave speed regions plotted in the (α, Λ)-plane. In region 1 waves travel slower than the horizontal base-state velocity at the interface for small wavenumbers, whilst in region 2 they travel faster. On the dividing lines, small wavenumber waves travel at the same speed as the base-state velocity.

values of α. The slowest waves in region 1 are found as α moves closer to 0 or 1 and at the same time Λ moves closer to zero or infinity. In region 2, the fastest waves are found as Λ becomes very small or large. In both cases there is an upper limit on the wave speed. For the small Λ limit, the upper limit on the wave speed increases as α moves closer to 1, whilst for the large Λ limit, the upper limit increases as α moves towards 0. The largest upper limit shown in these plots occurs when $\alpha = 0.1$, where the wave speed tends to 19 for large Λ. This is fairly large compared to 1, the velocity at the interface in the base-state, when we consider that Benjamin (1957) and Yih (1963) find that in the case of the flow of one fluid down an inclined plane, small wavelength waves travel at double the speed of the base flow at the free surface. These papers can be compared to our solution in the infinite Λ limit, which is essentially the same case as that of replacing the bottom fluid with air. However, in our case, by choosing $\hat{G} = \hat{G}_{u1}$, we force the pressure gradient to be $O(\Lambda)$ in size. At the interface, this results in an $O(\Lambda)$ shear rate, $\partial u/\partial y$, in fluid 1 (explaining the fast travelling waves when Λ is large) and an $O(1)$ shear in fluid 2, as opposed to the $O(1)$ shear in fluid 1 and $O(\Lambda^{-1})$ shear in fluid 2 that occurs in these papers and our solution in this fluid if the pressure gradient is $O(1)$.

In the general wavenumber solution we label the wave speed at which the deviation is greatest from that of the base-state flow, c_{Rdev} and the wavenumber at which this occurs, k_{dev}. We begin by letting $\hat{C} = \Gamma = Pe_{21} = 1$ and considering the effects of varying α and Λ. When we fix Λ and vary α, we find that k_{dev} is always zero except for when α is close to 0 or 1 (for instance, when $\alpha = 0.1$ and 0.9) and so the behaviour of c_{Rdev} is given by the small wavenumber solution. In figure 5.13 we plot k_{dev} and c_{Rdev} when we fix α at 0.1 and vary Λ, finding that c_{Rdev} has similar behaviour to c_R in the small k solution (as seen in figure 5.12a). As we increase Λ, however, we find that k_{dev} decreases to zero, suggesting that in the large Λ limit c_{Rdev} can again be found from the small k solution. In the cases where we sit on the dividing lines in figure 5.11 any

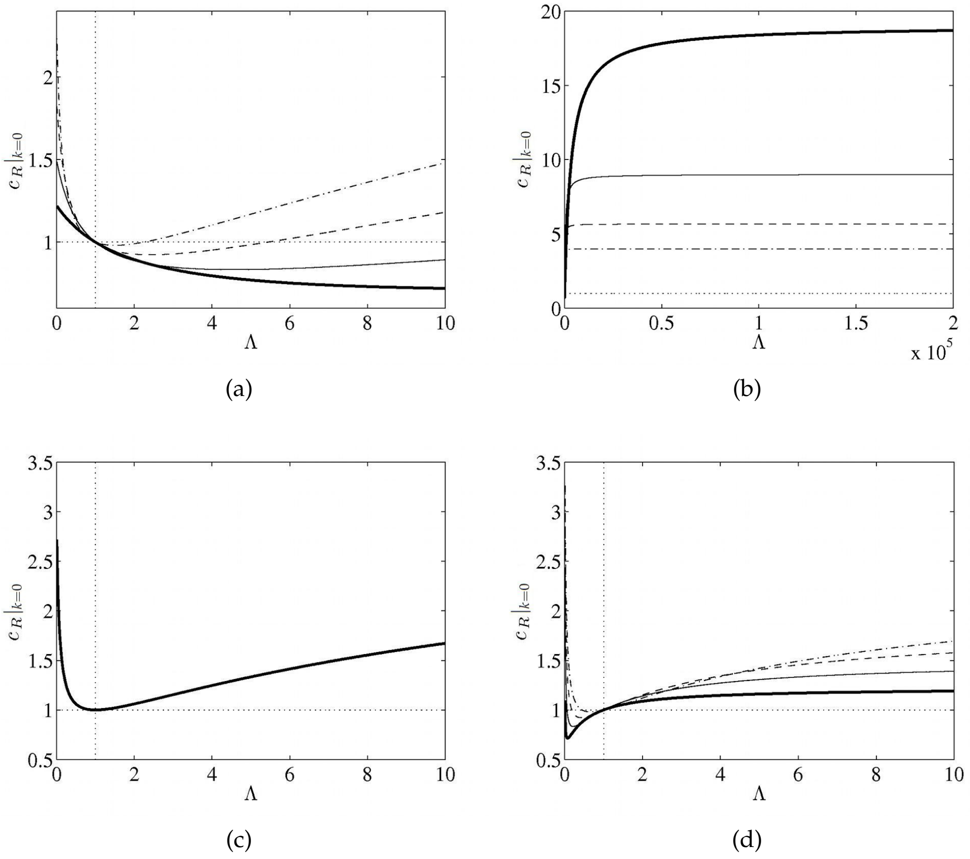

Figure 5.12: From the small wavenumber solution, $c_R|_{k=0}$ plotted against Λ in the case $\hat{G} = \hat{G}_{u1}$. In (a), and for larger Λ in (b), $\alpha = 0.1$ (thick solid line), 0.2 (solid line), 0.3 (dashed line) and 0.4 (dash-dotted line), in (c) $\alpha = 0.5$ and in (d) $\alpha = 0.6$ (dash-dotted line), 0.7 (dashed line), 0.8 (solid line) and 0.9 (thick solid line). The dotted lines represent the lines $x = y = 1$.

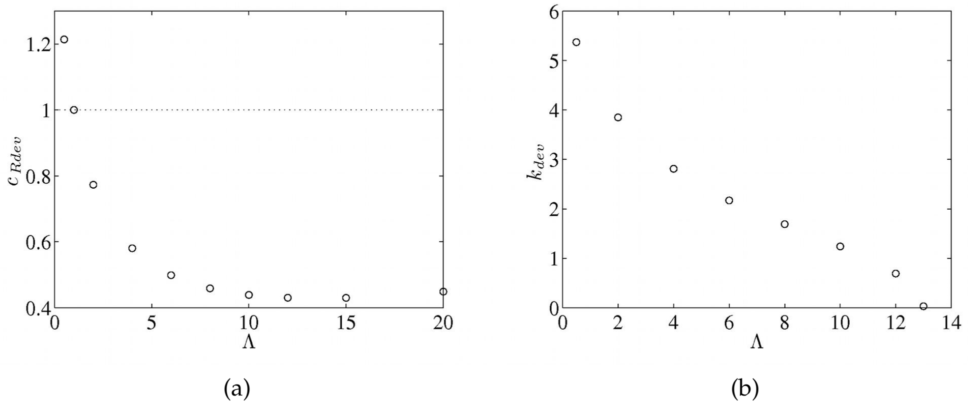

Figure 5.13: When $\hat{C} = \Gamma = Pe_{21} = 1$ and $\alpha = 0.1$ in the case $\hat{G} = \hat{G}_{u1}$, plots against Λ of (a) the maximum deviation from the base-state flow, c_{Rdev}, and (b) the wavenumber at which this occurs, k_{dev}.

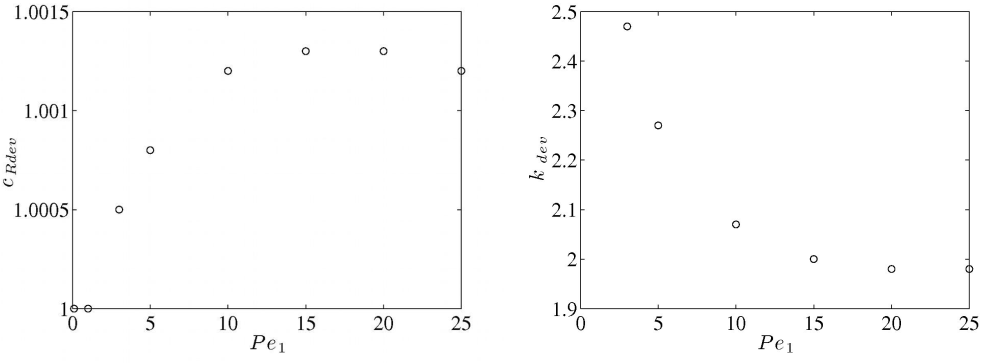

(a) (b)

Figure 5.14: When $\Lambda = \hat{C} = \Gamma = Pe_2 = 1$ and $\alpha = 0.1$ in the case $\hat{G} = \hat{G}_{u1}$, plots against Pe_1 of (a) the maximum deviation from the base-state flow, c_{Rdev}, and (b) the wavenumber at which this occurs, k_{dev}.

deviation away from the speed of the base-state flow at general wavenumbers is found to be very small (at a level beyond the accuracy of our program). Here we may conclude that we obtain the first form of solution for c_R, so that the wave speed is the same as that of the basic state flow for all wavenumbers.

When we fix $\Lambda = \hat{C} = \Gamma = Pe_2 = 1$ and vary Pe_1, we find that any deviation away from the basic-state flow is more noticeable for α closer to 0 or 1. In these cases the solution for c_R takes either the fourth or fifth form, so that it is either greater than or less than the speed of the base-state flow for moderate wavenumbers. In figure 5.14 we consider the case $\alpha = 0.1$ and plot c_{Rdev} and k_{dev} against Pe_1, finding that whilst for $Pe_{12} < 1$ any deviation is so small that we may assume that waves travel at the speed of the base-state flow for all wavenumbers, as Pe_{12} increases from 1, c_{Rdev} increases from the base-state flow speed, before decreasing again in the large Pe_{12} limit. We note that in the case $Pe_1 = Pe_2 \to \infty$, ${C_1}^{(1)}(\alpha)$ is purely real (given by (5.44)) and when $\Lambda = 1$ and $\hat{G} = \hat{G}_{u1}$, we find that $c_R = 1$, the speed of the base-state flow. The corresponding wavenumber, k_{dev}, on the other hand, is found to decrease as Pe_{12} increases, so that as c_R tends to the speed of the base-state flow for all wavenumbers in the large Pe_{12} limit, the position of the maximum wave speed tends to a constant value. If we instead consider the case $\alpha = 0.9$, we find that it is now for $Pe_{12} < 1$ that c_R deviates from the speed of the base-state flow, with waves traveling more slowly in this case, whilst for $Pe_{12} > 1$, any deviation is so small that it can be disregarded.

Letting $\Lambda = Pe_{21} = 1$ and $\alpha = 0.1$, we find that for smaller magnitudes of $\hat{C}$ and Γ, any deviation is small enough to be negligible (and therefore, due to the constraints on the lower limits of these parameters, (5.13), taking either $\hat{C}$ or Γ to be negative produces no noticeable deviation from the speed of the base-state flow). For larger magnitudes of $\hat{C}$ and Γ we find that c_R takes the sixth form, decreasing to a speed less than that of the base-state flow as we increase the wavenumber before increasing to a greater speed and then returning to the base-state flow speed for large wavenumbers. The magnitudes of both the maximum and minimum in c_R increase as $\hat{C}$ and Γ increase, as do the critical wave numbers at which they occur. For large $\hat{C}$ and Γ the growth of the maximum and minimum in c_R looks to be linear, whilst the wave numbers at which these occur asymptotes to a constant value.

We briefly comment on how the previously suggested mechanism for instability may also be relevant in determining the behaviour of c_R. We have already noted that one of the curves in (α, Λ)-parameter space dividing the regions of slower and faster travelling waves in the small wavenumber limit (in figure 5.11) is the same curve that divides the stability regions (in figure 5.3). In the stability analysis this curve represents the case in which $c_I = 0$, for which we would we would expect the interface to sit at the centre of the closed streamlines described in the case $\hat{G} = 0$ (and shown in figure 5.8) and the magnitude of the velocity above and below the interface to be the same. We suggest that either side of this curve, a velocity difference is established in the $O(\epsilon)$ flow which can act to speed up or slow down interfacial waves, depending on whether the viscosity ratio Λ is greater than or less than 1. Since the second curve dividing the wave speed limits in figure 5.11 is the line $\Lambda = 1$, it appears that a viscosity difference is necessary for the interfacial wave speed to deviate from the base-state flow speed by this mechanism. When $\Lambda = 1$, at least for smaller wavenumbers, when the choice of α, Pe_{21}, $\hat{C}$ and Γ results in a wave speed that is different from that of the base-state flow, in the cases in which c_R is found to be slower than the flow speed, c_I is found to have increased with the addition of a pressure gradient, whilst where c_R is found to be faster, c_I is decreased. This suggests that a convective instability may be responsible for any deviation is these cases, so that where c_I is increased, energy is propagated into a turbulent region downstream (not modelled here), causing waves to travel more slowly, whilst where c_I is decreased, energy is drawn less from the system through this mechanism, resulting in a faster wave speed at the interface. To determine the exact workings of this mechanism would require further analysis, for instance using Briggs (1964) method for convective instabilities. However this is outside the scope of this thesis and a possible future topic of research.

5.4 Removing the Channel Walls

We briefly consider the case where the walls are removed from our problem and a simple shear flow taken instead in the base-state. Here the vertical length scale, h_2, represents the distance over which the dimensional base-state concentration, varies by one unit, ΔC, which, if the surface tension gradient is taken to be $\gamma_1/\Delta C$, corresponds to the dimensional base-state surface tension varying by one unit, γ_1. The non-dimensional parameter Γ is now replaced by

$$\Gamma_w = \frac{\gamma_1 C_0}{\gamma_0 \Delta C}, \tag{5.65}$$

corresponding to the non-dimensional surface tension gradient and, taking the shear flow as described in the case of flow next to an elastic wall, (4.5), the non-dimensional base-state streamfunction and pressure in fluid j are instead described by

$$\psi_j{}^{(0)} = Ca\left(\frac{\mu_2}{\mu_j}\frac{y^2}{2} + \alpha(\Lambda-1)(j-1)y\right) \tag{5.66}$$

$$p_j{}^{(0)} = p_0, \tag{5.67}$$

where p_0 is again a prescribed constant pressure. Here instead of the pressure gradient, $\hat{G}$, the non-dimensional capillary number,

$$Ca = \frac{G\mu_1 h_2}{\gamma_0}, \tag{5.68}$$

results, where G is now taken to be the horizontal shear as $y \to \infty$.

Since we require the disturbance velocities to tend to zero at infinity, the boundary conditions at the walls, (5.14), are replaced by the far field conditions,

$$\frac{d\psi_1{}^{(1)}}{dy}(-\infty) = \frac{d\psi_2{}^{(1)}}{dy}(\infty) = \psi_1{}^{(1)}(-\infty) = \psi_2{}^{(1)}(\infty) = 0. \tag{5.69}$$

In addition, the velocity continuity and kinematic conditions at the interface, (1.22) and (1.23), now give us

$$\psi_1{}^{(1)}(\alpha) = \psi_2{}^{(1)}(\alpha) = \alpha\left(c - \alpha Ca\Lambda\right), \tag{5.70}$$

$$\frac{d\psi_1{}^{(1)}}{dy}(\alpha) - \frac{d\psi_2{}^{(1)}}{dy}(\alpha) = \alpha Ca\left(1-\Lambda\right), \tag{5.71}$$

replacing equations (5.15) and (5.16).

Then, we again solve the non-dimensionalised version of the biharmonic equation, (1.5), subject to conditions (5.18), (5.19) and (5.69) to (5.71), where we again use the non-dimensional form of the first of equations (1.3) to find the pressure. Letting

$$\begin{aligned}\Gamma_{w1} &= 1 + \Gamma_w\left(1 + \frac{Pe_{12}\hat{C}\alpha}{\left(Pe_{12}-1\right)\alpha+1}\right),\\ \Gamma_{w2} &= \Gamma_w\left(\frac{Pe_{12}\hat{C}\alpha}{\left(Pe_{12}-1\right)\alpha+1} + C_1{}^{(1)}(\alpha)\right),\end{aligned} \tag{5.72}$$

the disturbance streamfunction and pressure in fluids 1 and 2 are found to be

$$\begin{aligned}\psi_1{}^{(1)} &= -\frac{1}{2\left(1+\Lambda\right)}\left(\alpha i\Gamma_{w1} - \left(2\alpha Ca\Lambda + \alpha ik\Gamma_{w1} + i\Gamma_{w2}\right)\left(y-\alpha\right)\right)e^{k(y-\alpha)},\\ \psi_2{}^{(1)} &= -\frac{1}{2\left(1+\Lambda\right)}\left(\alpha i\Gamma_{w1} + \left(2\alpha Ca\left(1-\Lambda\right) + \alpha ik\Gamma_{w1} - i\Gamma_{w2}\right)\left(y-\alpha\right)\right)e^{-k(y-\alpha)},\end{aligned} \tag{5.73}$$

and

$$\begin{aligned} {p_1}^{(1)} =& -\frac{ik}{(1+\Lambda)}\left(2\alpha Ca\Lambda + \alpha ik\Gamma_{w1} + i\Gamma_{w2}\right)e^{k(y-\alpha)}, \\ {p_2}^{(1)} =& \frac{i\Lambda k}{(1+\Lambda)}\left(2\alpha Ca\left(1-\Lambda\right) + \alpha ik\Gamma_{w1} - i\Gamma_{w2}\right)e^{-k(y-\alpha)}, \end{aligned} \tag{5.74}$$

and the wave speed is

$$c = \alpha Ca\Lambda - \frac{i}{2(1+\Lambda)}\Gamma_{w1}. \tag{5.75}$$

Given the second of conditions (5.13) and since Λ is always greater than zero, the imaginary part of the wave speed is always negative and the flow is found to be stable for all values of the parameters. We note that since there is no longer a physical length scale in the vertical direction, the wave speed is independent of k. In addition, c is independent of ${C_1}^{(1)}(\alpha)$ and so, solving equations (5.21), (5.22) and (5.30) and letting $y = \alpha$, we now obtain an explicit rather than implicit equation for ${C_1}^{(1)}(\alpha)$.

The stability of the solution is also found to be independent of the base-state flow. We therefore ignore the pressure gradient (let $Ca \to 0$) and let $k \gg h_2$ (whilst fixing α) in our previous solution for c, (5.29), to compare to the unbounded case. We take the latter limit since in the dimensional solution the wavenumber always appears in the grouping kh_2, and so taking the walls to infinity can be achieved by letting $kh_2 \to \infty$ whilst fixing h_1 and h_2. We find good graphical evidence that the resulting growth rate, c_I, is also given by the term multiplying i in (5.75). In addition, a large k analysis reveals that the two expressions for the imaginary part of c are identical if $O({C_1}^{(1)}(\alpha)) < \exp(2k\alpha)/k$, with plots of ${C_1}^{(1)}(\alpha)$ clearly showing a lack of exponential behaviour for large k. This suggests that the presence of walls is necessary for instability.

Returning to the case without walls, in the limit $Ca \to 0$ we find that since the streamline cells described previously are no longer constrained, the interface is now always restrained from growing by its position on the closed streamlines (when Γ_w and $\hat{C}$ are the same sign, the interface always sits at the top half of the cells as in figure 5.8c, whilst when Γ_w and $\hat{C}$ are opposite signs, the interface always sits at the bottom half of the cells), suggesting a possible reason for the lack of unstable solutions in this case. The importance of walls for an unstable solution has been noted previously by Pozrikidis and Hill (2011) when considering the linear stability of simple shear driven Stokes flow of two fluids in the presence of an insoluble surfactant at the interface. They commented that a reflected flow propagates from the wall(s) which may act to intensify waves at the interface. However, since a base flow is not required for unstable solutions in our case, our instability differs from a surfactant based instability such as theirs and in fact bears more resemblance to a thermocapillary instability such as that found in the work of Zeren and Reynolds (1972) and subsequent work.

5.5 Discussion

We have considered the linear stability of two-fluid channel flow under the influence of a solute concentration which is linearly proportional (to within a constant) to the surface tension coefficient.

We have focussed on two cases. In case (i) the pressure gradient was taken to be zero and in case (ii) it was taken to be non-zero. In case (i) a fully analytical solution is possible, but requires the solution of an implicit equation using the secant method. A single solution of interest is found for the wave speed, which is purely imaginary. This solution takes one of two forms. In the first the solution is unstable for small wavenumber disturbances and stable for large wavenumbers, whilst in the second the solution is always stable. The depth ratio, α, and viscosity ratio, Λ, are found to be fundamental in defining the regions of stability, whilst the signs of the concentration ratio and surface tension gradient are instrumental in determining which of the two forms the solution takes in each region. In the limit of zero surface tension or concentration gradient the first solution becomes stable for all wavenumbers. The same is true as the Péclet number in either fluid tends to zero or infinity, or in the case where the two Péclet numbers are equal and both tend to infinity. Streamlines are found to be closed cells, each separated by vertical lines on which the streamfunction is zero. We conjecture that the instability is a result of the interface sitting in a favourable vertical position on these cells, such that perturbations are free to grow under the influence of the Marangoni force.

In case (ii) the solution may be obtained through the use of the shooting method. Again, a single solution of interest is found for the wave speed, which is now complex. The stability regions are the same as those in case (i). The real part of the wave speed is found to take one of six forms. In all cases it tends to the speed of the base-state horizontal velocity at the interface for large wavenumbers. For other wavenumbers the real wave speed may be greater or less than the base-state velocity, depending on the choice of parameters. In particular we have plotted the regions in (α, Λ)-space that govern the real wave speed of small wavenumber disturbances. It is found that one of the defining curves matches the curve defining the stability regions, suggesting that the conjectured mechanism for instability may also affect the speed that waves travel.

We find that the presence of the channel walls is necessary for an unstable solution and compare our work to Pozrikidis and Hill (2011), who drew the same conclusion in the case of shear driven Stokes flow of two fluids with surfactant at the interface. We suggest that when the walls are removed, the interface is always restricted from growing due to its position on the closed streamlines.

Throughout this chapter, we find that in general, the magnitudes reached by c_I and the deviation of c_R from the base-state velocity are fairly small. However, this is simply due to our chosen length and time scales. Changing theses scales, by choosing a length scale based on the distance over which the surface tension changes by one unit, for instance, would not alter the results qualitatively, but would simply change the numerical scalings multiplying them. Blyth and Pozrikidis (2004) consider the stability of two fluid Stokes flow in an inclined channel under the influence of an insoluble surfactant at the fluid interface. It is interesting to compare our results to the work in this paper, in which the wave growth rate is of a similar magnitude. Similarly to in our work, unstable modes are found for small wavenumbers. Considering a long wavelength analysis, Blyth and Pozrikidis (2004) find that when both layers have the same width, the channel inclination is zero and the viscosity ratio is 0.5, the flow is very close to being neutrally stable for small wavenumbers, in agreement with our results. They also find that increasing the viscosity ratio can be stabilising, as we have found when Γ and $\hat{C}$ are of opposite signs.

Our solutions also agree with the findings of other workers in the field of surface tension driven flow, such as Scriven and Sternling (1964), Busse (1982), Renardy and Joseph (1985), Frenkel and Halpern (2002) and Halpern and Frenkel (2003). Here, where surface tension effects are destabilising, it is found to be for long wavelengths, with the solution found to be always stable for shorter wavelengths. Changes in the viscosity ratio, channel geometry and direction of surface tension gradient are also found have great influence on the limits of stability, in agreement with our results.

In the next chapter we consider the more general case of Navier–Stokes flow through a diverging channel with periodically moving walls.

Chapter 6

A Slowly Diverging Channel with Oscillating Walls

6.1 Introduction

In this chapter we relax the assumption that our model only describes the flow very close to one of the walls of the DGM body and take some time to consider a slightly more general flow field. Here we limit our study to a single fluid. By taking into account the two-dimensional flow field surrounding the region considered in previous chapters, we may gauge its influence on this region. Such an understanding of the flow field is useful when describing the base-state flow field or solute concentration field in a more realistic version of the previous chapters.

We briefly consider some general, preliminary results using a two-dimensional, plane polar co-ordinate system, (r, θ), where $\mathbf{u}(r, \theta, t) = (u_r, u_\theta)$ denotes the velocity field (in radial and transverse components) and $p(r, \theta, t)$ the pressure. In this case, the streamfunction, $\psi(r, \theta, t)$, is defined by

$$u_r = \frac{1}{r}\frac{\partial \psi}{\partial \theta}, \quad u_\theta = -\frac{\partial \psi}{\partial r}. \tag{6.1}$$

Here we consider a very simple representation of the elastic cone constituting the DGM body in order to gain an (extremely primitive) idea of the overall flow field.

Considering the conical shape of the DGM body, the problem of two semi-infinite, hinged plates, as described by Moffatt and Duffy (1980), appears to be a good starting point for our studies. Here a single fluid fills the space between two plates at $\theta = \pm\alpha(t)$, $0 < \alpha < \pi/2$, which move with angular speed $d\alpha/dt$. Due to the absence of a length scale in the radial direction, the streamfunction may be obtained by seeking a similarity solution to the biharmonic equation, (1.5), in plane polar co-ordinates. This yields the solution

$$\psi = -\frac{1}{2}\frac{d\alpha}{dt}r^2\frac{\sin(2\theta) - 2\theta\cos(2\alpha)}{\sin(2\alpha) - 2\alpha\cos(2\alpha)}. \tag{6.2}$$

Allowing each of the plates to oscillate about a constant mean position, figure 6.1a shows a typical plot of the resulting streamlines in the (x,y) plane. Typical particle paths (which differ from the streamlines since the flow is unsteady) are shown in figure 6.1b. These paths are self-similar in the radial direction. For small plate oscillations fluid particles move back and forth on straight lines. For larger oscillations the trajectories generally become curved. Particles are projected in the x-direction at increasing speeds as they near the line $\theta = 0$. Given that α is periodic in time, the position of the particles can also be shown to vary periodically with time. However, the solution is always time-periodic, implying that fluid mixing does not occur.

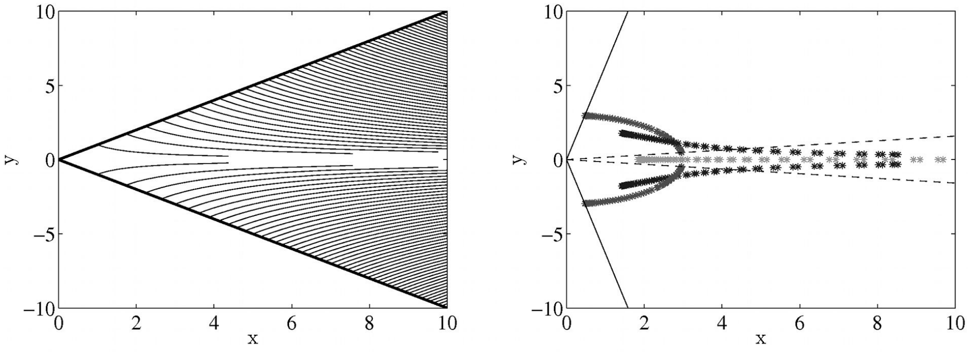

(a) (b)

Figure 6.1: For the case of the two hinged plates described by Moffatt and Duffy (1980), typical plots of (a) the streamlines (thin lines) between the plates (thick lines) and (b) the particle paths, where each fluid particle's progress is saved as the plates move and the walls are plotted when α is at its largest (solid line) and smallest (dashed line).

We may build on this model by allowing the two plates to move independently of each other, so that the problem is now asymmetric about the x-axis and the upper and lower plates are located at $\theta = \alpha^+(t)$ and $\theta = \alpha^-(t)$, respectively. However, by making the transformation

$$\hat{\theta} = \theta - \frac{1}{2}\left(\alpha^+ - \alpha^-\right), \quad \alpha = \frac{1}{2}\left(\alpha^+ + \alpha^-\right), \quad \hat{\psi} = \psi + \frac{1}{4}r^2\left(\frac{d\alpha^+}{dt} - \frac{d\alpha^-}{dt}\right), \tag{6.3}$$

we may recover the solution for symmetric hinged plates, with the streamfunction given by $\hat{\psi}$ and the angular co-ordinate by $\hat{\theta}$. This implies that the asymmetric and symmetric hinged plate solutions differ only by a time-dependent, solid body rotation. Therefore, although the asymmetric hinged plate problem allows for some interesting motions (by allowing the plates to move in a superposition of independent motions, fluid particles may travel in closed orbits, for example), it does not allow fluid mixing to occur.

A key limitation of the hinged-plates model, therefore, is that fluid mixing does not occur in any form. It may seem contradictory to expect mixing in time-reversible Stokes flow in the absence of a fluid interface, for example. However, there are ways to induce mixing of fluid particles by imposing a certain geometry. The use of non-reciprocal motions, for example, can be effective. An interesting example of this can be seen in Cartwright *et al.* (2012), in which non-reciprocal movements of eccentric cylinders can mix a fluid even though the final positions of the cylinders coincide with their initial positions.

It may be possible to induce fluid mixing in our problem by considering the addition of a semi-circular free surface at $r = R(t)$, where R changes with time such that the enclosed sector area is conserved. However, reconciling the resulting boundary conditions on the plates with those on the free surface is far from trivial. In the radial direction the no-slip boundary condition on the plates and the condition arising from a moving free surface lead to a discontinuity at the intersection between the two, whilst in the θ-direction, the boundary condition on the moving plates renders the condition on the free surface obsolete. In order to make sense of the discontinuity in boundary conditions, it would be necessary either to consider the problem on a microscopic level or to treat the discontinuity as a singularity (since the velocity gradient must be infinite here). Hills (2001) considered Stokes flow in a fixed corner with a scraping circular boundary (or honing circular arc) and overcame the resulting discontinuity by satisfying the boundary conditions on the walls before discretising the problem and attempting to approximate numerically the boundary conditions on the arc as closely as possible. However, this method relies on the existence of an analytic streamfunction, which cannot be counted upon in our problem. Another possibility is to allow the plates to stretch such that the radial velocity on each of them is proportional to r. However, the application of such a method is far from straightforward.

Inspired by the work of Lugt and Schwiderski (1964) and in an effort to include some element of fluid flow at the walls of the model, we consider a steady solution to the biharmonic equation, (1.5), in plane polar co-ordinates of the form

$$\psi = r^{\lambda} \left(A \sin(\lambda\theta) + B \sin((\lambda - 2)\theta) \right), \tag{6.4}$$

where A, B and λ are complex constants and it is understood that we take the real part of ψ for our solution. By taking λ to have both a real and imaginary part and imposing the boundary conditions $u_r = 0$ and $u_\theta = u_{\tilde{\theta}}$ on the walls $\theta = \pm\tilde{\theta}$, we may describe the problem of a steady sinusoidal velocity flux across fixed hinged plates. Here $u_{\tilde{\theta}} = -\partial\psi/\partial r(\theta = \tilde{\theta})$ is determined by our choice of λ and $\tilde{\theta}$. This is effectively the same problem as that of plates which move with a wave-like motion, but is much simpler to implement. Some typical streamlines in the (r, θ) plane are given in figure 6.2 as well as a visualisation of these streamlines in the (x, y) plane. We note that it is not possible to replace any of the streamlines of constant r with a free surface since they do not satisfy the stress condition, (1.21), in polar co-ordinates. Therefore this solution is no help in overcoming the above mentioned problems when adding a free surface to the hinged plates problem. Interestingly, the flux into one of the "cells" (whose boundary is the x axis, one of the two plates and two of the streamlines of constant r) is given

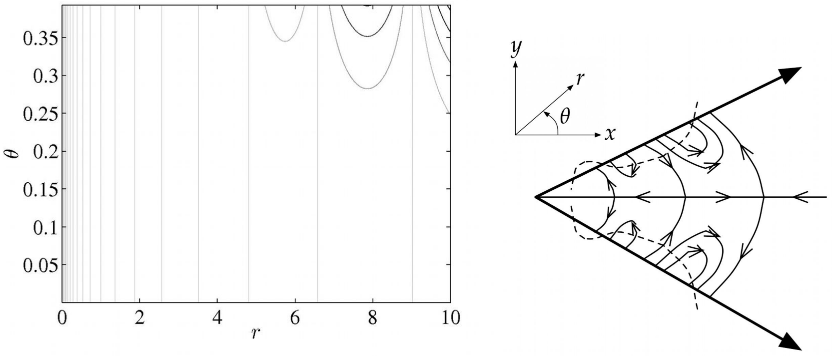

(a) (b)

Figure 6.2: For the case of a sinusoidal velocity flux across two fixed hinged plates, (a) typical plots of the streamlines in the (r, θ) plane and (b) a representation of these streamlines in the (x, y) plane. In (a) we choose $\lambda = 2 + 10i$ and $\tilde{\theta} = \pi/8$ and find that $A = 0$ and $B = 1/(10 \sinh(10\pi/8))$.

solely by the flux across the relevant portion of the plate. It can be shown that the flux into such a cell is zero and hence the total flux along the wall is also zero.

Given the complexity of considering a relevant problem in polar co-ordinates, we again consider a Cartesian co-ordinate system. We also extend our analysis to include general Reynolds numbers in order to investigate any inertia-related instabilities due to the moving walls. We consider an extension to the problem of channel flow with periodically moving walls, as studied by Hall and Papageorgiou (1999). Here the authors consider a stagnation-point type solution to the full Navier–Stokes equations. In our model we let the channel walls have a small slope, so that we are dealing with an oscillating, diverging channel. We seek a similarity solution, so that any end effects are not accounted for. Therefore, the diverging channel can be thought of as modelling the local flow field in a small strip taken at some point through the middle of the DGM main body.

6.2 Problem Description

We consider general-Reynolds-number flow in a gradually diverging channel with periodically oscillating walls at $y^* = \pm H^*(x^*, t^*)$. Here starred variables are dimensional variables with a non-dimensional counterpart. We define H^* by assuming a small perturbation (denoted by the superscript (1)) to the base-state of oscillating, parallel walls, $y^* = \pm {H^{(0)}}^*(t^*)$, (denoted by superscript (0)). This base-state is essentially equivalent to the problem described by Hall and Papageorgiou (1999). In the work of Hall and Papageorgiou (1999), however, the frame of reference is taken to sit at the bottom wall, whilst here it is taken to lie at the centre of the channel. Letting non-starred variables be non-dimensional, we write

$$H^* = hH^{(0)}(t) + \delta x H^{(1)}(t), \tag{6.5}$$

where h is the time-average width of the channel in the base-state, δ is the slope of the upper wall (as shown in figure 6.3), such that $0 < \delta \ll 1$, and $H^{(0)}$ and $H^{(1)}$ are of $O(1)$. Terms of $O(\delta^2)$ and smaller are neglected from the wall description. As usual, we introduce the streamfunction, $\psi^*(x^*, y^*, t^*)$, which satisfies the incompressibility condition, as well as the velocity field $\mathbf{u}^*(x^*, y^*, t^*) = (u^*, v^*)$ and pressure, $p^*(x^*, y^*, t^*)$. The solution for ψ^* and p^* is described by the base-state solution plus a small perturbation, such that

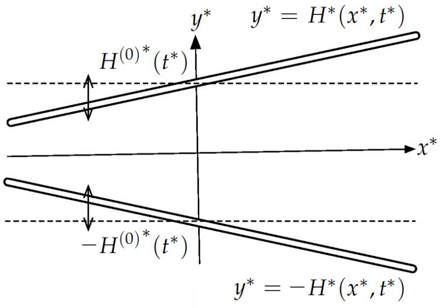

Figure 6.3: Schematic diagram of flow in a diverging channel with a periodic wall motion. The unperturbed, flat wall position is $y^* = \pm H^{(0)^*}(t^*)$.

$$\begin{aligned}
(\psi^*, p^*) &= \left(h^2\omega x \psi^{(0)}(y,t), \mu\omega p^{(0)}(x,y,t)\right) + \delta\left(h^2\omega\psi^{(1)}(x,y,t), \mu\omega p^{(1)}(x,y,t)\right),\\
p^{(0)} &= \frac{x^2}{2}{p_1}^{(0)}(t) + {p_2}^{(0)}(y,t), \quad \psi^{(1)} = x^2{\psi_1}^{(1)}(y,t) + {\psi_2}^{(1)}(y,t),\\
p^{(1)} &= \frac{x^3}{3}{p_1}^{(1)}(t) + x{p_2}^{(1)}(y,t) + {p_3}^{(1)}(t),
\end{aligned} \tag{6.6}$$

where ω is the frequency of the wall oscillations and μ is the dynamic viscosity of the fluid. Here the particular forms of the pressure and the $O(\delta)$ streamfunction are chosen in order to satisfy the governing equations and boundary conditions.

We satisfy the Navier–Stokes equations for general fluid flow (neglecting any body forces). These are given by the two-dimensional form of the first of equations (1.2). Differentiating the first component with respect to y^* and subtracting the second differentiated with respect to x^*, we may eliminate the pressure. We then obtain the vorticity equation,

$$\frac{\partial \Psi^*}{\partial t^*} + \frac{\partial \psi^*}{\partial y^*}\frac{\partial \Psi^*}{\partial x^*} - \frac{\partial \psi^*}{\partial x^*}\frac{\partial \Psi^*}{\partial y^*} = \nu\nabla^{*2}\Psi^*, \quad \Psi^* = \nabla^{*2}\psi^* = \frac{\partial \psi^*}{\partial x^{*2}} + \frac{\partial^2 \psi^*}{\partial y^{*2}}, \tag{6.7}$$

where ν is the kinematic viscosity of the fluid.

Substituting the streamfunction from (6.6) into equation (6.7) and considering the leading-order terms and the terms multiplied by δx^2, we obtain equations for $\psi^{(0)}$ and ${\psi_1}^{(1)}$ respectively,

$$\frac{\partial^3 \psi^{(0)}}{\partial t \partial y^2} + \frac{\partial \psi^{(0)}}{\partial y}\frac{\partial^2 \psi^{(0)}}{\partial y^2} - \psi^{(0)}\frac{\partial^3 \psi^{(0)}}{\partial y^3} = \frac{1}{Re}\frac{\partial^4 \psi^{(0)}}{\partial y^4}, \tag{6.8}$$

and

$$\frac{\partial^3 {\psi_1}^{(1)}}{\partial t \partial y^2} + 2\frac{\partial \psi^{(0)}}{\partial y}\frac{\partial^2 {\psi_1}^{(1)}}{\partial y^2} + \frac{\partial {\psi_1}^{(1)}}{\partial y}\frac{\partial^2 \psi^{(0)}}{\partial y^2} - \psi^{(0)}\frac{\partial^3 {\psi_1}^{(1)}}{\partial y^3} - 2{\psi_1}^{(1)}\frac{\partial^3 \psi^{(0)}}{\partial y^3} = \frac{1}{Re}\frac{\partial^4 {\psi_1}^{(1)}}{\partial y^4}, \tag{6.9}$$

where the Reynolds number,

$$Re = \frac{h^2 \omega}{\nu}. \tag{6.10}$$

In Hall and Papageorgiou (1999) the streamfunction is defined as $nbx(V(\eta, t) - dH/dt)$, where $\eta = y/(bH) - 1$, $t = nt^*$ and the walls are situated at $y = 0,\ 2bH(t)$. Our equation (6.8) is equivalent to their equation for $V(\eta, t)$.

Since ${\psi_2}^{(1)}$ itself is not needed for our solution, we may simply solve for ${\hat{\psi}_2}^{(1)} \equiv \partial {\psi_2}^{(1)}/\partial y$. We find ${\hat{\psi}_2}^{(1)}$ from the Navier–Stokes equations, which are given by the first of (1.2). Substituting the streamfunction and pressure from (6.6) into these equations, the terms multiplied by δx and δx^0 give us equations to find ${p_2}^{(1)}$ in terms of ${\psi_1}^{(1)}$ and ${\hat{\psi}_2}^{(1)}$ in terms of ${p_2}^{(1)}$ respectively,

$$-2\frac{\partial {\psi_1}^{(1)}}{\partial t} + 2\psi^{(0)}\frac{\partial {\psi_1}^{(1)}}{\partial y} = -\frac{1}{Re}\left(\frac{\partial {p_2}^{(1)}}{\partial y} + 2\frac{\partial^2 {\psi_1}^{(1)}}{\partial y^2}\right), \tag{6.11}$$

$$\frac{\partial^2 {\hat{\psi}_2}^{(1)}}{\partial t} + \frac{\partial \psi^{(0)}}{\partial y}{\hat{\psi}_2}^{(1)} - \psi^{(0)}\frac{\partial^2 {\hat{\psi}_2}^{(1)}}{\partial y} = \frac{1}{Re}\left(-{p_2}^{(1)} + 2\frac{\partial {\psi_1}^{(1)}}{\partial y} + \frac{\partial^3 {\hat{\psi}_2}^{(1)}}{\partial y^2}\right). \tag{6.12}$$

By considering the other terms of the Navier-Stokes equations, we may obtain further equations from which we may fully determine the pressure. However, these equations are not needed for our analysis.

The above equations are complemented by boundary conditions at the walls. Considering the kinematic condition at the moving walls, (1.9), the leading-order and $O(\delta)$ terms respectively give us

$$\left(\psi^{(0)}\right)_{y=\pm H^{(0)}} = \mp\frac{dH^{(0)}}{dt}, \tag{6.13}$$

$$\left({\psi_1}^{(1)}\right)_{y=\pm H^{(0)}} = \mp\frac{1}{2}\frac{dH^{(1)}}{dt}. \tag{6.14}$$

Here we have used the no-slip condition, (1.14), which gives us, considering terms multiplied by 1, δx^2 and δx^0 respectively,

$$\left(\frac{\partial \psi^{(0)}}{\partial y}\right)_{y=\pm H^{(0)}} = 0, \tag{6.15}$$

$$\left(\frac{\partial {\psi_1}^{(1)}}{\partial y} \pm H^{(1)} \frac{\partial^2 \psi^{(0)}}{\partial y^2}\right)_{y=\pm H^{(0)}} = 0, \tag{6.16}$$

$$\left(\hat{\psi_2}^{(1)}\right)_{y=\pm H^{(0)}} = -H^{(1)} \frac{dH^{(0)}}{dt}. \tag{6.17}$$

Lastly, we choose to take

$$\left({p_2}^{(1)}\right)_{y=-H^{(0)}} = 0. \tag{6.18}$$

We note that it is these boundary conditions that dictate our choice of the $O(\delta)$ streamfunction. Replacing $x^2{\psi_1}^{(1)}(y,t)$ in (6.6) by $x{\psi_1}^{(1)}(y,t)$ or $x^n{\psi_1}^{(1)}(y,t)$ for $3 < n \in \mathbb{N}$ would satisfy (6.7), but would only satisfy the kinematic condition if the $O(\delta)$ wall description had a different x dependence. We note that the x-dependencies required are as expected; whilst for the symmetric $O(1)$ channel, we expect that the horizontal velocity will be odd in x (squeezed away from the centre in both directions), we would expect that the asymmetric $O(\delta)$ correction is even (unidirectionally squeezed). The no-slip condition necessitates the inclusion of ${\psi_2}^{(1)}$.

6.3 The Solution at Zero Reynolds Number

In the zero Reynolds number limit it is possible to obtain an analytical solution. Solving equations (6.8), (6.9), (6.11) and (6.12) subject to boundary conditions (6.13) to (6.18) in this limit gives us

$$\psi^{(0)} = \frac{3}{2{H^{(0)}}^3} \frac{dH^{(0)}}{dt} \left(\frac{y^2}{3} - {H^{(0)}}^2\right) y, \tag{6.19}$$

$${\psi_1}^{(1)} = \frac{3}{4{H^{(0)}}^3} \frac{dH^{(1)}}{dt} \left(\frac{y^2}{3} - {H^{(0)}}^2\right) y - \frac{3H^{(1)}}{2{H^{(0)}}^4} \frac{dH^{(0)}}{dt} \left(y^2 - {H^{(0)}}^2\right) y. \tag{6.20}$$

$$\begin{aligned}\hat{\psi_2}^{(1)} = &-\frac{1}{4{H^{(0)}}^3} \frac{dH^{(1)}}{dt} \left(y^2 - {H^{(0)}}^2\right)\left(y^2 - 5{H^{(0)}}^2\right) \\ &+ \frac{3H^{(1)}}{2{H^{(0)}}^4} \frac{dH^{(0)}}{dt} \left(y^4 - 4{H^{(0)}}^2 y^2 - {H^{(0)}}^4\right).\end{aligned} \tag{6.21}$$

To leading order, this solution agrees with Hall and Papageorgiou (1999) and so, as mentioned in their paper, in the horizontal direction the velocity locally takes the form of Poiseuille flow modulated periodically in time. We might expect to be able to draw a similar comparison at $O(\delta)$.

To derive the solution for steady Poiseuille flow in a slowly diverging channel we write

$$(H,u,v,p) = \left(H^{(0)}, u^{(0)}(y), 0, p^{(0)}(x)\right) \\ + \delta\left(xH^{(1)}, \frac{\partial f^{(1)}}{\partial y}(x,y), -\frac{\partial f^{(1)}}{\partial x}(x,y), p^{(1)}(x,y)\right), \tag{6.22}$$

where

$$f^{(1)} = x{f_1}^{(1)}(y) + {f_2}^{(1)}(y), \quad p^{(1)} = \frac{x^2}{2}{p_1}^{(1)} + x{p_2}^{(1)}, + {p_3}^{(1)}(y), \tag{6.23}$$

and $H^{(0)}$, $H^{(1)}$, ${p_1}^{(1)}$ and ${p_2}^{(1)}$ are constants. This satisfies the incompressibility condition given by the non-dimensional version of the second of equations (1.3). Again, the forms of the pressure and $O(\delta)$ velocities are chosen in order to satisfy the governing equations and boundary conditions. It is not strictly necessary to include ${f_2}^{(1)}$, but we do so in order to compare with our above solution. Its inclusion necessitates the inclusion of ${p_2}^{(1)}$. We can think of ${f_2}^{(1)}$ as a superimposed flow, as noted in Secomb (1978), who considered a similar problem. We again solve for $\hat{f_2}^{(1)} \equiv d{f_2}^{(1)}/dy$ since ${f_2}^{(1)}$ itself does not appear in our solution. In the limit of Stokes flow the Navier–Stokes equations reduce to the non-dimensional version of the first of (1.3). Substituting (6.22) into these equations and considering leading-order terms, terms multiplied by δx and terms multiplied by δx^0, respectively, we find equations for $u^{(0)}$, ${f_1}^{(1)}$ and $\hat{f_2}^{(1)}$,

$$\frac{d^2u^{(0)}}{dy^2} = \frac{dp^{(0)}}{dx}, \tag{6.24}$$

$$\frac{d^3{f_1}^{(1)}}{dy^3} = {p_1}^{(1)}, \tag{6.25}$$

$$\frac{d^2\hat{f_2}^{(1)}}{dy^2} = {p_2}^{(1)}. \tag{6.26}$$

Linearising the non-dimensional form of the kinematic condition (1.9), we now obtain

$$\left({f_1}^{(1)} \pm H^{(1)}u^{(0)}\right)_{y=\pm H^{(0)}} = 0, \tag{6.27}$$

whilst the no-slip condition (1.14) gives us, considering leading-order terms, terms multiplied by δx and terms multiplied by δx^0, respectively,

$$\left(u^{(0)}\right)_{y=\pm H^{(0)}} = 0, \tag{6.28}$$

$$\left(\frac{d{f_1}^{(1)}}{dy} \pm H^{(1)}\frac{du^{(0)}}{dy}\right)_{y=\pm H^{(0)}} = 0, \tag{6.29}$$

$$\left(\hat{f_2}^{(1)}\right)_{y=\pm H^{(0)}} = 0. \tag{6.30}$$

We note that both sides of equation (6.24) must be constant. Denoting the dimensional pressure gradient, $dp^{(0)^*}/dx^*$, by $-G$ results in the non-dimensional pressure gradient,

$$\hat{G} = \frac{Gh}{\mu\omega}. \tag{6.31}$$

Then, solving equations (6.24) to (6.26) subject to conditions (6.27) to (6.30), we obtain the solution,

$$u^{(0)} = -\frac{\hat{G}}{2}\left(y^2 - H^{(0)^2}\right), \tag{6.32}$$

$$f_1{}^{(1)} = \frac{\hat{G}H^{(1)}}{2H^{(0)}}y\left(y^2 - H^{(0)^2}\right), \tag{6.33}$$

$$\hat{f_2}^{(1)} = \frac{p_2{}^{(1)}}{2}\left(y^2 - H^{(0)^2}\right). \tag{6.34}$$

Here if we again choose to take $p_2{}^{(1)} = 0$ at $y = -H^{(0)}$ then we find that $p_2{}^{(1)}$, and hence $\hat{f_2}^{(1)}$, is zero for all y.

Now that we have completed the analysis, we compare this solution to our small Reynolds number limit solution, (6.19) to (6.21). Taking $H^{(1)}$ to be independent of t, we conclude that in this limit, the $O(\delta)$ horizontal velocity essentially takes the local form of Poiseuille flow in a diverging channel modulated periodically in time. Due to the fact that the $O(1)$ vertical velocity is not zero and the $O(1)$ horizontal velocity depends on x^2, however, there is an extra term in $\hat{\psi_2}^{(1)}$ that does not appear in $\hat{f_2}^{(1)}$ and $\hat{\psi_2}^{(1)} \neq 0$ for all y.

6.4 Numerical Method for Arbitrary Reynolds Number

In order to solve the full system (6.8), (6.9) and (6.11) to (6.18), we must seek a numerical solution. We use the numerical scheme described by Blyth *et al.* (2003), which is based on a method of E and Liu (1996). This scheme introduces the non-dimensional vorticity, $\Omega\hat{\mathbf{k}} = \nabla \times \mathbf{u}$, where $\hat{\mathbf{k}}$ is the unit vector pointing in the direction perpendicular to the $x - y$ plane, and uses a fourth-order Runge–Kutta method to integrate the equations of motion with respect to time and a second-order central difference method for representing derivatives with respect to the vertical co-ordinate. To implement this scheme, we re-scale, similarly to Hall and Papageorgiou (1999), such that our domain becomes the region between fixed flat walls. This is done by making the transformation

$$\eta = \frac{y}{H(X,t)}. \tag{6.35}$$

We let the vorticity be written in the form

$$\Omega = x\Omega^{(0)}(\eta,t) + \delta\left(x^2\Omega_1{}^{(1)}(\eta,t) + \Omega_2{}^{(1)}(\eta,t)\right), \tag{6.36}$$

so that, defining the operator $L \equiv \partial/\partial\eta$,

$$\begin{aligned}
L^2\psi^{(0)} &= -{H^{(0)}}^2\Omega^{(0)}, && (6.37)\\
L^2{\psi_1}^{(1)} &= -2H^{(0)}H^{(1)}\Omega^{(0)} - {H^{(0)}}^2{\Omega_1}^{(1)}, && (6.38)\\
{\Omega_2}^{(1)} &= -2{\psi_1}^{(1)} - \frac{1}{H^{(0)}}L{\hat{\psi}_2}^{(1)}. && (6.39)
\end{aligned}$$

We choose to focus on the case where $H^{(1)}$ is a (prescribed) constant (the walls oscillate, but have a fixed slope) and, like Hall and Papageorgiou (1999), we let

$$H^{(0)} = 1 + \Delta\cos(2t), \quad 0 < \Delta < 1. \tag{6.40}$$

In this case, considering the leading-order terms and terms multiplied by δx^2 in the vorticity equation, (6.7), gives us

$$\begin{aligned}
\frac{\partial\Omega^{(0)}}{\partial t} =& M^{(0)}(t, \psi^{(0)}, \Omega^{(0)}; Re),\\
M^{(0)} =& \frac{1}{Re{H^{(0)}}^2}\frac{\partial^2\Omega^{(0)}}{\partial\eta^2} - \frac{1}{H^{(0)}}\left(-\left(\frac{dH^{(0)}}{dt}\eta + \psi^{(0)}\right)\frac{\partial\Omega^{(0)}}{\partial\eta} + \frac{\partial\psi^{(0)}}{\partial\eta}\Omega^{(0)}\right),
\end{aligned} \tag{6.41}$$

and

$$\begin{aligned}
\frac{\partial{\Omega_1}^{(1)}}{\partial t} =& {M_1}^{(1)}(t, \psi^{(0)}, {\psi_1}^{(1)}, \Omega^{(0)}, {\Omega_1}^{(1)}; Re),\\
{M_1}^{(1)} =& \frac{1}{Re{H^{(0)}}^2}\left(\frac{\partial^2{\Omega_1}^{(1)}}{\partial\eta^2} - \frac{2H^{(1)}}{H^{(0)}}\frac{\partial^2\Omega^{(0)}}{\partial\eta^2}\right)\\
& - \frac{1}{H^{(0)}}\Bigg(-\left(\frac{dH^{(0)}}{dt}\eta + \psi^{(0)}\right)\left(\frac{\partial{\Omega_1}^{(1)}}{\partial\eta} - \frac{H^{(1)}}{H^{(0)}}\frac{\partial\Omega^{(0)}}{\partial\eta}\right)\\
& \qquad + \frac{\partial\psi^{(0)}}{\partial\eta}\left(2{\Omega_1}^{(1)} + \frac{H^{(1)}}{H^{(0)}}\Omega^{(0)}\right) + \frac{\partial{\psi_1}^{(1)}}{\partial\eta}\Omega^{(0)} - 2{\psi_1}^{(1)}\frac{\partial\Omega^{(0)}}{\partial\eta}\Bigg).
\end{aligned} \tag{6.42}$$

Considering terms multiplied by δx^0, the Navier–Stokes equations (given by the first of (1.2)) give us

$$\begin{aligned}
\frac{\partial{\hat{\psi}_2}^{(1)}}{\partial t} =& {M_2}^{(1)}(t, \psi^{(0)}, {\psi_1}^{(1)}, {\hat{\psi}_2}^{(1)}, {p_2}^{(1)}; Re),\\
{M_2}^{(1)} =& \frac{1}{Re}\left(\frac{1}{H^{(0)}}\left(2\frac{\partial{\psi_1}^{(1)}}{\partial\eta} + \frac{1}{H^{(0)}}\frac{\partial^2{\hat{\psi}_2}^{(1)}}{\partial\eta^2}\right) - {p_2}^{(1)}\right)\\
& + \frac{1}{H^{(0)}}\left(\frac{\partial{\hat{\psi}_2}^{(1)}}{\partial\eta}\left(\frac{dH^{(0)}}{dt}\eta + \psi^{(0)}\right) - \frac{\partial\psi^{(0)}}{\partial\eta}{\hat{\psi}_2}^{(1)}\right).
\end{aligned} \tag{6.43}$$

From the terms multiplied by δx (substituting $\partial{p_2}^{(0)}/\partial\eta$ from the equations to leading order), we find that

$$\begin{aligned} L{p_2}^{(1)} =& {M_p}^{(1)}(t, \psi^{(0)}, {\psi_1}^{(1)}, \Omega^{(0)}, {\Omega_1}^{(1)}; Re), \\ {M_p}^{(1)} =& 2Re\left(H^{(1)}\frac{\partial \psi^{(0)}}{\partial t} + H^{(0)}\frac{\partial {\psi_1}^{(1)}}{\partial t} - \left(\frac{dH^{(0)}}{dt}\eta + \psi^{(0)}\right)\frac{\partial {\psi_1}^{(1)}}{\partial \eta}\right) \\ & + 2H^{(1)}\Omega^{(0)} + 2H^{(0)}{\Omega_1}^{(1)}, \end{aligned} \tag{6.44}$$

where integrating equations (6.37) and (6.38) with respect to t and using (6.41) and (6.42) gives us

$$\frac{\partial \psi^{(0)}}{\partial t} = L^{-2}\left(-2H^{(0)}\frac{dH^{(0)}}{dt}\Omega^{(0)} - {H^{(0)}}^2 M^{(0)}\right), \tag{6.45}$$

and

$$\frac{\partial {\psi_1}^{(1)}}{\partial t} = L^{-2}\left(-2\frac{dH^{(0)}}{dt}H^{(1)}\Omega^{(0)} - 2H^{(0)}H^{(1)}M^{(0)} - 2H^{(0)}\frac{dH^{(0)}}{dt}{\Omega_1}^{(1)} - {H^{(0)}}^2{M_1}^{(1)}\right). \tag{6.46}$$

From the leading-order and $O(\delta)$ terms of the kinematic boundary condition, (1.9), we find that

$$\psi^{(0)}(\eta = \pm 1, t) = \mp\frac{dH^{(0)}}{dt}, \tag{6.47}$$

$${\psi_1}^{(1)}(\eta = \pm 1, t) = 0, \tag{6.48}$$

whilst the leading-order terms, the terms multiplied by δx^2 and the terms multiplied by δx^0 in the no-slip condition, (1.14), give us

$$\frac{\partial \psi^{(0)}}{\partial \eta}(\eta = \pm 1, t) = 0, \tag{6.49}$$

$$\frac{\partial {\psi_1}^{(1)}}{\partial \eta}(\eta = \pm 1, t) = 0, \tag{6.50}$$

$${\hat{\psi}_2}^{(1)}(\eta = \pm 1, t) = -H^{(1)}\frac{dH^{(0)}}{dt}. \tag{6.51}$$

We also choose that

$${p_2}^{(1)}(\eta = -1, t) = 0. \tag{6.52}$$

Solving equations (6.41) to (6.44) subject to boundary conditions (6.47) to (6.51) in the zero Reynolds number limit now gives us

$$\begin{aligned}
\psi^{(0)} =& \frac{3}{2}\frac{dH^{(0)}}{dt}\left(\frac{\eta^2}{3}-1\right)\eta, && (6.53)\\
{\psi_1}^{(1)} =& 0, && (6.54)\\
\hat{\psi}_2{}^{(1)} =& \frac{H^{(1)}}{8}\frac{dH^{(0)}}{dt}\left(\eta^4-6\eta^2-3\right). && (6.55)
\end{aligned}$$

This solution may also be obtained by substituting equations (6.19) to (6.21) into (6.6), replacing y using (6.35) and considering the terms of various orders.

We now discretise our domain in the η direction. Letting the distance between grid points be $\Delta\eta = 2/(N-1)$, we define $\eta_i = (i-1)\Delta\eta - 1$, for $i = 1, \cdots, N$. This gives us N regularly spaced points where $\eta_1 = -1$ and $\eta_N = 1$ correspond to the lower and upper walls, respectively. Given a function, $f(\eta, t)$, the first and second derivatives with respect to η are represented by

$$\frac{\partial f}{\partial \eta} = \frac{f(\eta+\Delta\eta) - f(\eta-\Delta\eta)}{2\Delta\eta}, \quad \frac{\partial^2 f}{\partial \eta^2} = \frac{f(\eta+\Delta\eta) - 2f(\eta) + f(\eta-\Delta\eta)}{\Delta\eta^2}, \qquad (6.56)$$

discarding terms of $O(\Delta\eta^2)$ and smaller.

We use the notation $f^k(\eta) = f(\eta, t_k)$ at time t_k, where $k = 1, 2, 3, \cdots$ and our timesteps are taken to be of length Δt. For brevity we let

$$t_{n1} = t_n + \frac{\Delta t}{2}, \quad t_{n2} = t_n + \Delta t, \qquad (6.57)$$

and then, applying a fourth-order Runge–Kutta method to equations (6.37) and (6.41), we first obtain

$$\begin{aligned}
{\Omega^{(0)}}_1 &= {\Omega^{(0)}}^n + \frac{\Delta t}{2} M^{(0)}\left(t_n, {\psi^{(0)}}^n, {\Omega^{(0)}}^n\right), \quad {\psi^{(0)}}_1 = L^{-2}\left(-{H^{(0)}}^2\left(t_{n1}\right){\Omega^{(0)}}_1\right), && (6.58)\\
{\Omega^{(0)}}_2 &= {\Omega^{(0)}}^n + \frac{\Delta t}{2} M^{(0)}\left(t_{n1}, {\psi^{(0)}}_1, {\Omega^{(0)}}_1\right), \quad {\psi^{(0)}}_2 = L^{-2}\left(-{H^{(0)}}^2\left(t_{n1}\right){\Omega^{(0)}}_2\right), && (6.59)\\
{\Omega^{(0)}}_3 &= {\Omega^{(0)}}^n + \Delta t M^{(0)}\left(t_{n1}, {\psi^{(0)}}_2, {\Omega^{(0)}}_2\right), \quad {\psi^{(0)}}_3 = L^{-2}\left(-{H^{(0)}}^2\left(t_{n2}\right){\Omega^{(0)}}_3\right), && (6.60)\\
{k^{(0)}}_4 &= \Delta t M^{(0)}\left(t_{n2}, {\psi^{(0)}}_3, {\Omega^{(0)}}_3\right), && (6.61)
\end{aligned}$$

and then, given the solution at time t_n, the $O(1)$ solution at time t_{n+1} can be described by

$$\begin{aligned}
{\Omega^{(0)}}^{n+1} &= \frac{1}{3}\left(-{\Omega^{(0)}}^n + {\Omega^{(0)}}_1 + 2{\Omega^{(0)}}_2 + {\Omega^{(0)}}_3\right) + \frac{1}{6}{k^{(0)}}_4,\\
{\psi^{(0)}}^{n+1} &= L^{-2}\left(-{H^{(0)}}^2\left(t_{n2}\right){\Omega^{(0)}}^{n+1}\right). && (6.62)
\end{aligned}$$

For the $O(\delta)$ solution applying the Runge-Kutta method to equations (6.38) and (6.42) gives us

$$
\begin{aligned}
{\Omega_1^{(1)}}_1 &= {\Omega_1^{(1)}}^n + \frac{\Delta t}{2} M_1^{(1)}\left(t_n, {\psi^{(0)}}^n, {\psi_1^{(1)}}^n, {\Omega^{(0)}}^n, {\Omega_1^{(1)}}^n\right),\\
{\psi_1^{(1)}}_1 &= L^{-2}\left(-2H^{(0)}\left(t_{n1}\right)H^{(1)}{\Omega^{(0)}}_1 - {H^{(0)}}^2\left(t_{n1}\right){\Omega_1^{(1)}}_1\right), \qquad (6.63)\\
{\Omega_1^{(1)}}_2 &= {\Omega_1^{(1)}}^n + \frac{\Delta t}{2} M_1^{(1)}\left(t_{n1}, {\psi^{(0)}}_1, {\psi_1^{(1)}}_1, {\Omega^{(0)}}_1, {\Omega_1^{(1)}}_1\right),\\
{\psi_1^{(1)}}_2 &= L^{-2}\left(-2H^{(0)}\left(t_{n1}\right)H^{(1)}{\Omega^{(0)}}_2 - {H^{(0)}}^2\left(t_{n1}\right){\Omega_1^{(1)}}_2\right), \qquad (6.64)\\
{\Omega_1^{(1)}}_3 &= {\Omega_1^{(1)}}^n + \Delta t M_1^{(1)}\left(t_{n1}, {\psi^{(0)}}_2, {\psi_1^{(1)}}_2, {\Omega^{(0)}}_2, {\Omega_1^{(1)}}_2\right),\\
{\psi_1^{(1)}}_3 &= L^{-2}\left(-2H^{(0)}\left(t_{n2}\right)H^{(1)}{\Omega^{(0)}}_3 - {H^{(0)}}^2\left(t_{n2}\right){\Omega_1^{(1)}}_3\right), \qquad (6.65)\\
{k_1^{(1)}}_4 &= \Delta t M_1^{(1)}\left(t_{n2}, {\psi^{(0)}}_3, {\psi_1^{(1)}}_3, {\Omega^{(0)}}_3, {\Omega_1^{(1)}}_3\right), \qquad (6.66)
\end{aligned}
$$

and then

$$
\begin{aligned}
{\Omega_1^{(1)}}^{n+1} &= \frac{1}{3}\left(-{\Omega_1^{(1)}}^n + {\Omega_1^{(1)}}_1 + 2{\Omega_1^{(1)}}_2 + {\Omega_1^{(1)}}_3\right) + \frac{1}{6}{k_1^{(1)}}_4,\\
{\psi_1^{(1)}}^{n+1} &= L^{-2}\left(-2H^{(0)}\left(t_{n2}\right)H^{(1)}\Omega^{(0)n+1} - {H^{(0)}}^2\left(t_{n2}\right){\Omega_1^{(1)}}^{n+1}\right), \qquad (6.67)
\end{aligned}
$$

and applying to equations (6.43) and (6.44) gives us

$$
\begin{aligned}
{p_2^{(1)}}^n &= L^{-1}M_p^{(1)}\left(t_n, {\psi^{(0)}}^n, {\psi_1^{(1)}}^n, {\Omega^{(0)}}^n, {\Omega_1^{(1)}}^n\right),\\
{\hat{\psi}_2^{(1)}}_1 &= {\hat{\psi}_2^{(1)}}^n + \frac{\Delta t}{2} M_2^{(1)}\left(t_n, {\psi^{(0)}}^n, {\psi_1^{(1)}}^n, \hat{\psi}_2^{(1)n}, {p_2^{(1)}}^n\right), \qquad (6.68)\\
{p_2^{(1)}}_1 &= L^{-1}M_p^{(1)}\left(t_{n1}, {\psi^{(0)}}_1, {\psi_1^{(1)}}_1, {\Omega^{(0)}}_1, {\Omega_1^{(1)}}_1\right),\\
{\hat{\psi}_2^{(1)}}_2 &= {\hat{\psi}_2^{(1)}}^n + \frac{\Delta t}{2} M_2^{(1)}\left(t_{n1}, {\psi^{(0)}}_1, {\psi_1^{(1)}}_1, {\hat{\psi}_2^{(1)}}_1, {p_2^{(1)}}_1\right), \qquad (6.69)\\
{p_2^{(1)}}_2 &= L^{-1}M_p^{(1)}\left(t_{n1}, {\psi^{(0)}}_2, {\psi_1^{(1)}}_2, {\Omega^{(0)}}_2, {\Omega_1^{(1)}}_2\right),\\
{\hat{\psi}_2^{(1)}}_3 &= {\hat{\psi}_2^{(1)}}^n + \Delta t M_2^{(1)}\left(t_{n1}, {\psi^{(0)}}_2, {\psi_1^{(1)}}_2, {\hat{\psi}_2^{(1)}}_2, {p_2^{(1)}}_2\right), \qquad (6.70)\\
{p_2^{(1)}}_3 &= L^{-1}M_p^{(1)}\left(t_{n2}, {\psi^{(0)}}_3, {\psi_1^{(1)}}_3, {\Omega^{(0)}}_3, {\Omega_1^{(1)}}_3\right),\\
{k_2^{(1)}}_4 &= \Delta t M_2^{(1)}\left(t_{n2}, {\psi^{(0)}}_3, {\psi_1^{(1)}}_3, {\hat{\psi}_2^{(1)}}_3, {p_2^{(1)}}_3\right), \qquad (6.71)
\end{aligned}
$$

and then

$$
{\hat{\psi}_2^{(1)}}^{n+1} = \frac{1}{3}\left(-\hat{\psi}_2^{(1)n} + {\hat{\psi}_2^{(1)}}_1 + 2{\hat{\psi}_2^{(1)}}_2 + {\hat{\psi}_2^{(1)}}_3\right) + \frac{1}{6}{k_2^{(1)}}_4. \qquad (6.72)
$$

The initial conditions (the solution when $k = 1$) are chosen to be consistent with (6.37) to (6.39) and the boundary conditions, (6.47) to (6.51). We next consider the boundary conditions themselves at time t_k. For the leading order solution, from (6.47) and (6.49),

$$\psi^{(0)^k}(\eta_1) = -\psi^{(0)^k}(\eta_N) = \frac{dH^{(0)}}{dt}(t_k),$$
$$\psi^{(0)^k}(\eta_0) = \psi^{(0)^k}(\eta_2), \quad \psi^{(0)^k}(\eta_{N-1}) = \psi^{(0)^k}(\eta_{N+1}), \tag{6.73}$$

and for the $O(\delta)$ solution, from (6.48) and (6.50) to (6.52),

$$\psi_1{}^{(1)^k}(\eta_1) = \psi_1{}^{(1)^k}(\eta_N) = 0, \quad \psi_1{}^{(1)^k}(\eta_0) = \psi_1{}^{(1)^k}(\eta_2), \quad \psi_1{}^{(1)^k}(\eta_{N-1}) = \psi_1{}^{(1)^k}(\eta_{N+1}), \tag{6.74}$$

$$\hat{\psi}_2{}^{(1)^k}(\eta_1) = \hat{\psi}_2{}^{(1)^k}(\eta_N) = -H^{(1)}\frac{dH^{(0)}}{dt}(t_k), \tag{6.75}$$

$$p_2{}^{(1)^k}(\eta_1) = 0, \tag{6.76}$$

where we introduce fictitious points outside the domain at η_0 and η_{N+1}.

Performing the inversion, L^{-2}, in equations (6.58) to (6.67) involves solving a tridiagonal matrix system comprising of the uninverted equations for $i = 2, \cdots, N-1$ plus the first two of boundary conditions (6.73) or (6.74). This may be done using the Thomas algorithm (where we note that although the matrix is diagonally dominant, it is not strictly diagonally dominant and so we cannot prove that the Thomas algorithm will be stable, although in practice it is). At each timestep, four such tridiagonal systems for $\psi^{(0)}$ and four for $\psi_1{}^{(1)}$ must be solved.

The inversion, L^{-1}, in equations (6.68) to (6.72) may be achieved simply by using the trapezium rule. In general, using equation (6.44), we may write

$$p_2{}^{(1)^k}(\eta) = \int_{-1}^{\eta_{max}} M_p{}^{(1)^k}(\eta)d\eta, \quad -1 < \eta_{max} \leq 1, \tag{6.77}$$

and so we may integrate by writing

$$p_2{}^{(1)^k}(\eta_{i+1}) = p_2{}^{(1)^k}(\eta_i) + \frac{1}{2}\Delta\eta\left(M_p{}^{(1)^k}(\eta_i) + M_p{}^{(1)^k}(\eta_{i+1})\right), \quad i = 1, \cdots, N-1, \tag{6.78}$$

giving us an algorithm with which to calculate $p_2{}^{(1)}$ at every point in η given (6.76). Here we must make use of the second two of boundary conditions (6.74) when evaluating $M_p{}^{(1)}$ at η_1 and η_N. Also, in order to calculate $M_p{}^{(1)}$, we need to know $\partial\psi^{(0)}/\partial t$ and $\partial\psi_1{}^{(1)}/\partial t$ at $\eta_1, \cdots, \eta_N$. This can be achieved by performing the two inversions in equations (6.45) and (6.46). Here the uninverted equations for $i = 2, \cdots, N-1$, are supplemented by the first two of boundary conditions (6.73) and (6.74), differentiated with respect to time. We may again use the Thomas algorithm to invert the resulting system. At each time step, eight such tridiagonal systems must be solved. The equations for $\hat{\psi}_2{}^{(1)}$ in (6.68) to (6.72) when $i = 2, \cdots, N-1$ are complimented by boundary conditions (6.75), giving us the solution for $\hat{\psi}_2{}^{(1)}$ everywhere.

In the equations for the vorticities in (6.58) to (6.67), since $\Omega^{(0)}$ and ${\Omega_1}^{(1)}$ are not known at the fictitious points η_0 and η_{N+1}, it is only possible to take $i = 2, \cdots, N-1$, giving us the solution at $\eta_2, \cdots, \eta_{N-1}$. The vorticities at η_1 and η_N may be obtained from equations (6.37) and (6.38) applied when $i = 1$ and N, making use of boundary conditions (6.73) and (6.74). For instance, at time step t_k we have

$$\Omega^{(0)^k}(\eta_1) = -\frac{2}{\left(H^{(0)}(t_k)\,\Delta\eta\right)^2}\left(\psi^{(0)^k}(\eta_2) - \frac{dH^{(0)}}{dt}(t_k)\right), \tag{6.79}$$

$$\Omega^{(0)^k}(\eta_N) = -\frac{2}{\left(H^{(0)}(t_k)\,\Delta\eta\right)^2}\left(\psi^{(0)^k}(\eta_{N-1}) + \frac{dH^{(0)}}{dt}(t_k)\right), \tag{6.80}$$

$${\Omega_1}^{(1)^k}(\eta_1) = -\frac{2}{{H^{(0)}}^2(t_k)}\left(\frac{{\psi_1}^{(1)^k}(\eta_2)}{\Delta\eta^2} + H^{(0)}(t_k)\,H^{(1)}\Omega^{(0)^k}(\eta_1)\right), \tag{6.81}$$

$${\Omega_1}^{(1)^k}(\eta_N) = -\frac{2}{{H^{(0)}}^2(t_k)}\left(\frac{{\psi_1}^{(1)^k}(\eta_{N-1})}{\Delta\eta^2} + H^{(0)}(t_k)\,H^{(1)}\Omega^{(0)^k}(\eta_N)\right). \tag{6.82}$$

At any time, ${\Omega_2}^{(1)}$ can be found from equation (6.39). Here ${\hat{\psi}_2}^{(1)}$ must be defined at the fictitious points η_0 and η_{N+1}. From equation (6.43) at η_1 and η_N, using boundary conditions (6.75) differentiated with respect to time as well as boundary conditions (6.73) and the second two of conditions (6.74), we find that

$$\begin{aligned}
{\hat{\psi}_2}^{(1)^k}(\eta_0) &= 2{\hat{\psi}_2}^{(1)^k}(\eta_1) - {\hat{\psi}_2}^{(1)^k}(\eta_2) \\
&\qquad + \Delta\eta^2 {H^{(0)}}^2(t_k)\left({p_2}^{(1)^k}(\eta_1) - Re\frac{d^2H^{(0)}}{dt^2}(t_k)H^{(1)}\right), \\
{\hat{\psi}_2}^{(1)^k}(\eta_{N+1}) &= 2{\hat{\psi}_2}^{(1)^k}(\eta_N) - {\hat{\psi}_2}^{(1)^k}(\eta_{N-1}) \\
&\qquad + \Delta\eta^2 {H^{(0)}}^2(t_k)\left({p_2}^{(1)^k}(\eta_N) - Re\frac{d^2H^{(0)}}{dt^2}(t_k)H^{(1)}\right).
\end{aligned} \tag{6.83}$$

E and Liu (1996) discuss the numerical stability of this method. The method is found to have good stability properties for large Reynolds numbers. As either $Re \to 0$ or $\Delta\eta \to 0$, considering equations (6.41) to (6.43), we see that $M^{(0)}$, ${M_1}^{(1)}$ and ${M_2}^{(1)}$ all tend to infinity and we require that $\Delta t \to 0$ to maintain accuracy when stepping forward in time. When $Re = 0$, the analytic solution may be used. The numerical consistency of our results is checked by increasing the number of data points in η and t and ensuring that the resulting solution converges.

6.5 Results

6.5.1 The Leading-Order Solution

We briefly recount the results for the $O(1)$ solution, as found by Hall and Papageorgiou (1999).

For sufficiently small Reynolds numbers there exists a unique, stable solution which is π-periodic in time (synchronised with the $O(1)$ wall motion as described in (6.40)). As $Re \to 0$ this solution reduces at any point in time to a Poiseuille type flow in the horizontal direction, as described in the zero Reynolds number section. The streamfunction, $\psi^{(0)}$ is found to be odd with respect to η. In this case we choose the symmetric initial conditions, ${\psi^{(0)}}^1(\eta_i) = -\eta_i(dH^{(0)}/dt(t_1)) = 0$. The numerical program is run until a periodic solution is reached. Figure 6.4 shows the zero Reynolds number solution and plots of our numerical solution for the lower wall shear, $\partial^2\psi^{(0)}/\partial\eta^2(-1,t)$. When $Re = 25$, our solution is plotted alongside the solution from Hall and Papageorgiou (1999), which we plot using digitising software. We find that taking 101 points in the η-direction and Δt between 5×10^{-4} and 10^{-4} is sufficient to produce a close reproduction.

As Re passes a critical value Re_c, which depends on Δ, the flow remains synchronised with the wall motion, but a bifurcation can be observed such that there now exists a π-periodic, asymmetric solution. This solution remains stable until Re passes a second critical value, where it in turn loses stability. The asymmetric solution is not unique since a second solution may be obtained by replacing η with $-\eta$ and changing the sign of $\psi^{(0)}$. In addition to the asymmetric solution, the unstable, symmetric solution still exists, so that the solution has undergone a pitchfork bifurcation. It is the asymmetric solution that we focus on in this thesis. Using the trapezium rule, we may plot

$$I(Re) = \int_T^{T+\pi} |\psi^{(0)}(0,t)|dt, \tag{6.84}$$

where the point $t = T$ is taken to be large enough for any initial transients in our solution to have decayed. This gives an indication of the point at which symmetry is lost since a symmetric solution will clearly result in $I = 0$ and so $I \neq 0$ signifies an asymmetric solution. We note that comparing our results with Hall and Papageorgiou (1999), it is clear that they have used the above integrand, rather than $\psi^{(0)}(0,t)^2$, as they state in their paper. For quicker convergence of our results, we take an asymmetric initial condition. We choose ${\psi^{(0)}}^1(\eta_i) = -(\eta_i+1)^2(\eta_i-1)^3$. As we move closer to the bifurcation from either below or above, we are required to run the numerical scheme for increasingly longer times before the solution settles. In figure 6.5 we plot I and the lower wall shear when $Re = 48$ for the cases $\Delta = 0.45$ and 0.65, alongside the results of Hall and Papageorgiou (1999). We note that it is also clear from our plots, and the computed values in the rest of their results, that it is the case $\Delta = 0.65$ that they plot, rather than $\Delta = 0.45$, as stated in their paper. We find that as we decrease $\Delta\eta$, our

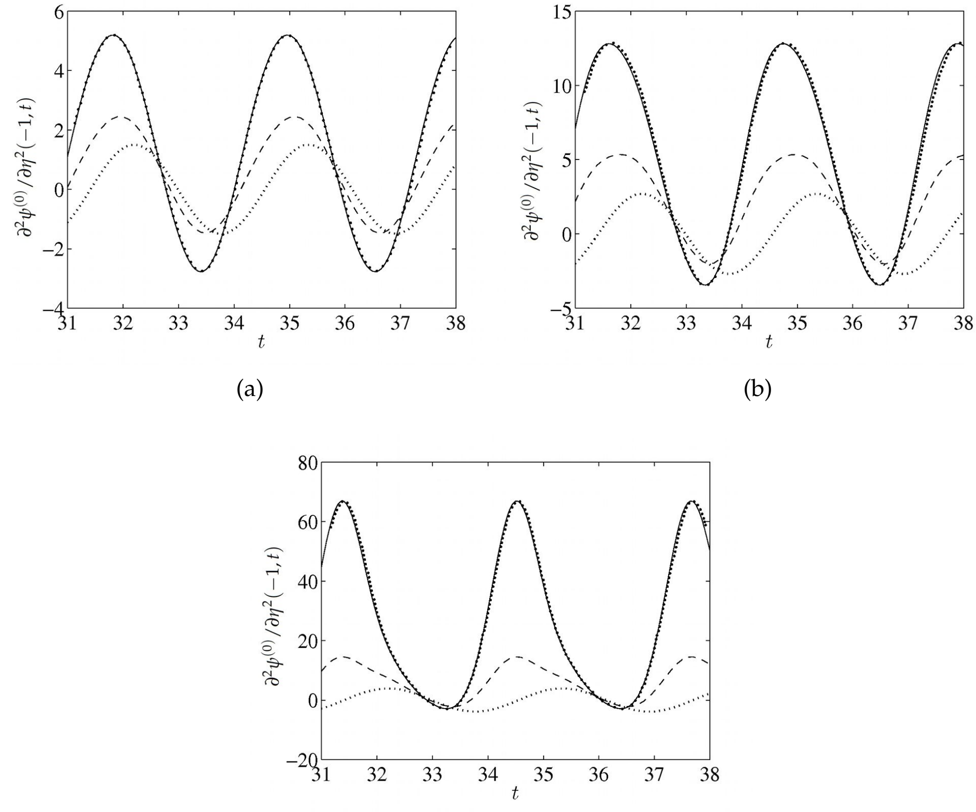

(a)

(b)

(c)

Figure 6.4: The leading-order lower wall shear, $\partial^2\psi^{(0)}/\partial\eta^2(-1,t)$, when $Re = 0$ (dotted line), 5 (dashed line) and 25 (solid line), when $\Delta =$ (a) 0.25, (b) 0.45 and (c) 0.65. When $Re = 25$, the black circles correspond to the results of Hall and Papageorgiou (1999).

solution converges to that of Hall and Papageorgiou (1999). Taking 401 points in η and $\Delta t = 10^{-4}$ is sufficient to reproduce their results, although to maintain accuracy for smaller Reynolds numbers it is necessary to take 351 points (since a smaller Δt is too computationally expensive).

For large enough wall amplitudes (such as $\Delta = 0.65$), above a second critical Reynolds number, Re_{c2} (which is 60.39 when $\Delta = 0.65$), the asymmetric solution loses stability such that successive period doubling of the solution is seen and the solution takes a Feigenbaum route to chaos. Above a certain Reynolds number, the solution is always chaotic and below this there exist windows of time-periodic solutions interspersed with chaotic solutions. For fairly large Δ (for instance 0.5, 0.55 or 0.6) there is also a second chaotic attractor, this time originating from a period doubling that originates from a solution with period 3π. In this case the solution disappears below a certain Reynolds number. Hall and Papageorgiou (1999) comment that other attractors must exist that cannot be reached from an initial state of zero flow everywhere (the initial conditions that give rise to the symmetric solution), and also find other attractors originating from the zero flow initial state, in particular one that originates from 11π periodic flow at

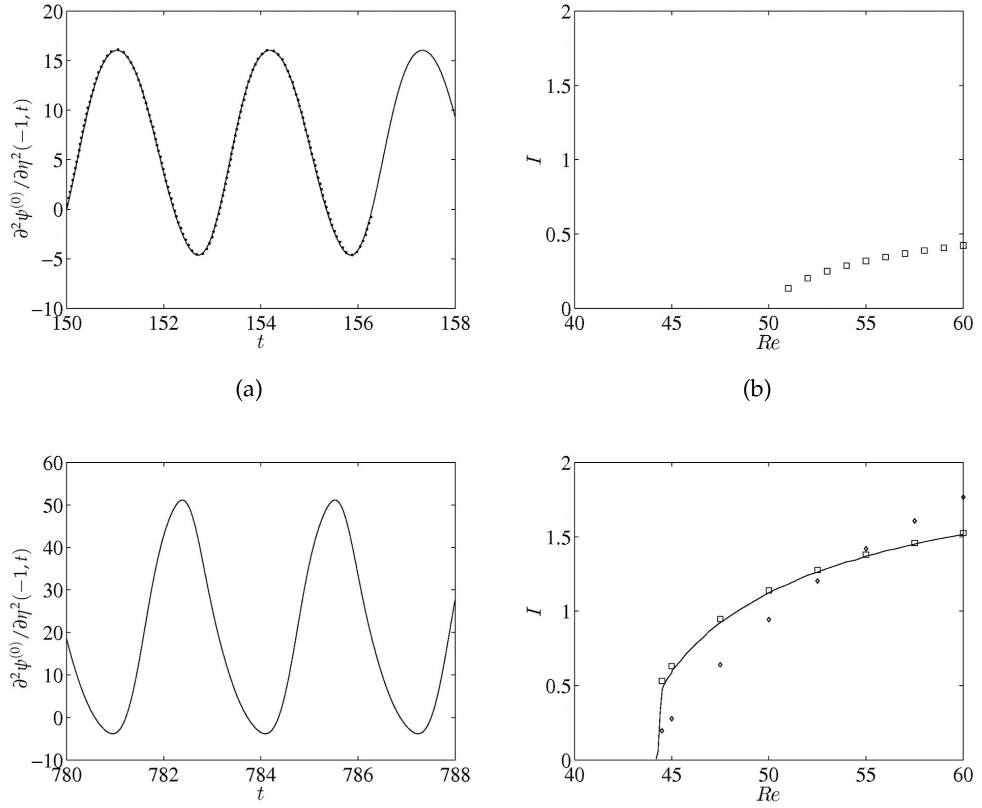

(a) (b)

(c) (d)

Figure 6.5: For the asymmetric solution, plots of the leading-order lower wall shear, $\partial^2\psi^{(0)}/\partial\eta^2(-1,t)$, when $Re = 48$ and the integral I (denoted by squares) when $\Delta =$ (a) and (b) 0.45 and (c) and (d) 0.65. In 6.5a and 6.5d the black circles and the solid line respectively correspond to the results of Hall and Papageorgiou (1999). In the plots of I diamonds correspond to the solution if we instead take the integrand in I to be $\psi^{(0)}(0,t)^2$.

$Re = 87.9$. For Δ small enough (less than 0.4), as Re is increased, there is a Hopf bifurcation to a quasi-periodic solution, before a Feigenbaum cascade on one of the frequencies again leads to a chaotic solution at large Re. At intermediate Δ (such as 0.45), a 4π periodic solution emerges from the quasi-periodic solution, after which chaotic and 4π solutions alternate, with the solution ultimately remaining chaotic for a large enough Re.

6.5.2 The First-Order Solution

6.5.2.1 Lower Reynolds Numbers

For the $O(\delta)$ solution we take ${\psi_1^{(1)}}^1(\eta_i) = {\hat{\psi}_2^{(1)}}^1(\eta_i) = 0$ as our initial conditions. We first consider smaller Reynolds numbers ($Re < Re_c$) and general Δ. Here we take 201 points in η (except for the case $\Delta = 0.65$ and $Re = 5$, where we must take 101 points) and $\Delta t = 10^{-4}$. In figures 6.6, 6.7 and 6.8 we show typical plots for the lower wall shears, $\partial^2{\psi_1}^{(1)}/\partial\eta^2(-1,t)$ and $\partial^2{\psi_2}^{(1)}/\partial\eta^2(-1,t)$, for the zero Reynolds number solution and our numerical solution. Recalling that we have defined $H^{(1)}$ to be constant, we choose it to be 0.5. Increasing or decreasing $H^{(1)}$ simply results in the wall shears having a larger or smaller amplitude, respectively. In general, we find that for low enough Reynolds numbers $\partial^2{\psi_1}^{(1)}/\partial\eta^2(-1,t)$ and $\partial^2{\psi_2}^{(1)}/\partial\eta^2(-1,t)$ are π-periodic, in a similar way to the $O(1)$ solution. Replacing η with $-\eta$, $\psi^{(0)}$ with $-\psi^{(0)}$ and ${\psi_1}^{(1)}$ with $-{\psi_1}^{(1)}$ in equations (6.38), (6.42) and boundary conditions (6.48) and (6.50) results in the same system of equations. We therefore expect that there exists a solution with ${\psi_1}^{(1)}$ odd with respect to η, also in the same manner as the $O(1)$ solution. Therefore it is no surprise that the π-periodic solution for ${\psi_1}^{(1)}$ is found to be odd. However, ${\hat{\psi}_2}^{(1)}$ is found to be even. As we might expect then, we find that in equations (6.39), (6.43) and boundary conditions (6.51), we must keep ${\hat{\psi}_2}^{(1)}$ the same sign in addition

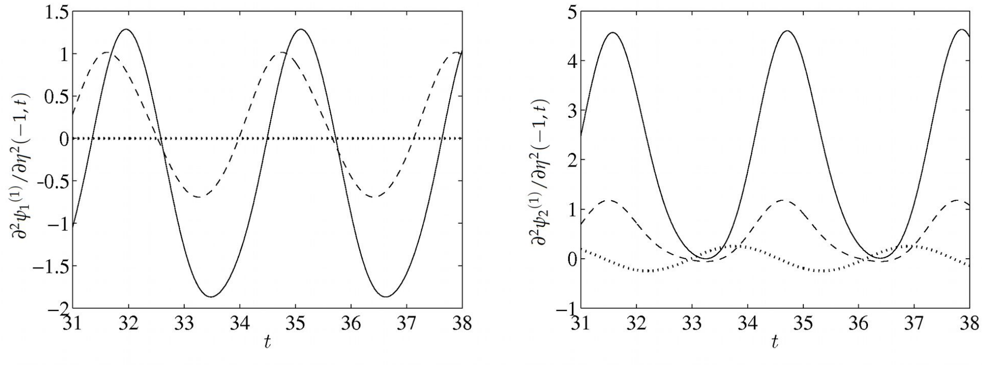

(a) (b)

Figure 6.6: When $H^{(1)} = 0.5$ and $\Delta = 0.25$, the first-order lower wall shears, (a) $\partial^2{\psi_1}^{(1)}/\partial\eta^2(-1,t)$ and (b) $\partial^2{\psi_2}^{(1)}/\partial\eta^2(-1,t)$, when $Re = 0$ (dotted line), 5 (dashed line) and 25 (solid line).

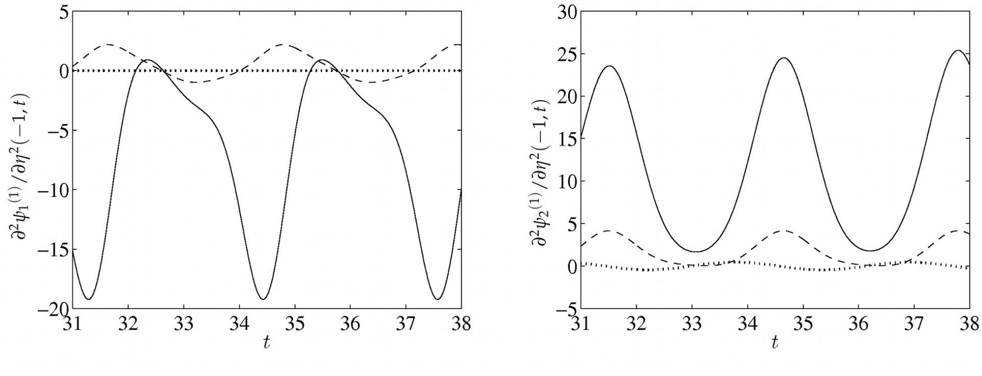

(a) (b)

Figure 6.7: When $H^{(1)} = 0.5$ and $\Delta = 0.45$, the first-order lower wall shears, (a) $\partial^2{\psi_1}^{(1)}/\partial\eta^2(-1,t)$ and (b) $\partial^2{\psi_2}^{(1)}/\partial\eta^2(-1,t)$, when $Re = 0$ (dotted line), 5 (dashed line) and 25 (solid line).

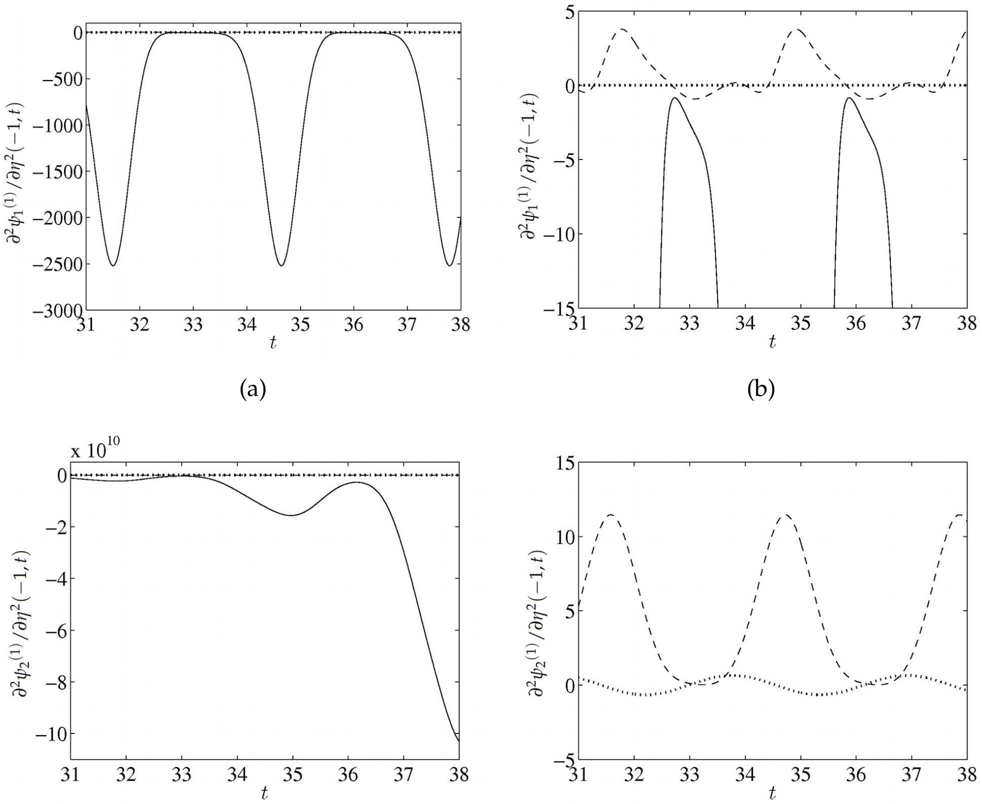

(a) (b)

(c) (d)

Figure 6.8: When $H^{(1)} = 0.5$ and $\Delta = 0.65$, the first-order lower wall shears, $\partial^2{\psi_1}^{(1)}/\partial\eta^2(-1,t)$ (shown in (a) with a close up in (b)), and $\partial^2{\psi_2}^{(1)}/\partial\eta^2(-1,t)$ (shown in (c) with a close up in (d)), when $Re = 0$ (dotted line), 5 (dashed line) and 25 (solid line).

to the above sign changes to obtain the same system. When $\Delta = 0.65$ and $Re = 25$, $\partial^2{\psi_2}^{(1)}/\partial\eta^2(-1,t)$ grows exponentially (although $\hat{\psi_2}^{(1)}$ remains even), with peaks and troughs becoming successively larger at intervals of π in time (so that the solution is still synchronised with the wall motion). This can be seen by taking the solution about any peak or trough, multiplying by a constant, m, (which depends on the Reynolds number) and superposing on top of the solution about the next peak or trough, from which it can be seen that the two curves are identical (as seen in figure 6.9). This series of actions describes the solution for all time. More research shows that when $\Delta = 0.65$, this behaviour occurs for $Re \geq 8$ (to the nearest whole number).

We now consider increasing the Reynolds number further for two different, interesting cases, $\Delta = 0.65$ and $\Delta = 0.25$.

6.5.2.2 Higher Reynolds Numbers, Case (i); $\Delta = 0.65$

We first focus on the case $\Delta = 0.65$, again taking $H^{(1)}$ to be 0.5. For $Re \leq 37.5$ we find that we must take 201 points in η. For $37.5 < Re \leq 45$ we may take 351 and

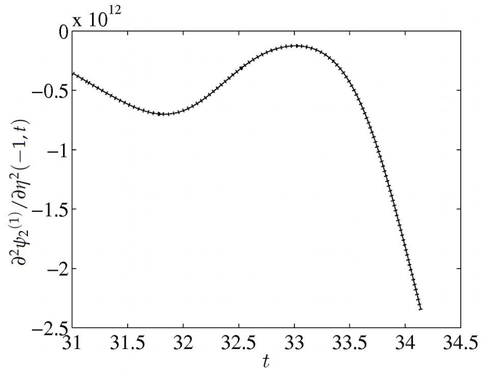

Figure 6.9: In the case $\Delta = 0.65$, $H_1 = 0.5$ and $Re = 25$, the solid line shows a plot of the first-order lower wall shear, $\partial^2 {\psi_2}^{(1)}/\partial\eta^2(-1,t)$, after taking the solution about a peak (shown by the dotted line), shifting along by π and multiplying by $m = 6.69$.

for higher Reynolds numbers, 401 points. In all cases we take $\Delta t = 10^{-4}$. We first consider the $O(\delta)$ solution as Re increases from 25 and passes $Re_c = 43.77$. Up until $Re = 38$ (to the nearest whole number), the lower wall shears, $\partial^2 {\psi_1}^{(1)}/\partial\eta^2(-1,t)$ and $\partial^2 {\psi_2}^{(1)}/\partial\eta^2(-1,t)$, are qualitatively the same as when $Re = 25$ (as in figure 6.8).

As we pass $Re = 38$, $\partial^2 {\psi_1}^{(1)}/\partial\eta^2(-1,t)$ grows exponentially in the same way as $\partial^2 {\psi_2}^{(1)}/\partial\eta^2(-1,t)$ in figure 6.8 when $Re = 25$, with successively larger peaks occurring at intervals of π in time. Interestingly, if we omit the terms in equation (6.42) in which $\partial^n {\psi_1}^{(1)}/\partial\eta^n$ or $\partial^n {\Omega_1}^{(1)}/\partial\eta^n$ are multiplied by $\partial^n \psi^{(0)}/\partial\eta^n$ or $\partial^n \Omega^{(0)}/\partial\eta^n$ for $n = 0, 1$ or 2, the solution is no longer unstable, suggesting that these terms are crucial for this behaviour. In this case plots of ${\psi_1}^{(1)}$ against η show that the solution is no longer odd, but appears to change from asymmetric for small t to even as time progresses (see figure 6.10). Plots of $\hat{\psi_2}^{(1)}$ against η show an asymmetric solution. These results seem to suggest that the $O(\delta)$ solution has bifurcated to an asymmetric solution at a value of Re lower than 43.77 - the critical Reynolds number for the $O(1)$ solution. We note that we must use asymmetric initial conditions for the $O(1)$ solution in order to successfully latch onto this solution. Figure 6.11 shows typical plots of the lower wall shears. Since the program is run until any transients in the $O(1)$ solution have decayed, the magnitudes reached in these plots are very large.

Since the coefficients of our governing equations for the $O(\delta)$ solution, (6.38), (6.39) and (6.42) to (6.44), have periodic coefficients, this suggests the use of Floquet theory to analyse the exponential growth seen in our solutions. Joseph (1976) gives a good summary of this theory. A description of our method of calculating the Floquet exponent is given in appendix C. In general, given a particular solution, we perturb about the underlying periodic solution. Here the underlying solution is the symmetric, π periodic solution that is obtained for smaller Reynolds numbers. We let the perturbation be given by $\exp(\gamma t)F^+(\eta, t)$, where $\gamma = \gamma_R + i\gamma_I$ is the Floquet exponent and where here F^+ is a π periodic function. The real part of the Floquet exponent, γ_R, gives us a measure of the growth of perturbations to the periodic solution. In figure 6.12 we plot

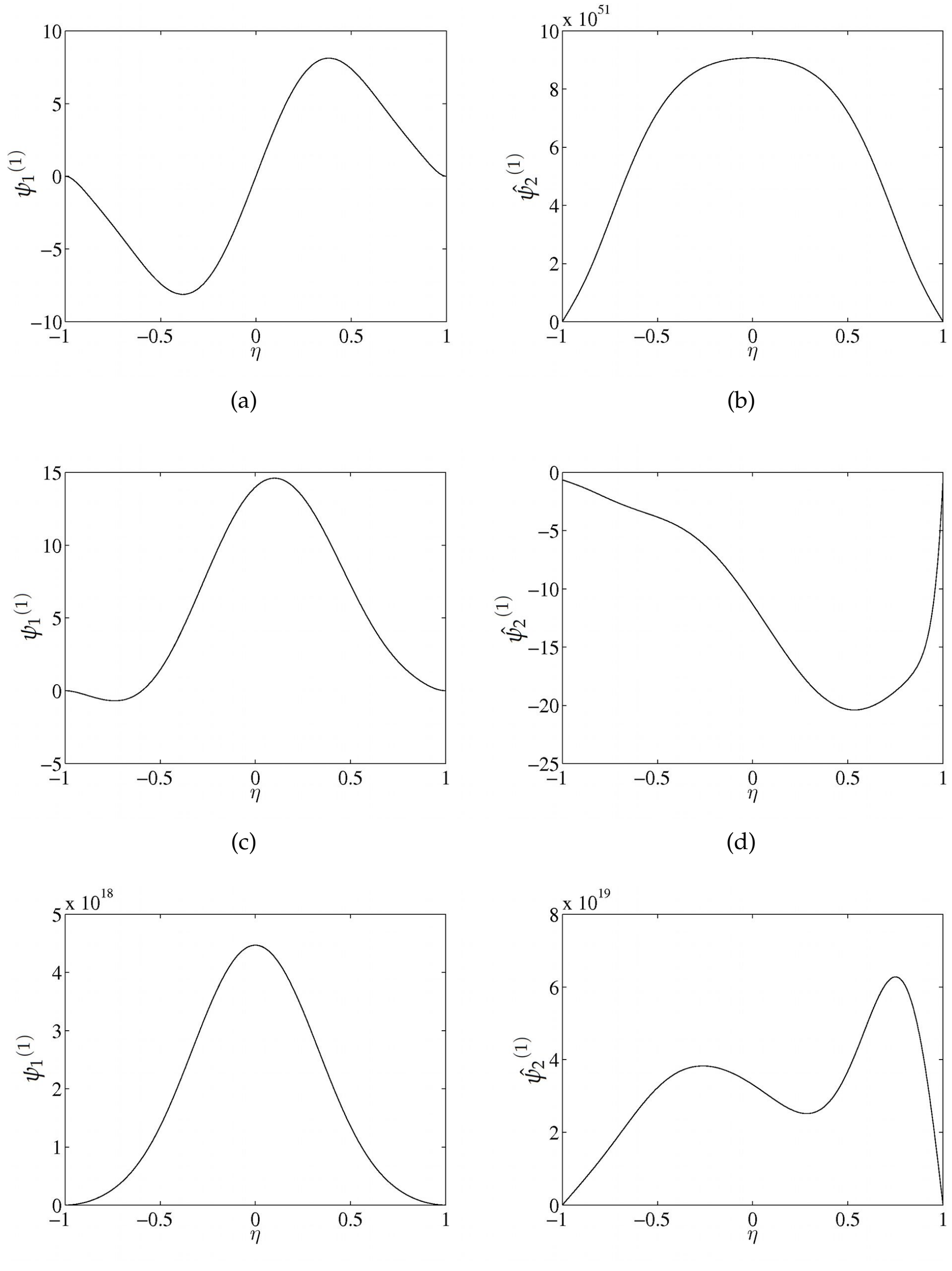

(a) (b)

(c) (d)

(e) (f)

Figure 6.10: When $\Delta = 0.65$ and $H^{(1)} = 0.5$, plots against η of the first-order solutions, ${\psi_1}^{(1)}$ (left panels) and $\hat{\psi_2}^{(1)} \equiv (1/H^{(0)})\partial\psi_2^{(1)}/\partial\eta$ (right panels), when (a) and (b) $Re = 35$ and $t = 565$ and when $Re = 40$ and $t =$ (c) and (d) 15 and (e) and (f) 265.

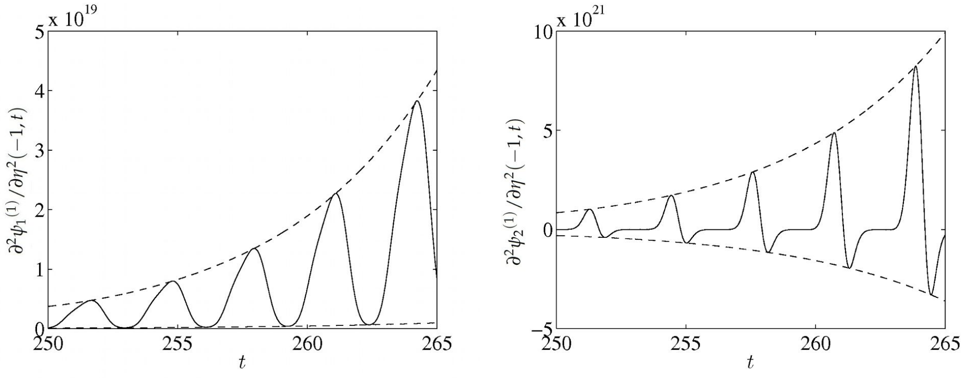

(a) (b)

Figure 6.11: When $\Delta = 0.65$ and $H^{(1)} = 0.5$, taking asymmetric initial conditions, typical plots of the first-order lower wall shears, $\partial^2\psi_1{}^{(1)}/\partial\eta^2(-1,t)$ and $\partial^2\psi_2{}^{(1)}/\partial\eta^2(-1,t)$, in the region $38 \leq Re < 43.77 = Re_c$. In this case $Re = 40$. The dashed lines show the exponential nature of the growth.

γ_R in the region $Re < 43.77 = Re_c$, showing the points at which the solutions for $\psi_1{}^{(1)}$ and $\hat{\psi_2}^{(1)}$ start to grow. Plotting $\exp(\gamma_R \pi)$ alongside the multiplicative constant, m, we

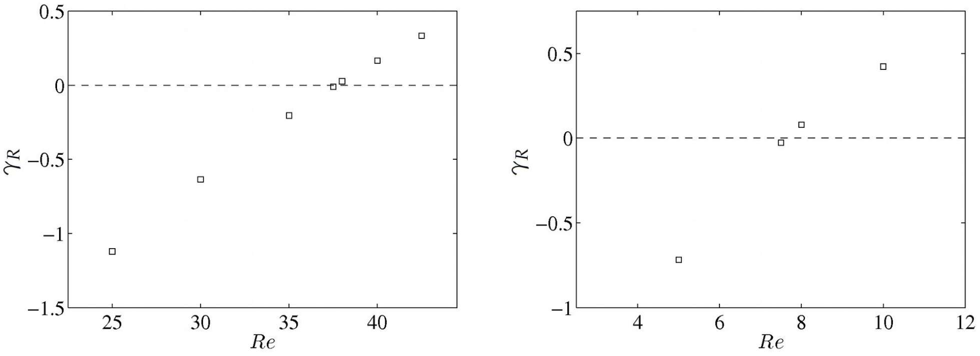

(a) (b)

Figure 6.12: When $\Delta = 0.65$ and $H^{(1)} = 0.5$, the Floquet exponent, γ_R, plotted against Re in the region $Re < 43.77 = Re_c$ when we examine the first-order solutions, (a) $\psi_1{}^{(1)}$ and (b) $\hat{\psi_2}^{(1)}$. The dashed line is $\gamma_R = 0$.

find that in the case of the solution for $\psi_1{}^{(1)}$, the two are in good agreement (see figure 6.13). This suggests that in these cases, the solution is given by the perturbation part of the Floquet solution itself. When $\psi_1{}^{(1)}$ is large, equations (6.38) and (6.42) become

$$L^2\psi_1{}^{(1)} = -{H^{(0)}}^2\Omega_1{}^{(1)}, \tag{6.85}$$

and

$$\begin{aligned}\frac{\partial {\Omega_1}^{(1)}}{\partial t} =& {M_1}^{(1)}(t,\psi^{(0)},{\psi_1}^{(1)},\Omega^{(0)},{\Omega_1}^{(1)};Re),\\ {M_1}^{(1)} =& \frac{1}{ReH^{(0)^2}}\frac{\partial^2 {\Omega_1}^{(1)}}{\partial \eta^2} - \frac{1}{H^{(0)}}\Bigg(-\left(\frac{dH^{(0)}}{dt}\eta + \psi^{(0)}\right)\frac{\partial {\Omega_1}^{(1)}}{\partial \eta}\\ &+ 2\frac{\partial \psi^{(0)}}{\partial \eta}{\Omega_1}^{(1)} + \frac{\partial {\psi_1}^{(1)}}{\partial \eta}\Omega^{(0)} - 2{\psi_1}^{(1)}\frac{\partial \Omega^{(0)}}{\partial \eta}\Bigg), \qquad (6.86)\end{aligned}$$

to be solved alongside boundary conditions (6.48) and (6.50). These equations are equivalent to the equations for the perturbation part of ${\psi_1}^{(1)}$ in the Floquet analysis (equations (C.3), (C.4) and (C.8) in appendix C), explaining why this is true. In the case of ${\hat{\psi}_2}^{(1)}$, below the bifurcation of the solution for ${\psi_1}^{(1)}$, where ${\hat{\psi}_2}^{(1)}$ is growing and is therefore large, equations (6.39) and (6.43) become

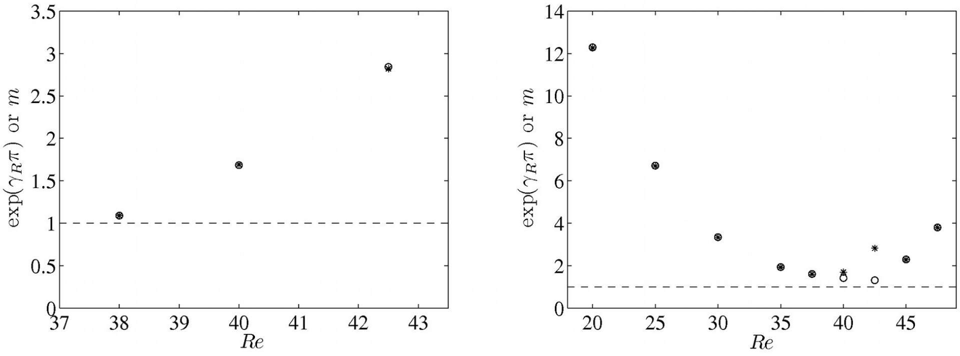

(a) (b)

Figure 6.13: When $\Delta = 0.65$ and $H^{(1)} = 0.5$, $\exp(\gamma_R\pi)$ (circles) and m (asterisks) plotted against Re in the region $Re < 49$ when we examine the growing first-order solutions, (a) ${\psi_1}^{(1)}$ and (b) ${\hat{\psi}_2}^{(1)}$. The dashed line is $m = 1$.

$${\Omega_2}^{(1)} = -\frac{1}{H^{(0)}}L{\hat{\psi}_2}^{(1)}, \qquad (6.87)$$

and

$$\begin{aligned}\frac{\partial {\hat{\psi}_2}^{(1)}}{\partial t} =& {M_2}^{(1)}(t,\psi^{(0)},{\hat{\psi}_2}^{(1)};Re),\\ {M_2}^{(1)} =& \frac{1}{ReH^{(0)^2}}\frac{\partial^2 {\hat{\psi}_2}^{(1)}}{\partial \eta^2} + \frac{1}{H^{(0)}}\left(\frac{\partial {\hat{\psi}_2}^{(1)}}{\partial \eta}\left(\frac{dH^{(0)}}{dt}\eta + \psi^{(0)}\right) - \frac{\partial \psi^{(0)}}{\partial \eta}{\hat{\psi}_2}^{(1)}\right), \qquad (6.88)\end{aligned}$$

and boundary conditions (6.51) become

$$\frac{\partial {\hat{\psi}_2}^{(1)}}{\partial \eta}(\eta = \pm 1, t) = 0. \qquad (6.89)$$

Here since ${p_2}^{(1)}(\eta = -1, t)$ is chosen to be zero, (6.44) gives us that ${p_2}^{(1)} = 0$. These equations are equivalent to the equations for the perturbation part of $\hat{\psi_2}^{(1)}$ in the Floquet analysis (equations (C.5), (C.6) and (C.9) in appendix C). Therefore, at this point $\exp(\gamma_R \pi)$ and m agree. However, once ${\psi_1}^{(1)}$ starts to grow, $\exp(\gamma_R \pi)$ and m no longer agree. This is due to the fact that $\hat{\psi_2}^{(1)}$ depends on the growth of ${\psi_1}^{(1)}$ as well as any growth that results independently of ${\psi_1}^{(1)}$. Since ${\psi_1}^{(1)}$ and $\hat{\psi_2}^{(1)}$ are of a similar magnitude, most of the growth of $\hat{\psi_2}^{(1)}$ must be due to ${\psi_1}^{(1)}$ and (6.39), (6.43) and (6.44) are no longer equivalent to the equations for the perturbation in the Floquet analysis.

Just above $Re = Re_c = 43.77$, the bifurcation point for the $O(1)$ solution, we find that there exists an asymmetric $O(\delta)$ solution with qualitatively the same time dependence as when $Re = 25$ (as shown in figure 6.8). For this solution the $O(1)$ solution has become asymmetric. This solution coexists with the unstable asymmetric $O(\delta)$ solution described above, for which the $O(1)$ solution is symmetric. We focus on following the branch of solutions emanating from the first of these solutions in our analysis. In this case $\exp(\gamma_R \pi)$ and m for the solution for ${\psi_2}^{(1)}$ again agree. This can be seen in figure 6.13.

Above around $Re = 49$, plots of $\partial^2 {\psi_2}^{(1)}/\partial \eta^2(-1, t)$ do not alter in form, but plots of $\partial^2 {\psi_1}^{(1)}/\partial \eta^2(-1, t)$ show an exponentially growing solution with successive peaks occurring at intervals of 2π in time (see figure 6.14). This indicates that ${\psi_1}^{(1)}$ behaves like an exponential multiplied by a function with double the period than that for smaller Reynolds numbers (at a lower Re than period doubling occurs in the $O(1)$ solution). For this solution, when using Floquet analysis, F^+ is taken to be a 2π periodic function. In this interval, as well as plots of $\exp(2\gamma_R \pi)$ and m being in good agreement for the solution for ${\psi_1}^{(1)}$, $\exp(\gamma_R \pi)$ and m also agree for the solution for ${\psi_2}^{(1)}$ (see figure 6.15). Here the magnitude of $\hat{\psi_2}^{(1)}$ is found to be much larger than that of ${\psi_1}^{(1)}$, suggesting that a large part of the growth of $\hat{\psi_2}^{(1)}$ is independent of ${\psi_1}^{(1)}$ and (6.39), (6.43) and

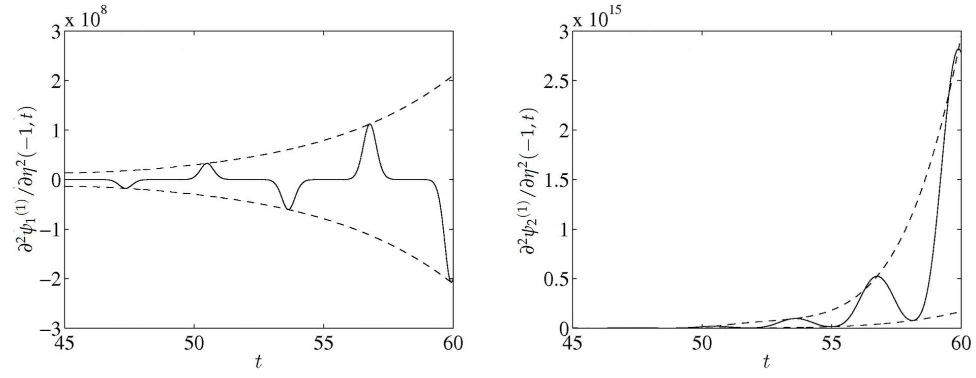

(a) (b)

Figure 6.14: When $\Delta = 0.65$ and $H^{(1)} = 0.5$, taking asymmetric initial conditions, typical plots of the first-order lower wall shears, $\partial^2 {\psi_1}^{(1)}/\partial \eta^2(-1, t)$ and $\partial^2 {\psi_2}^{(1)}/\partial \eta^2(-1, t)$, in the region $49 \leq Re < 60.39 = Re_{c2}$. In this case $Re = 50$. The dashed lines show the exponential nature of the growth.

(6.51) again reduce to (6.87) and are equivalent to the equations for the perturbation in the Floquet analysis.

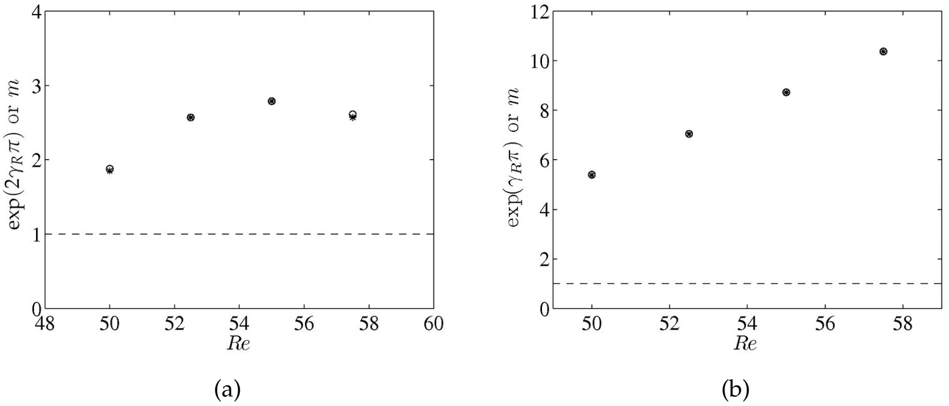

(a)

(b)

Figure 6.15: When $\Delta = 0.65$ and $H^{(1)} = 0.5$, in the region $49 < Re < 60.39 = Re_{c2}$, plots against Re of (a) $\exp(2\gamma_R\pi)$ (circles) and m (asterisks) when we examine the growing first-order solution for ${\psi_1}^{(1)}$ and (b) $\exp(\gamma_R\pi)$ (circles) and m (asterisks) when we examine the growing first-order solution for $\hat{\psi_2}^{(1)}$. The dashed line is $m = 1$.

For higher Reynolds numbers it is convenient to label the period of the $O(1)$ solution $T^{(0)}$ and the distance between consecutive peaks in the $O(\delta)$ solutions ${T_1}^{(1)}$ and ${T_2}^{(1)}$ in the case of ${\psi_1}^{(1)}$ and $\hat{\psi_2}^{(1)}$, respectively. Above $Re = Re_{c2} = 60.39$, the leading-order solution doubles in period so that there is a bifurcation to a 2π periodic solution ($T^{(0)} = 2\pi$). As we increase Re further, $T^{(0)}$ doubles again and again. We then have a period doubling cascade. At Re_{c2}, ${T_1}^{(1)}$ remains equal to 2π and ${T_2}^{(1)}$ becomes 2π. Increasing Re, both ${\psi_1}^{(1)}$ and $\hat{\psi_2}^{(1)}$ continue to grow, but ${T_1}^{(1)}$ and ${T_2}^{(1)}$ also double again and again (although not necessarily at the same Reynolds number as $T^{(0)}$).

The behaviour of ${T_j}^{(1)}$ up until until the period of $\psi^{(0)}$ has reached 32π is summarised in table 6.1, where we focus on a couple of Reynolds numbers in each interval. In this region, for our Floquet analysis we take F^+ to be an $m\pi$ periodic function when ${T_j}^{(1)} = m\pi$, $j = 1$ or 2. In general, the distance between consecutive peaks matches the period of the $O(1)$ solution. However, in some cases, we find evidence that the solution for ${\psi_1}^{(1)}$ again bifurcates early. It is possible that this occurs in every interval, but unfortunately as we move closer to the boundaries at which the the $O(1)$ solution doubles in period, longer and longer runs are required to obtain the settled solution and it is not feasible for us to look any closer. Since $\hat{\psi_2}^{(1)}$ depends on ${\psi_1}^{(1)}$, we would expect that $\hat{\psi_2}^{(1)}$ also bifurcates early in these instances. However, since $\hat{\psi_2}^{(1)}$ is of a much larger magnitude than ${\psi_1}^{(1)}$, this bifurcation is not picked up on in our results. Also shown in the table are calculated values of $\exp(\gamma_R {T_1}^{(1)})$ and $\exp(\gamma_R {T_2}^{(1)})$, accurate to two decimal places. We find that these values are in good agreement with the values of m_1 and m_2, the values of m calculated in the case of the growing solution for ${\psi_1}^{(1)}$ and $\hat{\psi_2}^{(1)}$, respectively. As expected, in all cases, running the programs for longer times and

Interval of Re	Re	${T_1}^{(1)}$	$\exp\left(\gamma_R {T_1}^{(1)}\right) = m_1$	${T_2}^{(1)}$	$\exp\left(\gamma_R {T_2}^{(1)}\right) = m_2$
60.39 to 74.6	70	2π	17.49	2π	214.41
$T^{(0)} = 2\pi$	74	2π	37.30	2π	218.03
74.605 to 78.46	76.5	4π	1.25×10^3	4π	5.01×10^4
$T^{(0)} = 4\pi$	78.2	4π	675.94	4π	5.32×10^4
78.465 to 79.199	78.5	8π	1.70×10^5	8π	2.81×10^9
$T^{(0)} = 8\pi$	78.8	16π	4.37×10^{11}	8π	2.82×10^9
79.2 to 79.3545	79.25	16π	2.22×10^{12}	16π	7.88×10^{18}
$T^{(0)} = 16\pi$	79.34	16π	3.04×10^{12}	16π	7.87×10^{18}
79.355 to 79.385	79.36	32π	1.00×10^{25}	32π	6.20×10^{37}
$T^{(0)} = 32\pi$	79.38	32π	1.01×10^{25}	32π	6.20×10^{37}

Table 6.1: When $\Delta = 0.65$ and $H^{(1)} = 0.5$, in the region $Re_{c2} = 60.39 < Re$, the calculated values of ${T_j}^{(1)}$ and $\exp(\gamma_R {T_j}^{(1)})$, $j = 1, 2$, when we examine the first-order growing solutions for ${\psi_1}^{(1)}$ and ${\hat{\psi}_2}^{(1)}$.

increasing the number of data points in our program increases the accuracy and hence the agreement between $\exp(\gamma_R {T_j}^{(1)})$ and m_j.

We note that since the equations used in the Floquet analysis are independent of $H^{(1)}$, γ_R remains the same regardless of the value that we choose for this parameter. Equally, increasing or decreasing $H^{(1)}$ is found simply to increase or decrease the magnitude of the lower wall shear proportionally at each point, so that m does not change. In fact as Re becomes very large, $H^{(1)}$ affects the solution less and less, perhaps because it becomes less important compared to Re.

It is found that $Re = R_\infty = 79.4$ is the accumulation point beyond which the $O(1)$ solution is chaotic. Above this value small windows exist for which the solution is periodic. For instance when $Re = 80$ (where the period is 20π), 85 (3π) and 86 (6π). The $O(1)$ solution is found to be chaotic in the case $Re = 100$. To examine the chaotic region, we construct the vectors

$$\mathbf{x}^{(0)} = \left(\psi^{(0)}(-0.5, t), \psi^{(0)}(0, t), \psi^{(0)}(0.5, t)\right) - \frac{dH^{(0)}}{dt}(t)\,(1, 1, 1), \tag{6.90}$$

$$\mathbf{x}_1{}^{(1)} = e^{-at}\left({\Omega_1}^{(1)}(-0.5, t), {\Omega_1}^{(1)}(0, t), {\Omega_1}^{(1)}(0.5, t)\right), \tag{6.91}$$

$$\mathbf{x}_2{}^{(1)} = e^{-bt}\left({\Omega_2}^{(1)}(-0.5, t), {\Omega_2}^{(1)}(0, t), {\Omega_2}^{(1)}(0.5, t)\right), \tag{6.92}$$

where a and b depend on Re and are estimated by trial and error as closely as possible such that the quantities in the vectors ${\bf x}_1{}^{(1)}$ and ${\bf x}_2{}^{(1)}$ do not show exponential growth or decay over time. We use the vector ${\bf x}^{(0)}$ to compare our results to those of Hall and Papageorgiou (1999), whose horizontal axis lies in a different position to ours in the original setup. The $O(\delta)$ vectors have been chosen using a sensible physical flow quantity. Each vector represents a trajectory in a 3-dimensional (x_1, x_2, x_3) space over time. By considering the intersection with the $x_1 - x_2$ plane, we obtain Poincaré cross-sections. Here n points denotes an $n\pi$ periodic solution, a circular plot that "just misses" (thus creating a spiral shape) denotes a quasi-periodic solution and a collection of points that forms a complex, self-similar structure is characteristic of a chaotic solution. We also consider the time series given by the first entry of each vector and, labelling its value at the ith maximum m_i, we plot m_{i+1}/m_i for $i = 1, 2, \cdots$ against time. We do the same with the minima. If the time series is $n\pi$ periodic, this will result in n straight lines, whilst a seemingly unstructured plot denotes chaos. We also plot the set of points (m_i, m_{i+1}), giving us a return map. Here n points denotes an $n\pi$ periodic solution, filled lines or sets of lines denote a quasi-periodic solution and a self-similar structure denotes a chaotic solution. All plots are obtained once the solution has settled and in all cases we use zero initial conditions.

In figure 6.16 we plot the evolution of the minima and maxima, return maps and Poincaré cross-section for the $O(1)$ solution when $Re = 100$. We find that we are able to reproduce the plots of Hall and Papageorgiou (1999). We obtain good evidence that above $Re = R_\infty = 79.4$, the $O(\delta)$ solution is also chaotic. Figures 6.17 and 6.18 show the evolution of the minima and maxima, return maps and Poincaré cross-sections for the $O(\delta)$ solution when $Re = 100$. We see that the evolution of the minima and maxima is seemingly irregular, whilst the return maps and Poincaré cross-sections exhibit self-similar behaviour and underlying structure with evidence of folding.

We note that even longer computational runs and the inclusion of even more data points in our program would allow us to estimate the constants a and b more accurately. This would then give us a better representation of the chaotic structure glimpsed in our plots. This is, however, two computationally expensive to include in this thesis and is left as a possible topic of future research.

In figure 6.19 we summarise the changing behaviour of the $O(\delta)$ solution with increasing Reynolds number for the case $\Delta = 0.65$. We show the onset of exponential growth in the solution for $\hat{\psi_2}^{(1)}$, the early symmetry-breaking bifurcation of the $O(\delta)$ solution (at which point the solution for ${\psi_1}^{(1)}$ also grows exponentially) and the early doubling of ${T_1}^{(1)}$ in the solution for ${\psi_1}^{(1)}$, before a $T^{(0)}$ and ${T_j}^{(1)}$ doubling cascade (in which ${T_1}^{(1)}$ at times doubles before $T^{(0)}$) leads to a fully chaotic solution.

There is also evidence of small regions for which ${T_1}^{(1)}$ is much larger than the period of the $O(1)$ solution. These regions appear to occur at the beginning of the region for which $T^{(0)} = 2\pi$. However, we are not able to define accurately the boundaries of these regions, and this is left as another possible topic of future research.

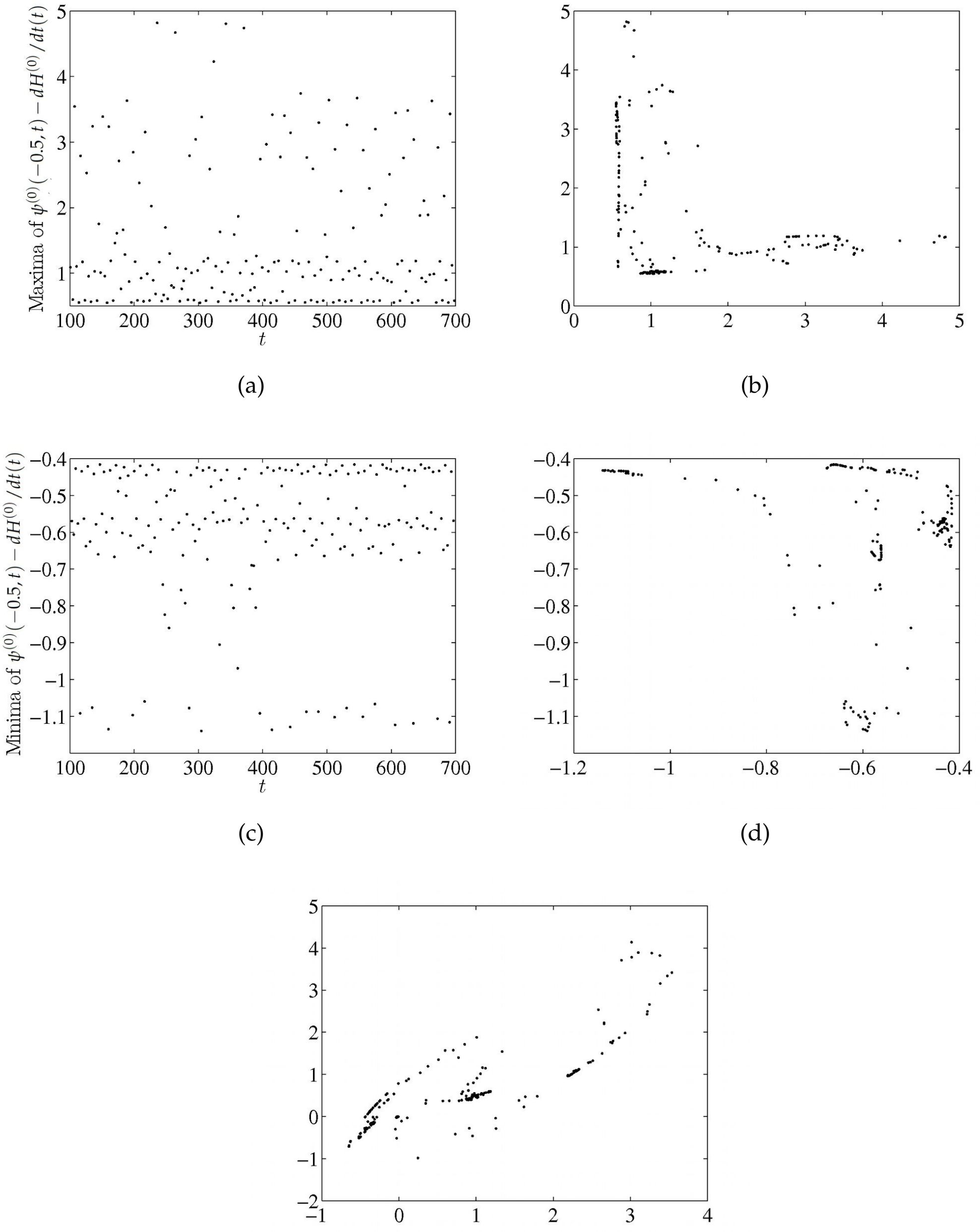

(a) (b)

(c) (d)

(e)

Figure 6.16: When $\Delta = 0.65$, $H^{(1)} = 1$ and $Re = 100$, taking t from 100 to 700, for the leading-order solution, the evolution of (a) the maxima and (c) the minima of $\psi^{(0)}(-0.5,t) - dH^{(0)}/dt(t)$, (b) and (d) the corresponding return maps and (e) the Poincaré cross-section obtained by considering the intersection of $\mathbf{x}^{(0)}$ with the $x_1 - x_2$ plane.

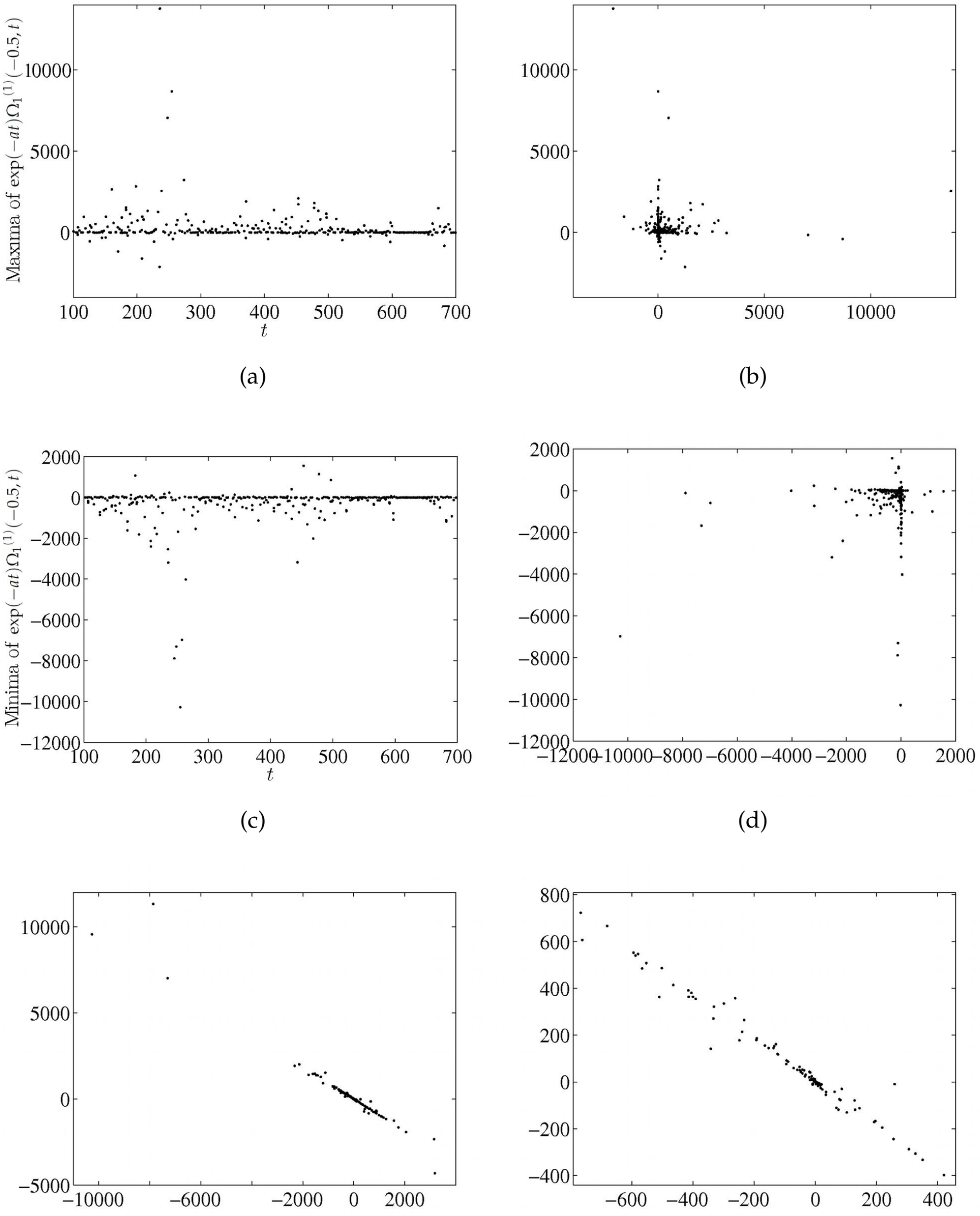

(a) (b)

(c) (d)

(e) (f)

Figure 6.17: When $\Delta = 0.65$, $H^{(1)} = 1$ and $Re = 100$, taking t from 100 to 700, for the first-order solution, the evolution of (a) the maxima and (c) the minima of $\exp(-at){\Omega_1}^{(1)}(-0.5, t)$, (b) and (d) the corresponding return maps and (e), and enlarged in (f), the Poincaré cross-section obtained by considering the intersection of ${\mathbf{x}_1}^{(1)}$ with the $x_1 - x_2$ plane. In this case $a = 0.55$ to two decimal places.

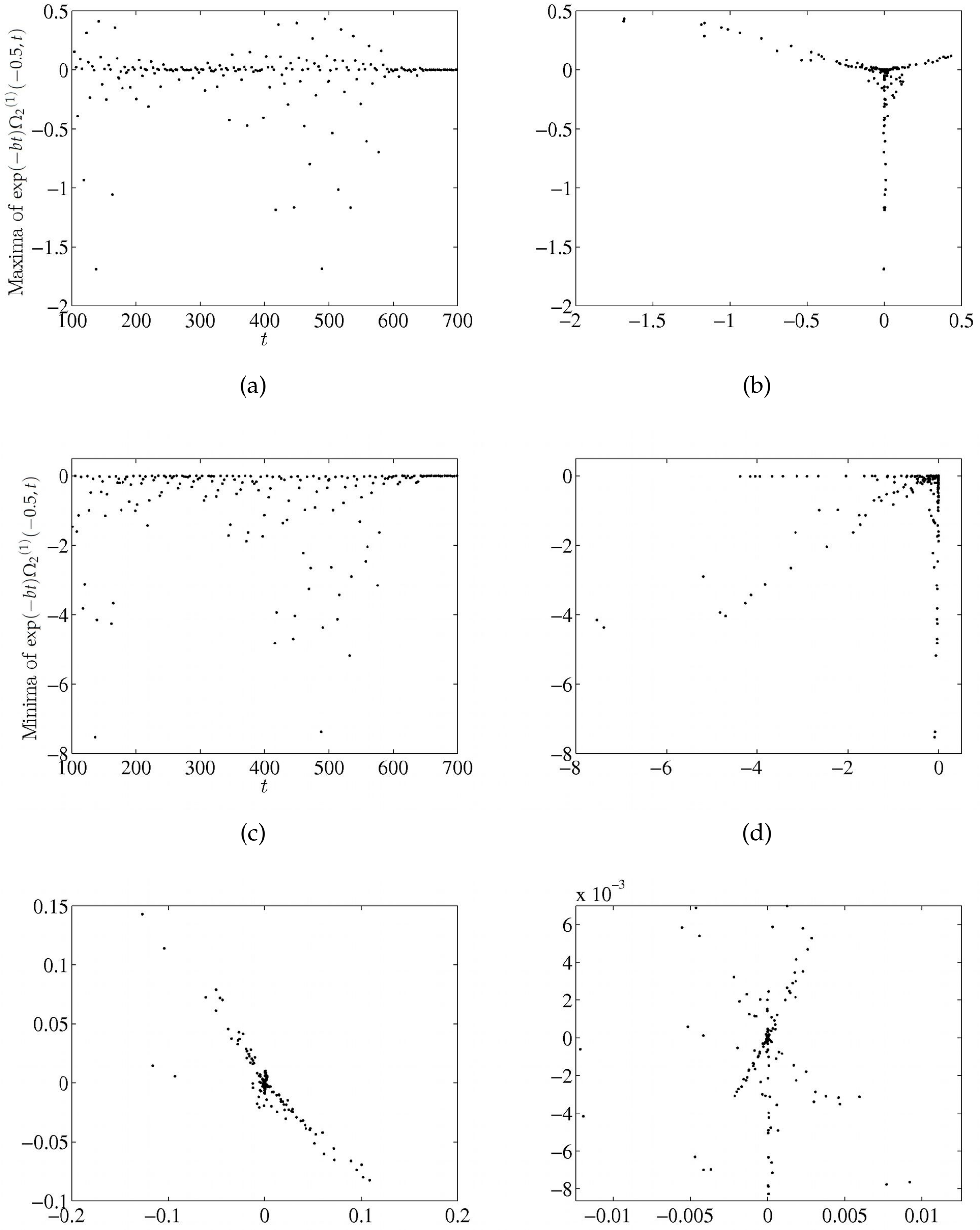

(a) (b)

(c) (d)

(e) (f)

Figure 6.18: When $\Delta = 0.65$, $H^{(1)} = 1$ and $Re = 100$, taking t from 100 to 700, for the first-order solution, the evolution of (a) the maxima and (c) the minima of $\exp(-bt)\Omega_2{}^{(1)}(-0.5, t)$, (b) and (d) the corresponding return maps and (e), and enlarged in (f), the Poincaré cross-section obtained by considering the intersection of $\mathbf{x}_2{}^{(1)}$ with the $x_1 - x_2$ plane. In this case $b = 0.87$ to two decimal places.

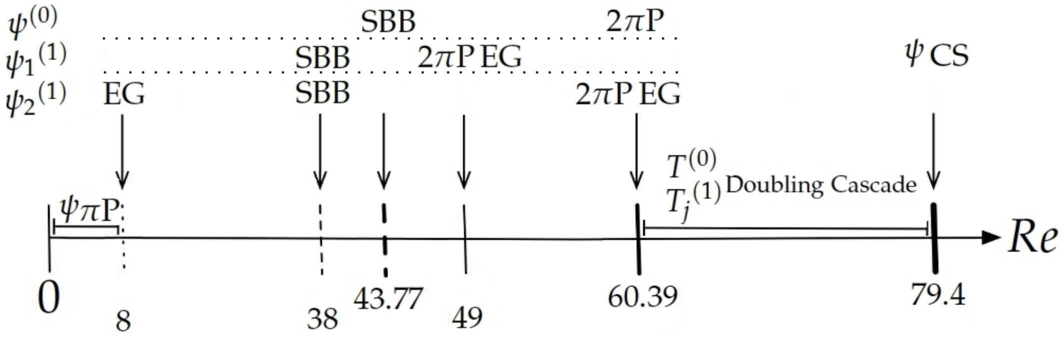

Figure 6.19: A summary of the changing behaviour of the $\Delta = 0.65$ streamfunction with increasing Reynolds number, where $\psi = x\psi^{(0)} + \delta(x^2\psi_1{}^{(1)} + \psi_2{}^{(1)})$ and $\hat{\psi}_2{}^{(1)} \equiv (1/H^{(0)})\partial\psi_2^{(1)}/\partial\eta$. Here $n\pi$P denotes an $n\pi$ periodic solution, EG a bifurcation to an exponentially growing solution, SBB a symmetry breaking bifurcation and CS the accumulation point above which the solution is chaotic. $T^{(0)}$ is the period of $\psi^{(0)}$ and for $j = 1$ or 2, $T_j{}^{(1)}$ is the distance between consecutive peaks in the solution for $\psi_1{}^{(1)}$ or $\hat{\psi}_2{}^{(1)}$.

6.5.2.3 Higher Reynolds Numbers, Case (ii); $\Delta = 0.25$

We next focus on the case $\Delta = 0.25$ and again take $H^{(1)}$ to be 0.5. For all Reynolds numbers we may take 401 points in η and $\Delta t = 10^{-4}$. In this case the first bifurcation of the $O(1)$ solution occurs when $Re = Re_c = 135.6$. The $O(\delta)$ solution remains qualitatively the same as shown in figure 6.6 up until $Re = 85$ (to the nearest whole number).

Above $Re = 85$ both $\partial^2\psi_1{}^{(1)}/\partial\eta^2(-1,t)$ and $\partial^2\psi_2{}^{(1)}/\partial\eta^2(-1,t)$ grow exponentially in the same manner noted when $\Delta = 0.65$, but with a slower typical growth rate. Typical plots of the lower wall shears are shown in figure 6.20. In both cases peaks occur at intervals of π in time. Also similarly to when $\Delta = 0.65$, plots of $\psi_1{}^{(1)}$ against η show a

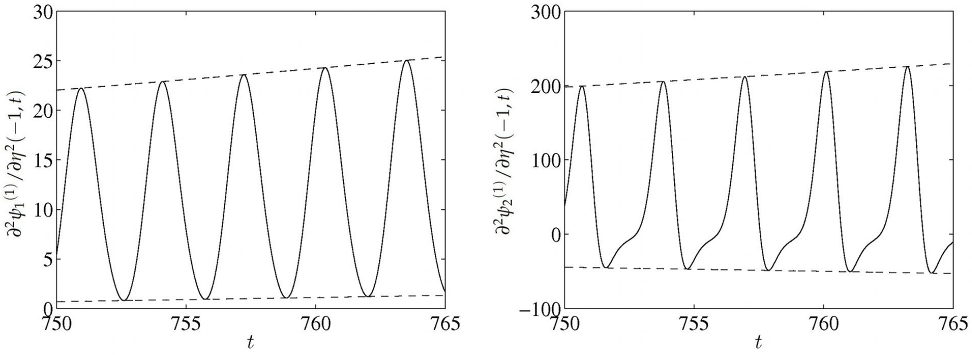

(a) (b)

Figure 6.20: When $\Delta = 0.25$ and $H^{(1)} = 0.5$, taking asymmetric initial conditions, typical plots of the first-order lower wall shears, $\partial^2\psi_1{}^{(1)}/\partial\eta^2(-1,t)$ and $\partial^2\psi_2{}^{(1)}/\partial\eta^2(-1,t)$, in the region $85 \leq Re < 135.6 = Re_c$. In this case $Re = 90$. The dashed lines show the exponential nature of the growth.

solution that changes from asymmetric to even with time, and plots of ${\psi_2}^{(1)}$ against η show an asymmetric solution (see figure 6.21). However, in this case, for even smaller times we find that ${\psi_1}^{(1)}$ is odd and ${\hat{\psi}_2}^{(1)}$ is even and so both have the same properties as for smaller Reynolds numbers. As time passes, ${\psi_1}^{(1)}$ becomes asymmetric and this is eventually noticeable in plots of ${\psi_2}^{(1)}$, which also becomes asymmetric. Again, this

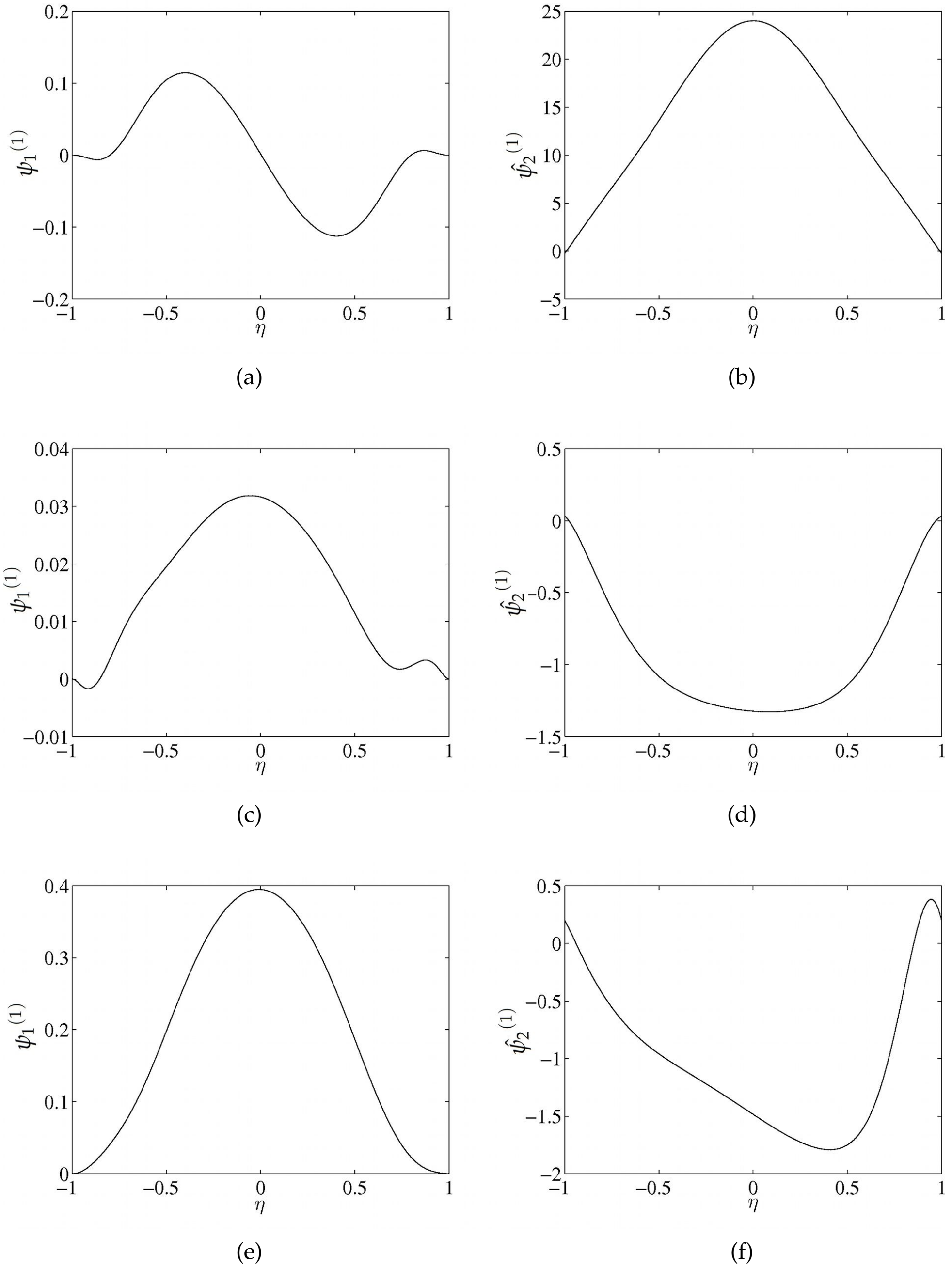

(a) (b)

(c) (d)

(e) (f)

Figure 6.21: When $\Delta = 0.25$ and $H^{(1)} = 0.5$, plots against η of the first-order solutions, ${\psi_1}^{(1)}$ (left panels) and ${\hat{\psi}_2}^{(1)} \equiv (1/H^{(0)})\partial\psi_2^{(1)}/\partial\eta$ (right panels), when $Re = 100$ and $t =$ (a) and (b) 15, (c) and (d) 190 and (e) and (f) 265.

behaviour implies that the $O(\delta)$ solution bifurcates to an asymmetric solution at a lower value than 135.6, the bifurcation point for the $O(1)$ solution. We must use asymmetric initial conditions for the $O(1)$ solution in order to latch onto this solution.

In figure 6.22 we plot the real part of the Floquet exponent, γ_R, in the region $Re < 135.6 = Re_c$ for ${\psi_1}^{(1)}$ and ${\hat{\psi_2}}^{(1)}$. Here F^+ is a π periodic function. Above $Re = 85$, γ_R is

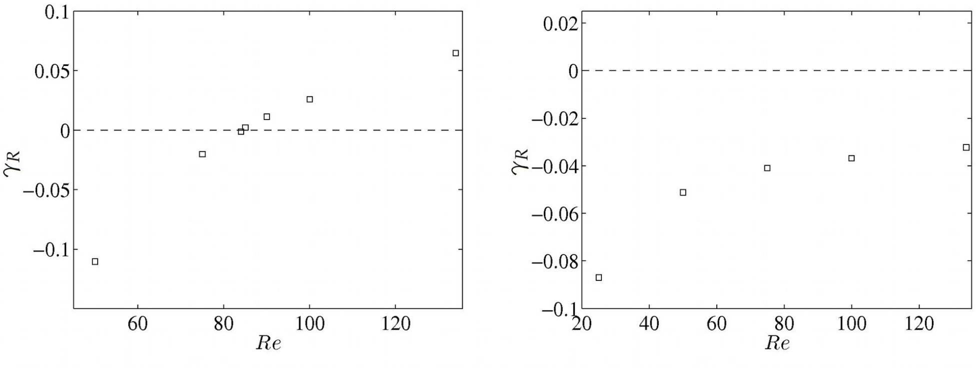

(a) (b)

Figure 6.22: When $\Delta = 0.25$ and $H^{(1)} = 0.5$, the Floquet exponent, γ_R, plotted against Re in the region $Re < 135.6 = Re_c$ when we examine the first-order solutions, (a) ${\psi_1}^{(1)}$ and (b) ${\hat{\psi_2}}^{(1)}$. The dashed line is $\gamma_R = 0$.

positive when examining the solution for ${\psi_1}^{(1)}$, explaining why ${\psi_1}^{(1)}$ and ${\hat{\psi_2}}^{(1)}$ grow. We note that ${\hat{\psi_2}}^{(1)}$ grows regardless of the fact that the Floquet exponent was found to be negative. This implies that the growth of ${\hat{\psi_2}}^{(1)}$ is entirely due to its dependence on ${\psi_1}^{(1)}$. This also explains why ${\psi_1}^{(1)}$ and ${\hat{\psi_2}}^{(1)}$ are of similar magnitudes. In this case, therefore, equations (6.39), (6.43) and (6.51) are dominated by ${\psi_1}^{(1)}$ and are not equivalent to the equations for the perturbation in the Floquet analysis. Hence in the case of ${\hat{\psi_2}}^{(1)}$, unlike ${\psi_1}^{(1)}$ (for which equations (6.38), (6.42), (6.48) and (6.50) reduce to (6.85)), the solution is not given by the perturbation part of the Floquet solution itself. This can be seen in figure 6.23, where plots of $\exp(\gamma_R \pi)$ and the multiplicative constant, m, agree when the solution is given by the Floquet perturbation and do not agree otherwise.

Above $Re = Re_c$, as in the case $\Delta = 0.65$, we find that a solution exists for which the $O(1)$ solution is asymmetric and the $O(\delta)$ solution has qualitatively the same time dependence as in figure 6.6. We follow this branch of solutions rather than the branch for which the $O(1)$ solution is symmetric and the $O(\delta)$ solution is unstable and asymmetric. Following this solution, above around $Re = 160$, plots of $\partial^2 {\psi_1}^{(1)} / \partial \eta^2 (-1, t)$ do not change qualitatively, but plots of $\partial^2 {\psi_2}^{(1)} / \partial \eta^2 (-1, t)$ show an exponentially growing solution with peaks at intervals of π in time (see figure 6.24). In figure 6.25 we plot γ_R for the solution for ${\hat{\psi_2}}^{(1)}$ in the region $160 \leq Re < 255$, showing the point at which the solution starts to grow. In this case, like the solution when $\Delta = 0.65$ for smaller Reynolds numbers (when $Re = 25$, for example), ${\hat{\psi_2}}^{(1)}$ grows independently of ${\psi_1}^{(1)}$. Therefore, in this region plots of $\exp(\gamma_R \pi)$ and m now agree (see figure 6.23b), suggesting that (6.39), (6.43) and (6.51) become the system (6.87) and so the solution is now

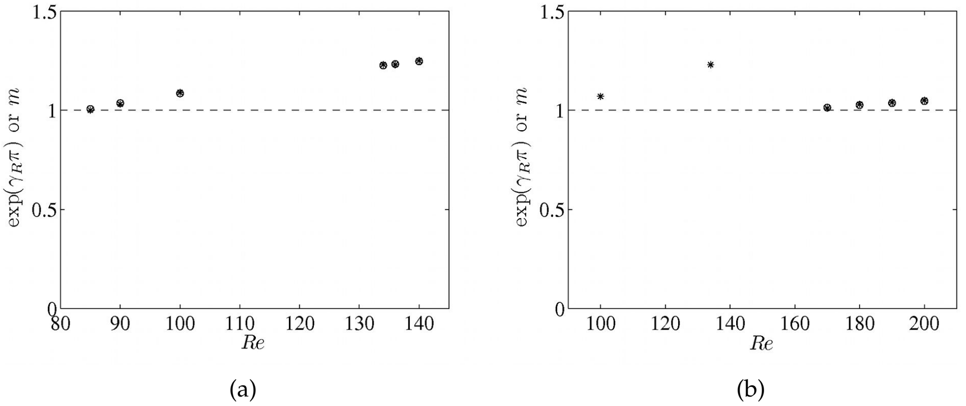

Figure 6.23: When $\Delta = 0.25$ and $H^{(1)} = 0.5$, $\exp(\gamma_R \pi)$ (circles) and m (asterisks) plotted against Re in the region $Re > 85$ when we examine the growing first-order solutions, (a) ${\psi_1}^{(1)}$ and (b) ${\hat{\psi_2}}^{(1)}$. The dashed line is $m = 1$.

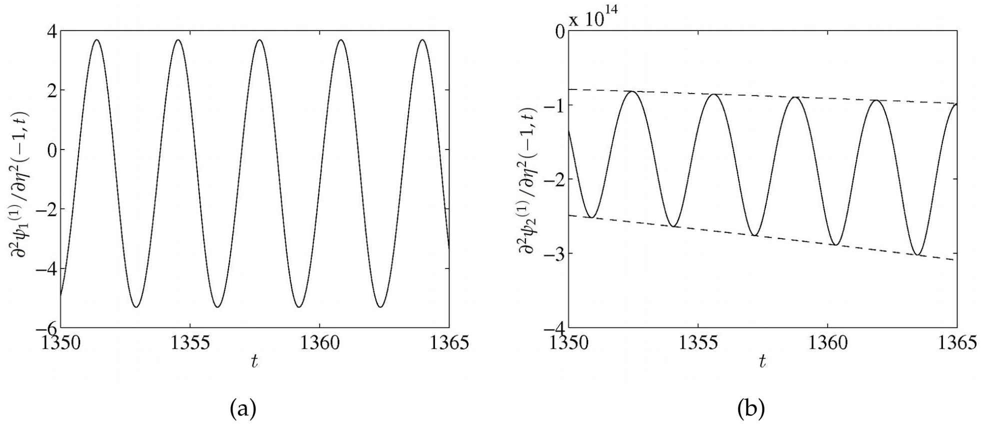

Figure 6.24: When $\Delta = 0.25$ and $H^{(1)} = 0.5$, taking asymmetric initial conditions, typical plots of the first-order lower wall shears, $\partial^2{\psi_1}^{(1)}/\partial\eta^2(-1,t)$ and $\partial^2{\psi_2}^{(1)}/\partial\eta^2(-1,t)$, in the region $160 < Re < 255$. In this case $Re = 200$. The dashed lines show the exponential nature of the growth.

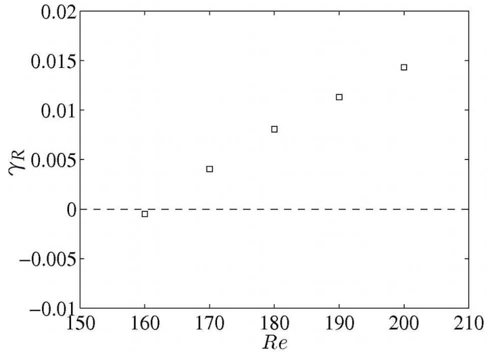

Figure 6.25: When $\Delta = 0.25$ and $H^{(1)} = 0.5$, the Floquet exponent, γ_R, plotted against Re in the region $160 \leq Re < 255$ when we examine the first-order solution for ${\hat{\psi_2}}^{(1)}$. The dashed line is $\gamma_R = 0$.

given by the Floquet perturbation, as we would expect.

Above $Re = 255$ (to the nearest whole number), we find evidence that the $O(\delta)$ solution takes the form of a quasi-periodic function multiplied by an exponentially growing function. The $O(1)$ solution bifurcates to a quasi-periodic solution at $Re \approx 544$. This suggests that the $O(\delta)$ solution bifurcates at a lower Reynolds number than the $O(1)$ solution. However, we are not able to verify the accuracy of the solution in this region.

We may use Floquet analysis in the same way as for the $O(\delta)$ solution to perturb about the $O(1)$, π periodic, asymmetric solution. In general, this is again achieved by letting the perturbation be given by $\exp(\gamma t)F^{+}(\eta, t)$, where $\gamma = \gamma_R + i\gamma_I$ is the Floquet exponent and F^{+} is a π periodic function. At the point at which the $O(1)$ solution becomes quasi-periodic, it is found that a complex-conjugate pair of eigenvalues cross the γ_I axis into the $\gamma_R > 0$ plane. Since Floquet analysis gives us the eigenvalue with the largest real part, this means that whilst the first frequency of the quasi-periodic solution corresponds to the driving frequency, the second corresponds to the imaginary part of the Floquet exponent, γ_I. For even higher Reynolds numbers a period-doubling cascade occurs on the second frequency, which Hall and Papageorgiou (1999) speculate leads to chaotic solutions in the large Reynolds number limit.

In figure 6.26 we summarise our analysis of how the behaviour of the $O(\delta)$ solution changes with increasing Reynolds number for the case $\Delta = 0.25$. We show the early symmetry breaking bifurcation of the $O(\delta)$ solution (at which point this solution grows exponentially) and, following the stable $O(\delta)$ solution above the bifurcation of the $O(1)$ solution, the onset of exponential growth in the solution for $\hat{\psi}_2{}^{(1)}$. We also show the point at which we tentatively suggest that the $O(\delta)$ solution behaves like a quasi-periodic function multiplied by an exponentially growing function, before the $O(1)$ solution becomes quasi-periodic, at $Re \approx 255$.

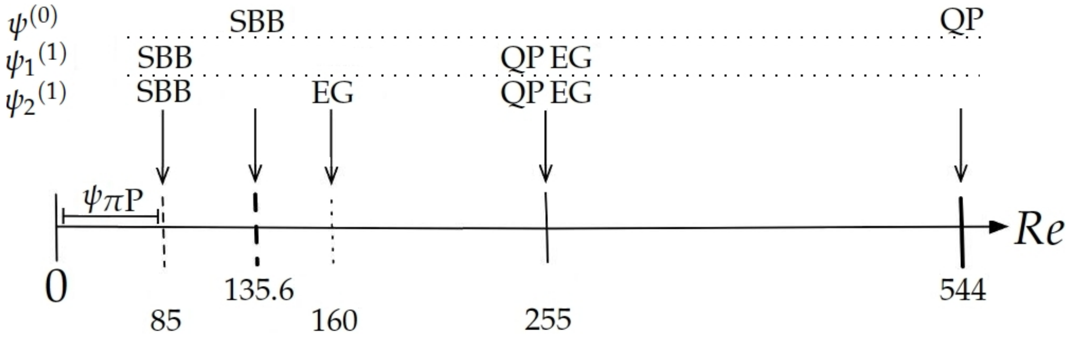

Figure 6.26: A summary of the changing behaviour of the $\Delta = 0.25$ streamfunction with increasing Reynolds number, where $\psi = x\psi^{(0)} + \delta(x^2\psi_1{}^{(1)} + \psi_2{}^{(1)})$ and $\hat{\psi}_2{}^{(1)} \equiv (1/H^{(0)})\partial\psi_2^{(1)}/\partial\eta$. Here πP denotes a π periodic solution, EG a bifurcation to an exponentially growing solution, SBB a symmetry breaking bifurcation and QP a quasi-periodic solution.

6.6 The Solution for Large Reynolds Numbers and Small Wall Amplitudes

In their paper Hall and Papageorgiou (1999) predict a simplified asymptotic structure for the $O(1)$ solution in the large Reynolds number limit when $\Delta \to 0$ in such a way that $Re^{1/2}\Delta = O(1)$. Here a steady streaming flow is found to occur in a boundary layer close to each wall. This flow is found to persist outside of these layers in the core-region. We attempt to extend this analysis to the streamfunction variable, ${\psi_1}^{(1)}$. This is done in the hope of drawing some more light on the exponentially growing solutions found in our results for the $O(\delta)$ correction (especially those for which the symmetry of the solution changed with time and suggested an asymmetric solution). Once the $O(\delta)$ solution becomes sufficiently large, the assumption that it is smaller than the $O(1)$ solution in equations (6.6) is no longer valid and formally, our analysis would need to be reconsidered. We also wish to better understand the evidence of an exponentially growing, quasi-periodic solution found in the case $\Delta = 0.25$. Taking the large Re limit can be likened to taking the frequency of the wall oscillations, ω, to infinity or, equally, taking the kinematic viscosity of the fluid, ν, to zero.

6.6.1 Setup

We begin by simplifying our governing equations by letting

$$\psi^{(0)} = -\eta \frac{dH^{(0)}}{dt} + {H^{(0)}}^3 f(\eta, t), \tag{6.93}$$

and

$${\psi_1}^{(1)} = \frac{3{H^{(0)}}^2 H^{(1)}}{2} f(\eta, t) + {H^{(0)}}^4 g(\eta, t), \tag{6.94}$$

where we write $\Delta = dRe^{-1/2}$ so that $H^{(0)} = 1 + dRe^{-1/2}\cos(2t)$ and we recall that $H^{(1)}$ is chosen to be constant. Using (6.37) and (6.38), equations (6.41) and (6.42) can be re-written as

$$\frac{\partial^3 f}{\partial t \partial \eta^2} + H^{(0)2}\left(\frac{\partial f}{\partial \eta}\frac{\partial^2 f}{\partial \eta^2} - f\frac{\partial^3 f}{\partial \eta^3}\right) = \frac{1}{ReH^{(0)2}}\frac{\partial^4 f}{\partial \eta^4}, \tag{6.95}$$

and

$$\begin{aligned}
&\frac{\partial^3 g}{\partial t \partial \eta^2} + \frac{3H^{(1)}}{2H^{(0)2}}\frac{\partial^3 f}{\partial t \partial \eta^2} + 2H^{(0)2}\frac{\partial f}{\partial \eta}\frac{\partial^2 g}{\partial \eta^2} + \left(\frac{7H^{(1)}}{2}\frac{\partial f}{\partial \eta} + H^{(0)2}\frac{\partial g}{\partial \eta}\right)\frac{\partial^2 f}{\partial \eta^2} \\
&- f\left(\frac{7H^{(1)}}{2}\frac{\partial^3 f}{\partial \eta^3} + H^{(0)2}\frac{\partial^3 g}{\partial \eta^3}\right) - 2H^{(0)2}\frac{\partial^3 f}{\partial \eta^3} g = \frac{1}{ReH^{(0)2}}\left(\frac{\partial^4 g}{\partial \eta^4} - \frac{H^{(1)}}{2H^{(0)2}}\frac{\partial^4 f}{\partial \eta^4}\right),
\end{aligned} \tag{6.96}$$

with boundary conditions, from (6.47) to (6.50),

$$f(\pm 1,t)=0, \quad \frac{\partial f}{\partial \eta}(\pm 1,t)=\frac{1}{H^{(0)^3}}\frac{dH^{(0)}}{dt}, \tag{6.97}$$

$$g(\pm 1,t)=0, \quad \frac{\partial g}{\partial \eta}(\pm 1,t)=-\frac{3H^{(1)}}{2H^{(0)^5}}\frac{dH^{(0)}}{dt}. \tag{6.98}$$

We may observe that replacing η with $-\eta$, f with $-f$ and g with $-g$ in these equations results in the same system. This shows that a basic, odd symmetric solution is possible (the same solution that becomes the unique, periodic solution for small enough Re).

In equations (6.95) and (6.96) the highest derivatives of η are multiplied by Re^{-1} so that a solution comprising an asymptotic expansion in powers of Re^{-1} will not satisfy one of the boundary conditions at each wall, and the infinite Re solution will not match the solution for general Re. This suggests a boundary layer region close to the walls where the solution changes rapidly. We let the boundary layer at each wall have thickness h and close to the walls we define a new variable, ζ, such that, at the upper wall for instance,

$$\eta = 1 - h\zeta, \quad \zeta = 0(1). \tag{6.99}$$

We let $\hat{f}(\zeta,t)$ and $\hat{g}(\zeta,t)$ denote the upper boundary-layer solution. Then (6.95) and (6.96) give us

$$\frac{1}{h^2}\frac{\partial^3 \hat{f}}{\partial t \partial \zeta^2}-\frac{H^{(0)^2}}{h^3}\left(\frac{\partial \hat{f}}{\partial \zeta}\frac{\partial^2 \hat{f}}{\partial \zeta^2}-\hat{f}\frac{\partial^3 \hat{f}}{\partial \zeta^3}\right)=\frac{1}{Reh^4 H^{(0)^2}}\frac{\partial^4 \hat{f}}{\partial \zeta^4}, \tag{6.100}$$

and

$$\begin{aligned}\frac{1}{h^2}\frac{\partial^3 \hat{g}}{\partial t \partial \zeta^2}+\frac{3H^{(1)}}{2h^2 H^{(0)^2}}\frac{\partial^3 \hat{f}}{\partial t \partial \zeta^2}-\frac{1}{h^3}\Bigg(2H^{(0)^2}\frac{\partial \hat{f}}{\partial \zeta}\frac{\partial^2 \hat{g}}{\partial \zeta^2}+\left(\frac{7H^{(1)}}{2}\frac{\partial \hat{f}}{\partial \zeta}+H^{(0)^2}\frac{\partial \hat{g}}{\partial \zeta}\right)\frac{\partial^2 \hat{f}}{\partial \zeta^2}\\ -\hat{f}\left(\frac{7H^{(1)}}{2}\frac{\partial^3 \hat{f}}{\partial \zeta^3}+H^{(0)^2}\frac{\partial^3 \hat{g}}{\partial \zeta^3}\right)-2H^{(0)^2}\frac{\partial^3 \hat{f}}{\partial \zeta^3}\hat{g}\Bigg)=\frac{1}{Reh^4 H^{(0)^2}}\left(\frac{\partial^4 \hat{g}}{\partial \zeta^4}-\frac{H^{(1)}}{2H^{(0)^2}}\frac{\partial^4 \hat{f}}{\partial \zeta^4}\right),\end{aligned} \tag{6.101}$$

with boundary conditions, from (6.97) and (6.98),

$$\hat{f}(0,t)=0, \quad \frac{\partial \hat{f}}{\partial \zeta}(0,t)=-\frac{h}{H^{(0)^3}}\frac{dH^{(0)}}{dt}, \tag{6.102}$$

$$\hat{g}(0,t)=0, \quad \frac{\partial \hat{g}}{\partial \zeta}(0,t)=\frac{3hH^{(1)}}{2H^{(0)^5}}\frac{dH^{(0)}}{dt}. \tag{6.103}$$

In addition, the boundary-layer solutions, $\hat{f}$ and $\hat{g}$, and core region solutions, f and g, must match at the edge of the boundary layer as $\zeta \to \infty$ (where $\zeta = O(1/h)$) and $\eta \to 1$.

We therefore have the matching conditions,

$$\hat{f}(\zeta \to \infty, t) \sim f(\eta \to 1, t), \tag{6.104}$$

$$\hat{g}(\zeta \to \infty, t) \sim g(\eta \to 1, t), \tag{6.105}$$

and equivalent matching conditions at the edge of the boundary layer at the lower wall, $\eta = -1$.

For a dominant balance between the unsteady and viscous terms in (6.100) and (6.101) we require the boundary layer at each wall to have thickness $h = Re^{-1/2}$, so that close to the upper wall,

$$\eta = 1 - Re^{-1/2}\zeta. \tag{6.106}$$

Then the second of equations (6.102) and (6.102) imply that $\hat{f}$ and $\hat{g}$ must be of $O(Re^{-1})$. Given the boundary layer thickness, we expand in powers of $Re^{-1/2}$ and $\hat{f}$ and $\hat{g}$ are given by the asymptotic expansions,

$$\hat{f} = \frac{1}{Re}\left(\hat{f}_0(\zeta, t) + \frac{1}{Re^{1/2}}\left(\hat{f}_{1T}(\zeta, t) + \hat{f}_{1M}(\zeta)\right) + O\left(\frac{1}{Re}\right)\right), \tag{6.107}$$

$$\hat{g} = \frac{1}{Re}\left(\hat{g}_0(\zeta, t) + \frac{1}{Re^{1/2}}\left(\hat{g}_{1T}(\zeta, t) + \hat{g}_{1M}(\zeta)\right) + O\left(\frac{1}{Re}\right)\right), \tag{6.108}$$

where to satisfy equations (6.100) to (6.103), we find that the first order terms must consist of a time dependent and a time independent part. Here we assume that $\hat{f}_{1T}$ and $\hat{g}_{1T}$ are time-periodic with zero mean. Meanwhile, we write the solution in the central region as

$$f = \frac{1}{Re}\left(f_{0T}(\eta, t) + f_{0M}(\eta, \tau) + \frac{1}{Re^{1/2}}f_1(\eta, t) + \frac{1}{Re}f_2(\eta, t) + O\left(\frac{1}{Re^{3/2}}\right)\right), \tag{6.109}$$

$$g = \frac{1}{Re}\left(g_{0T}(\eta, t) + g_{0M}(\eta, \tau) + \frac{1}{Re^{1/2}}g_1(\eta, t) + \frac{1}{Re}g_2(\eta, t) + O\left(\frac{1}{Re^{3/2}}\right)\right), \tag{6.110}$$

where it is necessary for the leading order terms to consist of both a time dependent and a time independent part due to the time independent terms in (6.107) and (6.108). Here, for convenience, we allow for a slow, modulating time-scale, defined by

$$\tau = \frac{1}{Re}t. \tag{6.111}$$

We assume that f_{0T} and g_{0T} are also time-periodic with zero mean.

6.6.2 The Matching Conditions

Substituting (6.109) and (6.110) into equations (6.95) and (6.96) gives us, to the highest order,

$$\frac{\partial^3 f_{0T}}{\partial t \partial \eta^2} = 0, \tag{6.112}$$

$$\frac{\partial^3 g_{0T}}{\partial t \partial \eta^2} + \frac{3}{2} H^{(1)} \frac{\partial^3 f_{0T}}{\partial t \partial \eta^2} = 0, \tag{6.113}$$

so that

$$f_{0T} = A_0(t)\eta + B_0(t), \tag{6.114}$$

$$g_{0T} = C_0(t)\eta + D_0(t), \tag{6.115}$$

where functions depending only on η are taken to be zero because f_{0T} and g_{0T} have zero mean over a period. Therefore, considering the time-dependent parts of the largest terms of the matching conditions, (6.104) and (6.105), we find that

$$\hat{f}_0(\zeta \to \infty, t) \sim A_0(t) + B_0(t), \tag{6.116}$$

$$\hat{g}_0(\zeta \to \infty, t) \sim D_0(t) + E_0(t). \tag{6.117}$$

Considering the time-independent parts, meanwhile, we find that

$$f_{0M}(1, \tau) \sim 0, \tag{6.118}$$

$$g_{0M}(1, \tau) \sim 0. \tag{6.119}$$

The next order terms of (6.95) and (6.96) give us

$$\frac{\partial^3 f_1}{\partial t \partial \eta^2} = 0, \tag{6.120}$$

$$\frac{\partial^3 g_1}{\partial t \partial \eta^2} - 3H^{(1)} d \cos(2t) \frac{\partial^3 f_{0T}}{\partial t \partial \eta^2} = 0, \tag{6.121}$$

and so

$$f_1 = A_1(t)\eta + B_1(t) + C_1(\eta), \tag{6.122}$$

$$g_1 = D_1(t)\eta + E_1(t) + F_1(\eta). \tag{6.123}$$

Therefore, the time-independent parts of the next order terms of (6.104) and (6.105) imply that

$$\hat{f}_{1M}(\zeta \to \infty, \tau) \sim -\zeta \frac{\partial f_{0M}}{\partial \eta}(1, \tau), \tag{6.124}$$

$$\hat{g}_{1M}(\zeta \to \infty, \tau) \sim -\zeta \frac{\partial g_{0M}}{\partial \eta}(1, \tau), \tag{6.125}$$

whilst the time-dependent parts give us

$$\hat{f}_{1T}(\zeta \to \infty, t) \sim -\zeta A_0(t) + A_1(t) + B_1(t) + C_1(1), \tag{6.126}$$

$$\hat{g}_{1T}(\zeta \to \infty, t) \sim -\zeta C_0(t) + D_1(t) + E_1(t) + F_1(1). \tag{6.127}$$

6.6.3 The Boundary-Layer Solution

Substituting the expansions (6.107) and (6.108) into equations (6.100) to (6.103), the largest terms give us the following system for $\hat{f}_0$ and $\hat{g}_0$:

$$\frac{\partial^3 \hat{f}_0}{\partial t \partial \zeta^2} = \frac{\partial^4 \hat{f}_0}{\partial \zeta^4}, \quad \hat{f}_0(0, t) = 0, \quad \frac{\partial \hat{f}_0}{\partial \zeta}(0, t) = 2d \sin(2t), \tag{6.128}$$

and

$$\frac{\partial^3 \hat{g}_0}{\partial t \partial \zeta^2} + \frac{3H^{(1)}}{2} \frac{\partial^3 \hat{f}_0}{\partial t \partial \zeta^2} = \frac{\partial^4 \hat{g}_0}{\partial \zeta^4} - \frac{H^{(1)}}{2} \frac{\partial^4 \hat{f}_0}{\partial \zeta^4}, \quad \hat{g}_0(0, t) = 0, \quad \frac{\partial \hat{g}_0}{\partial \zeta}(0, t) = -3dH^{(1)} \sin(2t). \tag{6.129}$$

These equations are supplemented by the matching conditions (6.116) and (6.117). We note that the first of each of these equations implies that $\hat{f}_0$ and $\hat{g}_0$ must be finite as $\zeta \to \infty$. Using these conditions and separation of variables, we obtain the solution to (6.128),

$$\hat{f}_0 = \frac{di}{(1+i)} e^{2it} \left(e^{-(1+i)\zeta} - 1 \right) + \text{c.c.}, \tag{6.130}$$

where c.c. denotes the complex conjugate. Equation (6.130) together with (6.129) suggests that $\hat{g}_{1\zeta\zeta} = A(\zeta) \exp(2it) +$ c.c., and we find that

$$\hat{g}_0 = -dH^{(1)} e^{2it} \left((1+i) \left(e^{-(1+i)\zeta} - 1 \right) + \frac{i}{2} \zeta e^{-(1+i)\zeta} \right) + \text{c.c.}. \tag{6.131}$$

Considering the next order terms of (6.100) to (6.103), using equations (6.130) and (6.131), we find that $\hat{f}_{1M}$ and $\hat{g}_{1M}$ satisfy the equations,

$$d^2 \left(4e^{-2\zeta} - (1+i) \left(2e^{-(1+i)\zeta} + e^{-(1-i)\zeta} \right) + \text{c.c.} \right) = \frac{\partial^4 \hat{f}_{1M}}{\partial \zeta^4},$$

$$\hat{f}_{1M}(0) = 0, \quad \frac{\partial \hat{f}_{1M}}{\partial \zeta}(0) = 0, \tag{6.132}$$

and

$$\begin{aligned}&d^2H^{(1)}\left(-2\left(2\zeta+1\right)e^{-2\zeta}+3i\zeta e^{-(1+i)\zeta}+(1+i)\left(5e^{-(1+i)\zeta}+\left(\zeta+1\right)e^{-(1-i)\zeta}\right)+\text{c.c.}\right)\\&=\frac{\partial^4\hat{g}_{1M}}{\partial\zeta^4}-\frac{1}{2}H^{(1)}\frac{\partial^4\hat{f}_{1M}}{\partial\zeta^4},\quad \hat{g}_{1M}(0)=0,\quad \frac{\partial\hat{g}_{1M}}{\partial\zeta}(0)=0.\end{aligned}\tag{6.133}$$

Here we use the technique of time-averaging, integrating the equations obtained from (6.100) to (6.103) over a period of π in time. From the remaining terms, we find that $\hat{f}_{1T}$ and $\hat{g}_{1T}$ satisfy

$$\begin{aligned}&\frac{\partial^3\hat{f}_{1T}}{\partial t\partial\zeta^2}-3d^2\left((1+i)e^{4it}e^{-(1+i)\zeta}+\text{c.c.}\right)=\frac{\partial^4\hat{f}_{1T}}{\partial\zeta^4},\\&\hat{f}_{1T}(0,t)=0,\quad \frac{\partial\hat{f}_{1T}}{\partial\zeta}(0,t)=-\frac{3i}{2}d^2e^{4it}+\text{c.c.},\end{aligned}\tag{6.134}$$

and

$$\begin{aligned}&\frac{\partial^3\hat{g}_{1T}}{\partial t\partial\zeta^2}+\frac{3}{2}H^{(1)}\frac{\partial^3\hat{f}_{1T}}{\partial t\partial\zeta^2}+d^2H^{(1)}\left(3i\zeta e^{4it}e^{-(1+i)\zeta}+(1+i)e^{4it}\left(6e^{-(1+i)\zeta}-e^{-2(1+i)\zeta}\right)+\text{c.c.}\right)\\&=\frac{\partial^4\hat{g}_{1T}}{\partial\zeta^4}-\frac{1}{2}H^{(1)}\frac{\partial^4\hat{f}_{1T}}{\partial\zeta^4},\quad \hat{g}_{1T}(0,t)=0,\quad \frac{\partial\hat{g}_{1T}}{\partial\zeta}(0,t)=\frac{15i}{4}d^2H^{(1)}e^{4it}+\text{c.c.}.\end{aligned}\tag{6.135}$$

These equations are supplemented by conditions (6.124) to (6.127). We may solve (6.132) and (6.133) to find that

$$\hat{f}_{1M}=d^2\left(\frac{(1+i)}{2}\left(e^{-(1+i)\zeta}-1\right)+\frac{(1+i)}{4}\left(e^{-(1-i)\zeta}-1\right)+\text{c.c.}+\frac{1}{4}\left(e^{-2\zeta}-1\right)+\frac{3}{2}\zeta\right),\tag{6.136}$$

$$\begin{aligned}\hat{g}_{1M}=&-d^2H^{(1)}\left(i\left(\frac{3}{4}\zeta-1\right)e^{-(1+i)\zeta}+\frac{5(1+i)}{2}\left(e^{-(1+i)\zeta}-1\right)+\frac{(1+i)}{8}\left(e^{-(1-i)\zeta}-1\right)\right.\\&\left.+\frac{(1+i)}{4}\zeta e^{-(1-i)\zeta}+\text{c.c.}+\frac{1}{4}\zeta e^{-2\zeta}+\frac{1}{2}\left(e^{-2\zeta}-1\right)+\frac{11}{4}\zeta\right).\end{aligned}\tag{6.137}$$

Here, in order to satisfy the second of the boundary conditions in (6.132) and (6.133), we require a term multiplied by ζ in $\hat{f}_{1M}$ and $\hat{g}_{1M}$, explaining the need for f_{0M} and g_{0M} in our expansions. Letting $\hat{f}_{1T}=B(\zeta)e^{4it}+$ c.c. and $\hat{g}_{1T}=C(\zeta)e^{4it}+$ c.c. in (6.134) and (6.135), we find that

$$\hat{f}_{1T}=\frac{3(1+i)d^2}{4}\left(2^{1/2}\left(e^{-2^{1/2}(1+i)\zeta}-1\right)-\left(e^{-(1+i)\zeta}-1\right)\right)e^{4it}-A_0(t)\zeta+\text{c.c.},\tag{6.138}$$

$$\begin{aligned}\hat{g}_{1T}=&\frac{d^2H^{(1)}}{4}\left(-\frac{115(1+i)}{2^{5/2}}\left(e^{-2^{1/2}(1+i)\zeta}-1\right)+\frac{33(1+i)}{2}\left(e^{-(1+i)\zeta}-1\right)\right.\\&\left.+3i\zeta e^{-(1+i)\zeta}+\frac{(1+i)}{8}\left(e^{-2(1+i)\zeta}-1\right)-12i\zeta e^{-2^{1/2}(1+i)\zeta}\right)e^{4it}-C_0(t)\zeta+\text{c.c.},\end{aligned}\tag{6.139}$$

where we have made use of the matching conditions (6.126) and (6.127), which imply that $\hat{f}_{1T}$ and $\hat{g}_{1T}$ contain a term proportional to ζ as well as terms independent of ζ.

6.6.4 The Core-Flow Solution

Equations (6.114), (6.115), (6.122) and (6.123) may be fully determined by matching with the upper boundary-layer solution using equations (6.116), (6.117), (6.126) and (6.127), and by making use of similar conditions at the lower wall, $\eta = -1$. These equations, however, are not needed for our analysis.

Integrating the equations resulting from the next order terms of (6.95) and (6.96) over a period π in time, and because f_{0T} and g_{0T} have zero mean in time and f_2 and g_2 are assumed to be periodic in time, we find that

$$\frac{\partial^3 f_{0M}}{\partial\tau\partial\eta^2} + \frac{\partial f_{0M}}{\partial\eta}\frac{\partial^2 f_{0M}}{\partial\eta^2} - f_{0M}\frac{\partial^3 f_{0M}}{\partial\eta^3} = \frac{\partial^4 f_{0M}}{\partial\eta^4}, \tag{6.140}$$

$$\begin{aligned}&\frac{\partial^3 g_{0M}}{\partial\tau\partial\eta^2} + \frac{3H^{(1)}}{2}\frac{\partial^3 f_{0M}}{\partial\tau\partial\eta^2} + 2\frac{\partial f_{0M}}{\partial\eta}\frac{\partial^2 g_{0M}}{\partial\eta^2} + \left(\frac{7H^{(1)}}{2}\frac{\partial f_{0M}}{\partial\eta} + \frac{\partial g_{0M}}{\partial\eta}\right)\frac{\partial^2 f_{0M}}{\partial\eta^2}\\ &\quad - f_{0M}\left(\frac{7H^{(1)}}{2}\frac{\partial^3 f_{0M}}{\partial\eta^3} + \frac{\partial^3 g_{0M}}{\partial\eta^3}\right) - 2\frac{\partial^3 f_{0M}}{\partial\eta^3}g_{0M} = \frac{\partial^4 g_{0M}}{\partial\eta^4} - \frac{H^{(1)}}{2}\frac{\partial^4 f_{0M}}{\partial\eta^4}.\end{aligned} \tag{6.141}$$

From (6.118), (6.119), (6.124) and (6.125) and similar matching conditions at the lower wall, $\eta = -1$, equations (6.140) and (6.141) are accompanied by the boundary conditions,

$$f_{0M}(\eta = \pm 1) = 0, \quad \frac{\partial f_{0M}}{\partial\eta}(\eta = \pm 1) = -\frac{3}{2}d^2, \tag{6.142}$$

$$g_{0M}(\eta = \pm 1) = 0, \quad \frac{\partial g_{0M}}{\partial\eta}(\eta = \pm 1) = \frac{11}{4}d^2 H^{(1)}. \tag{6.143}$$

Letting $f_{0M} = (3d^2/2)\check{f}$ and $g_{0M} = (3d^2/2)H^{(1)}\check{g}$, as well as $\tau = (3d^2/2)^{-1}\check{\tau}$, in equations (6.140) to (6.143), we may re-write the system as

$$\begin{aligned}&\frac{\partial^3 \check{f}}{\partial\check{\tau}\partial\eta^2} + \frac{\partial \check{f}}{\partial\eta}\frac{\partial^2 \check{f}}{\partial\eta^2} - \check{f}\frac{\partial^3 \check{f}}{\partial\eta^3} = \frac{1}{Re_s}\frac{\partial^4 \check{f}}{\partial\eta^4}, \quad Re_s = \frac{3d^2}{2},\\ &\check{f}(\eta = \pm 1) = 0, \quad \frac{\partial \check{f}}{\partial\eta}(\eta = \pm 1) = -1,\end{aligned} \tag{6.144}$$

and

$$\begin{aligned}&\frac{\partial^3 \check{g}}{\partial\check{\tau}\partial\eta^2} + \frac{3}{2}\frac{\partial^3 \check{f}}{\partial\check{\tau}\partial\eta^2} + 2\frac{\partial \check{f}}{\partial\eta}\frac{\partial^2 \check{g}}{\partial\eta^2} + \left(\frac{7}{2}\frac{\partial \check{f}}{\partial\eta} + \frac{\partial \check{g}}{\partial\eta}\right)\frac{\partial^2 \check{f}}{\partial\eta^2} - \check{f}\left(\frac{7}{2}\frac{\partial^3 \check{f}}{\partial\eta^3} + \frac{\partial^3 \check{g}}{\partial\eta^3}\right)\\ &- 2\frac{\partial^3 \check{f}}{\partial\eta^3}\check{g} = \frac{1}{Re_s}\left(\frac{\partial^4 \check{g}}{\partial\eta^4} - \frac{1}{2}\frac{\partial^4 \check{f}}{\partial\eta^4}\right), \quad \check{g}(\eta = \pm 1) = 0, \quad \check{g}_\eta(\eta = \pm 1) = \frac{11}{6}.\end{aligned} \tag{6.145}$$

Here Re_s is the steady-streaming Reynolds number. This system can be thought of as our original forced system, (6.95) to (6.98), but with a steady forcing from the walls. Like the general case, this system allows a solution that is odd in η. For small d (equivalent to small Reynolds numbers) the system (6.144) and (6.145) suggests that we expand as follows:

$$\check{f} = \check{f}_1 + d^2 \check{f}_2 + O(d^4), \tag{6.146}$$

$$\check{g} = \check{g}_1 + d^2 \check{g}_2 + O(d^4). \tag{6.147}$$

Then, to leading order we are left with the viscous terms so that the solution is given by

$$\check{f} = \frac{1}{2}\left(\eta - \eta^3\right) + O(d^2), \tag{6.148}$$

$$\check{g} = -\frac{11}{12}\left(\eta - \eta^3\right) + O(d^2). \tag{6.149}$$

6.6.5 Stability of the Odd Steady-Streaming Solution

The linear stability of the steady, odd solution may be analysed by writing

$$\check{f} = \check{f}_{SS}(\eta) + \check{f}_P(\eta, \check{\tau}), \tag{6.150}$$

$$\check{g} = \check{g}_{SS}(\eta) + \check{g}_P(\eta, \check{\tau}), \tag{6.151}$$

for $\check{f}_P$, $\check{g}_P$ small. For small d $\check{f}_{SS}$ and $\check{g}_{SS}$ are given by (6.148) and (6.149), whilst for general d they satisfy the steady form of equations (6.144) and (6.145). The resulting boundary value problem may be solved using the Matlab solver *bvp4c* with a symmetric initial guess. Then, neglecting terms of order smaller than $\check{f}_P$ or $\check{g}_P$, (6.144) and (6.145) give us

$$\begin{aligned}
&\frac{\partial^3 \check{f}_P}{\partial \check{\tau} \partial \eta^2} + \frac{\partial \check{f}_{SS}}{\partial \eta}\frac{\partial^2 \check{f}_P}{\partial \eta^2} + \frac{\partial \check{f}_P}{\partial \eta}\frac{\partial^2 \check{f}_{SS}}{\partial \eta^2} - \check{f}_{SS}\frac{\partial^3 \check{f}_P}{\partial \eta^3} - \check{f}_P \frac{\partial^3 \check{f}_{SS}}{\partial \eta^3} = \frac{1}{Re_s}\frac{\partial^4 \check{f}_P}{\partial \eta^4}, \\
&\check{f}_P(\eta = \pm 1, t) = 0, \quad \frac{\partial \check{f}_P}{\partial \eta}(\eta = \pm 1, t) = 0,
\end{aligned} \tag{6.152}$$

and

$$\begin{aligned}
&\frac{\partial^3 \check{g}_P}{\partial \check{\tau} \partial \eta^2} + \frac{3}{2}\frac{\partial^3 \check{f}_P}{\partial \check{\tau} \partial \eta^2} + 2\frac{\partial \check{f}_{SS}}{\partial \eta}\frac{\partial^2 \check{g}_P}{\partial \eta^2} + 2\frac{\partial \check{f}_P}{\partial \eta}\frac{\partial^2 \check{g}_{SS}}{\partial \eta^2} + \left(\frac{7}{2}\frac{\partial \check{f}_{SS}}{\partial \eta} + \frac{\partial \check{g}_{SS}}{\partial \eta}\right)\frac{\partial^2 \check{f}_P}{\partial \eta^2} \\
&+ \left(\frac{7}{2}\frac{\partial \check{f}_P}{\partial \eta} + \frac{\partial \check{g}_P}{\partial \eta}\right)\frac{\partial^2 \check{f}_{SS}}{\partial \eta^2} - \check{f}_{SS}\left(\frac{7}{2}\frac{\partial^3 \check{f}_P}{\partial \eta^3} + \frac{\partial^3 \check{g}_P}{\partial \eta^3}\right) - \check{f}_P\left(\frac{7}{2}\frac{\partial^3 \check{f}_{SS}}{\partial \eta^3} + \frac{\partial^3 \check{g}_{SS}}{\partial \eta^3}\right) \\
&- 2\frac{\partial^3 \check{f}_{SS}}{\partial \eta^3}\check{g}_P - 2\frac{\partial^3 \check{f}_P}{\partial \eta^3}\check{g}_{SS} = \frac{1}{Re_s}\left(\frac{\partial^4 \check{g}_P}{\partial \eta^4} - \frac{1}{2}\frac{\partial^4 \check{f}_P}{\partial \eta^4}\right), \\
&\check{g}_P(\eta = \pm 1, t) = 0, \quad \frac{\partial \check{g}_P}{\partial \eta}(\eta = \pm 1, t) = 0.
\end{aligned} \tag{6.153}$$

These equations may be solved using the method described in section 6.4. Here we use the initial conditions, $\check{f}_P(\eta, 0) = (\eta + 1)^2(\eta - 1)^2$, $\check{g}_P(\eta, 0) = 0$. Again, numerical consistency is checked by increasing the number of grid points in our numerical program. Since our solutions are found to converge, we can be sure that our results are accurate.

Hall and Papageorgiou (1999) find that the odd solution loses stability to a steady, even mode (so that, overall, the solution is asymmetric). This suggests that we may write $\check{f}_P = A_f(\eta)\exp(S_f\check{\tau})$ and $\check{g}_P = A_g(\eta)\exp(S_g\check{\tau})$ and consider $\log(\check{f}_{P\eta\eta}(-1, \check{\tau}))$ and $\log(\check{g}_{P\eta\eta}(-1, \check{\tau}))$, the gradient of which, once the solution has settled in time, will give us the (real) growth rates, S_f and S_g. We seek an approximation to the value of d (and therefore the Reynolds number) for which the growth rates change from negative to positive and the symmetric solution loses stability.

Plots of S_f and S_g against d are given in figure 6.27. We find that $\check{f}_{SS}$ loses symmetry for d between 3.39 and 3.40, in agreement with Hall and Papageorgiou (1999) (who find $d = 3.39$). We note that from our plots it appears that d is closer to 3.40 than 3.39, but that greater accuracy could only be achieved by increasing the number of grid points

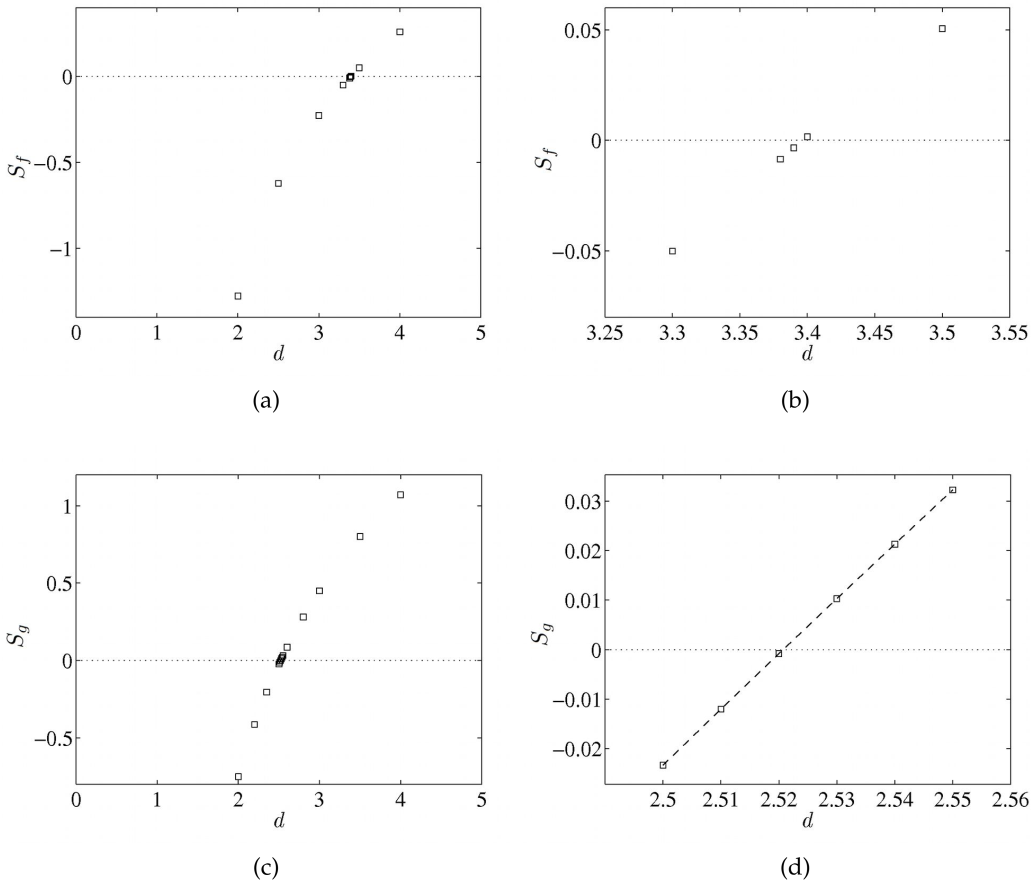

(a) (b)

(c) (d)

Figure 6.27: When $Re \to \infty$, $\Delta = O(Re^{-1/2})$, the growth rates, S_f and S_g ((a) and (c) and close up in (b) and (d)), plotted against d when perturbing about the steady, symmetric solutions, $\check{f}_{SS}$ and $\check{g}_{SS}$. The dashed line in (d) shows a best fit line through the data points.

in the numerical program. Hall and Papageorgiou (1999) note that Watson *et al.* (2008) (whose results are noted to be unlikely to be correct to 3 significant figures) also find d to be 3.40. Surprisingly, in the case of $\check{g}_{SS}$, symmetry is lost at an earlier value than $\check{f}_{SS}$ (at $d = 2.52$ to 2 decimal places). Examination of $\check{g}_P$ reveals that in this case too, stability is lost to an even mode (see figure 6.28).

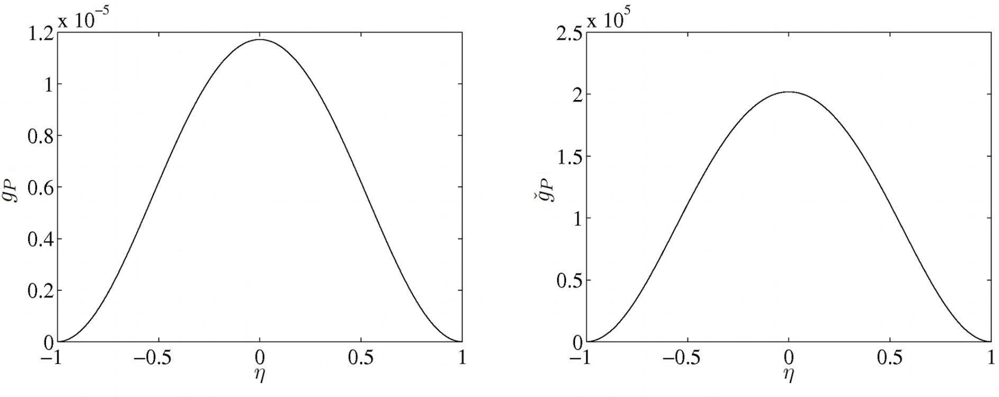

(a) (b)

Figure 6.28: When $Re \to \infty$, $\Delta = O(Re^{-1/2})$, $\check{g}_P$ plotted against η when perturbing about the steady, symmetric solutions, $\check{f}_{SS}$ and $\check{g}_{SS}$. Here $t = 20$ and (a) $d = 2$ and the solution is stable and (b) $d = 3$ and the solution is unstable.

We next consider the full equations, (6.144) and (6.145), which may also be solved using the method described in section 6.4, again being careful that our solutions converge when we increase the number of grid points in our program. Above the bifurcation of the $O(\delta)$ solution we must use asymmetric initial conditions ($\check{f}(\eta, 0) = -(\eta+1)^2(\eta-1)^3$, $\check{g}(\eta, 0) = 0$) to obtain the asymmetric solution for $\check{g}$. In these equations, above the bifurcation in the case of the $O(1)$ solution, the inclusion of nonlinear terms restrict unlimited growth of $\check{f}_P$, resulting in a stable asymmetric solution. In the $O(\delta)$ system, however, there are no such nonlinear terms present and the growing even mode is unbounded. Here the solution grows exponentially for all time (see figure 6.29, where we plot $\log(\check{g}_{\eta\eta}(-1, \check{t}))$ against $\check{t}$ just above the bifurcation of the $O(\delta)$ solution, obtaining a linearly increasing function once the solution has settled). We note that the boundary conditions in the system (6.145) are still satisfied, but since $\check{g}_P$ is growing exponentially with time, the solution for $\check{g}_{SS}$ (which has gradient 11/6 at $\eta = \pm 1$) is eclipsed by comparison. If we substitute (6.151) into equation (6.145) whilst assuming that $\check{g}_P \gg \check{g}_{SS}, \check{f}_{SS}$ (and $\check{f}_{SS} \gg \check{f}_P$), we find that to first order, the slope of $\check{g}$ is zero at $\eta = \pm 1$. This can also be seen in figure 6.30, where we find that the solution for $\check{g}$ appears to change from odd to asymmetric to even in η with increasing $\check{t}$ as the relative sizes of $\check{g}_{SS}$ and $\check{g}_P$ change.

We have therefore found a mechanism by which it is possible for the $O(\delta)$ solution to bifurcate to an asymmetric solution before the $O(1)$ solution found by Hall and Papageorgiou (1999). This also suggests that had we included nonlinear terms in our

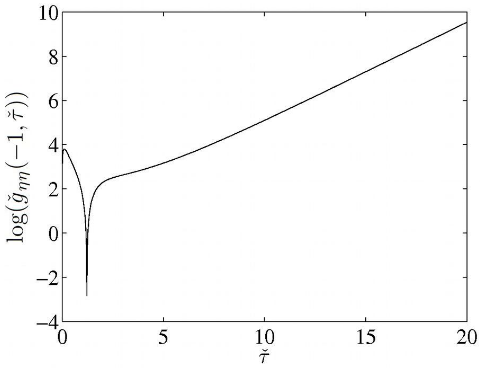

Figure 6.29: When $Re \to \infty$, $\Delta = O(Re^{-1/2})$, starting with asymmetric initial conditions when $d = 3$, $\log(\check{g}_{\eta\eta}(-1,\check{\tau}))$ plotted against $\check{\tau}$.

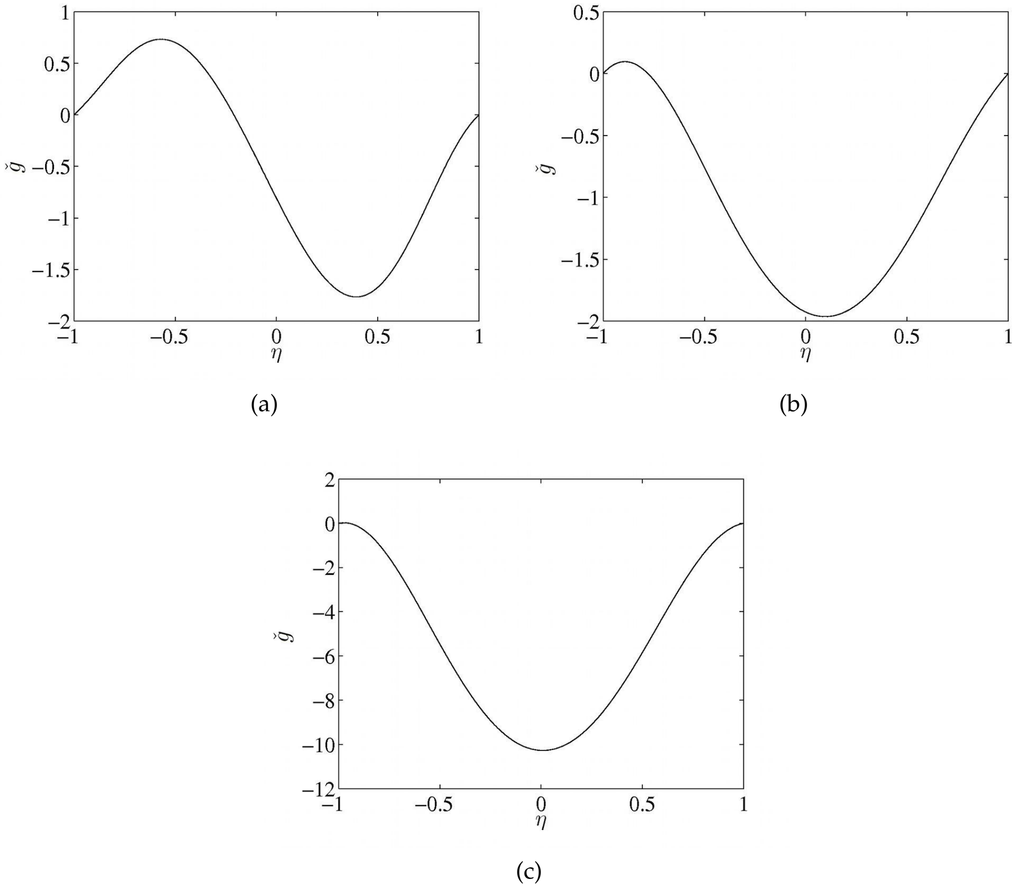

Figure 6.30: When $Re \to \infty$, $\Delta = O(Re^{-1/2})$, starting with asymmetric initial conditions when $d = 3$, plots of $\check{g}$ against η when $\check{\tau} =$ (a) 1, (b) 4 and (c) 8.

analysis for the $O(\delta)$ solution, we would obtain a stable asymmetric solution above this bifurcation.

This analysis is greatly helpful in understanding the exponentially growing solutions found in our numerical results for general Re and Δ. Moreover, we have confirmation that in the cases when we obtain a growing, even solution for ${\psi_1}^{(1)}$ (at a Reynolds number below the bifurcation of the $O(1)$ solution to an asymmetric solution) our solution is in fact asymmetric here. If we had solved the full nonlinear equations for ${\psi_1}^{(1)}$ rather than using a linear approximation, we would expect to obtain a π-periodic, asymmetric solution at this point. Since ${\hat{\psi}_2}^{(1)}$ is even for small Re, when this solution loses stability to an even mode, the symmetry is not changed. When the odd ${\psi_1}^{(1)}$ loses stability and becomes asymmetric, however, its appearance in the equations for ${\hat{\psi}_2}^{(1)}$ means that ${\hat{\psi}_2}^{(1)}$ clearly becomes asymmetric. We can therefore conclude that this is the point at which the $O(\delta)$ solution becomes asymmetric.

Since $\Delta = dRe^{-1/2}$, when $\Delta = 0.25$, our above analysis predicts that the asymmetric bifurcation of the $O(1)$ solution occurs at $Re = 3.39^2/\Delta^2 + \cdots \approx 184$, compared with the value of $Re \approx 135.6$ found from the numerical calculations (we must take Δ less than around 0.15 for a very close match). The bifurcation of the $O(\delta)$ solution is predicted to occur at $Re = 2.52^2/\Delta^2 + \cdots \approx 102$ compared to $Re \approx 85$ from the numerical calculations and so we find that we have as good an agreement as Hall and Papageorgiou (1999).

6.6.6 Stability of the Asymmetric Steady-Streaming Solution

We next perform a similar linear stability analysis on the steady, asymmetric solution which occurs when d is greater than 3.39, writing

$$\check{f} = \check{f}_{SA}(\eta) + \check{f}_P(\eta, \check{\tau}), \tag{6.154}$$

$$\check{g} = \check{g}_{SA}(\eta) + \check{g}_P(\eta, \check{\tau}). \tag{6.155}$$

Here we change the initial conditions in the boundary value problem for $\check{f}_{SA}$ and $\check{g}_{SA}$ appropriately to obtain $\check{f}_{SA}$ and find that it is possible to obtain a steady, asymmetric solution for $\check{g}_{SA}$. This suggests that above the bifurcation of the $O(1)$ solution, as well as the unstable asymmetric solution for $\check{g}$, there also exists a stable asymmetric solution for which the equivalent $O(1)$ solution is stable asymmetric.

Hall and Papageorgiou (1999) note that the $O(1)$ steady, asymmetric solution loses stability, via a Hopf bifurcation, to a periodic mode. Since this mode is periodic on the timescale $\tau \ll t$, where t is the timescale of the wall forcing, this means that there are two different periodicity timescales and the overall flow is quasi-periodic. We therefore write $\check{f}_P = A_f(\eta)\exp(S_f\check{\tau})$ and $\check{g}_P = A_g(\eta)\exp(S_g\check{\tau})$, where $S_f = S_{fR} + iS_{fI}$ and $S_g = S_{gR} + iS_{gI}$ for S_{fR}, S_{fI}, S_{gR} and S_{gI} real. At a bifurcation to a quasi-periodic solution, a pair of complex conjugate eigenvalues with imaginary parts equal to $\pm iS_{fI}$ or $\pm iS_{gI}$ cross the imaginary axis into the $S_{fR} > 0$ or $S_{gR} > 0$ plane. Therefore, above a certain d, S_f and S_g have an imaginary as well as a real part and we are required to find best fitting lines through the peaks of $\check{f}_{P\eta\eta}(-1, \check{\tau})$ and $\check{g}_{P\eta\eta}(-1, \check{\tau})$ using polynomial interpolation before taking the logarithm of these lines in order to obtain the growth rates, S_{fR} and S_{gR}.

Figure 6.31 shows plots of S_{fR} and S_{gR} against d. We find that $\check{f}_{SA}$ loses stability for

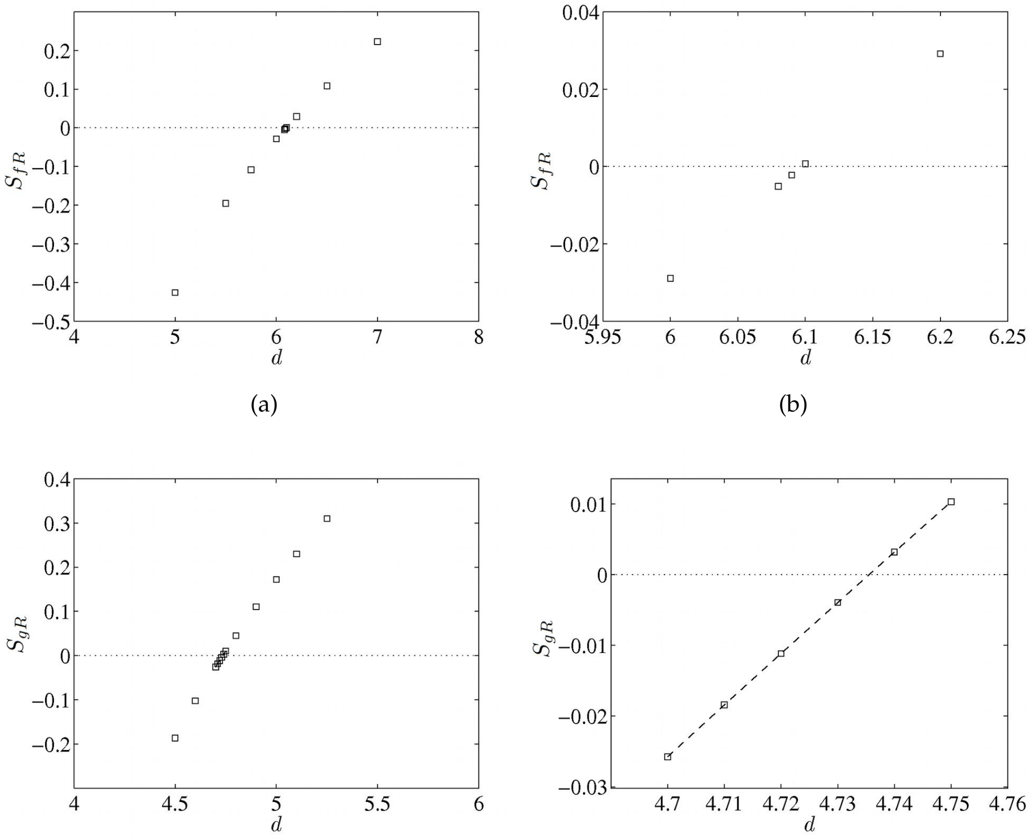

(a) (b)

(c) (d)

Figure 6.31: When $Re \to \infty$, $\Delta = O(Re^{-1/2})$, the growth rates, S_{fR} and S_{gR} ((a) and (c) and close up in (b) and (d)), plotted against d when perturbing about the steady, asymmetric solutions, $\check{f}_{SA}$ and $\check{g}_{SA}$. The dashed line in (d) shows a best fit line through the data points.

d between 6.09 and 6.10, which is again in closer agreement with Watson *et al.* (2008) (who find that the critical d is 6.09) than Hall and Papageorgiou (1999) (who find that $d = 5.99$). Again, increasing the number of grid points in our program may improve our estimate. We find that in the case of $\check{g}_{SA}$, again the bifurcation occurs early and stability is lost at an earlier value than $\check{f}_{SA}$ (at around $d = 4.74$ to 2 decimal places). Like for the $O(1)$ solution, stability is lost to a periodic mode (see figure 6.32). Interestingly, the distance between peaks is not the same for the $O(\delta)$ and $O(1)$ solutions, suggesting that $S_{fI} \neq S_{gI}$. Although the distances vary slightly depending on d, to 2 significant figures, we find that in the $O(1)$ case, the period in $\check{\tau}$ of the destabilising mode is 3.4, whilst in the $O(\delta)$ case, it is 3.2. Since $t = 2/(3\Delta^2)\check{\tau}$, taking $\Delta = 0.25$, for example, this

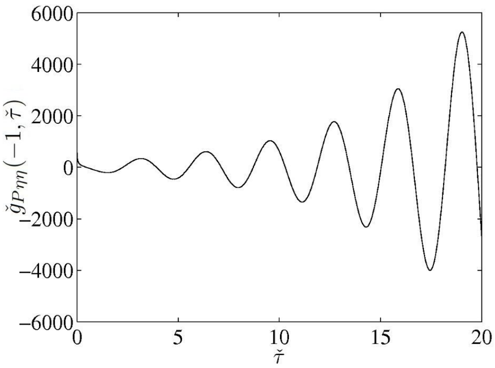

Figure 6.32: When $Re \to \infty$, $\Delta = O(Re^{-1/2})$, $\check{g}_{P\eta\eta}(-1, \check{\tau})$ plotted against $\check{\tau}$ when perturbing about the steady, asymmetric solutions, $\check{f}_{SA}$ and $\check{g}_{SA}$, when $d = 5$.

predicts that the $O(1)$ solution loses stability to a mode with a period of around 36 in t, compared to around 34 for the $O(\delta)$ solution.

We again consider the full equations, (6.144) and (6.145). Just below the bifurcation of the $O(\delta)$ solution to a growing, quasi-periodic solution, we find that we are able to latch onto the stable, asymmetric solution for the $O(\delta)$ solution. Above the bifurcation, we again find that unlike in the case of the $O(1)$ solution where the inclusion of nonlinear terms prohibit unlimited growth, in the case of the $O(\delta)$ solution, the periodic mode grows exponentially (see figure 6.33, where we have plotted $\log(p(\check{g}_{\eta\eta}(-1, \check{\tau})))$, where $p(y)$ defines the peaks of y, obtaining a linearly increasing function once the solution has settled). Above the bifurcation of the $O(1)$ solution to a quasi-periodic solution, we find that our program still naturally detects the exponentially growing, quasi-periodic $O(\delta)$ solution.

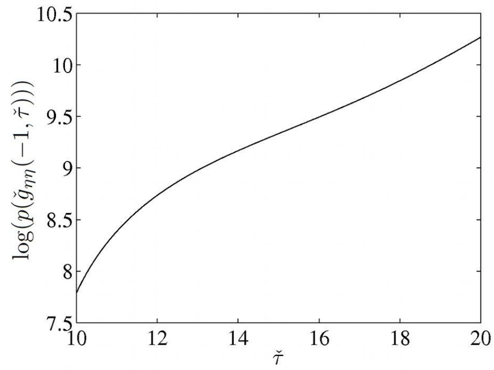

(a)

Figure 6.33: When $Re \to \infty$, $\Delta = O(Re^{-1/2})$, starting with asymmetric initial conditions when $d = 5$, $\log(p(\check{g}_{\eta\eta}(-1, \check{\tau})))$ plotted against $\check{\tau}$ (where $p(y)$ defines the peaks of y).

Relating these findings back to our numerical results in the case $\Delta = 0.25$, our suspicions that we obtain a quasi-periodic solution for the $O(\delta)$ solution at a lower Reynolds number than the $O(1)$ solution seem to be justified. Again, had we solved the full nonlinear equations for the $O(\delta)$ correction, we would expect that the solution would remain stable above the bifurcation.

When $\Delta = 0.25$, the $O(1)$ solution is predicted to bifurcate to a quasi-periodic solution at $Re = 5.99^2/\Delta^2 + \cdots \approx 574$, compared with $Re \approx 544$ from the numerical calculations. The $O(\delta)$ solution, meanwhile, is predicted to bifurcate at $Re = 4.74^2/\Delta^2 + \cdots \approx 359$, in comparison with our tentative estimation of $Re \approx 255$ from the numerical results.

A summary of how the solution changes with increasing d in the $Re \to \infty$, $\Delta = O(Re^{-1/2})$ limit is shown in figure 6.34. Shown is the early symmetry breaking bifurcation of the $O(\delta)$ solution and, following the steady, asymmetric $O(\delta)$ solution above the symmetry breaking bifurcation of the $O(1)$ solution, the point at which the $O(\delta)$ solution becomes quasi-periodic before the $O(1)$ solution.

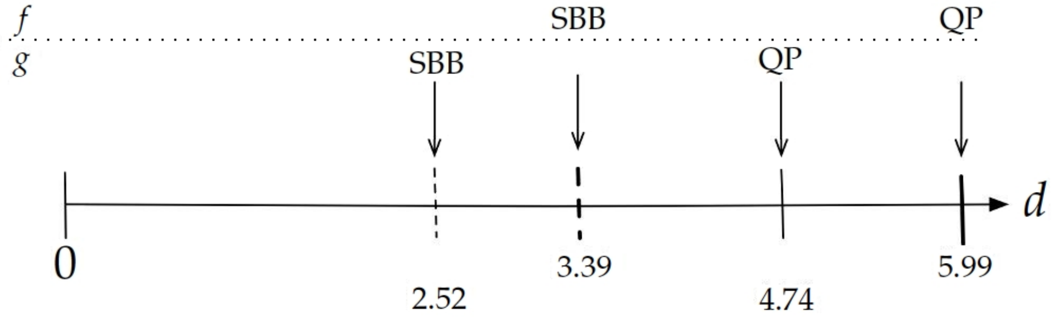

Figure 6.34: A summary of the changing behaviour of the $Re \to \infty$, $\Delta = O(Re^{-1/2})$ streamfunction with increasing d, where $\psi = x\psi^{0)} + \delta(x^2{\psi_1}^{(1)} + {\psi_2}^{(1)})$, $\psi^{(0)} = -\eta dH^{(0)}/dt + {H^{(0)}}^3 f$ and ${\psi_1}^{(1)} = -3{H^{(0)}}^2 H^{(1)} f/2 + {H^{(0)}}^4 g$. Here SBB denotes a symmetry breaking bifurcation and QP a quasi-periodic solution.

For d above 5.99 $\check{f}$ undergoes successive period doubling and there is a Feigenbaum cascade to chaos. This leads Hall and Papageorgiou (1999) to suggest, with reference to the case $\Delta = 0.25$, that chaotic solutions can indeed be found for all Δ if Re is taken large enough. We might expect the same to be true for the $O(\delta)$ solution.

6.7 Discussion

We have built on the work of Hall and Papageorgiou (1999), who considered general-Reynolds-number fluid flow in a channel with periodically oscillating walls. Here it was found that for small Reynolds numbers a unique, periodic, symmetric solution exists and the solution is synchronised with the wall motion. As the Reynolds number increases, a bifurcation to a periodic, asymmetric solution can be observed, before further bifurcations eventually lead to a chaotic solution. On route to chaos the solution may include a Feigenbaum cascade or quasi-periodic solutions, depending on the wall amplitude. In our case we have considered walls that vary gradually. We have satisfied the vorticity equation by assuming a similarity solution for the leading order and perturbation streamfunction. This leads to a series of partial differential equations that depend on time and the vertical co-ordinate only. At zero Reynolds number, it is possible to solve analytically and we can draw a comparison between our solution and Poiseuille flow in a diverging channel modulated periodically in time.

For an arbitrary value of the Reynolds number, *Re*, we have solved using a fourth-order Runge–Kutta integration in time and second-order central differences in space. Concentrating on two different wall amplitudes, we find that the sequence of behaviours for increasing *Re* mirrors the behaviour of the leading order solution. In fact, our results indicate that for the perturbed, symmetric channel, the solution loses symmetry at a lower Reynolds number than the solution for the unperturbed, symmetric channel and also suggest early period doubling and quasi-periodicity. However, in these cases we find that the perturbation solution grows exponentially. An examination of the solution in the large Reynolds number, small wall amplitude limit reveals that such growth is a result of having solved linearised approximations to the equations for the perturbation streamfunction (since we have assumed that the channel walls vary slowly). A result of this growth is that the similarity solution ceases to exist for the linear approximation and we are required to solve the full equations.

Chapter 7

Conclusion

7.1 General Conclusions

With a view to gaining a better understanding of fluid mixing in the physical, *in vitro* DGM, we have attempted to produce a simple, two-dimensional mathematical model, relevant to the main body. We have been especially interested in describing the "onion peeling" effect, which results when gastric secretions hydrate the food bolus. Working together with wall movements, these secretions cause the lower viscosity material around the edge of the bolus to "slough off", before a background flow draws this material into the antrum. All fluids were assumed to be homogeneous, immiscible, incompressible, isothermal and Newtonian with equal, constant densities. An analysis of characteristic values inside the DGM suggested that the Reynolds number is very small (of the $O(10^{-1})$), and so we initially took our governing equations to be those of Stokes flow.

Given the complexity of modelling the global flow in the DGM main body, we decided to focus our attention on a local description of the flow close to the wall. Our primary concern then became the temporal stability of a perturbed fluid interface between two fluids, which represented two separate phases of partially digested food mixed with gastric secretions. In chapter 2 a first attempt at modelling such a problem comprised two-fluid flow next to a sinusoidal wall, which moved with small amplitude in a prescribed way. This wall represented the body wall. After the decay of an initial transient, the solution is found to be stable and periodic, and the phase difference between the wall and interface is between zero and $\pi/2$. The amplitude of the interface is largest (equal to the amplitude of the wall) for small wavenumber disturbances. Streamline plots reveal two rows of closed cells and in this case it is hypothesised that transverse motions of the interface must be comparable in size to normal motions for appearance of the second row.

Larger wall amplitudes were studied in chapter 3, where we considered the flow of a single thin film next to a sinusoidally moving wall. The wall was held horizontal in case (i), and inclined at an angle to the horizontal in case (ii), where gravity was included in the analysis. After the decay of an initial transient the solution is again found to be periodic. In case (i) the x-dependence of the interface is always the same as the wall, whereas in case (ii) this is not necessarily true. For small wavenumbers of the wall and large capillary numbers the phase and amplitude of the interface tend to that of the wall (and here the interface amplitude is largest). Rows of cells similar to those seen in earlier chapters are observed in streamline plots in case (i). In case (ii) these cells are superposed with a prevailing flow that runs roughly parallel to the wall. Wave steepening can be observed at early times in case (ii), but breaking only occurs for an infinite capillary number. We briefly studied the solution when a constant shear stress was added at the free surface. The results suggested that including a second fluid above the thin film will not worsen wave steepening such that breaking occurs.

In chapter 4 we investigated two-fluid flow next to an elastic beam, moving with small amplitude. An instability is found at small wavenumbers for one of the two solutions for the wave speed. The instability appears to coincide with a phase difference between the wall and interface and also seems to require both the wall and interface to be free to move. Our solution necessitated that the tension in the beam was approximated as constant, resulting in a lower bound on the range of valid wavenumbers. However, amongst this range there still exist small wavenumbers for which the solution is unstable. In a brief study of a periodic pressure forcing below the elastic wall, it is relevant to the DGM that this promotes a periodic wall motion.

In chapter 5 we included a second wall, which represented the solid, undigested food bolus. We studied the problem of flow through a channel with fixed walls under the influence of a scalar material field, which represented the gastric secretions. The concentration of material was taken to be linearly proportional (to within a constant) to the surface tension at the interface. A single solution is found for the wave speed. Depending on the parameter choices, the solution is either stable for all wavenumbers or unstable for small wavenumbers. It is conjectured that the instability results when the interface sits in a favourable position on the single row of closed cells that correspond to the streamlines. Here interfacial perturbations are free to grow under the influence of the Marangoni force. We have found evidence that the presence of channel walls is necessary for this instability and hypothesised that in the case without walls, growth of the interface is always restricted by its position on the closed streamlines. For large wavenumbers waves always travel at the speed of the base-state horizontal velocity at the interface. For other wavenumbers they may travel faster or slower depending on the choice of parameters. For small wavenumbers there is found to be a correspondence between the stability regions and regions of faster or slower wave speed.

Lastly, in chapter 6, we extended our analysis to include the region surrounding that studied in previous chapters. Such an analysis is necessary to gauge the influence of the wider flow field on the previously studied region. In an initial study using plane polar co-ordinates to consider the flow of a single fluid between semi-infinite, hinged plates, it was found to be difficult to induce mixing of fluid particles in such a geometry under the assumption of creeping flow. We therefore chose to consider Navier–Stokes flow and, building on the work of Hall and Papageorgiou (1999), we investigated flow through a gradually diverging channel as a model of the local flow field in a strip taken through the middle of the main body. For small Reynolds numbers a unique, periodic, symmetric solution exists. As the Reynolds number, *Re*, is increased, we find evidence that there is a bifurcation to an asymmetric solution at a value of *Re* that is lower than for the case of an unperturbed channel. Increasing the Reynolds number further, for smaller wall amplitudes a bifurcation to a quasi-periodic solution may be seen. In general, a Feigenbaum cascade leads to chaos for higher Reynolds numbers. Our results also suggest early period-doubling and early quasi-periodicity in the case of the diverging channel compared to the uniform-width channel. The occurrence of early bifurcations in our results was accompanied by an exponentially growing solution. This growth was shown to be due to taking a linear approximation in the equations for the perturbation streamfunction.

7.2 Relation of Results to the DGM Main Body

Since the layer of gastric juice at the wall of the DGM body is likely to be thin and the idealised mathematical description in chapters 2 to 5 considers flow in a thin layer close to the body wall, we are particularly interested in a wall with long wavelength (small wavenumber). The small wavenumber instability found in chapters 4 and 5 is therefore particularly relevant. In both chapters 4 and 5 typical parameter values for the DGM suggest that an unstable solution is possible. In the DGM the thin layer of material found at the wall tends to have low pH and low viscosity, comprising for the most part of gastric juice, whilst the liquid material in the bulk tends to be of higher pH and higher viscosity. This suggests that the viscosity ratio, Λ, will be greater than one. In chapter 4, since none of the other parameters will be zero or infinite, we are well within the range of values for the unstable mode to occur. In chapter 5 the thinness of the layer next to the wall also suggests that the depth ratio, α, can be taken to be much less than one. If the material gradient in chapter 5 is taken to represent the pH of simulated secretions, the above suggests that the concentration ratio, $\hat{C}$, will be positive. In certain situations an increase in pH may facilitate certain chemical processes that increase the surface tension. Here the surface tension gradient, Γ, may also be taken to be positive. Alternately, should we take the material gradient to represent the presence of a surfactant found in the gastric juice, then this would suggest that $\hat{C}$ and Γ are both negative. We therefore have two examples where $\hat{C}$ and Γ have the same sign. An examination of figure 5.3 confirms that in these cases, the solution is likely to be unstable for small wavenumbers in our region of interest. Interestingly, figure 5.11 also suggests that the unstable waves will travel slower than the horizontal base-state velocity at the interface. We have therefore gained evidence that both the presence of an elastic wall and the addition of simulated gastric secretions may be instrumental for the growth of perturbations at the interface between fluid phases close to the wall of the DGM body. Consequently both are likely to be important for fluid mixing.

In chapter 6, since we now consider a region that spans the entire width of the DGM body, we may be justified in taking a larger typical length scale than that previously quoted (perhaps of the $O(10^{-1})$). In the case of a liquid meal, such as water, the dynamic viscosity is likely to be lower than our quoted value for gastric juice and it may be possible for the Reynolds number to reach values of the $O(10)$. In such a case the early symmetry breaking bifurcation found in our solution may be relevant, suggesting that it might be possible for the system to support an asymmetric, periodic flow field.

7.3 Open Questions

There are a number of open questions arising from our results. In chapter 4 we were unable to map fully the regions of valid, unstable solutions in parameter-space. Perhaps a more relevant problem would be to examine how the stability of the solution is affected if we allow the tension to vary over the length of the beam so that there is no longer a limit on the range of valid solutions, although it is likely that this would require a full numerical analysis. The results in chapter 5 highlight the need for a more thorough examination of the influence of the pressure gradient on the growth rate of disturbances. These results also point to a convective instability as a possible mechanism for any changes due to an altered pressure gradient, and we suggest the method of Briggs (1964) for further investigation.

The majority of chapters in this thesis have dealt with a linear analysis. The only exceptions to this were in the introduction of chapter 6, where we considered some simple results in plane polar co-ordinates, and chapter 3, where in order to progress we assumed that we were dealing with a thin film. It would be particularly interesting to consider the linear stabilities found in chapters 4 and 5 in terms of a nonlinear regime and to investigate any new instabilities that may arise. It would also be worth returning to the diverging channel problem studied in chapter 6 without linearising the equations for the perturbation streamfunction. Together with a more thorough examination of the space of solutions, this would give a clearer picture of the nature of early bifurcations when comparing to the case of a uniform-width channel.

In our work we have considered a simplified picture of the flow-field in the DGM body. There is scope to improve on our idealised model. The unstable solutions found in chapter 5 motivate further research in which a more complicated relationship between surface tension and chemical activity is considered, moving walls are reintroduced and, perhaps together with a nonlinear analysis, steepening or breaking waves may be observed at the interface. This would be a good likeness to the “onion peeling” effect observed in the stomach and DGM. In addition, it would be interesting to allow for concentration absorption at the fluid interface as in Frenkel and Halpern (2002) and Halpern and Frenkel (2003). This would give rise to a second solution for the wave speed. It is also worth noting that in chapter 5 the base-state concentration field and interfacial perturbation are imposed, whilst in the DGM body a concentration field is fully established through the flow. This concentration field may then act to perturb and possibly destabilise the fluid interface. A further improvement on our model could be the addition of either a sinusoidal flux of concentration at the walls or an imposed, uniform concentration pool at one end of the channel, which is advected using a Poiseuille-type flow. It would then be interesting to see how the advancing profile would affect an initially flat interface. Due to the difficulty of attempting to solve this problem analytically, the governing equations would likely need to be solved numerically, using a boundary integral method to account for the moving interface.

Alternatively, an improved model could use a phase field or diffuse-interface type method. Here a fixed grid is used, such that the fluid interface and any concentration discontinuity at this interface are treated as continuous and distributed over a thin area. Modelling the interface in this way would be a much easier task than tracking a moving free-boundary with a moving grid. In these methods, in general, the force due to surface tension may be calculated at each grid point using the field properties and the effect of this force on the fluid continuum is encapsulated through an extra term in the Navier–Stokes equations. In addition, the advection-diffusion equation is replaced with a continuum advection-diffusion equation (Cahn–Hilliard type equation).

In this thesis we have focussed on a local description of the flow in the DGM main body. It would be interesting to couple this small-scale description with a global analysis, such as that considered in terms of the human stomach by Pal *et al.* (2004) and Pal *et al.* (2007) using the lattice-Boltzmann method. Such a model would typically be more concerned with the transportation of material and would lend itself naturally to the validation of results using experimental data from the DGM.

The possibility also exists to model the antrum section of the DGM. Preliminary work investigating flow through a two-dimensional channel with small occlusions has revealed peaks in the shear stress on a circular element of fluid located at the centre of the channel. Future studies could include a calculation of the stress on a solid, suspended particle as a model of the stress experienced by a particle of food in the machine.

Appendices

Appendix A

Derivation of the Beam Equations

We derive the boundary condition at a thin, elastic wall, $y = s(x,t)$, modelled as a beam. We allow only small perturbations away from the state where the wall is flat, so that $s = O(\epsilon)$, where $0 < \epsilon \ll 1$ is a small parameter. We begin by considering a small element, dl, where l is arc length along the wall. Due to the deformation, this element is subject to an external force, $\mathbf{f}$, per unit length, an in-plane tension, τ, in the tangential direction, transverse shear tension, q, in the normal direction and a bending moment, m, as shown in figure A.1. Neglecting terms of $O(\epsilon^2)$ and smaller, the unit normal and tangential vectors to the curve $y = s$ are given by

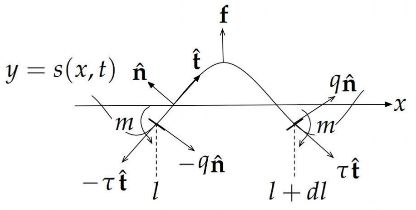

Figure A.1: The forces and moments on a small element, dl, of the elastic wall, $y = s$.

$$\hat{\mathbf{n}}(-s_x, 1), \quad \hat{\mathbf{t}} = (1, s_x), \tag{A.1}$$

where the unit normal vector to the curve is taken to point upwards.

Assuming that the element is in equilibrium (has negligible inertia), a force balance gives us

$$\tau(l+dl)\hat{\mathbf{t}}(l+dl) + q(l+dl)\hat{\mathbf{n}}(l+dl) - \tau(l)\hat{\mathbf{t}}(l) - q(l)\hat{\mathbf{n}}(l) + \mathbf{f}dl = \mathbf{0}. \tag{A.2}$$

Expanding in Taylor series about l, neglecting terms of $O(dl^2)$ and smaller and dividing by dl, we obtain

$$\tau\frac{d\hat{\mathbf{t}}(l)}{dl} + \frac{d\tau(l)}{dl}\hat{\mathbf{t}} + q\frac{d\hat{\mathbf{n}}(l)}{dl} + \frac{dq(l)}{dl}\hat{\mathbf{n}} + \mathbf{f} = \mathbf{0}. \tag{A.3}$$

The curvature of the element, κ, is defined such that $d\hat{\mathbf{t}}/dl = -\kappa\hat{\mathbf{n}}$. This implies that to leading order,

$$\kappa = -s_{xx}. \tag{A.4}$$

By differentiating the quantities $\hat{\mathbf{n}} \cdot \hat{\mathbf{t}} = 0$ and $\hat{\mathbf{n}} \cdot \hat{\mathbf{n}} = 1$ with respect to l we can also deduce that $d\hat{\mathbf{n}}/dl = \kappa\hat{\mathbf{t}}$. Therefore, the normal and tangential components of (A.3) are respectively

$$-\kappa\tau + \frac{dq}{dl} + \mathbf{f} \cdot \hat{\mathbf{n}} = 0, \quad \frac{d\tau}{dl} + q\kappa + \mathbf{f} \cdot \hat{\mathbf{t}} = 0. \tag{A.5}$$

A moment balance about l in the anticlockwise direction gives us

$$q(l + dl)dl - m(l + dl) + m(l) = 0, \tag{A.6}$$

which, dividing by dl, implies that

$$q = \frac{dm}{dl}. \tag{A.7}$$

We assume that the beam is under a state of plane stress (there are no forces acting in the z-direction, where z points in the direction of $\hat{\mathbf{t}} \times \hat{\mathbf{n}}$), as described in Prescott (1961) and Howell *et al.* (2009). Here, since the longitudinal stresses in the beam are found to be much larger than the transverse stresses, it is assumed that σ_{yy} may be neglected compared to σ_{xx}. It is then found that $\sigma_{xx} = \kappa E y$, where E is Young's modulus (a measure of the stiffness equal to the tensile stress divided by the tensile strain of the beam) and so the net moment on a cross-section A of the beam is given by

$$m = \iint_A y\sigma_{xx} dydz = \kappa EI = \kappa E_B, \tag{A.8}$$

where the second moment of inertia of A about the z-axis is

$$I = \iint_A y^2 dydz, \tag{A.9}$$

and $E_B > 0$ is the bending modulus. Here we choose m to be positive at a maximum, i.e. where s_{xx} is negative. Since the wall is only deformed by a small amount, we may assume that differentiation with respect to l (along the arc) is the same as differentiation with respect to x. Then, neglecting terms of $O(\epsilon^2)$ and smaller and substituting in q and κ, equations (A.5) become the beam equations,

$$-E_B s_{xxxx} + \tau s_{xx} = -\mathbf{f} \cdot \hat{\mathbf{n}}, \quad \frac{d\tau}{dx} = -\mathbf{f} \cdot \hat{\mathbf{t}} \quad \text{on} \quad y = s. \tag{A.10}$$

Appendix B

Newton's Method As Used in the Shooting Method

We describe Newton's method, as used in chapter 5 for finding a γ such that $\boldsymbol{\xi}(\gamma) \to \mathbf{0}$, where

$$\boldsymbol{\xi}\left(\gamma\right) = \left(\begin{array}{c} \xi_1 \\ \xi_2 \end{array}\right), \quad \gamma = \left(\begin{array}{c} \gamma_1 \\ \gamma_2 \end{array}\right). \tag{B.1}$$

Here $\boldsymbol{\xi}$ depends on γ since ξ_1 and ξ_2 depend on our guesses for γ_1 and γ_2. We increment γ_1 and γ_2 by small changes s_1 and s_2 respectively, so that

$$\boldsymbol{\xi}(\gamma + \mathbf{s}) = \boldsymbol{\xi}(\gamma) + \mathbf{s} \cdot \mathbf{J}(\gamma), \quad \mathbf{s} = \left(\begin{array}{c} s_1 \\ s_2 \end{array}\right), \quad \mathbf{J} = \nabla \boldsymbol{\xi}, \tag{B.2}$$

where we neglect terms of $O(\mathbf{s}^2)$ and smaller. Here we may compute the $(1,1)$ entry of the Jacobian, $\mathbf{J}$, for instance, by writing

$$\frac{\partial \xi_1}{\partial \gamma_1}(\gamma_1, \gamma_2) = \frac{\xi_1(\gamma_1 + \delta, \gamma_2) - \xi_1(\gamma_1, \gamma_2)}{\delta}, \tag{B.3}$$

where $0 < \delta \ll 1$. In this equation, to compute $\xi_1(\gamma_1 + \delta, \gamma_2)$, we must integrate $d\mathbf{W}_1/dy$ from $y = 0$ to α with the initial guess γ_1 replaced by $\gamma_1 + \delta$ to give us $W_1(\alpha)$, but may use the earlier results of integrating $d\mathbf{W}_2/dy$ from $y = 1$ to α to give us $W_2(\alpha)$. In order to move ξ_1 and ξ_2 towards zero, we now let $\boldsymbol{\xi}(\gamma + \mathbf{s}) = 0$ in (B.2), giving us

$$\mathbf{s} \cdot \mathbf{J} = -\boldsymbol{\xi}(\gamma). \tag{B.4}$$

Since $\mathbf{J}$ and $\boldsymbol{\xi}$ are known, (B.4) may be solved using Gaussian elimination to obtain $\mathbf{s}$. Our updated guess for γ is then given by $\gamma + \mathbf{s}$.

Appendix C

Calculating the Floquet Exponent

In chapter 6 we calculate the Floquet exponents for our solution. A good summary on the subject of Floquet theory can be found in Joseph (1976). The method is as follows. We use the technique described in Hall and Papageorgiou (1999), assuming that the solution comprises a base state (subscript B) and a much smaller perturbation (subscript P), both functions of η and t. When examining the solution for $\psi_1{}^{(1)}$, we let

$$\left(\psi_1{}^{(1)}, \Omega_1{}^{(1)}\right) = \left(\psi_1{}^{(1)}{}_B, \Omega_1{}^{(1)}{}_B\right) + \left(\psi_1{}^{(1)}{}_P, \Omega_1{}^{(1)}{}_P\right), \tag{C.1}$$

whilst, when examining the solution for $\psi_2{}^{(1)}$, we take

$$\left(\hat{\psi_2}{}^{(1)}, \Omega_2{}^{(1)}, p_2{}^{(1)}\right) = \left(\hat{\psi_2}{}^{(1)}{}_B, \Omega_2{}^{(1)}{}_B, p_2{}^{(1)}{}_B\right) + \left(\hat{\psi_2}{}^{(1)}{}_P, \Omega_2{}^{(1)}{}_P, p_2{}^{(1)}{}_P\right). \tag{C.2}$$

In the case $Re < Re_c$ we take $\psi^{(0)}$ to be the symmetric, π periodic solution, whilst for $Re \geq Re_c$ it is taken to be the asymmetric, $n\pi$ periodic solution, where $n = 1, 2, 3, \cdots$ depends on the Reynolds number. The base solution in (C.1) or (C.2) can then be thought of as the underlying periodic solution for $\psi_1{}^{(1)}$ or $\hat{\psi_2}{}^{(1)}$.

Substituting (C.1) into equations (6.38) and (6.42) and (C.2) into (6.39), (6.43) and (6.44), to leading order we obtain the same equations but for the base solutions, whilst to first order, we find equations for the perturbations,

$$\begin{aligned}
L^2\psi_1{}^{(1)}{}_P =& -H^{(0)^2}\Omega_1{}^{(1)}{}_P, \qquad\qquad\qquad\qquad\qquad\qquad\qquad\qquad\qquad\qquad\qquad\qquad \text{(C.3)}\\
\frac{\partial \Omega_1{}^{(1)}{}_P}{\partial t} =& M_1{}^{(1)}{}_P(t, \psi^{(0)}, \psi_1{}^{(1)}{}_P, \Omega^{(0)}, \Omega_1{}^{(1)}{}_P; Re),\\
M_1{}^{(1)}{}_P =& \frac{1}{ReH^{(0)^2}}\frac{\partial^2\Omega_1{}^{(1)}{}_P}{\partial\eta^2} - \frac{1}{H^{(0)}}\Bigg(-\left(\frac{dH^{(0)}}{dt}\eta + \psi^{(0)}\right)\frac{\partial\Omega_1{}^{(1)}{}_P}{\partial\eta}\\
&+ 2\frac{\partial\psi^{(0)}}{\partial\eta}\Omega_1{}^{(1)}{}_P + \frac{\partial\psi_1{}^{(1)}{}_P}{\partial\eta}\Omega^{(0)} - 2\psi_1{}^{(1)}{}_P\frac{\partial\Omega^{(0)}}{\partial\eta}\Bigg), \qquad \text{(C.4)}
\end{aligned}$$

and

$$\begin{aligned}
{\Omega_2}^{(1)}{}_P &= -\frac{1}{H^{(0)}}\frac{\partial {\hat{\psi_2}}^{(1)}{}_P}{\partial \eta}, && \text{(C.5)}\\
\frac{\partial {\hat{\psi_2}}^{(1)}{}_P}{\partial t} &= {M_2}^{(1)}{}_P(t, \psi^{(0)}, {\hat{\psi_2}}^{(1)}{}_P; Re),\\
{M_2}^{(1)} &= \frac{1}{ReH^{(0)2}}\frac{\partial^2 {\hat{\psi_2}}^{(1)}{}_P}{\partial \eta^2} + \frac{1}{H^{(0)}}\left(\frac{\partial {\hat{\psi_2}}^{(1)}{}_P}{\partial \eta}\left(\frac{dH^{(0)}}{dt}\eta + \psi^{(0)}\right) - \frac{\partial \psi^{(0)}}{\partial \eta}{\hat{\psi_2}}^{(1)}{}_P\right), && \text{(C.6)}\\
{p_2}^{(1)}{}_P &= 0, && \text{(C.7)}
\end{aligned}$$

where we have used that ${p_2}^{(1)}(\eta = -1, t) = 0$. From (6.48), (6.50) and (6.51), these equations are accompanied by the boundary conditions,

$${\psi_1}^{(1)}{}_P(\eta = \pm 1, t) = 0, \quad \frac{\partial {\psi_1}^{(1)}{}_P}{\partial \eta}(\eta = \pm 1, t) = 0, \tag{C.8}$$

and

$$\frac{\partial {\hat{\psi_2}}^{(1)}{}_P}{\partial \eta}(\eta = \pm 1, t) = 0. \tag{C.9}$$

We note that the Floquet analysis for ${\hat{\psi_2}}^{(1)}$ does not depend on ${\psi_1}^{(1)}$, only on $\psi^{(0)}$.

We solve equations (C.3), (C.4) and (C.8) or (C.5), (C.6) and (C.9) using the same method as for the full equations, using general, asymmetric initial conditions which satisfy the boundary conditions. Where the $O(1)$ solution is $n\pi$ periodic, the coefficients of (C.3) to (C.6) are $n\pi$ periodic and so, on the basis of Floquet theory, we may write

$$\begin{aligned}
&\left({\psi_1}^{(1)}{}_P, {\Omega_1}^{(1)}{}_P\right) = e^{\gamma t}\left({\psi_1}^{(1)+}(\eta, t), {\Omega_1}^{(1)+}(\eta, t)\right) + \text{c.c},\\
&{\psi_1}^{(1)+}(\eta, t + n\pi) = {\psi_1}^{(1)+}(\eta, t), \quad {\Omega_1}^{(1)+}(\eta, t + n\pi) = {\Omega_1}^{(1)+}(\eta, t),
\end{aligned} \tag{C.10}$$

or

$$\begin{aligned}
&\left(\hat{\psi}_{2P}^{(1)}, {\Omega_2}^{(1)}{}_P\right) = e^{\gamma t}\left({\hat{\psi_2}}^{(1)+}(\eta, t), {\Omega_1}^{(1)+}(\eta, t)\right) + \text{c.c.}\\
&{\hat{\psi_2}}^{(1)+}(\eta, t + n\pi) = {\hat{\psi_2}}^{(1)+}(\eta, t), \quad {\Omega_2}^{(1)+}(\eta, t + n\pi) = {\Omega_2}^{(1)+}(\eta, t),
\end{aligned} \tag{C.11}$$

where $\gamma = \gamma_R + i\gamma_I$ is the Floquet exponent in each case and c.c. denotes the complex conjugate. Letting $S(t)$ be the perturbation part of the lower wall shear, either $\partial^2 {\psi_1}^{(1)}{}_P/\partial \eta^2(-1, t)$ or $\partial^2 {\hat{\psi_2}}^{(1)}{}_P/\partial \eta^2(-1, t)$, we have

$$S = e^{\gamma t}S^+(t) + \text{c.c.} = 2r(t)e^{\gamma_R t}\cos(\gamma_I t + \theta(t)), \quad S^+(t + n\pi) = S^+(t), \tag{C.12}$$

where we let $S^+ = r(t)\exp(i\theta(t))$.

In the cases where ${\psi_1}^{(1)}$ or ${\psi_2}^{(1)}$ either has period $n\pi$, or behaves like an exponential to a real power multiplied by a function with period $n\pi$, we consider the change in the wall shear over time intervals of length $n\pi$. Using the second of equations (C.12),

$$\log\left(S(t+n\pi)\right) - \log\left(S(t)\right) = \gamma_R n\pi + \log\left(\frac{\cos(\gamma_I(t+n\pi)+\theta(t))}{\cos(\gamma_I t+\theta(t))}\right), \tag{C.13}$$

and so, since it must be true that $\gamma_I = 0$, γ_R (the growth rate of the perturbation) is given by

$$\gamma_R = \frac{1}{n\pi}\log\left(\frac{S(t+n\pi)}{S(t)}\right). \tag{C.14}$$

We note that there exist a whole family of eigenvalues, γ, and that this method gives us the eigenvalue with the largest real part.

When ${\psi_1}^{(1)}$ or ${\psi_2}^{(1)}$ behaves like an exponential to a real power multiplied by a function with period $m\pi$ (where m is some integer multiple of n), since $S+$ is $n\pi$ periodic, it must be true that a complex conjugate pair of eigenvalues cross the γ_I axis into the $\gamma_R > 0$ plane such that their real part is greater than the single eigenvalue on the γ_R axis and $\Re(\exp(i\gamma_I t))$ is $m\pi$ periodic. This implies that $\gamma_I = \pm 2/m$. In this case we instead consider an interval of length $m\pi$ and we find that

$$\gamma_R = \frac{1}{m\pi}\log\left(\frac{S(t+m\pi)}{S(t)}\right). \tag{C.15}$$

To check the validity of this method, we may apply the same technique to (6.41) and (6.37), the equations for $\psi^{(0)}$, perturbing about the π periodic, symmetric solution for $\psi^{(0)}$ in the region around the bifurcation, $Re = Re_c$. In this case our equations for the perturbation depend on the base state. Since it is the π periodic, asymmetric solution that is the most attracting for $Re > Re_c$, to ensure that we obtain the symmetric solution for this base state, we must solve in the half-interval from $\eta = -1$ to 0, specifying that at $\eta = 0$ the base state solution and its second derivative with respect to η are zero. We then extend to the full interval by symmetry. We find that, as expected, as we cross $Re = Re_c$, the Floquet exponent changes from negative to positive as the solution for $\psi^{(0)}$ changes from symmetric to asymmetric.

References

M. Abramowitz and I. A. Stegun. *Handbook of Mathematical Functions*. Dover Publications, New York, 1964.

D.J. Acheson. *Elementary Fluid Dynamics*. Oxford University Press, Oxford, 1990.

W. H. H. Banks, P. G. Drazin, and M. B. Zaturska. On perturbations of Jeffery–Hamel flow. *J. Fluid Mech.*, 186:559–581, 1988.

H. Bénard. Les tourbillons cellulaires dans une nappe liquide. *Rev. Gén. Sci. Pure Appl.*, 11:1261–1271, 1309–1328, 1900.

T. B. Benjamin. Wave formation in laminar flow down an inclined plane. *J. Fluid Mech.*, 2:554–574, 1957.

T. B. Benjamin. Effects of a flexible boundary on hydrodynamic stability. *J. Fluid Mech.*, 9:513–532, 1960.

T. B. Benjamin. The threefold classification of unstable disturbances in flexible surfaces bounding inviscid flows. *J. Fluid Mech.*, 16:436–450, 1963.

G. Beylkin, J. M. Keiser, and L. Vozovoi. A new class of time discretization schemes for the solution of nonlinear pdes. *J. Comp. Phys.*, 147:362–387, 1998.

M. G. Blyth. Effect of pulsations on two-layer channel flow. *Journal of Engineering Mathematics*, 59(1):123–137, 2007.

M. G. Blyth and P. Hall. Oscillatory flow near a stagnation point. *SIAM Journal on Applied Mathematics*, 63(5):1604–1614, 2003.

M. G. Blyth and C. Pozrikidis. Effect of surfactants on the stability of two-layer channel flow. *J. Fluid Mech.*, 505:59–86, 2004.

M. G. Blyth, P. Hall, and D. T. Papageorgiou. Chaotic flows in pulsating cylindrical tubes: a class of exact Navier–Stokes solutions. *J. Fluid Mech.*, 481:187–213, 2003.

R. J. Briggs. *Electron-Stream Interaction with Plasmas*. MIT press, Cambridge, MA, 1964.

N. M. Bujurke, V. B. Awati, and N. N. Katagi. Computer extended series solution for flow in a narrow channel of varying gap. *Applied Mathematics and Computation*, 186: 54–69, 2007.

F. H. Busse. Multiple solutions for convection in a two component fluid. *Geophys. Res. Lett.*, 9(5):519–522, 1982.

J. H. E. Cartwright, E. Gouillart, N. Piro, O. Piro, and I. Tuval. Geometric mixing. arXiv:1206.6894v1, June 2012.

C. F. Chen and C. C. Chen. Effect of surface tension on the stability of a binary fluid layer under reduced gravity. *Phys. Fluids*, 6:1482–1490, 1994.

C. F. Chen and T. F. Su. Effect of surface tension on the onset of convection in a double-diffusive layer. *Phys. Fluids A*, 4(11):2360–2367, 1992.

K. Chen. Wave formation in the gravity-driven low-Reynolds number flow of two liquid films down an inclined plane. *Phys. Fluids A*, 5(5):3038–3048, 1993.

S. M. Cox and P. C. Matthews. Exponential time differencing for stiff systems. *J. Comput. Phys.*, 176:430–455, 2002.

D. G. Crighton and J. E. Oswell. Fluid loading with mean flow. I. response of an elastic plate to localized excitation. *Phil. Trans. R. Soc. Lond. A*, 335:557–592, 1991.

C. Davies and P. W. Carpenter. Numerical simulation of the evolution of Tollmien–Schlichting waves over finite compliant panels. *J. Fluid Mech.*, 335:361–392, 1997.

P. G. Drazin. Flow through a diverging channel: instability and bifurcation. *Fluid Dyn. Res.*, 24(6):321–327, 1999.

W. E and J. G. Liu. Vorticity boundary condition and related issues for finite difference schemes. *J. Comput. Phys.*, 124:368–382, 1996.

L. Espin and D. T. Papageorgiou. Flow in a channel with accelerating or decelerating wall velocity: A comparison between self-similar solutions and Navier–Stokes computations in finite domains. *Phys. Fluids*, 21:113601 (17 pages), 2009.

A. L. Frenkel and D. Halpern. Stokes-flow instability due to interfacial surfactant. *Phys. Fluids*, 14:45–48, 2002.

F. D. Hains and J. F. Price. Effect of a flexible wall on the stability of Poiseuille flow. *Phys. Fluids*, 5:365 (1 page), 1962.

P. Hall and D. T. Papageorgiou. The onset of chaos in a class of Navier–Stokes solutions. *J. Fluid Mech.*, 393:59–87, 1999.

D. Halpern and A. L. Frenkel. Destabilization of a creeping flow by interfacial surfactant: Linear theory extended to all wavenumbers. *J. Fluid Mech.*, 485:191–220, 2003.

M. Hamadiche, J. Scott, and D. Jeandel. Temporal stability of Jeffery–Hamel flow. *J. Fluid Mech.*, 268:71–88, 1994.

M. Heil and S. L. Waters. Transverse flows in rapidly oscillating elastic cylindrical shells. *J. Fluid Mech.*, 547:185–214, 2006.

C. P. Hills. Eddy structures induced within a wedge by a honing circular arc. *Theoret. Comput. Fluid Dynamics*, 15:1–10, 2001.

P. Howell, G. Kozyreff, and J. Ockendon. *Applied Solid Mechanics*. Cambridge University Press, Cambridge, 2009.

O. E. Jensen, M. K. Horsburgh, D. Halpern, and D. P. Gaver III. The steady propagation of a bubble in a flexible-walled channel: Asymptotic and computational models. *Phys. Fluids*, 14(2):443–457, 2002.

D. D. Joseph. *Stability of Fluid Motions I*. Springer Tracts in Natural Philosophy, vol 27, Springer–Verlag, Berlin, Germany, 1976.

Y. O. Kabova, A. Alexeev, T. Gambaryan-Roisman, and P. Stephan. Marangoni-induced deformation and rupture of a liquid film on a heated microstructured wall. *Phys. Fluids*, 18:012104 (15 pages), 2006.

F. Kang and K. Chen. Gravity-driven two-layer flow down a slightly wavy periodic incline at low Reynolds numbers. *Int. J. Multiphase Flow*, 21(3):501–513, 1995.

A. R. A. Khaled and K. Vafai. Analysis of flow and heat transfer inside oscillatory squeezed films subject to a varying clearance. *International Journal of Heat and Mass Transfer*, 46:631–641, 2003.

F. Kong and R. P. Singh. Disintegration of solid foods in human stomach. *Journal of Food Science*, 73(5):68–80, 2008a.

F. Kong and R. P. Singh. A model stomach system to investigate disintegration kinetics of solid foods during gastric digestion. *Journal of Food Science*, 73(5):E202–E210, 2008b.

C. Krul, A. Luiten-Schuite, R. Baan, H. Verhagen, G. Mohn, V. Feron, and R. Havenaar. Application of a dynamic in vitro gastrointestinal tract model to study the availability of food mutagens, using heterocyclic aromatic amines as model compounds. *Food and Chemical Toxicology*, 38:783–792, 2000.

V. Kumaran and L. Srivatsan. Stability of fluid flow past a membrane. *Eur. Phys. J. B*, 2: 259–266, 1998.

M. T. Landahl. On the stability of a laminar incompressible boundary layer over a flexible surface. *J. Fluid Mech.*, 13:609–632, 1962.

A. J. Leger. *Mathematical and Numerical Modelling of Peristaltic Flow and Absorption in the Small Intestine*. PhD thesis, Bath University, 2005.

Y. Li and M. G. Blyth. Axisymmetric flow of two fluids in a pulsating pipe. *Journal of Engineering Mathematics*, 63(1):135–151, 2009.

R. J. Lingwood and N. Peake. On the causal behaviour of flow over an elastic wall. *J. Fluid Mech.*, 396:319–344, 1999.

D. S. Loewenherz and C. J. Lawrence. The effect of viscosity stratification on the stability of a free surface flow at low Reynolds number. *Phys. Fluids A*, 1(10):1686–1693, 1989.

H. J. Lugt and E. W. Schwiderski. Flows around dihedral angles. I. Eigenmotion analysis. *Proc. Roy. Soc. A.*, 285:382–399, 1964.

H. Luo and C. Pozrikidis. Shear-driven and channel flow of a liquid film over a corrugated or indented wall. *J. Fluid Mech.*, 556:167–188, 2006.

X. Y. Luo and T. J. Pedley. A numerical simulation of steady flow in a 2-D collapsible channel. *Journal of Fluids and Structures*, 9:149–174, 1995.

E. O. Macagno, J. Christensen, and C. L. Lee. Modeling the effect of wall movement on absorption in the intestine. *American Journal of Physiology*, 243:541–550, 1982.

T. R. Mahapatra and A. S. Gupta. Stagnation-point flow towards a stretching surface. *The Canadian Journal of Chemical Engineering*, 81:259–263, 2003.

L. Marciani, P. A. Gowland, R. C. Spiller, P. Manoj, R. Moore, P. Young, and A. Fillery-Travis. Effect of meal viscosity and nutrients on satiety, intragastric dilution and emptying assessed by MRI. *Am. J. Physiol. Gastrointest. Liver Physiol.*, 280(6):G1227–G1233, 2001.

L. Marciani, M. S. J. Wickham, and Singh G. Enhancement of intragastric acid stability of a fat emulsion meal delays gastric emptying and increases cholecystokinin release and gall bladder contraction. *American Journal of Physiology, Gastrointestinal and Liver Physiology*, 292:1607–1613, 2007.

A. McAlpine and P. G. Drazin. On the spatio-temporal development of small perturbations of Jeffery–Hamel flows. *Fluid Dyn. Res.*, 22:123–138, 1998.

A. Mercuri, A. Passalacqua, M. S. J. Wickham, R. M. Faulks, D. Q. M. Craig, and S. A. Barker. The effect of composition and gastric conditions on the self-emulsification process of ibuprofen-loaded self-emulsifying drug delivery systems: a microscopic and Dynamic Gastric Model study. *Pharm Res.*, 28:1540–1551, 2011.

H. K. Moffatt and B. R. Duffy. Local similarity solutions and their limitations. *J. Fluid Mech.*, 96:299–313, 1980.

M. A. Nicosia and J. G. Brasseur. A mathematical model for estimating muscle tension *in vivo* during esophageal bolus transport. *J. theor. Biol.*, 219:235–255, 2002.

W. Nusselt. The surface condensation of water vapour. *Z. Ver. D. Ing.*, 60:541–546, 569–578, 1916.

A. Pal, K. Indireshkumar, W. Schwizer, B. Abrahamsson, M. Fried, and J. G. Brasseur. Gastric flow and mixing studied using computer simulation. *The Royal Society*, 271: 2587–2594, 2004.

A. Pal, J. G. Brasseur, and B. Abrahamsson. A stomach road or "magenstrasse" for gastric emptying. *Journal of Biomechanics*, 40:1202–1210, 2007.

J. R. A. Pearson. On convection cells induced by surface tension. *J. Fluid Mech.*, 4: 489–500, 1958.

T. J. Pedley and X. Y. Luo. Modelling flow and oscillations in collapsible tubes. *Theoret. Comput. Fluid Dynamics*, 10:277–294, 1998.

C. Pozrikidis. A study of peristaltic flow. *J. Fluid Mech.*, 180:515–527, 1987.

C. Pozrikidis. The flow of a liquid film along a periodic wall. *J. Fluid Mech.*, 188:275–300, 1988.

C. Pozrikidis and A. I. Hill. Surfactant-induced instability of a sheared liquid layer. *IMA J. Appl. Math.*, 76(6):859–875, 2011.

J. Prescott. *Applied Elasticity*. Dover Publications, Inc., New York, 1961.

Y. Renardy and D. D. Joseph. Oscillatory instability in a Bénard problem of two fluids. *Phys. Fluids*, 28:788–793, 1985.

L. M. Rickett, R. Penfold, M. G. Blyth, M. J. Cooker, and R. Purvis. Incipient mixing in a dynamic model gut device. Manuscript in preparation, 2013.

J. Rotenberry and P. Saffman. Effect of compliant boundaries on weakly nonlinear shear waves in channel flow. *J. Appl. Maths*, 50:361–394, 1990.

C. Salles, A. Tarrega, P. Mielle, J. Maratray, P. Gorria, J. Liaboeuf, and J. J. Liodenot. Development of a chewing simulator for food breakdown and the analysis of *in vitro* flavor compound release in a mouth environment. *Journal of Food Engineering*, 82: 189–198, 2007.

L. E. Scriven and C. V. Sternling. The Marangoni effects. *Nature*, 187:186–188, 1960.

L. E. Scriven and C. V. Sternling. On cellular convection driven by surface-tension gradients: effects of mean surface tension and surface viscosity. *J. Fluid Mech.*, 19: 321–340, 1964.

T. W. Secomb. Flow in a channel with pulsating walls. *J. Fluid Mech.*, 88:273–288, 1978.

S. Shetty and R. L. Cerro. Flow of a thin film over a periodic surface. *Int. J. Multiphase Flow*, 19(6):1013–1027, 1993.

J. R. L. Skarda, D. Jacqmin, and F. E. McCaughan. Exact and approximate solutions to the double-diffusive Marangoni–Bénard problem with cross-diffusive terms. *J. Fluid Mech.*, 366:109–133, 1998.

P. Spratt, C. Nicolella, and D. L. Pyle. An engineering model of the human colon. *Trans IChemE C*, 83:147–157, 2005.

S. Sreenivasan and S. P. Lin. Surface tension driven instability of a liquid film flow down a heated incline. *International Journal of Heat and Mass Transfer*, 21:1517–1526, 1978.

B. R. Stoll, R. P. Batycky, H. R. Leipold, S. Milstein, and D. A. Edwards. A theory of molecular absorption from the small intestine. *Chemical Engineering Science*, 55: 473–489, 2000.

J. T. Stuart, R. C. DiPrima, P. M. Eagles, and A. Davey. On the instability of the flow in a squeeze lubrication film. *Proc. R. Soc. Lond. A*, 430:347–375, 1990.

R. M. Thaokar and V. Kumaran. Stability of fluid flow past a membrane. *J. Fluid Mech.*, 472:29–50, 2002.

A. Tharakan. *Modelling of Physical and Chemical Processes in the Small Intestine*. PhD thesis, University of Birmingham, 2008.

J. Thomson. On certain curious motions observable at the surfaces of wine and other alcoholic liquors. *Phil. Mag.*, 10:330–333, 1855.

L. N. Trefethen. *Spectral Methods in MATLAB*. SIAM, Philadelphia, 2000.

I. C. Trelea, S. Atlan, I. Déléris, A. Saint-Eve, M. Marin, and I. Souchon. Mechanistic mathematical model for in vivo aroma release during eating of semiliquid foods. *Chem. Senses*, 33:181–192, 2008.

D. Tseluiko and D. T. Papageorgiou. Nonlinear dynamics of electrified thin liquid films. *SIAM Journal on Applied Mathematics*, 67:1310–1329, 2006.

C. Y. Wang. Liquid film flowing slowly down a wavy incline. *AIChE J.*, 27:207–212, 1981.

E. B. B. Watson, W. H. H. Banks, M. B. Zaturska, and P. G. Drazin. On transition to chaos in two-dimensional channel flow symmetrically driven by accelerating walls. *J. Fluid Mech.*, 212:451–485, 2008.

H. H. Wei. Effect of surfactant on the long-wave instability of a shear-imposed liquid flow down an inclined plane. *Phys. Fluids*, 17(1):012103 (5 pages), 2008.

M. J. S. Wickham, R. M. Faulks, J. Mann, and G. Mandalari. The design, operation, and application of a Dynamic Gastric Model. *Dissolution Technol.*, 19(3):15–22, 2012.

A. Wierschem and N. Aksel. Instability of a liquid film flowing down an inclined wavy plane. *Physica D*, 186:221–237, 2003.

A. Wierschem, C. Lepski, and N. Aksel. Effect of long undulated bottoms on thin gravity-driven films. *Acta Mech.*, 179:41–66, 2005.

H. F. Woollard, J. Billingham, O. E. Jensen, and G. Lian. A multi-scale model for solute transport in a wavy-walled channel. *J. Eng. Math.*, 64:25–48, 2009.

C. S. Yih. Stability of a liquid flow down an inclined plane. *Phys. Fluids*, 6:321–334, 1963.

C. S. Yih. Instability due to viscosity stratification. *J. Fluid Mech.*, 27:337–352, 1967.

R. W. Zeren and W. C. Reynolds. Thermal instabilities in two-fluid horizontal layers. *J. Fluid Mech.*, 53:305–327, 1972.